

DOCTORAL THESIS

The Measurement and Modelling of Cosmic Ray Muons at KM3NeT Detectors

Author: Piotr Kalaczyński

Warsaw, September 2023



**NATIONAL
CENTRE
FOR NUCLEAR
RESEARCH**
ŚWIERK

A thesis submitted in fulfilment of the requirements
for the degree of Doctor of Philosophy
in the
High Energy Physics Division
Department of Fundamental Research
National Centre for Nuclear Research

Supervisor of the dissertation

Prof. dr hab. Ewa Rondio

Co-supervisor of the dissertation

Dr Piotr Mijakowski

I wish to dedicate my work to my deer* wife Daniela
who makes me a better person every day and who put up with me devoting
a large portion of the last few years to this work.

*pun intended

Quotes not necessarily related to the thesis that the author just fancied to have here:

‘By discovering nature, you discover yourself’

— Maxime Lagacé

‘I am the Super-Kamiokande’

— Piotr Mijakowski

‘Contra vim mortis non crescit salvia in hortis’

(No herb grows in the gardens against the power of death)

— Sigismund III Vasa on his deathbed

‘Woof woof woof!’

— Mecenás & Fiona (our dogs, expressing their irritation at me for writing this thesis instead of playing with them)

‘Indeed, we know what to do with space but do not know what to do about time, except to make it subservient to space. Most of us seem to labor for the sake of things of space. As a result we suffer from a deeply rooted dread of time and stand aghast when compelled to look into its face. Time to us is sarcasm, a slick treacherous monster with a jaw like a furnace incinerating every moment of our lives. Shrinking, therefore, from facing time, we escape for shelter to things of space.’

— Abraham Joshua Heschel: ‘The Sabbath: its meaning for modern man’

Declaration of Authorship

I, Piotr Kalaczyński, declare that this thesis, titled:

“The Measurement and Modelling of Cosmic Ray Muons at KM3NeT Detectors”

and the work presented in it is my own.

I confirm that:

- This work was done wholly or mainly while in candidature for a research degree at the National Centre for Nuclear Research.
- Where any part of this thesis has previously been submitted for a degree or any other qualification at the National Centre for Nuclear Research or any other institution, this has been clearly stated.
- Where I have consulted the published work of others, this is always clearly attributed.
- Where I have quoted from the work of others, the source is always given. Except for such quotations, this dissertation is entirely my work.
- I have acknowledged all main sources of help.
- Where the thesis is based on work done by myself jointly with others, I have made clear exactly what was done by others and what I have contributed myself.

Signed: _____

Date: _____

Abstract

Atmospheric muons are the most frequently observed form of cosmic radiation. Despite this, the existence of the muon flux component produced in decays of short-lived parent particles, called prompt muon flux still awaits experimental confirmation. This contribution to the muon flux is expected to start dominating at high energies, around PeV, since many of the prompt parent particles are heavy hadrons, containing charm and strange quarks. The aim of this thesis was two-fold: to evaluate the possibility of observing the prompt muon flux and to validate the performance of the KM3NeT detectors.

The KM3NeT experiment is a research network of underwater Cherenkov neutrino telescopes, currently under construction at two different locations in the Mediterranean Sea. The ARCA detector, dedicated to high-energy neutrino astronomy, is located near the coast of Italy at Portopalo di Capo Passero. The second one is ORCA, and it focuses on the low-energy atmospheric neutrino physics and is built offshore Toulon, in France. Even in their intermediate configurations, the KM3NeT detectors collect vast amounts of muon data. This work makes use of the muon data to evaluate the current operation of KM3NeT/ARCA and KM3NeT/ORCA and estimate their future potential.

To study the performance of KM3NeT detectors, an extensive Monte Carlo (MC) simulation of the muon events has been produced using the CORSIKA code, coupled with a chain of KM3NeT processing software. It was possible through significant improvements in the open-source KM3NeT application, responsible for the transport of simulated particles to the detector.

The MC simulation was put to use in the reconstruction of several observables: muon bundle energy, total primary energy and muon multiplicity. The regression of energy and multiplicity was carried out utilising machine learning tools. The bundle energy reconstruction beat the standard KM3NeT energy reconstruction by a large margin. Obtaining predictions of total primary energy and muon multiplicity allowed for the first measurements of such quantities by an underwater neutrino telescope.

The developed reconstruction was directly applied in the main physics analysis, which investigated the potential of KM3NeT detectors to observe the prompt atmospheric muon flux. The complete KM3NeT detectors should be able to confirm the prompt signal within 4–6 years of operation, possibly even sooner if their measurements are combined. Currently, the sensitivity is strongly limited by systematic uncertainties, which may be reduced by the time ARCA and ORCA are completed.

Streszczenie

Miony atmosferyczne to najczęściej obserwowana forma promieniowania kosmicznego. Pomimo tego, istnienie komponentu strumienia mionów powstającego w rozpadach krótko żyjących cząstek-rodziców, nazywanego natychmiastowym strumieniem mionów, wciąż pozostaje niepotwierdzone eksperymentalnie. Oczekuje się, że ten wkład do strumienia mionów powinien dominować przy wysokich energiach, około PeV, jako że wiele z cząstek-rodziców natychmiastowych mionów to ciężkie hadrony, zawierające kwarki powabne i dziwne. Cel tej dysertacji był dwojaki: oszacowanie możliwości obserwacji natychmiastowego strumienia mionów oraz weryfikacja wydajności detektorów KM3NeT'u.

Eksperyment KM3NeT jest siecią badawczą, składającą się z podwodnych czerenkowskich teleskopów neutrinowych, obecnie w fazie konstrukcji w dwóch różnych lokalizacjach w Morzu Śródziemnym. ARCA to detektor dedykowany astronomii neutrinowej wysokich energii, zlokalizowany niedaleko włoskiego wybrzeża przy Portopalo di Capo Passero. Drugi detektor to ORCA: skupia się on na fizyce niskoenergetycznych neutrin atmosferycznych i powstaje w pobliżu Tuluzy, we Francji. Nawet w ich pośrednich konfiguracjach, każdy z detektorów KM3NeT zbiera ogromne ilości danych mionowych. Ta praca korzysta z danych mionowych, aby przyjrzeć się obecnej efektywności KM3NeT/ARCA i KM3NeT/ORCA, oraz aby ocenić ich przyszły potencjał.

Aby ocenić wydajność detektorów KM3NeT, została wygenerowana rozległa symulacja Monte Carlo (MC) dla przypadków mionowych, przy użyciu programu CORSIKA oraz łańcucha oprogramowania symulacyjnego KM3NeT. Było to możliwe dzięki wprowadzeniu znacznych usprawnień w publicznie dostępnej aplikacji KM3NeT-u, transportującej wysymulowane cząstki do detektora.

Symulacja MC została użyta w rekonstrukcji kilku zmiennych: energii pęku mionów, całkowitej energii cząstki pierwotnej oraz krotności mionów. Wartości energii i krotności zostały estymowane przy użyciu narzędzi uczenia maszynowego. Rekonstrukcja energii pęku okazała się znacząco lepsza od standardowej rekonstrukcji energii używanej przez KM3NeT. Uzyskanie rekonstrukcji energii cząstki pierwotnej oraz krotności mionów umożliwiły ponadto pierwsze pomiary takich obserwacji przez podwodny teleskop neutrinowy.

Przygotowana rekonstrukcja została bezpośrednio zastosowana w głównej analizie fizycznej, badającej potencjał KM3NeT'u do obserwacji natychmiastowego strumienia mionów. Ukończone detektory KM3NeT powinny być w stanie potwierdzić sygnał od natychmiastowego strumienia w przeciągu 4-6 lat działania. Być może nawet wcześniej, jeżeli wyniki ich pomiarów zostaną połączone. Czulość jest obecnie mocno ograniczona przez niepewności systematyczne, z których część powinna zostać zredukowana do czasu ukończenia detektorów ARCA i ORCA.

Contents

Abstract	9
Streszczenie	11
1. Introduction	17
Motivation	19
2. Muons and neutrinos produced by cosmic rays	21
2.1. Muons	21
2.1.1. Interactions with matter	22
2.1.2. Sources of muons	23
2.2. Neutrinos	23
2.2.1. Neutrino sources	23
2.2.2. Neutrino interactions	24
2.2.3. Neutrino oscillations	25
2.3. Cosmic rays	27
2.3.1. Acceleration mechanisms	29
2.3.2. Sources	30
2.3.3. Extensive Air Showers	31
2.4. Atmospheric flux	34
2.4.1. Conventional	34
2.4.2. Prompt	34
3. KM3NeT Experiment	37
3.1. Neutrino telescopes in general	37
3.1.1. Cherenkov radiation	38
3.1.2. Photomultiplier Tubes	39
3.2. KM3NeT detectors and their physics case	40
3.2.1. ARCA	42
3.2.2. ORCA	42
3.2.3. Detector design	42
3.2.3.1. Digital Optical Modules	43
3.2.3.2. Detection Units	43
3.2.3.3. Building blocks	44
3.2.4. Event topologies	45

4. Simulation of atmospheric muons in KM3NeT	47
4.1. Event generators	47
4.1.1. CORSIKA	47
4.1.1.1. Implemented processes and particles	47
4.1.1.2. Models	47
4.1.2. MUPAGE	50
4.2. Event weighting	50
4.2.1. CORSIKA	50
4.2.2. MUPAGE	53
4.3. Muon simulation: from sea to reconstruction level	53
4.3.1. Sea level	54
4.3.2. Can level	55
4.3.3. Light level	55
4.3.4. Trigger level	56
4.3.5. Reconstruction level	56
4.3.5.1. Direction reconstruction	56
4.3.5.2. Energy reconstruction	57
4.3.5.3. Other observables	57
5. Reconstruction of muon bundle observables	59
5.1. Machine learning: a brief introduction	59
5.1.1. General workflow	60
5.1.2. Considered models	61
5.1.3. Performance assessment	65
5.2. Monte Carlo samples used	66
5.2.1. Preprocessing	68
5.2.2. Summary of datasets	69
5.3. Reconstruction of energy	69
5.3.1. Bundle energy	69
5.3.1.1. Choice of the best model	71
5.3.1.2. Inspection of learning	73
5.3.1.3. Feature importances	74
5.3.1.4. Results	77
5.3.2. Total primary energy	79
5.4. Reconstruction of multiplicity	81
5.4.1. Muon selection	81
5.4.2. Verification of the muon selection	87
5.4.3. Feature importances	88
5.4.4. Hyperparameter tuning	89
5.4.5. Results	89
6. Muon rate measurement with KM3NeT detectors	93
6.1. Simulated samples and experimental data	93

6.2. Systematic uncertainty study	94
6.2.1. Primary cosmic ray flux models	94
6.2.2. High-energy hadronic interaction models	95
6.2.3. Atmospheric density profiles	95
6.2.4. Photomultiplier tube efficiency	96
6.2.5. Light absorption length	96
6.2.6. Combined results	96
6.3. Event quality selection	98
6.3.1. ARCA6	99
6.3.2. ORCA6	101
6.4. Comparisons of data and Monte Carlo simulations	102
6.4.1. KM3NeT/ARCA	103
6.4.1.1. ARCA2	103
6.4.1.2. ARCA6	104
6.4.2. KM3NeT/ORCA	106
6.4.2.1. ORCA1	107
6.4.2.2. ORCA4	107
6.4.2.3. ORCA6	108
6.5. Summary	111
7. Sensitivity of KM3NeT detectors to the prompt muon flux	113
7.1. Separation of conventional and prompt muons	114
7.1.1. Parent particles	114
7.1.2. Parent particle generations	115
7.1.3. Definition of a prompt muon	117
7.2. Control plots for the selection	117
7.2.1. Muon arrival time	117
7.2.2. Muon energy share	118
7.2.3. Muon production point	119
7.3. Definition of signal and background	121
7.3.1. Reweighting of background	122
7.4. Significance test	123
7.4.1. Scaling with time and prompt normalisation	123
7.5. Selection of the critical region	124
7.6. Sensitivity results	127
8. Conclusions	131
8.1. Summary	131
8.1.1. CORSIKA Monte Carlo production	131
8.1.2. Muon bundle reconstruction	131
8.1.3. Data vs simulation comparisons	132
8.1.4. Prompt muon analysis	132

8.2. Outlook	132
8.2.1. CORSIKA Monte Carlo production	133
8.2.2. Muon bundle reconstruction	133
8.2.3. Data vs simulation comparisons	134
8.2.4. Systematic uncertainties	134
8.2.5. Prompt muon analysis	134
A. Appendix	137
A.1. CORSIKA	137
A.1.1. Simulation inputs	137
A.1.2. Fit of the atmosphere	140
A.1.3. Magnetic field strength	147
A.1.4. Benchmarking and energy thresholds	147
A.1.4.1. Surviving shower fraction	148
A.1.4.2. Storage and CPU time	149
A.2. Formulae	150
A.2.1. Errors for the weighted histograms	150
A.2.2. The shortest distance between a point and a line	150
A.2.3. Intersection of a point and a sphere	152
A.3. gSeaGen	152
A.3.1. Muon lateral deflection in water	153
A.3.2. Computation of DistaMax	155
A.3.3. Reorientation of CORSIKA showers	156
A.3.3.1. Computation of the required rotation	157
A.3.3.2. Rotation of showers around the Earth	159
A.4. Performance of JMuon reconstruction	160
A.4.1. Zenith reconstruction	160
A.4.2. Energy reconstruction	163
A.5. Muon bundle reconstruction	165
A.5.1. List of used features	165
A.5.2. Correlation matrices and dendrograms	167
A.5.3. Feature importances	173
A.5.4. Hyperparameter tuning	179
A.6. Prompt muon analysis	180
A.6.1. Hadrons implemented in CORSIKA	180
A.6.2. Classification of parent particles into conventional and prompt by lifetime	181
A.6.3. Verification of the prompt muon definition	184
Nomenclature	210

1. Introduction

While it is certainly true that neutrinos are the main focus of the KM3NeT experiment and still hold many exciting mysteries (see Sec. 2.2), they are not the only particles studied by neutrino telescopes like KM3NeT. From the perspective of such experiments, muons are primarily a background, since they are produced both in interactions of neutrinos, and decays of other particles. It is easy to fall prey to a deception that they have no secrets left, since they have been known to physicists and studied by them for much longer than neutrinos. Muons are a very convenient tool to indirectly study the physics of cosmic rays and put constraints on their flux. They offer valuable insight into the development of air showers, primary cosmic ray flux composition, production of particles associated with the charmed, strange, or even heavier quarks in the atmosphere and much more. Comparing the muon data against the Monte Carlo simulation allows testing and improves both the data acquisition and simulation of muon production. This thesis investigates the properties of the muon flux created in interactions of cosmic rays with the air molecules in the upper atmosphere with a particular emphasis on the prompt muon flux. The performance of the KM3NeT detectors is validated using the first collected data and a dedicated event reconstruction.

This work consists of 8 chapters in total. Below, their contents are briefly summarised:

1. Gives a preview of the matter of this dissertation, information on the original contribution of the author, and the motivation for undertaking this work.
2. Provides an overview of the relevant physics: muons, neutrinos, and cosmic rays. They are then tied together in the description of the current understanding of the observed atmospheric flux, with an emphasis on the muon flux, which is the subject of this thesis. The currently unconfirmed prompt component of the muon flux, originating from decays of heavy hadrons and light vector mesons, is of particular interest with Chap. 7 in mind.
3. Introduces the concept of the underwater neutrino telescopes in general, including a description of the Cherenkov radiation, which they observe. Furthermore, the KM3NeT experiment is described in much more detail, both in terms of hardware and its physics goal [1, 2]. The author of this dissertation is a member of the KM3NeT Collaboration and the results presented in further chapters were produced entirely in the KM3NeT context.
4. Describes how muons produced as a result of cosmic ray interactions in the atmosphere are simulated for the KM3NeT detectors. This includes a description of the necessary simulation software chain. The author of this thesis was heavily involved in foundational work in KM3NeT muon simulations. His contributions include:
 - a) Maintenance and development of the Corant software (see Sec. 4.3.1), taking care of computation of event weights and conversion of CORSIKA output files to the ASCII format. This code was used for the earliest results presented in Sec. 6.4 and its functionality was later directly incorporated into gSeaGen (see next point).

b) Maintenance and development of the gSeaGen software (see Sec. 4.3.2 and A.3), originally created by Carla Distefano to generate neutrino events and transport them to the boundary of the detector sensitive volume [3, 4]. The first important contribution of the author of this dissertation was the adaptation of gSeaGen to be able to propagate muons simulated by CORSIKA from the sea level to the detector sensitive volume. The initial approach was to first convert the CORSIKA output (sequential unformatted FORTRAN files [5]) with Corant and then read and process it further with gSeaGen. At this stage, the author of this thesis collaborated closely with Alfonso Andres Garcia Soto. Soon it was realised that, despite its convenience, conversion to text format done with Corant is in fact inefficient and limits the entire simulation chain. This inspired the author of this dissertation to pursue an alternative approach, i.e. directly read the CORSIKA output files with gSeaGen. This effort built upon the pre-existing basic readout scripts, which are distributed together with each CORSIKA release. The first results of these efforts were teased in the proceedings of the VLVnT2021 conference [6]. The author of this thesis expanded the amount of information extracted from CORSIKA to foster potential physics analyses.

Further endeavours moved towards a complete redesign of the muon propagation routine within gSeaGen, targeting a number of issues: the efficiency of the code in terms of memory management and runtime, the accuracy of propagation, and the treatment of the curvature of the Earth and overall simulation geometry. The resulting enhancement of the code was particularly noticeable in the case of high-energy simulations, where the average time needed to simulate 100 events dropped from 12 days to 40 minutes, making the large-scale simulation feasible. Supplementary material describing some of those developments is available in Sec. A.3. A publication on those specific improvements in gSeaGen is currently under internal review in the KM3NeT Collaboration, with the author of this thesis as the main author of the paper. In addition, the author of this dissertation has contributed to adapting gSeaGen to meet the criteria of the open software policy of KM3NeT, which was described in the proceedings of the VLVnT2021 conference [7].

c) Development of official KM3NeT simulation steering scripts, which control the running of the entire KM3NeT software chain. The author of this thesis has in particular worked on adapting the code to work in multiple computing environments and to integrate the CORSIKA processing into the scripts. This endeavour was necessary to proceed with the production of the large-scale CORSIKA simulation, described in the Chap. 4 and in Sec. A.1. During first three years of his work within KM3NeT, the author of this dissertation was the sole person responsible for the CORSIKA simulations. After that, he was joined by Andrey Romanov, who assisted him in the work, which included immense amounts of bookkeeping and monitoring. Suffice it to say that the actual running of the final simulations themselves took more than a year of continuous running on two computing clusters: Świerk Computing Centre (CIŚ) in Otwock, Poland and IN2P3's Computing Centre in Lyon, France. During the production of CORSIKA simulation, several issues

were identified and reported to the authors of the code, who addressed them in the release of version 7.7410 [8].

Completion of the CORSIKA simulation work was a crucial impulse for the creation of the cosmic ray physics working group in KM3NeT, led by Ronald Brujin. Almost all the current analyses in this group rely on those simulations, with some results already published in [9, 10, 11, 12]. Additional details on CORSIKA production and improvements in gSeaGen are given in the appendix in Sec. A.1–A.3.

5. Is dedicated to development of new reconstruction tools for KM3NeT by the author of this dissertation. The reconstructed quantities are the number of muons (multiplicity) and energy. To this end, the author made use of the machine learning tools and the aforementioned CORSIKA production. The chapter evaluates the performance of trained machine learning models and compares the results with existing KM3NeT reconstruction: JMuon, described in Chap. 4.
6. Presents the comparisons between the simulations and experimental data, performed on the first datasets from the KM3NeT detectors. The results were published by the author of this thesis in [13, 14, 11, 12, 10]. For early detector configurations only the distributions of reconstructed direction and energy were investigated. However, for the most recent ones the reconstruction of muon multiplicity and primary cosmic ray energy were included. The experimental datasets and the corresponding MUPAGE (the other muon simulation software used in KM3NeT, see Sec. 4.1.2) simulations were provided the KM3NeT data processing and simulation working groups respectively.
7. Is devoted to the main physics analysis of this work, carried out by the author of this dissertation within the cosmic ray working group. The author has developed a procedure to evaluate the contribution of the prompt component of the atmospheric muon flux or to set an upper limit on it by interpreting the KM3NeT data. The study made predictions of the expected sensitivity of KM3NeT detectors to measure the prompt muon flux in smaller configurations and with complete building blocks of ARCA and ORCA. The preliminary results of the analysis were published in [12, 11], and the publication of the final outcome is planned after completion of this thesis and submission of the gSeaGen paper.
8. Recapitulates all the obtained results and discusses possible improvements in the methodology and potential further studies.

The existence of the prompt component in the atmospheric lepton flux has not been experimentally confirmed yet, although it is widely accepted that this component must be present. So far, only the BUST experiment has claimed a significant measurement [15] and the other ones only set experimental upper bounds [16, 17, 18]. Furthermore, so far no neutrino experiment has performed muon bundle multiplicity (number of muons in a bundle) measurement. Currently, the KM3NeT detectors (see Chap. 3) are under construction. However, already with the muon data collected with the early detector configurations, it is possible to obtain first results and to validate the methodology for the full detectors. In particular, the reconstruction of multiplicity should already be possible with the current detector configurations and may be compared between the simulations and experimental data. All these remaining open questions constitute an exciting challenge, which was taken up in this thesis.

2. Muons and neutrinos produced by cosmic rays

The main background for observing neutrinos originating directly from distant astrophysical objects are muons and neutrinos created by interactions of particles coming from the outer space (cosmic rays, see Sec. 2.3) with the Earth's atmosphere. This chapter discusses the origin and properties of those particles and characteristics of the atmospheric muon and neutrino flux.

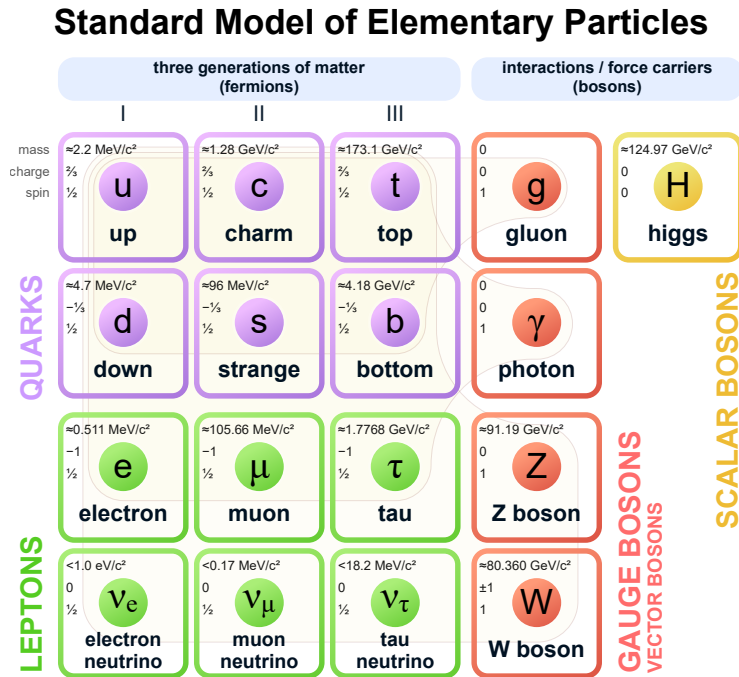


FIGURE 2.0.1.: The Standard Model of particle physics (SM), with all three neutrinos and their respective charged lepton counterparts [19].

2.1. Muons

Muons are charged leptons of intermediate mass (see Fig. 2.0.1). They are unstable and decay to electrons and neutrinos: $\mu^- \rightarrow e^- + \bar{\nu}_e + \nu_\mu$ (in $\approx 100\%$ cases) with a mean lifetime of $\tau_\mu = (2.1969811 \pm 0.000022) \mu\text{s}$ [20]. Their existence was first confirmed in a cloud chamber experiment conducted in 1937 by J. C. Street and E. C. Stevenson [21] and since then, muon properties have been a subject of extensive studies [22, 23, 16].

Due to the time dilation effect, muons produced in the atmosphere with sufficiently high energies may travel tens of kilometres and reach the surface of the Earth (or even a few km underground or underwater!) [24]. For example, a muon with total energy $E = 100 \text{ TeV}$ will live

on average $\tau = \frac{E}{m_\mu c^2} \tau_\mu \approx 2$ s, where $c = 299\,792\,458 \frac{\text{m}}{\text{s}}$ is the speed of light in vacuum and $m_\mu = (105.6583755 \pm 0.0000023) \frac{\text{MeV}}{c^2}$ is the muon mass [20]. This implies that if energy losses were neglected, the μ could travel $6 \cdot 10^5$ km in air! The real muon ranges are naturally shorter, since energy losses along such long paths are certainly not negligible. This holds true even in the air, let alone in more dense media, like water or rock. More details on the processes through which muons lose energy are given in the following subsection.

2.1.1. Interactions with matter

Muons carry electric charge and therefore undergo a number of processes that can lead to a decrease of their energy:

1. Ionisation – a portion of the electromagnetic field energy of the muon is transferred to electrons in nearby atoms, freeing some of them. This results in creation of net positive charge on the atoms and freely floating negative ions (electrons), hence the name of the process. Ionisation is dominant at low muon energies, as opposed to the other three processes (see Fig. 2.1.1).
2. Pair production – creation of electron-positron pairs by exchange of a photon with an atomic nucleus: $(N+) \gamma \rightarrow (N+) e^+ + e^-$. The process cannot take place in vacuum.
3. Bremsstrahlung – emission of photons by the muon when deflected by an electric charge, e.g. of an atomic nucleus.
4. Photonuclear interaction – inelastic scattering of the muon off an atomic nucleus through virtual photon exchange.

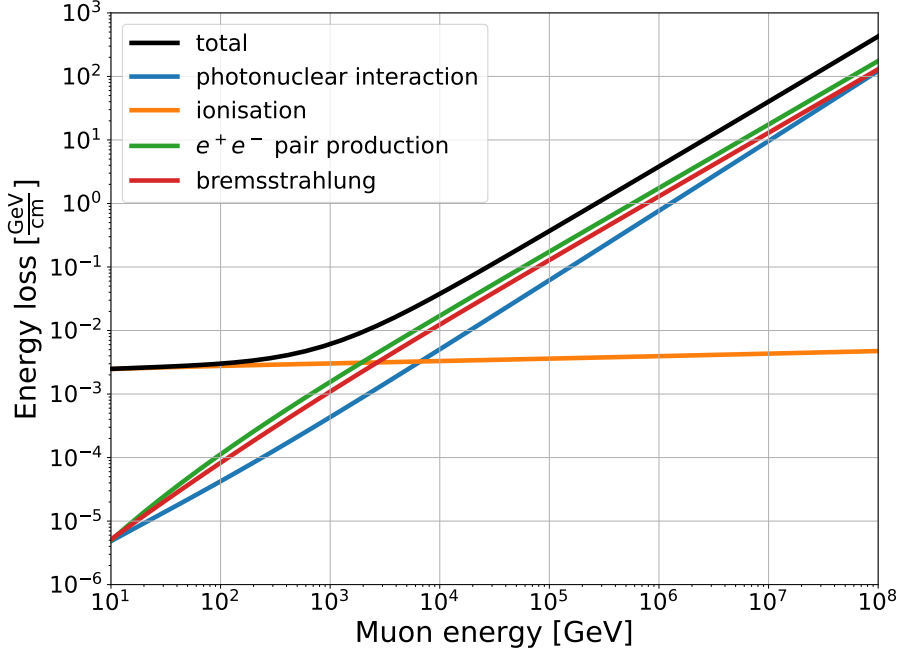


FIGURE 2.1.1.: Continuous muon energy losses in seawater as function of the total muon energy. The energy losses were computed using default parametrisations implemented in the PROPOSAL software [25], which was used to propagate muons in the gSeaGen code (see Sec. 4.3.2 and A.3).

An example with different contributions to muon energy loss in water is shown in Fig. 2.1.1. The muon ranges in seawater can be found in Fig. A.1.11.

2.1.2. Sources of muons

Muons are mostly produced in extensive air showers, caused by primary cosmic ray interactions in the atmosphere (see Sec. 2.3). Human-made muon beams can be achieved by colliding hadrons to produce a beam containing charged pions and kaons. Those mesons subsequently decay to muons:

$$\begin{aligned}\pi^+ &\longrightarrow \mu^+ + \nu_\mu, \\ \pi^- &\longrightarrow \mu^- + \bar{\nu}_\mu, \\ K^+ &\longrightarrow \mu^+ + \nu_\mu, \\ K^- &\longrightarrow \mu^- + \bar{\nu}_\mu.\end{aligned}$$

Such muons can be separated from the other collision products using a shielding (they penetrate much deeper than hadrons) and focused with a magnetic field. Examples of artificial muon production are μ beams created for the measurements of the anomalous magnetic dipole moment of the muon [26, 22] and nucleon structure [27, 28, 29, 30]. An important application of artificial muon beams will be the planned muon colliders [31, 32, 33]. They will take advantage of the properties of muons, such as:

- much lower energy losses through synchrotron radiation¹, compared to electrons,
- being elementary particles, unlike protons, which makes the entire kinetic energy available in the collision.

2.2. Neutrinos

Neutrinos are arguably the most elusive particles that have been ever detected. They only interact via weak and gravitational forces. The latter was experimentally confirmed in 1998 through the discovery of neutrino oscillations, which implied that neutrinos must have non-zero masses (see Sec. 2.2.3). This discovery was awarded with a shared Nobel Prize in Physics for Takaaki Kajita² and Arthur B. McDonald³ in 2015 [34].

2.2.1. Neutrino sources

All neutrinos are created in weak interactions. Depending on the environment, in which they are produced, one can distinguish between a number of neutrino source categories:

- Human-made:
 - Nuclear fission reactors: $\bar{\nu}_e$ are a standard byproduct of nuclear reactor operation. They are created via the β decay: $n \rightarrow p + e^- + \bar{\nu}_e$. There was a number of measurements

¹Emission of γ by relativistic charged particles, when experiencing acceleration in the direction perpendicular to the direction of motion.

²Super-Kamiokande (SK) Collaboration

³Sudbury Neutrino Observatory (SNO) Collaboration

of such neutrinos by KamLAND, Chooz, Double Chooz, Daya Bay, RENO, DANSS, NEOS, STEREO, SoLid, and CHANDLER experiments [35, 36, 37, 38, 39, 40, 41, 42, 43, 44]. The last five are still taking data.

- Particle accelerators: neutrinos are produced mostly together with muons as products of pion and kaon decays (see Sec. 2.1.2). These mesons are typically produced by colliding accelerated protons on a fixed target. The most abundant products are muon (anti-)neutrinos, however there is also a contribution of electron (anti-)neutrinos, which come e.g. from muon decays or less probable pion or kaon decay channels. A neutrino beam is produced e.g. at the Japan Proton Accelerator Research Complex (J-PARC) for the Tokai to Kamioka (T2K) experiment [45].
- Solar: ν_e are created in nuclear reactions occurring in our star. The leading contribution comes from the proton-proton chain: $p + p \rightarrow {}_1^2d + e^+ + \nu_e$. Solar neutrinos have been extensively studied, first by the Homestake experiment, and then by a number of follow-up projects, including SAGE, GALLEX, Borexino, SNO, Kamiokande, and SK [46, 47, 48, 49, 50, 51, 52].
- Atmospheric: all three flavours of neutrinos (see Fig. 2.0.1) are created in particle cascades produced by the cosmic rays colliding with atomic nuclei in the upper atmosphere. Measurements of the atmospheric neutrinos have been performed by IMB, Kamiokande, SK, ANTARES, IceCube, KM3NeT, and other experiments [53, 54, 2, 55, 50, 56].
- Cosmic: neutrinos of all flavours directly originating from astrophysical objects, such as active galactic nuclei (AGNs) and pulsars, or transient events: gamma ray bursts (GRBs) and supernovae (SNe). Additionally, ν coming from the Greitsen-Zatsepin-Kuzmin (GZK) cutoff and relic neutrinos from the Big Bang nucleosynthesis are counted here. Experiments trying to observe such sources are KM3NeT, IceCube, SK and Baikal GVD [2, 17, 57, 58], with first successful observation of a flaring blazar by IceCube: [59, 60].
- Geological: neutrinos produced in decays of radioactive isotopes naturally present in the Earth. Most commonly, these are $\bar{\nu}_e$ stemming from β^- decay branches of ${}^{40}\text{K}$, ${}^{232}\text{Th}$ and ${}^{238}\text{U}$. Only the last two are detectable by inverse beta decay (IBD): $\bar{\nu}_e + p \rightarrow n + e^+$, since ${}^{40}\text{K}$ decays produce neutrinos below the IBD energy threshold of 1.8 MeV. Measurements of geoneutrinos were performed by the Borexino and KamLAND experiments [61, 62].

2.2.2. Neutrino interactions

As already mentioned, neutrinos interact only gravitationally and via weak force. However, gravitational effects are too faint to be detected. Weak interactions occur through exchange of W^\pm or Z^0 gauge boson and can be divided into three classes: charged current (CC), neutral current (NC), and elastic scattering (ES) interactions:

$$\begin{aligned}
 \text{CC} : \quad & \nu_l + N \xrightarrow{W^\pm} l + X \\
 \text{NC} : \quad & \nu_l + N \xrightarrow{Z^0} \nu_l + X \quad , \\
 \text{ES} : \quad & \nu_l + l \xrightarrow{Z^0/W^\pm} \nu_l + l,
 \end{aligned}
 \tag{2.2.1}$$

where l is one of the lepton flavours: e , μ or τ , N is the target nucleus and X is the resulting hadronic cascade [63]. Interactions of neutrinos with leptons have lower cross-section (are less probable) than for interactions with nuclei. However, as can be seen in Fig. 2.2.1, theory predicts that they can become dominant in case of resonant production of a W^- boson, called Glashow resonance:

$$\bar{\nu}_e + e^- \longrightarrow W^-, \quad (2.2.2)$$

at the energy of $E_{\text{Glashow}} \approx \frac{m_{W^-}^2 c^2}{2m_e} \approx 6.3 \text{ PeV}$, where m_{W^-} is the W^- boson mass and m_e is the mass of an electron [20, 63, 64].

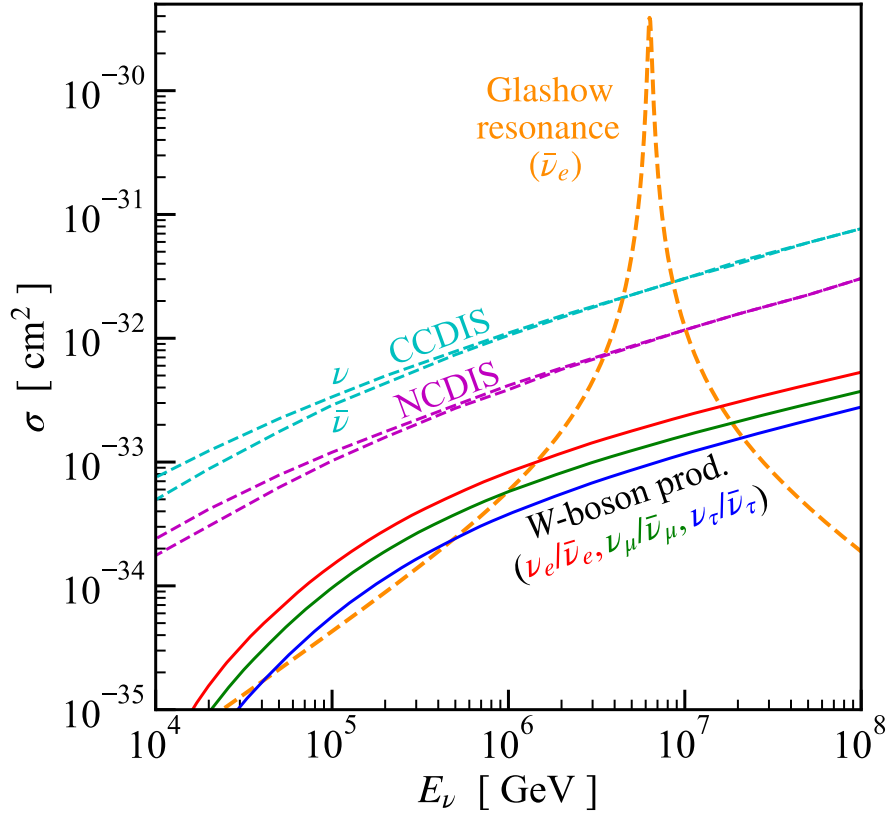


FIGURE 2.2.1.: Cross-sections for W^- boson production in (anti-)neutrino scattering on ^{16}O , compared to those for CC and NC deep inelastic scattering (DIS), and the predicted Glashow resonance at $E_\nu = 6.3 \text{ PeV}$ [65, 64]. The cross-sections are given as a function of the neutrino energy. The plot was taken from [64].

Charged particles are produced in all the processes described in this subsection. They can emit Cherenkov radiation (see Sec. 3.1.1), however the event signatures heavily depend on the incident neutrino flavour and interaction class (CC or NC). Event signatures and reconstruction for different categories of neutrino-induced events are described in Sec. 3.2.5 and 4.3.5.

2.2.3. Neutrino oscillations

Neutrino oscillations arise from the interference between the mass and flavour eigenstates of an operator \hat{U}_{osc} :

$$|\nu_\alpha\rangle = \sum_n \hat{U}_{\alpha n}^* |\nu_n\rangle, \quad (2.2.3)$$

$$|\nu_n\rangle = \sum_\alpha \hat{U}_{\alpha n} |\nu_\alpha\rangle, \quad (2.2.4)$$

where $*$ denotes the complex conjugate, $|\nu_\alpha\rangle$ is an $\alpha = e, \mu, \text{ or } \tau$ flavour eigenstate, and $|\nu_n\rangle$ is a mass eigenstate with eigenvalue m_n ($n = 1, 2, 3$). The operator $\hat{U}_{\alpha n}$ can be represented by the mixing matrix $U_{\alpha n}$, which is called Pontecorvo-Maki-Nakagawa-Sakata (PMNS) matrix. The PMNS matrix is typically parametrized in the following way:

$$U_{\alpha n} = \begin{bmatrix} U_{e1} & U_{e2} & U_{e3} \\ U_{\mu 1} & U_{\mu 2} & U_{\mu 3} \\ U_{\tau 1} & U_{\tau 2} & U_{\tau 3} \end{bmatrix} = \underbrace{\begin{bmatrix} 1 & 0 & 0 \\ 0 & c_{23} & s_{23} \\ 0 & -s_{23} & c_{23} \end{bmatrix}}_{\text{atmospheric and accelerator}} \underbrace{\begin{bmatrix} c_{13} & 0 & s_{13}e^{-i\delta_{\text{CP}}} \\ 0 & 1 & 0 \\ -s_{13}e^{i\delta_{\text{CP}}} & 0 & c_{13} \end{bmatrix}}_{\text{accelerator and reactor}} \underbrace{\begin{bmatrix} c_{12} & s_{12} & 0 \\ -s_{12} & c_{12} & 0 \\ 0 & 0 & 1 \end{bmatrix}}_{\text{solar and reactor}} \underbrace{\begin{bmatrix} e^{\frac{i\alpha_1}{2}} & 0 & 0 \\ 0 & e^{\frac{i\alpha_2}{2}} & 0 \\ 0 & 0 & 1 \end{bmatrix}}_{\text{Only if } \nu\text{'s are Majorana}}, \quad (2.2.5)$$

where $s_{kl} \equiv \sin\theta_{kl}$, $c_{kl} \equiv \cos\theta_{kl}$, δ_{CP} – CP-violating phase (charge-parity), and α_1, α_2 – Majorana phases [66, 67]. The latter are expected not to affect oscillations significantly [68]. Atmospheric, accelerator, solar, and reactor refer to the neutrino sources, described earlier in Sec. 2.2, for which the particular mixing of states is most relevant. Currently, the mixing parameter values in $U_{\alpha i}$ are still not measured with sufficient precision to exclude non-unitarity of this 3×3 matrix, i.e. $|U_{\alpha i}| = U_{\alpha i}^\dagger U_{\alpha i} \neq \mathbb{1}$ [69]. Non-unitarity would imply a violation of the postulate of Quantum Mechanics, stating that only unitary operators can describe the dynamics of quantum systems [70]. To preserve unitarity of the $\hat{U}_{\alpha i}$ operator in such a case, the 3×3 matrix would have to be extended by adding at least one row and column (become 4×4 or larger). In other words, there would have to exist at least one more additional species of neutrinos, referred to as sterile neutrinos. The term sterile neutrinos indicates that they do not undergo weak interactions (but do mix with non-sterile flavours through oscillations).

The probability of conversion from the flavour state α to flavour state β during the propagation is equal to

$$P_{\alpha \rightarrow \beta}(t) = |\langle \nu_\beta | \nu_\alpha(t) \rangle|^2, \quad (2.2.6)$$

where t is the time and $|\nu_\alpha(t)\rangle$ is the time-evolved flavour state. In the simplified scenario of 2-flavour ν oscillations in vacuum, Eq. 2.2.6 can be approximately solved as

$$P_{\alpha \rightarrow \beta}(L) = \delta_{\alpha\beta} - (2\delta_{\alpha\beta} - 1) \sin^2(2\theta_{kl}) \sin^2\left(\frac{c^3}{\hbar} \cdot \frac{\Delta m_{kl}^2 L}{4E_\nu}\right), \quad (2.2.7)$$

where θ_{kl} is the mixing angle for the 2-flavour scenario, $\delta_{\alpha\beta}$ is the Kronecker delta, $\hbar = \frac{h}{2\pi} = 1.054571817... \times 10^{-34} \text{ J} \cdot \text{s}$ is the reduced Planck constant, $\Delta m_{kl}^2 = m_k^2 - m_l^2$ is the squared mass difference, E_ν is the neutrino energy, and $L = t \cdot c$ is the distance travelled by the neutrino [20]. What is accessible in neutrino experiments is the number of observed events, which is proportional

to $P_{\alpha \rightarrow \beta}(L)$. Hence, one may infer from Eq. 2.2.7 that the accessible neutrino mixing observables are the mixing angles θ_{kl} and squared mass differences Δm_{kl}^2 , and that both must be non-zero for oscillations to occur. Their values have been measured to be:

$$\theta_{12} = \left(33.41_{-0.72}^{+0.75}\right)^\circ,$$

$$\Delta m_{21}^2 \equiv \Delta m_{\text{solar}}^2 = \left(7.41_{-0.20}^{+0.21}\right) \cdot 10^{-5} \text{ eV}^2,$$

and

$$\theta_{23} = \left(42.2_{-0.9}^{+1.1}\right)^\circ,$$

$$\theta_{13} = (8.58 \pm 0.11)^\circ,$$

$$\Delta m_{31}^2 \approx \Delta m_{32}^2 \equiv \Delta m_{\text{atmospheric}}^2 = \left(2.507_{-0.027}^{+0.026}\right) \cdot 10^{-3} \text{ eV}^2.$$

under assumption that $m_1 < m_2 < m_3$, referred to as normal neutrino mass ordering (favoured by the global fit) [20, 69]. The other possibility is inverted ν mass ordering: $m_3 < m_1 < m_2$, which would result in slightly different fit values and negative sign of $\Delta m_{\text{atmospheric}}^2$. The sign of $\Delta m_{\text{solar}}^2$ is already determined to be positive, as a result of the measurements of the solar ν spectra from the ^8B branch of the proton-proton chain [71].

Among other open questions in the neutrino sector, there are the uncertain value of the CP-violating phase δ_{CP} [72, 67], the mechanism by which the neutrinos obtain their masses [20], whether neutrinos are Majorana⁴ or Dirac particles [66, 73].

2.3. Cosmic rays

Cosmic rays (CRs) are charged particles originating from outer space, with energies sufficient to penetrate Earth's magnetic field. For the discovery of the CRs during his free balloon flight measurements, Victor Franz Hess was awarded the Nobel Prize in Physics in 1936 [74]. Protons and helium nuclei constitute the majority (99 %) of the cosmic rays. There is also a 1 % contribution to the total flux from heavier nuclei like lithium, beryllium, boron, carbon, nitrogen, oxygen, and so on up to iron and from electrons [75]. One may also observe CR positrons and antiprotons, however in even smaller numbers [76, 77, 20].

Theory predicts an upper limit $E_{\text{GZK}} \simeq 50 \text{ EeV}$ on the energy of the CRs reaching the Earth (see Fig. 2.3.1), called Greisen-Zatsepin-Kuzmin cutoff (GZK cutoff) [78, 79, 80]. The main cause for the GZK cutoff is the strong attenuation of proton energies in photopion production interactions with the cosmic microwave background (CMB) photons γ_{CMB} . The inelastic collisions result in a delta resonance, which subsequently decays producing pions:

⁴If neutrinos were Majorana particles, they could act as their own antiparticles.

$$\begin{aligned}
 p + \gamma_{\text{CMB}} &\rightarrow \Delta^+ \rightarrow n + \pi^+ \\
 p + \gamma_{\text{CMB}} &\rightarrow \Delta^+ \rightarrow p + \pi^0
 \end{aligned}
 \tag{2.3.1}$$

Such process on average leads to 20 % E loss per collision. This deceleration mechanism limits the maximal detectable energy for distant CR sources (further than about 150 million ly) [79, 78]. Alternative explanations of the falling slope at the end of the spectrum in Fig. 2.3.1 include intrinsic CR source limitations, neutrons being the dominant ultra-high-energy (UHE; with $E > 10^{18}$ eV) CRs instead of protons, Z burst model, top-down models, violation of Lorentz invariance etc., although these are not as well-established as GZK cutoff [81, 82, 83, 84, 85, 86, 87, 88, 89, 90, 80]. A popular explanation for the origin of the ankle feature right before the GZK cutoff (see Fig. 2.3.1) is the dominance of the extragalactic over the galactic CR flux at high energies [91].

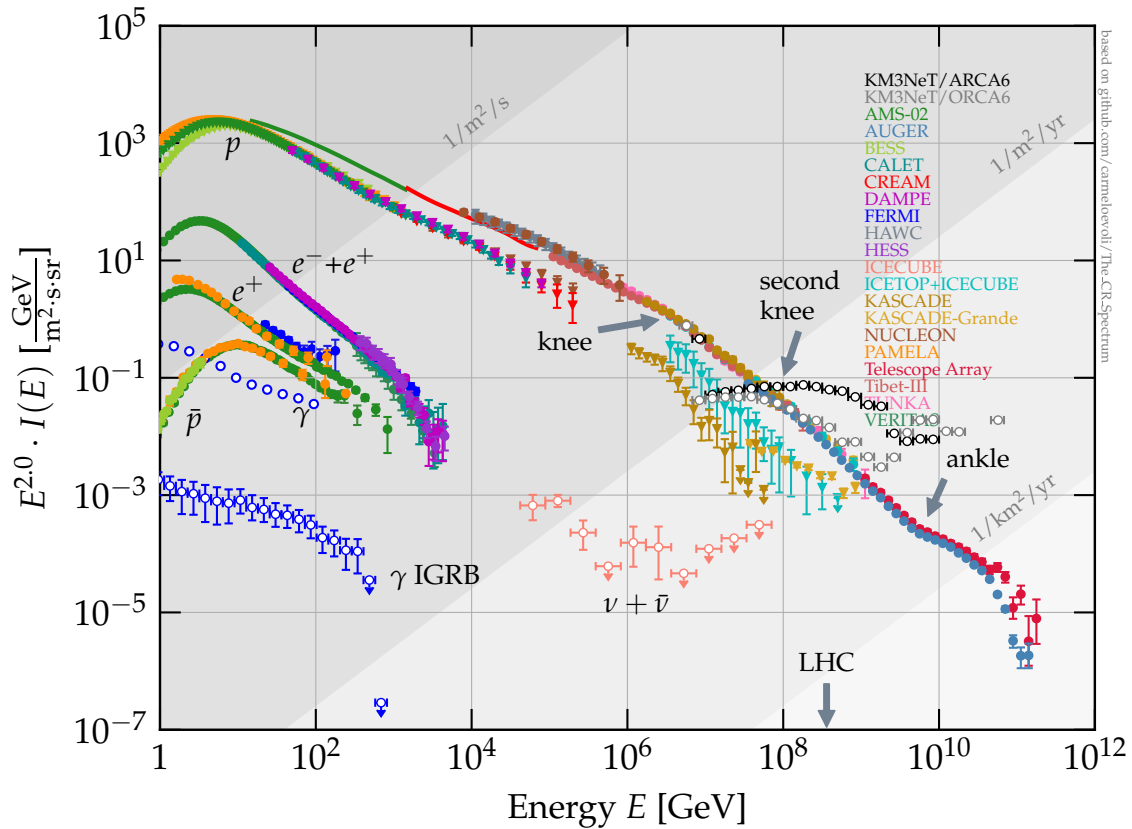


FIGURE 2.3.1.: The cosmic ray all-particle spectrum with data from several experiments as a function of the primary energy (per nucleus in case of nuclei) E . The figure was adapted from [92]. The particle intensity $I(E)$ is weighted by $E^{2.0}$ to improve the visibility of spectral features: the ‘knee’ at $\sim 3 \cdot 10^6$ GeV, the ‘second knee’ at $\sim 10^8$ GeV, and the ‘ankle’ at $\sim 5 \cdot 10^9$ GeV, separating regions that can be approximated by power laws. The fixed-target equivalent of the maximal collision energy at the large hadron collider (LHC) is marked on the x axis with a grey arrow for comparison. The shaded grey regions indicate the thresholds for the flux: 1 particle per $\text{m}^2 \cdot \text{s}$, per $\text{m}^2 \cdot \text{yr}$, and $\text{km}^2 \cdot \text{yr}$. [20, 93, 92].

2.3.1. Acceleration mechanisms

It remains unclear how CRs acquire such high energies as in Fig. 2.3.1. There are two categories of models that try to explain it:

1. Top-down models assume existence of extremely heavy remnant particles from the Big Bang, that deposit most of their energy into kinetic energy when decaying into SM particles. Such particles would need to have lifetimes on the order of the age of the Universe. Those models are disfavoured by cosmic photon flux measurements by experiments like Pierre Auger Observatory [90, 94, 95].
2. Bottom-up theories predict processes taking place in the present Universe that could accelerate particles to extreme energies. A popular example of such a process is Fermi acceleration, named after Enrico Fermi who proposed it in 1949 [96]. There are in fact two kinds: first and second order Fermi acceleration. They are both sketched in Fig. 2.3.2.

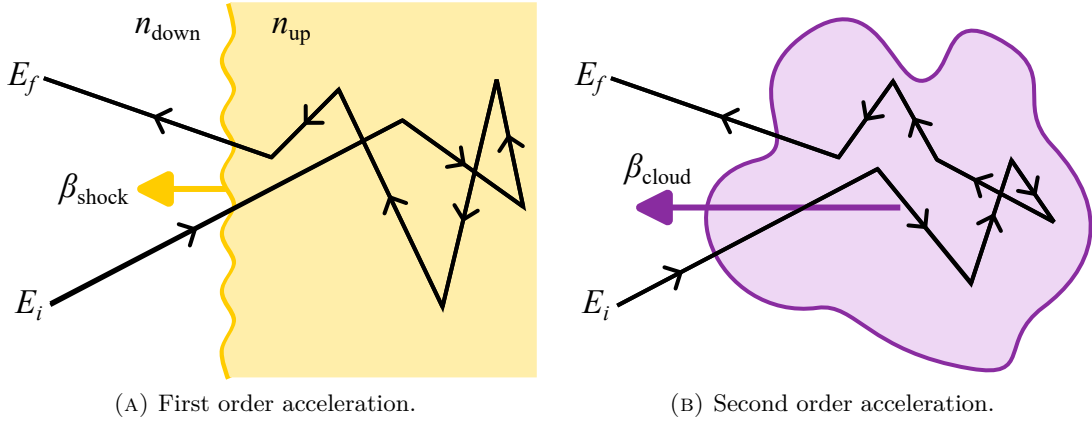


FIGURE 2.3.2.: Sketches of two Fermi acceleration mechanisms. E_i is the initial and E_f is final energy of the accelerated particle. β_{shock} and β_{cloud} are velocities (relative to the speed of light in vacuum) of the plasma shock front and magnetic cloud respectively. The particle densities are denoted by n_{down} for the downstream and n_{up} for the upstream plasma [97].

In Fermi acceleration, the order of the process is associated with the efficiency of acceleration:

$$\begin{aligned}
 \text{First order : } & \frac{\langle \Delta E \rangle}{E} \simeq \frac{4}{3} \beta_{\text{shock}} \\
 \text{Second order : } & \frac{\langle \Delta E \rangle}{E} \simeq \frac{4}{3} \beta_{\text{cloud}}^2
 \end{aligned} \tag{2.3.2}$$

The one originally proposed by Fermi, where relativistic particles gain energy by collisions with interstellar clouds is the second order acceleration. It results in a power law spectrum, but fails to explain the big abundance of UHE CRs (interstellar clouds are too thin) and the observed spectral index of about $\gamma = -2.7$ [96, 89]. The first order Fermi acceleration occurs through collisions of relativistic CRs with SN or AGN shockwaves, which is a more efficient mechanism ($|\beta| < 1$; see Eq. 2.3.2). When moving in a strong magnetic field, CR particles are deflected and cross the shockwave front repeatedly, gaining energy. This allows to produce a power law behaviour with a spectral index of $\gamma = -2.0$. When including CR propagation and acceleration inefficiencies, it is

compatible with the experimentally observed spectrum. First order Fermi acceleration allows to produce energies up to

$$E_{\max} \simeq Z \cdot \frac{B}{\mu\text{G}} \cdot \frac{R_{\text{src}}}{\text{kpc}} \cdot 10^9 \text{ GeV}, \quad (2.3.3)$$

where Z is the atomic number, B – magnetic field amplitude and R_{src} – characteristic size of the source [89].

2.3.2. Sources

Since CRs are electrically charged particles, they are deflected by the magnetic fields they traverse. This makes it nearly impossible to track a particular CR back to its source. It is only possible for the most energetic CRs, however at the highest energies insufficient statistics (see Fig. 2.3.1) and lack of knowledge about the CR flux composition become major problems. For these reasons UHE CR sources are so far unknown. There are however certain classes of objects, suspected of producing the UHE CRs as shown in Fig. 2.3.3.

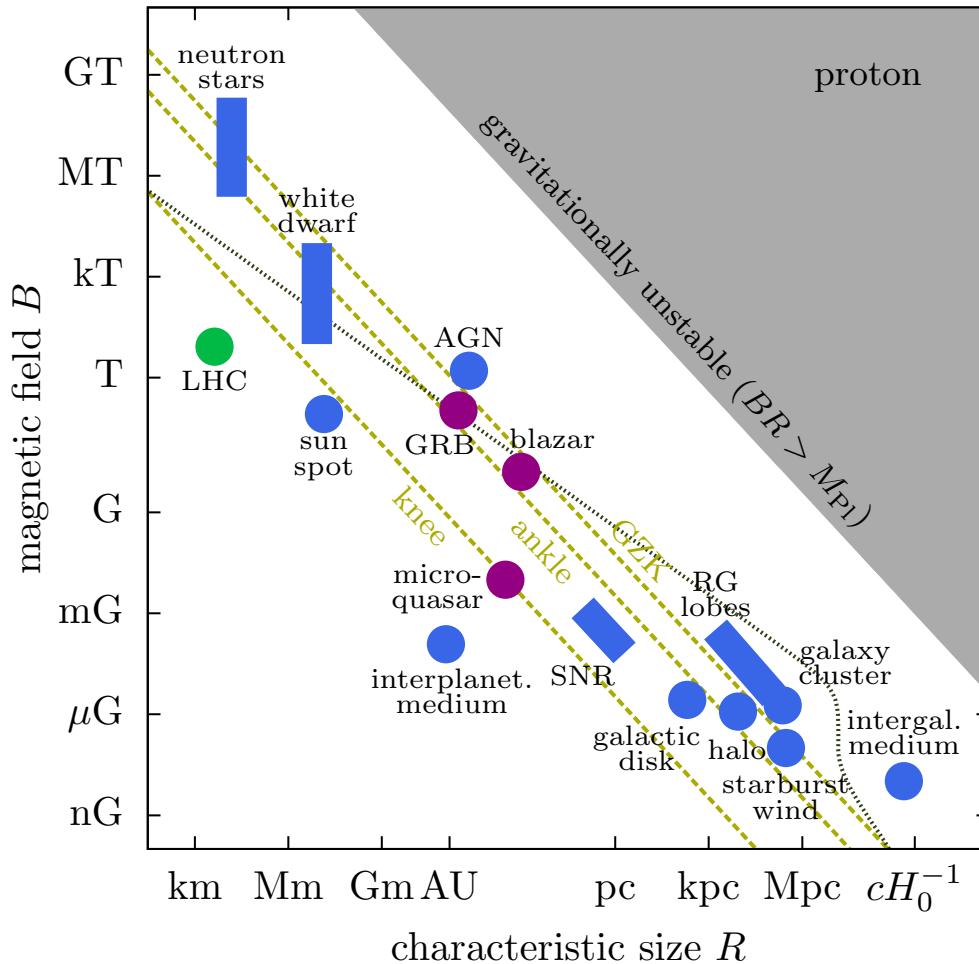


FIGURE 2.3.3.: The so-called Hillas plot. It visualises the energy limitation from Eq. 2.3.3. CR source candidates are coloured blue. Purple circles indicate jet-frame parameters for some object types. Dashed yellow lines are the lower limits for proton accelerators at knee, ankle and the GZK cutoff. The dotted grey line is the upper limit from synchrotron losses and interactions with the CMB. The grey area corresponds to gravitationally unstable extremely large magnetic field environments [98, 99, 97].

2.3.3. Extensive Air Showers

Extensive air showers (EAS), also referred to as simply air showers, are particle cascades induced by CRs in the upper atmosphere. They can extend through many kilometres, reaching the Earth's surface and deeper. Fig. 2.3.4 depicts what components a typical EAS consists of. Naturally, air showers vary a lot in produced secondary particles, depending on the primary CR type, energy, Earth's magnetic field, atmosphere properties, first interaction height, and so on. In general, showers caused by heavier primaries are wider and consist of a larger number of produced particles. Hence, it may be possible to distinguish between the showers initiated by the lightest (proton) and heaviest (iron) primary nuclei [100]. A bunch of selected processes present in air showers is displayed in Fig. 2.3.5.

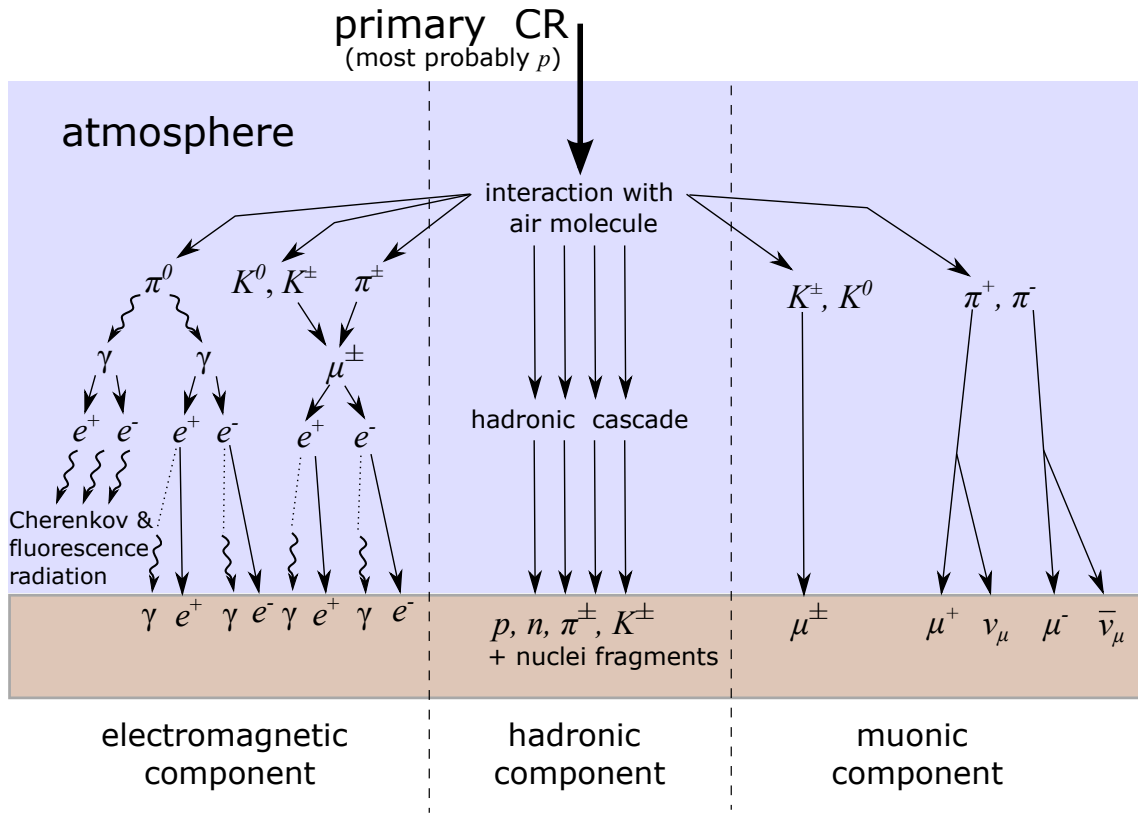


FIGURE 2.3.4.: Structure of an EAS with a separation into the electromagnetic, muonic and hadronic parts.

In the case of EAS started by more energetic primaries, the number of particles produced even in a single shower can be enormous (see Sec. 5.4). Despite this, secondary particles tend to be aligned close to the shower axis (original primary direction), due to large Lorentz boost in the forward direction.

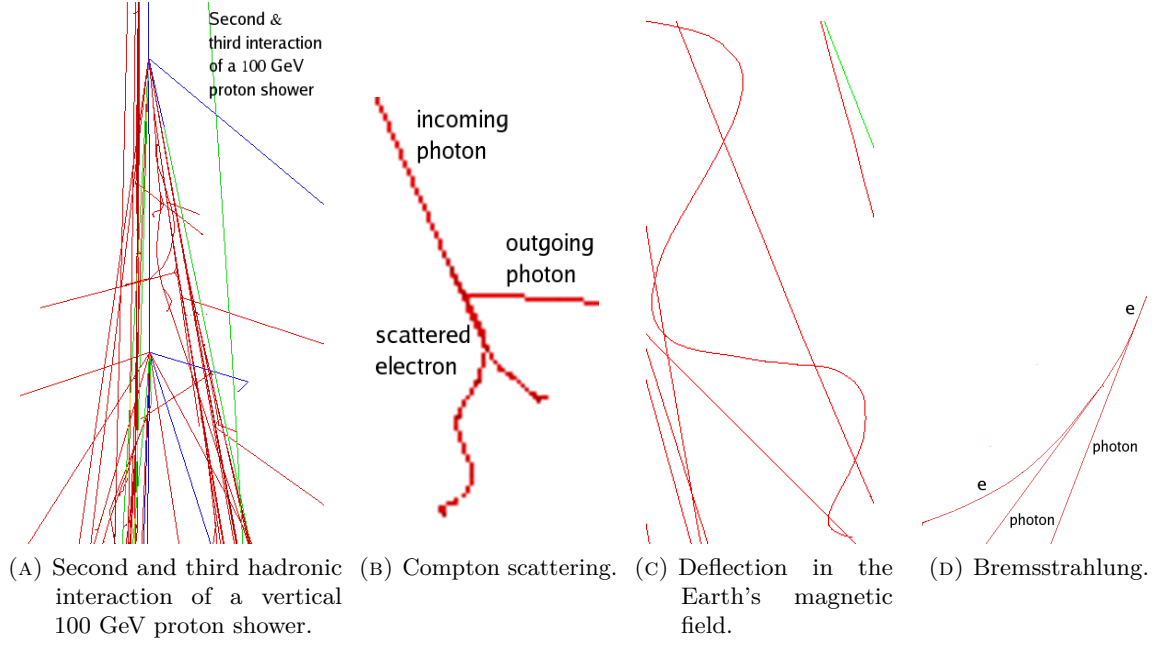


FIGURE 2.3.5.: Some processes cut out from the global shower pictures created using the CORSIKA event generator (see Sec. 4.1.1), taken from [100]. Electrons and photons are coloured red, muons: green and hadrons: blue. Colour scale is logarithmic and colours are mixed in case of overlapping tracks (e.g. red + green track \rightarrow yellow pixel), i.e. dark color indicates a high track density. [100].

In the context of this work, muons are the most important products of EAS.

Some of the characteristics describing a bundle include:

1. Muon multiplicity N_μ : number of muons in the bundle.
2. Bundle energy E_{bundle} : sum of energies of individual muons ($E_{\text{bundle}} = \sum_i E_{\mu_i}$).
3. Bundle direction $\cos \theta_{\text{zenith}}^{\mu \text{ bundle}}$: overall direction of the muon bundle in terms of the cosine of its zenith angle. Here, different approaches are possible (although all produce very similar results). One may consider:

a) arithmetic average of all muon directions: $\cos \theta_{\text{zenith}}^{\mu \text{ bundle}} = \frac{\sum_i \cos \theta_{\text{zenith}}^{\mu_i}}{N_\mu}$,

b) direction of the most energetic muon in the bundle,

c) energy-weighted average of all muon directions: $\cos \theta_{\text{bundle}} = \frac{\sum_i E_{\mu_i} \cdot \cos \theta_{\text{zenith}}^{\mu_i}}{\sum_i E_{\mu_i}} = \frac{\sum_i E_{\mu_i} \cdot \cos \theta_{\text{zenith}}^{\mu_i}}{E_{\text{bundle}}}$.

The option a) was used by default in this work.

4. Bundle width: maximal lateral spread of the bundle.
5. Bundle arrival time spread: difference between the arrival times of the first and the last muon at the sensitive volume of the detector.
6. Primary cosmic ray direction $\cos \theta_{\text{prim}}$. For primaries with high energies it is almost identical to $\cos \theta_{\text{bundle}}$.
7. Primary cosmic ray energy (either per nucleus: E_{prim} or total: $A \cdot E_{\text{prim}}$, where A is the atomic mass number).

Out of those listed variables, reconstruction of 1., 2., and 7. is discussed in Chap. 5, and a reconstruction of 3. with official KM3NeT software (see Chap. 3 and Sec. 4.3.5) is used in Chap. 6. The multiplicity and bundle energy results are also put to use in Chap. 7.

2.4. Atmospheric flux

Secondary particles produced in EAS are usually subdivided into two categories, based on their lifetimes. The long-lived ($t \gtrsim 10^{-8}$ s) ones contribute to the conventional and the short-lived ($t \lesssim 10^{-13}$ s) ones to the prompt atmospheric flux. Both components are described in this section. From the perspective of KM3NeT detectors (see Chap. 3), only muons and neutrinos are a relevant signal. In this work, the focus is on the atmospheric muon flux.

2.4.1. Conventional

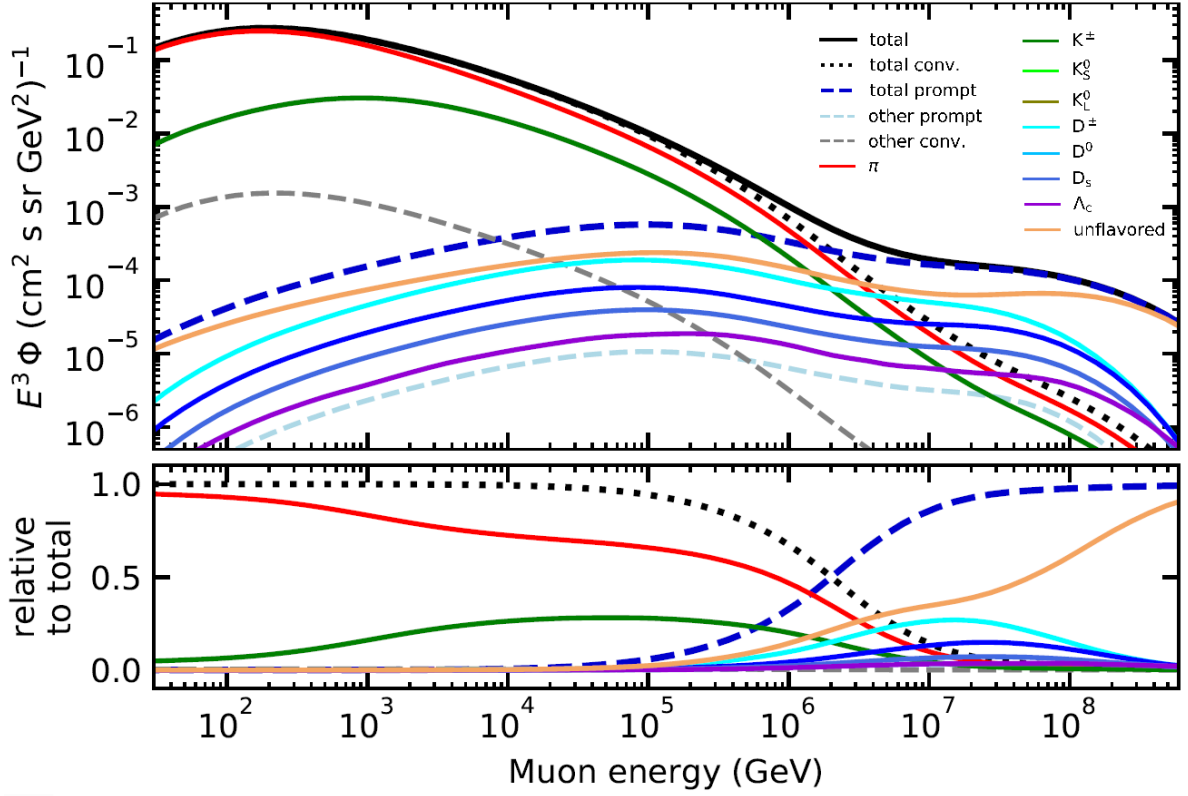
Conventional flux is the dominant component of the air showers. It can be subdivided into the following categories:

- π^0 producing electromagnetic (EM) cascades through consecutive bremsstrahlung and e^-e^+ pair creation. This part is in fact not relevant for this work, as EM cascades do not reach the KM3NeT detectors.
- Light charged mesons (π^\pm and K^\pm), producing hadronic cascades through scattering processes, and ν and μ through decays.

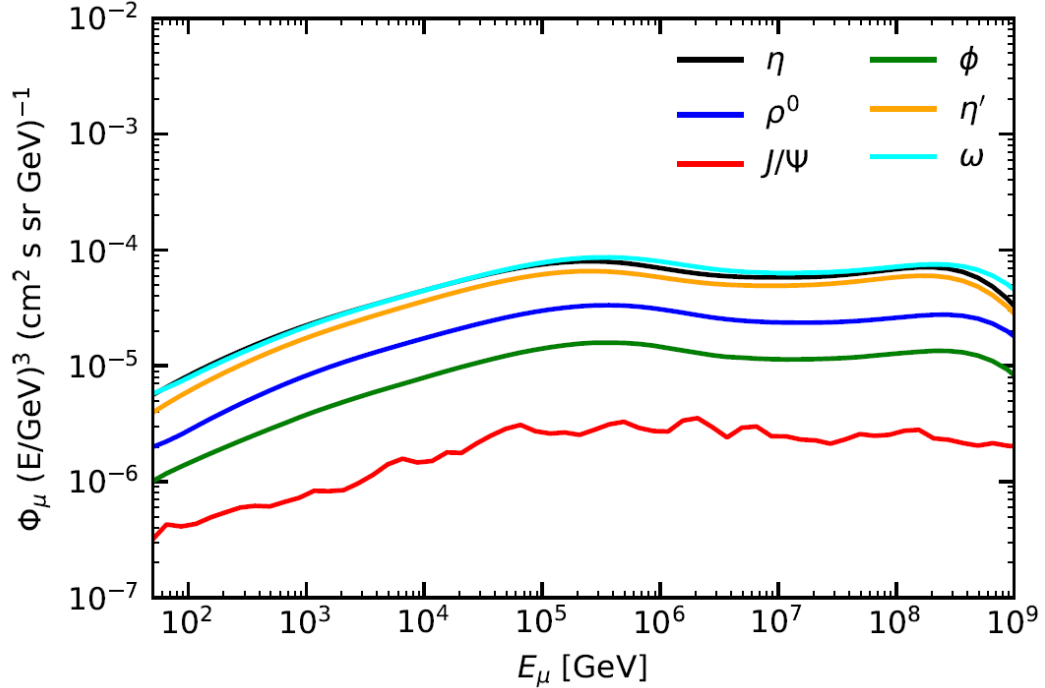
Conventional flux is rather well understood and measured [16, 17, 101].

2.4.2. Prompt

Prompt flux originates in semileptonic decays of heavy hadrons and light vector mesons into muons and neutrinos. The contribution of different parent particles to conventional and prompt components of muon energy spectrum is shown in Fig. 2.4.1. The crossing point, where the prompt flux starts to dominate over the conventional flux, is located around 1 PeV, which is well within the sensitivity of both KM3NeT detectors. Although the conventional flux is quite well understood and measured, no neutrino telescope has yet observed the prompt atmospheric muon or neutrino flux, there are only upper limits available from IceCube [16, 17, 101, 102]. ANTARES, KM3NET, and Baikal-GVD have not tackled the problem so far [103, 1, 57]. In order to predict the potential of KM3NeT to observe the prompt component, a CORSIKA MC simulation could be used (see Sec. 4.1.1) [104]. The ansatz taken in this work was to test the conventional-only hypothesis against the combination of prompt and conventional contributions, to evaluate the expected significance. The measurement in such a scenario would boil down to substituting the latter with the experimental data. The analysis is described in detail in Chap. 7.



(A) Different components of the atmospheric muon flux and some of the key contributing mother particles.



(B) Individual contributions to the unflavored component from Fig. 2.4.1a.

FIGURE 2.4.1.: Contributions to the atmospheric muon flux, taken from [105]. The plots were made using H3a CR flux model (see Sec. 4.1.1.2), PYTHIA 8 [106] for decays, and SIBYLL 2.3c as hadronic interaction model (see Sec. 4.1.1.2). The curves were plotted for a fixed zenith angle of $\theta_{\text{zenith}} = 60^\circ$ [107]. The unflavored component consists solely of hadrons with up and down valence quarks, as opposed to the D mesons (containing charm quarks) and kaons (strange quarks).

There are further subtleties concerning the prompt flux modelling, e.g. the so-called “intrinsic charm” [108], which is a contribution from virtual $c\bar{c}$ pairs inside the proton. Although virtual, such quark pairs can in principle hadronise into measurable particles. This effect is included in the SIBYLL 2.3d model (see Sec. 4.1.1.2), used as the default high-energy hadronic interaction model for this work [107, 109].

Examples of some relevant leptonic decay channels of short-lived hadrons in which muons are created directly are listed in Tab. 2.4.1.

TABLE 2.4.1.: Selected leptonic decays of short-lived hadrons resulting in direct muon production [20].

Decay channel	Branching fraction $\frac{\Gamma_i}{\Gamma}$ [%]
$J/\psi \rightarrow \mu^+ + \mu^-$	5.961 ± 0.033
$D^0 \rightarrow K^- + \mu^+ + \nu_\mu$	3.41 ± 0.04
$D_s^+ \rightarrow \mu^+ + \nu_\mu$	$(5.43 \pm 0.15) \cdot 10^{-3}$
$D^+ \rightarrow \mu^+ + \nu_\mu$	$(3.74 \pm 0.17) \cdot 10^{-4}$
$\eta \rightarrow \mu^+ + \mu^- + \gamma$	$(3.1 \pm 0.4) \cdot 10^{-4}$

The full list of mesons and baryons available in the CORSIKA simulation (see Sec. 4.1.1) used in this work, which may contribute to the prompt muon flux through their decays is compiled in Tab. A.6.2. The contributions of individual mother particles to the overall flux can be found in Fig. 7.1.1a.

Both the conventional and prompt flux are a background for the astrophysical neutrino flux searches, so far only observed by the IceCube experiment [17, 101]. Measuring the prompt flux is of utter importance for the future neutrino astronomy with KM3NeT/ARCA and KM3NeT/ORCA, and in collaboration with other experiments.

3. KM3NeT Experiment

KM3NeT is a network of neutrino telescopes located at the bottom of the Mediterranean Sea. The two sites at which the detectors are currently installed as well as the involved research institutes are shown in Fig. 3.1.1.

3.1. Neutrino telescopes in general

KM3NeT is neither the only nor the first water-based neutrino telescope in existence. In Fig. 3.1.1, currently operating experiments are shown, together with recently dismantled ANTARES [103]. This does not include the earlier projects, like e.g. AMANDA, the predecessor of IceCube at the South Pole [AMANDA=000026IC]. Except for IceCube, which uses Antarctic ice as the detector medium, all other neutrino telescopes use water in liquid state as the medium. However, there are still important differences to be noted. Baikal GVD is located in the freshwater of the lake Baikal in Russia [57]. Super Kamiokande (SK) uses artificially purified water, additionally loaded with $Gd_2(SO_4)_3 \cdot 8H_2O$ (gadolinium sulphate octahydrate) in 2020, enclosed inside a stainless steel tank [110]. The medium for ANTARES and KM3NeT are the salty waters of the Mediterranean Sea [103, 1]. Apart from the use of solid or liquid water as medium, all discussed neutrino telescopes share a common detection principle, based on the Cherenkov light emission in water.

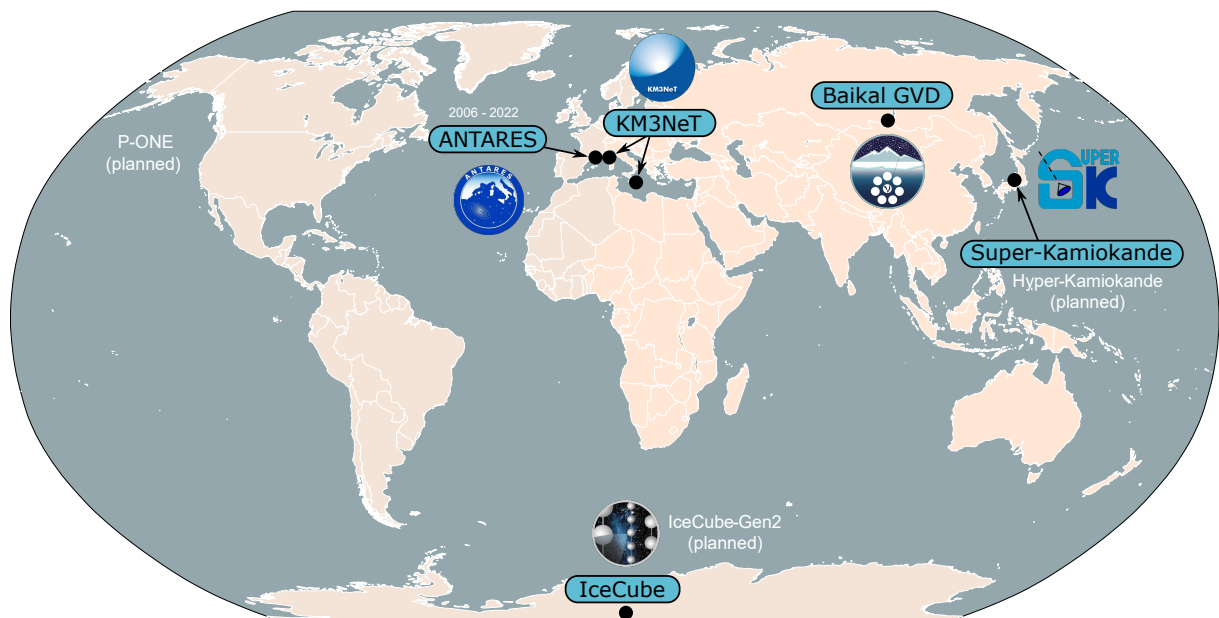


FIGURE 3.1.1.: World map showing the currently operating water- and ice-based neutrino telescopes. Additionally, the ANTARES detector is mentioned, as it has finished its duty only very recently in February 2022. In grey, some planned experiments and upgrades of existing ones are indicated.

3.1.1. Cherenkov radiation

Cherenkov radiation is a well-known phenomenon in particle physics. The effect was named after Pavel Alekseyevich Cherenkov, who shared the Nobel prize in physics with Ilya Frank and Igor Tamm in 1958 [111]. It occurs when an electrically charged particle traverses a medium with a velocity exceeding the speed of light in that medium. The passage of the charged particle excites atoms to higher energy levels. Upon returning to their ground states, the atoms emit photons uniformly in all directions. However, since the particle is moving faster than the photons themselves, a conical shock front, analogous to a supersonic wave behind a jet plane, is formed (see Fig. 3.1.2).

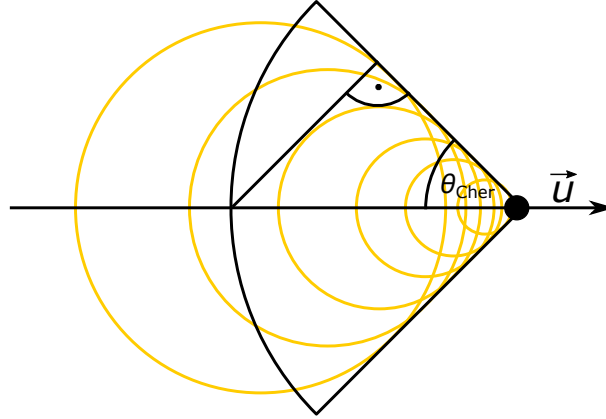


FIGURE 3.1.2.: Schematic geometry of Cherenkov radiation. \vec{u} is the velocity of the particle. Emitted light is coloured yellow, with only a few rings drawn for readability.

The opening angle of the cone θ_{Cher} can be computed by simple trigonometry from the paths the light and the charged particle will travel in a fixed time:

$$\cos(\theta_{\text{Cher}}) = \frac{1}{\beta n}, \quad (3.1.1)$$

where n is the refractive index of the medium and $\beta = \frac{u}{c}$ is the velocity of the charged particle, relative to the speed of light in vacuum c [112].

The threshold energy above which the effect occurs may be calculated by inserting Eq. 3.1.1 into the Einstein's energy-mass relation $E = mc^2$ [113] and setting $\cos(\theta_{\text{Cher}}) = 1$ (to obtain the extreme case):

$$E_{\text{threshold}} = \frac{m_0 c^2}{\sqrt{1 - \frac{1}{n^2}}}, \quad (3.1.2)$$

where m_0 is the rest mass of the particle. For seawater with a refractive index of about $n_{\text{sea}} \approx 1.383$ [114], the following threshold energies apply:

TABLE 3.1.1.: Summary of Cherenkov light emission threshold values computed for different particles in seawater ($n_{\text{sea}} \approx 1.383$).

Particle	Mass	$E_{\text{threshold}}$
e^{\pm}	$511.00 \frac{\text{keV}}{c^2}$	739.74 keV
μ^{\pm}	$105.66 \frac{\text{MeV}}{c^2}$	152.96 MeV
τ^{\pm}	$1.78 \frac{\text{GeV}}{c^2}$	2.57 GeV
π^{\pm}	$139.57 \frac{\text{MeV}}{c^2}$	202.05 MeV
K^{\pm}	$493.68 \frac{\text{MeV}}{c^2}$	714.67 MeV
p	$938.27 \frac{\text{MeV}}{c^2}$	1.35 GeV

As can be seen from Tab. 3.1.1, for high-energy neutrino astronomy applications, the Cherenkov threshold is not an issue. For the low-energy KM3NeT telescope ORCA (see Sec. 3.2.2), the minimum reconstructable energy will be in the range 1-5 GeV [2]. Knowing the refractive index, one may also compute the typical opening angle θ_{Cher} using Eq. 3.1.1, since $\beta \approx 1$ in the relevant energy range. For seawater this value is approximately equal 43.95° .

The amount of Cherenkov light that will be emitted can be estimated with the Frank-Tamm formula:

$$\frac{d^2N}{d\lambda dx} = \frac{2\pi\alpha z^2}{\lambda^2} \sin^2(\theta_{\text{Cher}}), \quad (3.1.3)$$

where $\alpha \approx \frac{1}{137}$ is the fine structure constant, z is the atomic charge number (for a muon, $z = 1$), and λ is the wavelength of the Cherenkov radiation [20]. For $\lambda=404$ nm (see the PMT specification in [2, 115]), translating into $E_\gamma = 3.07$ eV, the approximate number of emitted Cherenkov photons per track length, according to Eq. 3.1.3, is $\langle \frac{dN}{dx} \rangle \simeq 5.38 \cdot 10^4 \frac{1}{\text{m}}$. Assuming a monochromatic emission, this gives the energy loss due to Cherenkov effect of the order of $\left\langle \frac{dE}{dx} \right\rangle_{\text{Cher}} \simeq 165 \frac{\text{keV}}{\text{m}}$, which is negligible compared to the ionisation loss of about $\left\langle \frac{dE}{dx} \right\rangle_{\text{ion}} \simeq 200 \frac{\text{MeV}}{\text{m}}$ (see Fig. 2.1.1) [116].

3.1.2. Photomultiplier Tubes

The water-based neutrino telescopes study charged particles by observing the Cherenkov light emission they cause. The device, which enables this is called a photomultiplier tube (PMT). PMT can convert a faint light signal (potentially even a single photon!) into a massive cascade of electrons (typically $10^6 - 10^8$). Such a big current flow results in a voltage pulse strong enough to be recorded by the readout electronics. Fig. 3.1.3 visualizes qualitatively what is happening inside the PMT after an incident photon hits the photocathode and releases an electron through photoelectric effect. Such an electron cascade does not happen every time a γ hits the cathode: the probability of it happening is called quantum efficiency (QE) and is a property specific to the cathode [117]. It

can be calculated as the ratio of the number of emitted photoelectrons to the number of incident photons.

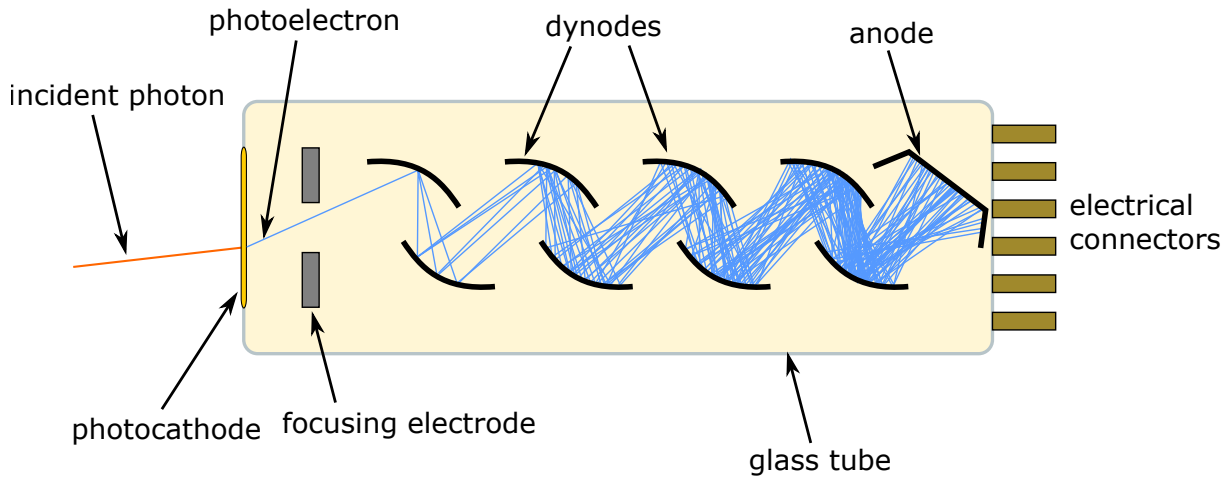


FIGURE 3.1.3.: Sketch of the amplification of the signal from a single photon by a PMT.

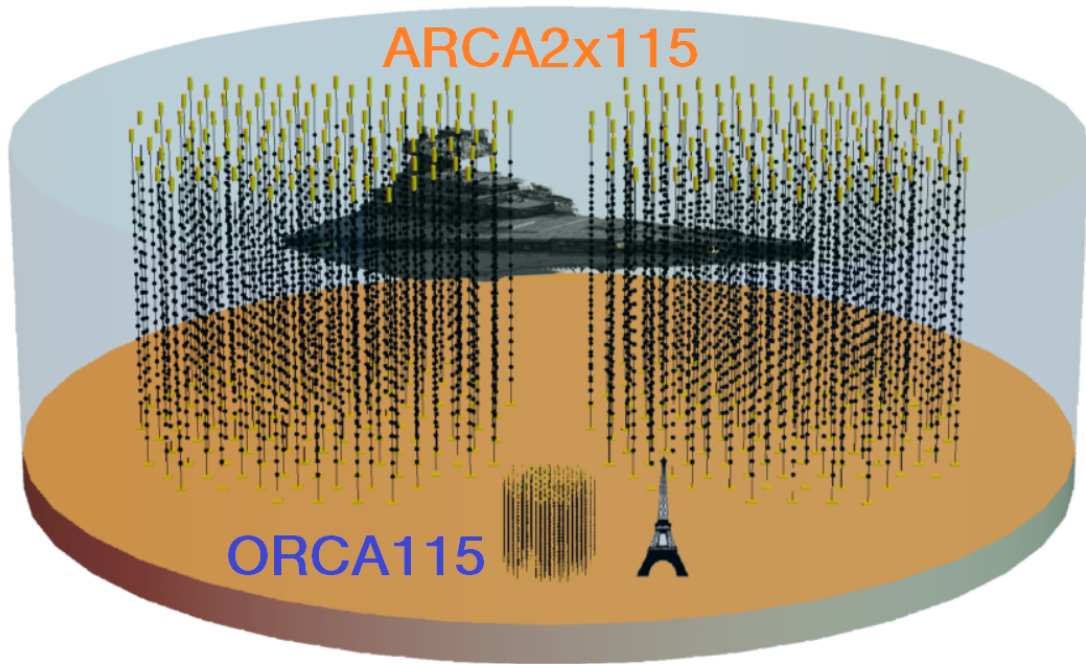
PMTs used in KM3NeT experiment are Hamamatsu R12199-02 with a hemispherical (mushroom) shape (80 mm diameter), 10 dynodes and a standard bi-alkali photocathode. They have QE of 20% at photon wavelength of 470 nm and 28% at 404 nm, dark count (PMT noise rate) of 1.5 kHz at 15 °C, according to their specification [2]. The stated working temperature matches the actual conditions at the bottom of the Mediterranean Sea [118, 119].

3.2. KM3NeT detectors and their physics case

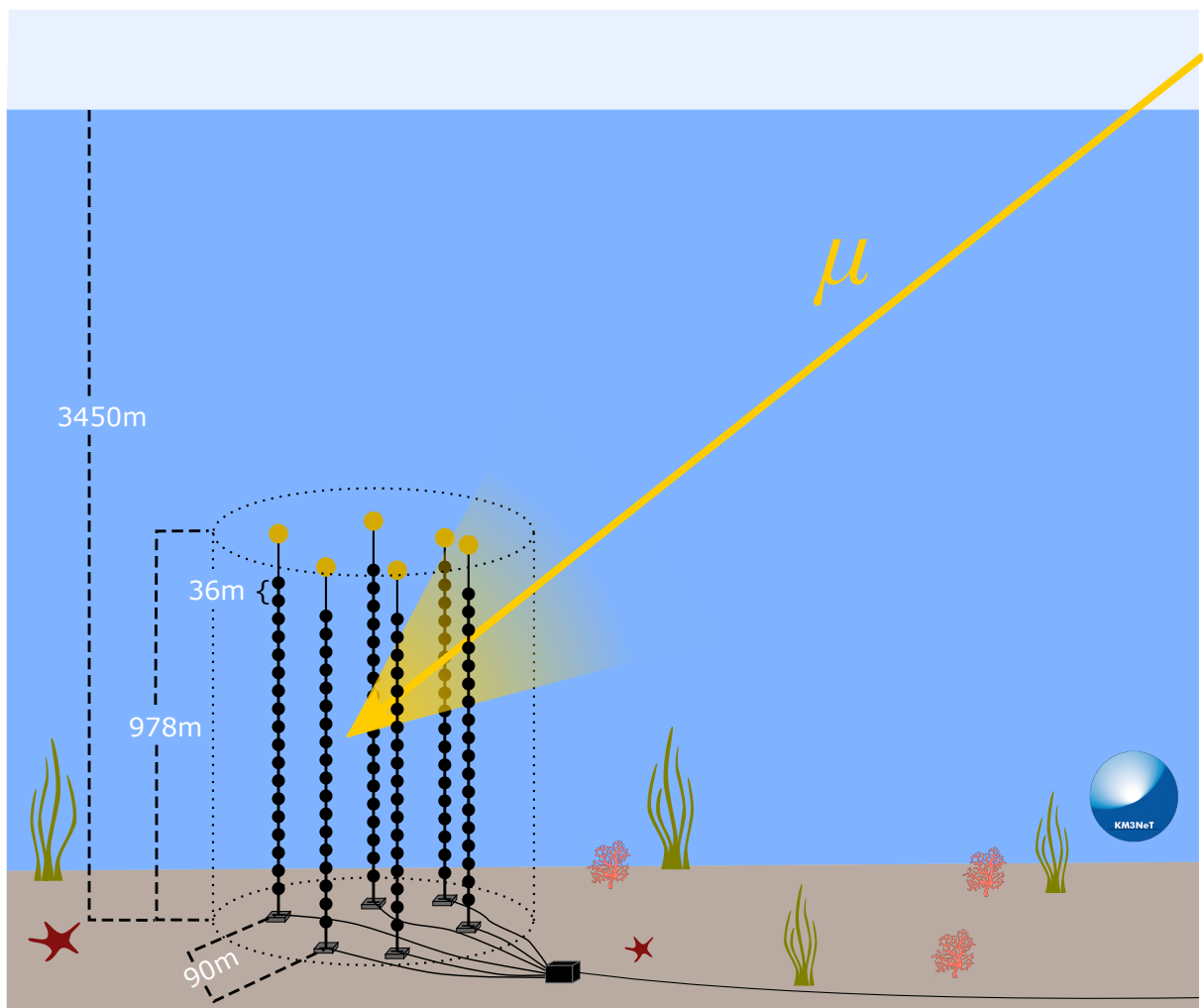
The points, where KM3NeT clearly stands out from the other experiments are:

- use of the identical technology under a single collaboration at multiple sites (which is highly beneficial in terms of systematic effect studies),
- the deepest underwater location (see Sec. 3.2.1),
- use of multi-PMT modules (see Sec. 3.2.3.1; much better spatial resolution).

KM3NeT detectors are sets of vertically oriented lines with digital optical modules (DOMs; see Sec. 3.2.3.1), called detection units (DUs; see Sec. 3.2.3.2 for more details), arranged in a cylindrical volume.



(A) Full KM3NeT detectors shown in comparison with the Eiffel tower and an imperial star destroyer from Star Wars. Credit: João Coelho.



(B) Sketch of the ARCA6 detector, i.e. ARCA detector with 6 DUs installed. Data from this detector configuration is used in Chapters 5, 6, and 7.

FIGURE 3.2.1.: Illustrations of the KM3NeT detector geometry.

In the following subsections, each detector is briefly described.

3.2.1. ARCA

ARCA stands for Astroparticle Research with Cosmics in the Abyss. It is the bigger of the two KM3NeT detectors, and in its final state it will consist of 2 building blocks, 115 DUs each (see Sec. 3.2.3.2 and 3.2.3.3). The radius of a building block is approximately 500 m (as in Fig. 3.2.4) and the bottom of the detector will be placed at a depth of 3.5 km at $36^{\circ}16'$ N $16^{\circ}06'$ E, about 100 km offshore from Portopalo di Capo Passero, Sicily, Italy. DOMs (see Sec. 3.2.3.1) on a DU are 36 m apart and the distance between DUs is 90m. The dimensions of the detector are optimized for astrophysical neutrino measurements. The big detector volume allows observing extremely energetic cosmic particles. The main objective of ARCA is to confirm the IceCube's (see 3.1) measurement of cosmic neutrino flux [17, 101] and allow for neutrino astronomy with an unprecedented precision thanks to a sub-degree angular resolution.

As of August 2023, the completion status of the first ARCA building block is 19/115 DUs. The construction of KM3NeT/ARCA is expected to conclude in 2032.

3.2.2. ORCA

ORCA (Oscillation Research with Cosmics in the Abyss) is more compact than ARCA, while maintaining the same number of DUs per building block. Complete ORCA will comprise a single building block of 115 DUs, distributed within a 100 m radius at a depth of 2.5 km at $42^{\circ}48'$ N $06^{\circ}02'$ E, about 40 km offshore from Toulon, France. The height of the detector is about 200 m, the spacing between DOMs on a DU: 9 m and the spacing between DUs: 20 m. As the name suggests, the detector is designed to study the phenomenon of neutrino oscillations. A particular emphasis is put on determining the neutrino mass ordering (see Sec. 2.2), since it has never been measured before and should be well within reach of ORCA. To achieve this, the few-GeV atmospheric neutrino flux will be studied, as in this energy range the differences between the expected flux for the assumption of normal and inverted ordering are very pronounced [120]. The need for a good energy resolution, especially for fainter events is the reason for ORCA's dense instrumentation. There are also plans for potential upgrades: making ORCA even more dense (Super-ORCA) [121], or shooting a neutrino beam from the Protvino accelerator in Russia to ORCA (Protvino to ORCA: P2O) [122].

As of August 2023, the ORCA detector consists of 16/115 operational DUs and should be completed in 2030.

3.2.3. Detector design

The basic design of both KM3NeT detectors (ARCA, ORCA) is sketched in Fig. 3.2.2 and their elements are described in what follows.

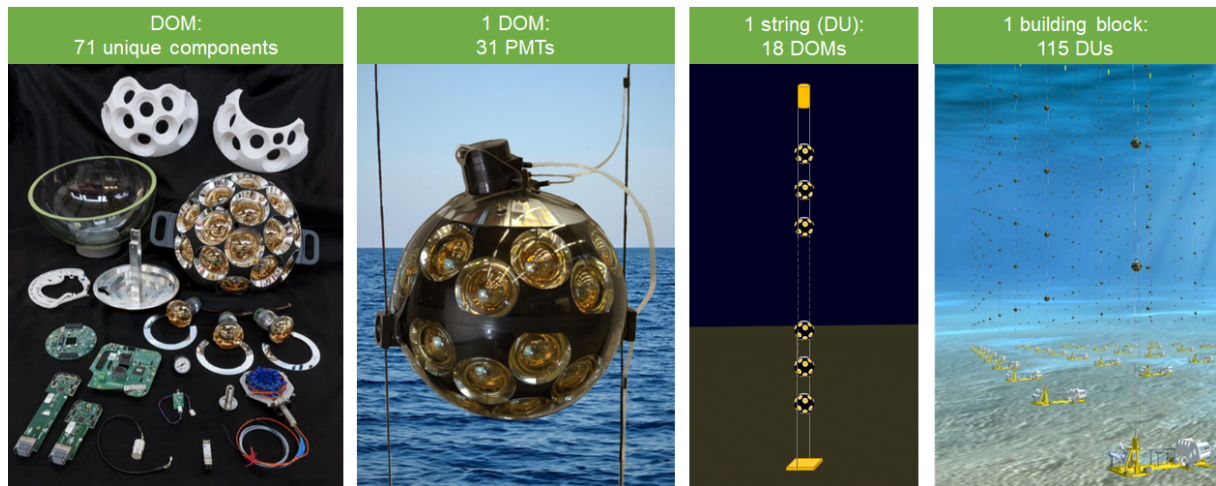


FIGURE 3.2.2.: The summary of the KM3NeT detector design, ordered from tiniest components to the complete building blocks. More detail on all the components may be found in [2, 123].

3.2.3.1. Digital Optical Modules

Digital optical module (DOM) is a hermetically enclosed 17" glass sphere, containing 31 PMTs, pressure, tilt and acoustic sensors, compass, readout electronics, and other equipment. A disassembled DOM is presented in Fig. 3.2.2 on the left. The use of multi-PMT DOMs instead of traditional optical modules with single large PMT (as e.g. in IceCube or SK) has significant advantages:

1. The total photo-cathode area per module is larger: more emitted photons can be collected.
2. The angular coverage is nearly uniform: light coming from any direction will be reconstructed equally well.
3. Each of the PMTs inside the DOM has slightly different position and orientation (see Fig. 3.2.2). The implication of this are varying light detection times at different PMTs, which adds to the directional information.
4. The environmental background (see Sec. 4.3.4) may be more efficiently eliminated by requiring the light signal to be observed by multiple PMTs on a DOM in coincidence [124].

3.2.3.2. Detection Units

A Detection Unit (DU) is a set of 18 DOMs attached with titanium collars to two Dyneema[®] ropes in the shape of a vertical string, mounted at the seabed with an anchor. DUs are connected to junction boxes at the bottom of the sea (which in turn are connected to the shore station) through the electro-optical cable, which contains power lines (400 VDC) and 18 optical fibres to transfer the data. On top of the DU line there is also a buoy to keep it as vertical as possible (deviations from the nominal position due to e.g. sea current are tracked, stored and included when analysing the data). DU deployment at the experimental site is shown in Fig. 3.2.3. Each DU is deployed in a launcher of optical modules (LOM), which makes sure that the structure will be properly aligned by guiding the unfurling process.

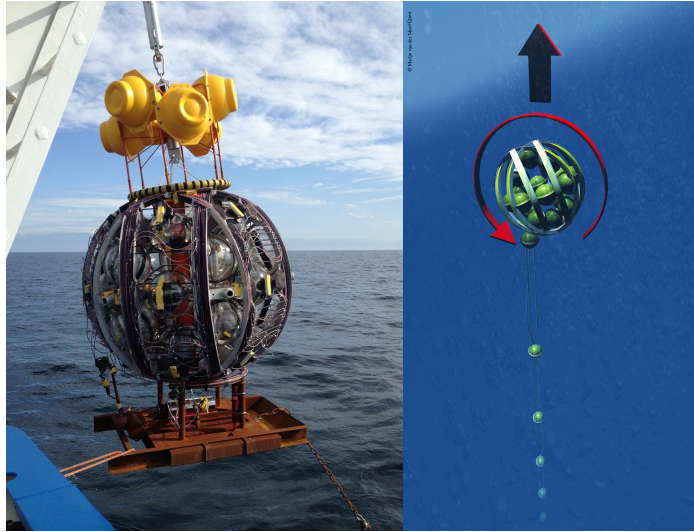


FIGURE 3.2.3.: On the left: a real photo of a DU during the deployment at the French site. Right: schematic drawing, showing how a LOM unfurls, releasing the DOMs.

3.2.3.3. Building blocks

For each detector, a building block consists of 115 DUs. It is powered by a set of junction boxes and connected via optical fibres to the shore station, where the digitized data from the DOMs is sent to and processed. The adopted approach is ‘all data to shore’, which means that there is no pre-selection of what will be saved. This implies a transfer rate up to $25 \frac{\text{GB}}{\text{s}}$ per building block (in total $75 \frac{\text{GB}}{\text{s}}$ for complete ARCA and ORCA).

The distribution of the DUs in a building block is shown in Fig. 3.2.4.

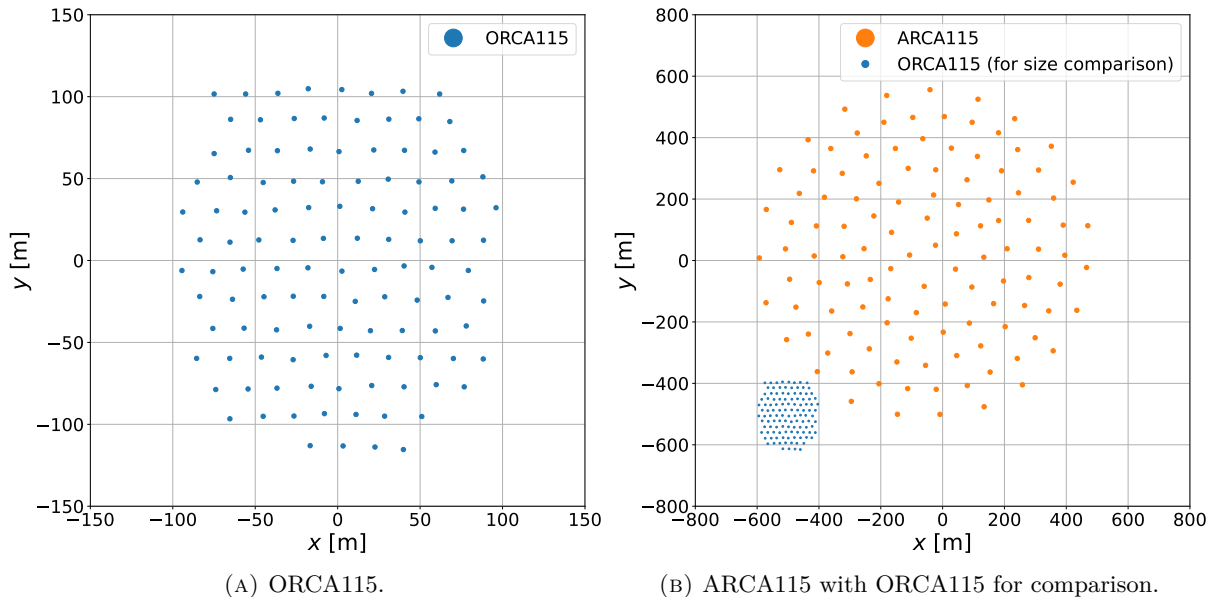


FIGURE 3.2.4.: KM3NeT detector footprints for complete building block configurations, as in the CORSIKA simulation used for Chap. 5–7.

3.2.4. Event topologies

Depending on the particle type, events inside the detector may look completely different (see Fig. 3.2.5). In terms of shape, we distinguish between two categories:

- track-like events, typically corresponding to muons (coming directly from the atmosphere or produced in ν_μ CC interactions), which do not lose a lot of energy at once (see Sec. 2.1)
- cascade-like (often also referred to as shower-like) events, mostly caused by ν_e or ν_τ interactions

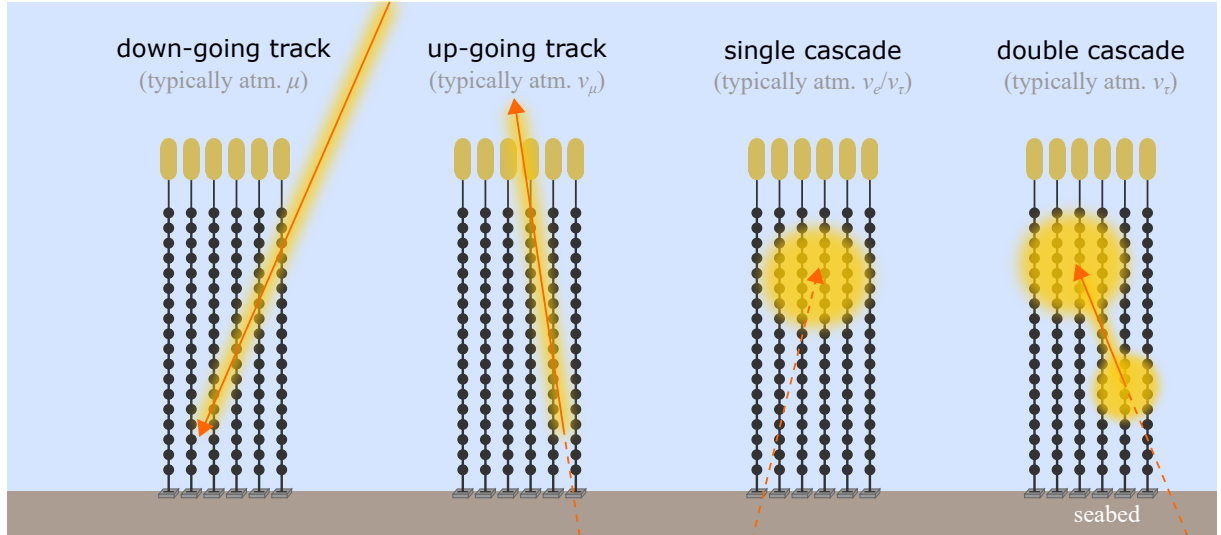


FIGURE 3.2.5.: The summary of different event topologies seen in KM3NeT detectors.

In case of particularly energetic ν_τ events (which are rare), two distinct cascades separated by a dim track may be observed: one from the ν_τ interaction in which the τ lepton is produced and the other from the decay of the τ . The separation between the cascades depends on tau neutrino energy E_{ν_τ} , since the τ decay length is approximately $\langle L_\tau \rangle \sim 50\text{m} \cdot \frac{E_\tau}{\text{PeV}}$ [2], which given the instrumentation density and energy resolution of ARCA and ORCA should allow to observe such events with full detectors.

4. Simulation of atmospheric muons in KM3NeT

This chapter describes the simulation of EAS (see Sec. 2.3.3) and their products that can be detected by KM3NeT detectors, with a particular emphasis on muons.

4.1. Event generators

The two main event generators used in this work: CORSIKA and MUPAGE [104, 125] are described in the following sections.

4.1.1. CORSIKA

CORSIKA stands for COsmic Ray SIMulations for KAscade and was developed for KASCADE (KArlsruhe Shower Core and Array DEtector) experiment at Karlsruhe Institute of Technology, measuring EAS [126]. It offers a full event-by-event simulation of air showers with many customization possibilities. There are various models of low- and high-energy hadronic interactions available. The simulation can be adapted to almost any imaginable primary CR flux and composition. The atmosphere density profile can be taken either from a predefined parametrization or from a custom fit, supplied by the user. More details on CORSIKA are given in the following subsections, in Sec. A.1, and in [104, 5]. Within this thesis CORSIKA7 was used and unless specified otherwise, CORSIKA always refers to this major version.

4.1.1.1. Implemented processes and particles

All the processes potentially relevant for EAS are implemented in CORSIKA and all the secondary particles are explicitly tracked, with their parameters stored at observation level (in case of KM3NeT simulations, it is the sea level) [104].

CORSIKA implements the properties of all leptons and most commonly occurring hadrons. The full list can be found either in [5], or in Tab. A.6.3.

4.1.1.2. Models

Here, different classes of physics models are briefly described.

Cosmic ray flux models Cosmic ray flux models describe the total primary CR flux arriving at the Earth and its composition. The default one used for event weighting (see Sec. 4.2) in the CORSIKA simulations for KM3NeT is the Gaisser-Stanev-Tilav model with 3 populations (GST3). It is a fit to CR data, performed with an assumption of 3 populations of particle sources:

1. Supernova remnants (SNR).
2. Other galactic sources.
3. Extragalactic sources.

Each population has a different magnetic rigidity ($R = \frac{p|c}{Ze}$) cutoff, nuclei groups, and spectral indices. The particle spectrum is approximated with the following formula:

$$\phi_i(E) = \sum_{j=1}^3 a_{i,j} E^{-\gamma_{i,j}} \cdot e^{-\frac{E}{Z_i R_{c,j}}}, \quad (4.1.1)$$

where E is the primary cosmic ray energy per nucleus, $i = (p, \text{He}, \text{C}, \text{O}, \text{Fe})$, $a_{i,j}$ are the normalization constants, $\gamma_{i,j}$ are the integral spectral indexes, Z_i are the atomic numbers, and $R_{c,j}$ are the characteristic magnetic rigidities [127]. The result of the fit is shown in Fig. 4.1.1.

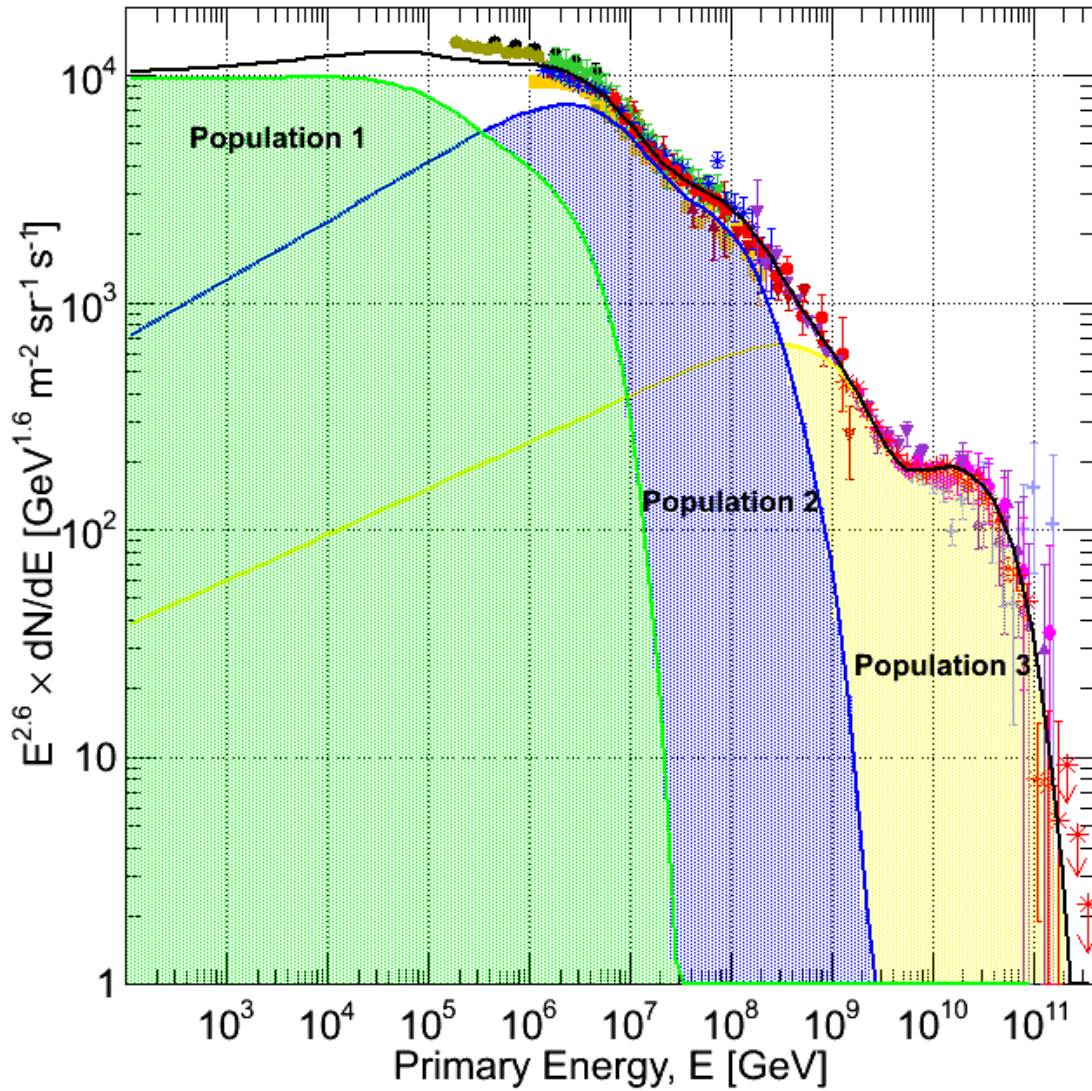


FIGURE 4.1.1.: Fit of the CR flux data to the 3-population scenario from [127].

Some of the other available CR flux models can be found in [128, 129, 130, 131, 132, 127, 133]. Selected ones were used in Sec. 6.2 to evaluate the systematic uncertainty related to primary CR flux modelling.

Hadronic interaction models The models of the hadronic interactions available within CORSIKA are divided into two categories: low-energy (LE) and high-energy (HE), with the threshold between the two set at 80 GeV [5].

The choice of LE hadronic interaction models is limited to three options: FLUKA, GHEISHA, and UrQMD [134, 135, 136]. In this work, the UrQMD model has been used, since it offers a good description of the physics processes and works stably down to the lowest energies possible in CORSIKA. It has been verified by the earlier CORSIKA productions, that GHEISHA implementation tends to fail at the lowest energies. FLUKA is a state-of-the-art low-energy hadronic interaction model, however due to limited access to the code and potential copyright issues, it has not been used. Due to the fact that the KM3NeT detectors are shielded by more than 2 kilometres of water above them (see Chap. 3), the adopted LE model is of marginal importance for muon studies. However, this would no longer hold true for the simulation of LE neutrino flux arising from the CR-induced showers.

HE hadronic interaction models are one of the most important choices made when compiling the CORSIKA code, as they determine the core behaviour of the program. There is a number of such models available: VENUS, NEXUS, DPMJET, QGSJET, EPOS, and SIBYLL [137, 138, 139, 140, 141, 107, 142, 143, 144]. However, only the latter three are relatively up to date and only DPMJET and SIBYLL explicitly treat charmed and strange hadron production. As this is a necessary prerequisite for the prompt muon analysis in Chap. 7, SIBYLL 2.3d (the most recent available version at the time) has been used as the default HE hadronic interaction model [109].

Model of the atmosphere In CORSIKA, the atmospheric density is modelled by dividing the atmosphere into 5 distinct layers. The thickness $T(h)$ $\left[\frac{\text{g}}{\text{cm}^2}\right]$ of the first 4 layers is parameterised exponentially:

$$T(h) = a_i + b_i \cdot e^{-\frac{h}{c_i}}, \quad (4.1.2)$$

and for the 5th layer linearly:

$$T(h) = a_5 - b_5 \cdot \frac{h}{c_5}, \quad (4.1.3)$$

where i is the layer number, a_i , b_i , c_i are the fitted parameters, and h is the altitude above the sea level. The upper boundaries of each layer h_i^{upper} can be adjusted to tune the fit accuracy (see Fig. A.1.10). CORSIKA comes with a set of predefined density models for different locations and epochs, and also tools to create custom models: `gdastool` (fitting the 5-layer atmosphere to the GDAS database [145]) and `bernlrohr` package [104]. In this work, a fit of the NRLMSIS-2.0 [146] atmosphere model was used. It was fitted to the 5 described by Eq. 4.1.2 and 4.1.3, using the fitting utilities of the SciPy package [147]. The details can be found in Sec. A.1.2.

4.1.2. MUPAGE

MUPAGE stands for fast atmospheric MUon GEnerator for neutrino telescopes based on PArametric formulas. As the name suggests, it is not a full Monte Carlo simulation [125]. It samples parametrized muon bundle distributions to generate muon events on the surface of a cylinder enclosing the detector (see Sec. 4.3.2). It was designed for the ANTARES experiment [103, 125] and was inherited by KM3NeT. The main advantage of MUPAGE over CORSIKA is that it is much faster, however the price for this is a smaller amount of information that can be extracted from the simulation, e.g. there is completely no information on particle history. There are ongoing efforts to update the code by performing new fits of internal MUPAGE parameters, using both the CORSIKA MC produced within this work [148, 10], and the currently available data from the KM3NeT detectors [149].

4.2. Event weighting

The MC generators simulate a given number of events, however to compare them against experimental data, a translation to the units of expected event rate is necessary. This can be achieved by employing event weights w_{event} . In the following, the weighting schemes for CORSIKA and MUPAGE are described.

4.2.1. CORSIKA

In CORSIKA muon simulations, there are four types of weights in use:

- $w_1 = S$ — the effective surface of the sensitive volume of the detector (see Sec. 4.3.2) [m^2],
- w_2 — contain the generation weight [$\text{GeV} \cdot \text{m}^2 \cdot \text{sr} \cdot \frac{\text{s}}{\text{year}}$],
- w_3 — so-called “global weights” in the unit of rate [$\frac{1}{\text{year}}$],
- w_{event} — final weights, used for comparisons between data and MC.

The generation weight w_2 can be calculated as:

$$w_2 = \underbrace{S}_{w_1} \cdot I_\theta \cdot I_{E_{\text{prim}}} \cdot E_{\text{prim}}^\gamma \cdot F, \quad (4.2.1)$$

where:

$I_\theta = 2\pi [\cos(\theta_{\text{max}}) - \cos(\theta_{\text{min}})]$ [sr] — angular phase space factor,

$$I_{E_{\text{prim}}} = \begin{cases} \frac{E_{\text{prim}}^{1-\gamma}|_{\text{max}} - E_{\text{prim}}^{1-\gamma}|_{\text{min}}}{1-\gamma} & \text{if } \gamma \neq 1 \\ \ln\left(\frac{E_{\text{prim}}|_{\text{max}}}{E_{\text{prim}}|_{\text{min}}}\right) & \text{if } \gamma = 1 \end{cases} \quad \text{— energy phase space factor,}$$

E_{prim} — primary energy per nucleus,

γ — generation spectral index,

$F = 3600 \cdot 24 \cdot 365.2422$ — average number of seconds in a year.

The CORSIKA simulation produced in this work was split into four sub-productions, divided into distinct E_{prim} ranges, reflected in their names: TeV_low, TeV_high, PeV, and EeV. The simulated primary energy spectrum E_{prim}^γ , called generation spectrum, is different for every CORSIKA sub-production and was tuned to compensate for the effects of propagation through air and water. It has

nothing to do with the actual CR spectrum observed in nature, it is merely a way to optimize the statistics of the simulation, similarly to the number of generated showers for each sub-production. In addition, the numbers of generated showers (see Eq. 4.2.3) per primary have been adjusted, based on the computation time and disk space constrains. The details of the CORSIKA production settings are summarised in Tab. A.1.2.

The w_3 weights are derived from w_2 by multiplying them with an assumed CR primary particle flux ϕ [$\frac{1}{\text{GeV}\cdot\text{m}^2\cdot\text{sr}\cdot\text{s}}$]:

$$w_3 = w_2 \cdot \phi. \quad (4.2.2)$$

As mentioned in Sec. 4.1.1.2, in the case of CORSIKA simulations the GST3 CR flux model is used [127]. The predicted CR flux ϕ for the primary energy range relevant for KM3NeT is shown in Fig. 4.2.1.

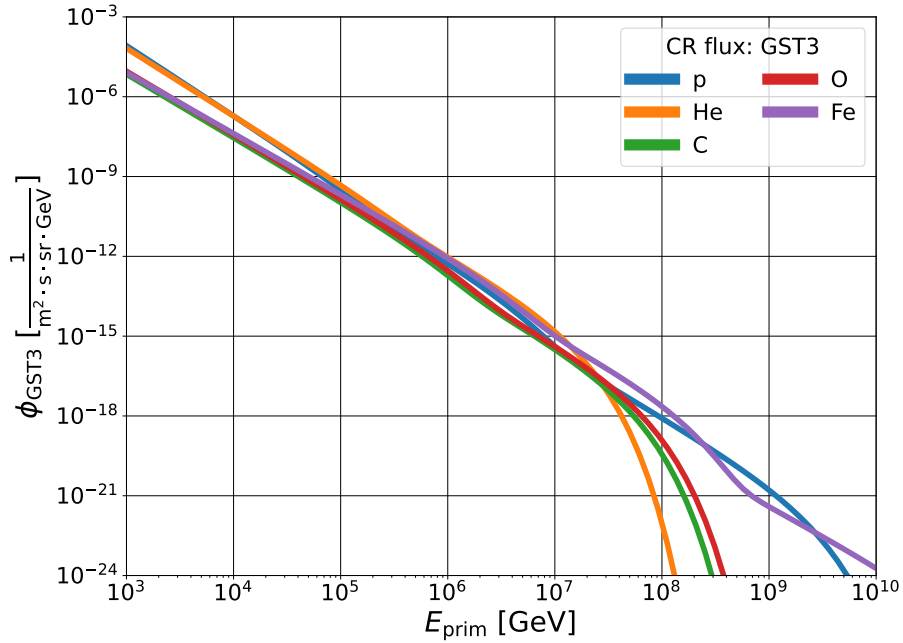


FIGURE 4.2.1.: Flux predicted by the GST3 model as function of the primary energy for each of the primary particles used in CORSIKA simulation [127]. In the flux of iron primaries, the transition between the second and third source population at around 10^9 GeV can be seen (see Sec. 4.1.1.2).

To obtain the expected event rates, the final event weights w_{event} have to be computed:

$$w_{\text{event}}(\text{prim}, E_{\text{prim}}) = \frac{w_3}{n_{\text{generated showers}}(\text{prim}, E_{\text{prim}})}, \quad (4.2.3)$$

which boils down to dividing w_3 by the appropriate number of generated showers. This will result in an event rate in units of $\frac{1}{\text{s}}$. If one prefers to have it in $\frac{1}{\text{year}}$, the result has to be multiplied by F . It has to be emphasized that $n_{\text{generated showers}}$ is in principle a different number for each primary and for each sub-production, hence the prim and E_{prim} dependence in Eq. 4.2.3. If the sub-productions overlapped, the $n_{\text{generated showers}}$ in the overlapping regions would be the sum of all the showers from the overlapping sub-productions. No such overlap was used in the CORSIKA production,

with the intent of avoiding confusion and potential misuse of the weights by users unaware of such subtlety. The event weight example for ARCA115 CORSIKA MC is shown in Fig. 4.2.2.

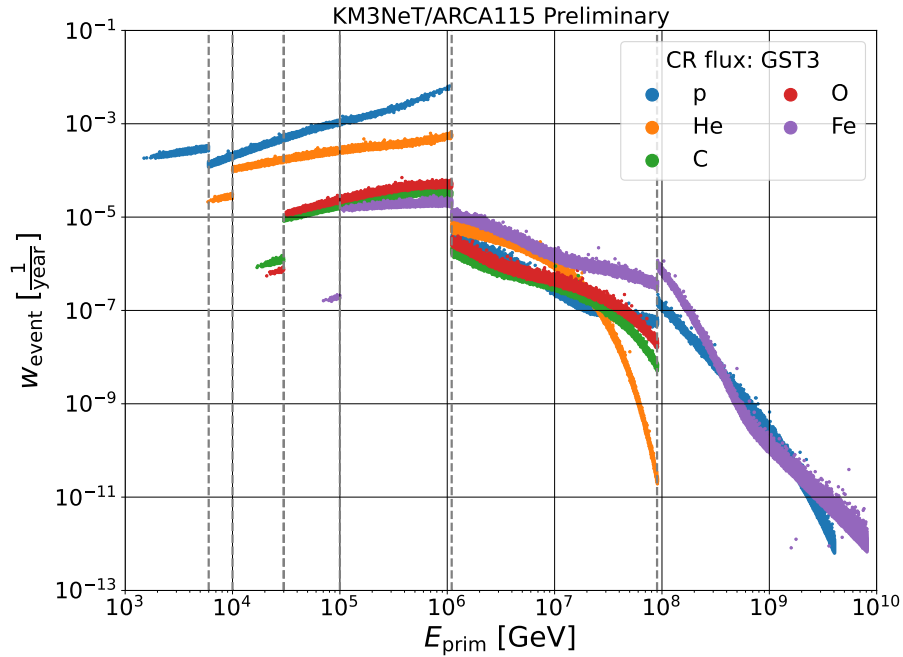


FIGURE 4.2.2.: Event weights as function of the primary energy shown for each of the primaries separately. The horizontal dashed grey lines are the boundaries of CORSIKA sub-productions (see Tab. A.1.2). The vertical spread of the data points comes from the angular dependence of the event weights (see Eq. 4.2.1). The plot was made using the ARCA115 MC.

As bizarre as it may seem, such weights as in Fig. 4.2.2 do produce a smooth prediction of the expected rates, as e.g. shown in Fig. 4.2.3. It is possible because all the apparent discontinuities and different slopes in Fig. 4.2.2 are exactly accounting for the underlying statistics with which the CORSIKA MC has been generated.

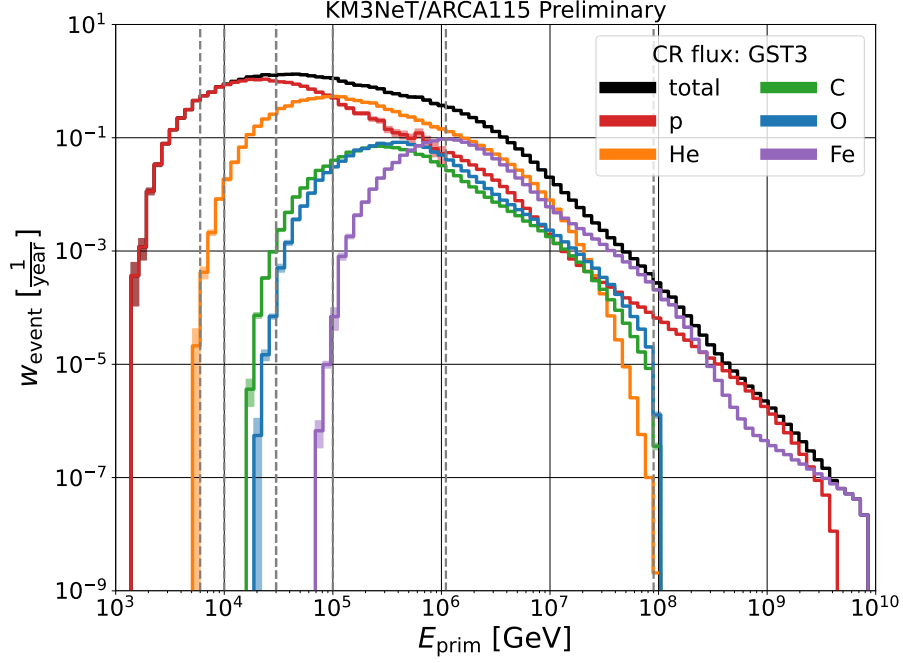


FIGURE 4.2.3.: Weighted primary energy distribution showing the contribution of each of the primaries. The horizontal dashed grey lines are the boundaries of the CORSIKA sub-productions (see Tab. A.1.2). The errors are shown by shaded rectangles around the bins and were computed using Eq. A.2.1.

One more important thing to note is that in the left part of Fig. 4.2.3 there is quite a drastic cutoff in the spectra, which is not present in the CR flux itself (Fig. 4.2.1). This is an effect of the propagation of the shower products (muons). It is present even directly in the CORSIKA output at the observation level (sea level in our case), since only the showers reaching the observation level are saved in CORSIKA. The effect becomes even more pronounced after propagation through water.

4.2.2. MUPAGE

In the case of MUPAGE, the weighting is rather trivial and the weights are:

$$w_{\text{MUPAGE}} = \frac{1}{t_{\text{live}}}, \quad (4.2.4)$$

where t_{live} is the total simulated livetime (active data taking time), which is analogous to how the experimental data is weighted for data vs MC comparisons (see Chap. 6). The resulting weighted distributions are event rates.

4.3. Muon simulation: from sea to reconstruction level

The muon simulations in KM3NeT are typically multi-staged, since after the muons are generated, they still need to be propagated through seawater to the detector. Afterwards, the light emission and its subsequent detection by the PMTs is simulated. A schematic structure of the KM3NeT

muon simulation and data processing software chain is depicted in Fig. 4.3.1. All of the following subsections delve into more detail of each of the processing stages, also called levels.

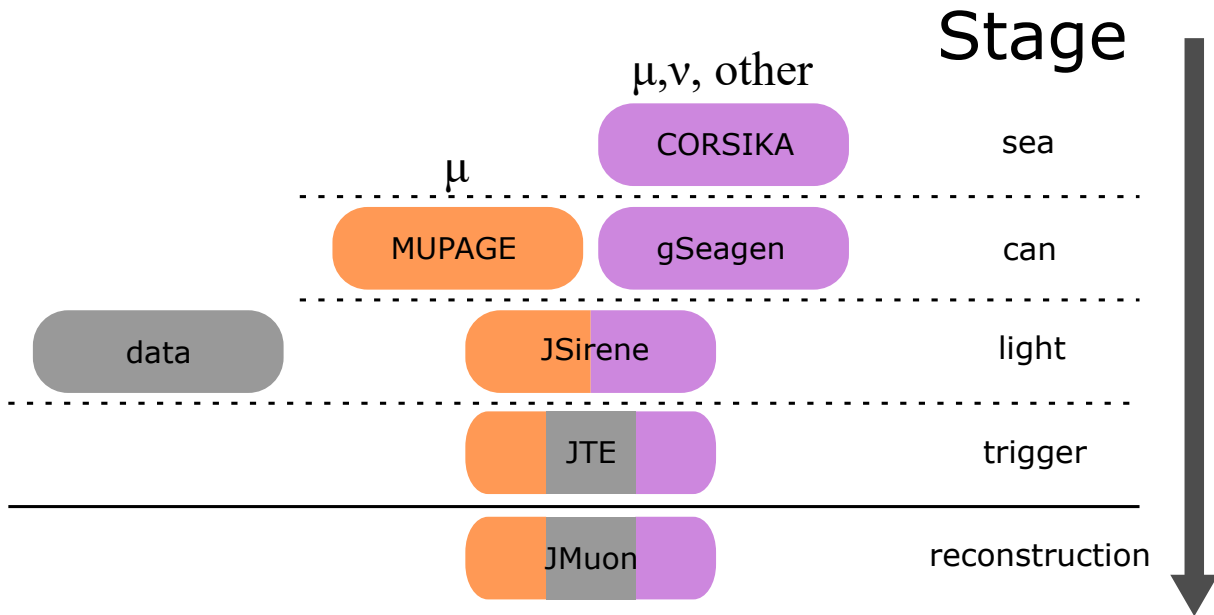


FIGURE 4.3.1.: KM3NeT processing chain. Software used for muon MC simulation (MUPAGE and CORSIKA) and experimental data processing is colour-coded respectively. Chain is also subdivided into stages (levels), starting from the sea level all the way to the reconstruction level. For MC generators the produced particle types are indicated.

4.3.1. Sea level

In context of KM3NeT, the output of CORSIKA simulation is uniquely at the sea level. The particles are stored at the sea surface, taking into account the curvature of the Earth, which can be non-negligible for high-energy horizontal showers [5]. The sole reason why the observation level for the KM3NeT CORSIKA simulations is chosen to be the sea surface is that the propagation through mixed media (i.e. air + seawater) is currently not supported in CORSIKA7. However, this will change in the coming release of CORSIKA8 [150].

The standard CORSIKA output is stored in sequential unformatted FORTRAN files [5]. To further work with such data, it is convenient to convert it to a more suitable format.

For the older CORSIKA productions (used e.g. for the ARCA2 and ORCA1 results in Chap. 6), this was achieved with the internal KM3NeT software called Corant. It was written in C++ and performed a conversion to the ASCII (text) format, preliminarily computed the event weights (the event weights are final only at the can level; see Sec. 4.2 and 4.3.2) and translated the particle tracks to the KM3NeT reference system. The author of this thesis has contributed a number of developments to the Corant code and is its current maintainer.

An alternative is to process the file to the can level (see next section) with gSeaGen using the ‘-write 2’ option, which preserves the complete CORSIKA sea-level information. The user may pick between ASCII and ROOT output file formats.

4.3.2. Can level

The name can level stems from the cylindrical shape of the KM3NeT detectors. If simulation is at the can level, it means that the secondary particles (muons and/or neutrinos) are inside the active volume of the detector. This volume is typically the instrumented volume (minimal cylinder enclosing the detector) enlarged by 4 light absorption lengths in seawater¹, to take into account the fact that the light emitted before reaching the detector may still be observed [151].

MUPAGE (described in Sec. 4.1.2) directly generates muon bundles from parametrised zenith, energy, and multiplicity distributions at the can level. It is possible owing to the fact that it was tuned on data corresponding roughly to ORCA (and ANTARES) depth [125]. This approach has its drawbacks, for instance MUPAGE does not necessarily describe the muon flux at other depths (e.g. ARCA) equally well. This is one of the reasons why a more detailed muon simulation was needed.

CORSIKA is such a comprehensive muon MC. As already mentioned in previous section, the tool allowing to process CORSIKA output is gSeaGen. gSeaGen is a code, which can generate neutrino events using GENIE [152] (NOT used in this work) and propagate μ and ν . It can be linked to different libraries that perform the propagation: MUSIC [153], PROPOSAL [25], Jpp [154], or use its own built-in routine — PropaMuon [4]. Numerous contributions to gSeaGen software have been made in scope of this thesis, and some of them are described in A.3. gSeaGen is publicly available as an open-source code under git.km3net.de/opensource/gseagen. The program is maintained and developed by the author of this thesis.

4.3.3. Light level

At light level, emission of Cherenkov radiation along the path of muons and detection of the photons by the PMTs are simulated. An instance when a PMT records a signal exceeding its voltage threshold (adjusted during the detector calibration) is called a hit. There are three codes dedicated to light simulation within KM3NeT, however only one is used for this work, as indicated in Fig. 4.3.1.

The default choice for most MC productions, including the CORSIKA MC, is JSirene. It is a custom application developed for KM3NeT, which uses multidimensional interpolation tables to speed up the computation in certain routines [154]. JSirene is a part of the Jpp framework, consisting of many KM3NeT-specific utility functions, programs, and services.

The first alternative is KM3Sim. It propagates particles in water, using the Geant4 software [155]. It comes with all the advantages and setbacks of Geant4, which means it offers detailed simulation of various energy loss processes, however the price to be paid is a rather high CPU time required for computation.

Km3 is a FORTRAN-based code for parametric simulation of light propagation, which was historically developed by the ANTARES experiment [156]. The parametrizations have been obtained from GEANT3 simulations [157]. Km3 has been adapted from the ANTARES version to incorporate the characteristics of KM3NeT DOMs and PMTs.

¹4 · 70 m = 280 m, this value was also used for the CORSIKA MC

4.3.4. Trigger level

Simulation of the event triggers is performed using the JTriggerEfficiency (JTE) package from the Jpp framework [154]. It mimics the environmental optical background due to the bioluminescence and radioactive decays of ^{40}K (in 89.52% of the cases a β decay producing a 1.31 MeV electron [158]). On top of adding the simulated background, JTE emulates the detector response, taking into account the effects of front-end electronics. The trigger-level simulation may be performed in a run-by-run (rbr) mode, i.e. reproducing each data taking run separately (which is typically done for MUPAGE). The alternative is the non-rbr mode, which is used by default for the CORSIKA MC, since producing sufficient statistics for each run with CORSIKA would be too costly. The non-rbr MC provides a prediction of a mean muon flux, with averaged trigger settings and PMT parameters used throughout the whole simulation. The trigger algorithms applied to identify potentially interesting events are exactly the same ones as used for the real data. There is a number of those, corresponding to different event classes. For the MC productions considered within this thesis only two were used: 3DMuon and 3DShower, which are triggers for muon tracks and for shower-like events respectively. After applying the trigger algorithms, merging of events overlapping in time is performed, and the number of overlaying events² is computed. Here it has to be stressed that the definition of an event in JTE deviates from what is used throughout the rest of this thesis (1 event being equivalent to 1 EAS). Here, an event is any collection of triggered hits within a certain time window (the exact value depends on the trigger algorithm). Such hits should be more likely to originate from actual particle interactions, however they still contain a contribution from the experimental background.

4.3.5. Reconstruction level

Since the main focus of the work is on the muons, the most relevant event topology are tracks, despite the fact that muons can sometimes undergo catastrophic energy losses and produce cascade-like signatures in the detectors [159]. Track events are reconstructed with help of JMuon algorithm and cascades (showers) are reconstructed using one of the 2 codes: Aashowerfit (used for ARCA) and JShowerfit (used for ORCA) [154, 160]. In this work, only JMuon has been used. In the following sections, reconstruction algorithms for different observables are discussed.

4.3.5.1. Direction reconstruction

The direction of an event is inferred from the timing and charge deposition information from the PMTs by performing a maximum-likelihood fit. The assumptions for the fit are that the particle propagates with the speed of light in vacuum, producing Cherenkov light in the detector, and that the track is a straight line. The fit takes into account factors like the optical properties of water and properties of the DOMs [2]. The best angular resolution is obtained for tracks (smaller than 1° , depending on the energy) and the cascades can be reconstructed with a median angular resolution of $\sim 15^\circ$. Thanks to the high energy and hence also velocity, the muon and muon neutrino directions are almost parallel. The average angular deviation of the muon from the neutrino direction can be parametrized as $0.7^\circ \cdot \frac{\text{TeV}}{E_\nu}$ [2].

²Also referred to as overlays, which was one of the features used in Chap. 5.

Cascade direction is harder to reconstruct due to the almost spherical event topology. For ARCA, the fact that the DOM spacing is bigger than a typical cascade size of 10 m additionally impairs the spatial resolution [2].

In Chap. 6, the muon bundle zenith reconstructed with JMuon is compared between the data and simulations for a number of intermediate configurations of KM3NeT detectors.

4.3.5.2. Energy reconstruction

The energy deposited by the muon is proportional to the amount of the light seen by the PMTs and allows to approximate its total energy. The method is likelihood maximization, as for directional reconstruction. Here it has to be stressed that JMuon always operates on the assumption of a single muon track, even if the event is in fact a high-multiplicity muon bundle (see Sec. 2.3.3), which affects the reconstruction quality.

In case of energy reconstruction, the cascades are easier to reconstruct, since the number of photons per each deposited GeV of energy is approximately constant over a broad range of energies [2, 160]. This is not the case for tracks. There are additional complications, e.g. the fact that for energies above 100 GeV the tracks are often uncontained (extending beyond the detector volume).

In Chap. 5, the existing JMuon energy reconstruction is compared against the dedicated muon bundle energy reconstruction, developed for this work. In addition, both the standard (JMuon) and new reconstruction are applied to the data vs MC comparisons in Chap. 6.

4.3.5.3. Other observables

Aside from muon direction and energy, JMuon code also reconstructs the muon vertex (the point in space at which the first seen Cherenkov photon was emitted), however this information is not used in any way in this work [2].

In Sec. 2.3.3 it was mentioned that muon bundles possess certain characteristic properties, among them the incident primary direction and energy, lateral width, multiplicity, and bundle energy. None of them has an explicit standard reconstruction within the KM3NeT simulation framework. The reconstruction of the primary direction, lateral width, and multiplicity was attempted in the dissertation of Stefan Reck, in parallel to this work [9]. In Chap. 5, reconstruction of the multiplicity and bundle and primary energies is described. The primary energy reconstruction is especially important from the point of view of CR composition studies. Chap. 6 shows the application of all the developed reconstructions to the data. As shown in Sec. 7.5, muon multiplicity and bundle energy are observables that are important for the prompt muon production.

5. Reconstruction of muon bundle observables

This chapter shortly introduces the concepts of machine learning (ML) and presents the reconstruction of muon bundle properties (see Sec. 2.3.3), performed by the author of this thesis using ML tools. Prediction of three characteristics was attempted: bundle energy E_{bundle} , total primary energy $E_{\text{prim}} \cdot A$ (where A is the number of nucleons in the nucleus), and muon multiplicity N_{μ} . A number of ML regression models were tested and the best one was further tuned and used for all the reconstructions. The E_{bundle} reconstruction results were compared against the existing KM3NeT energy reconstruction JMuon (see Sec. 4.3.5.2).

5.1. Machine learning: a brief introduction

Machine learning is a branch of artificial intelligence where the codes ‘learn’ to make decisions based on data they have been exposed to. What is explicitly programmed is not the exact response but rather a method in which the program, often called a model, will learn the task. The first ML models date back to 1950s. Their architecture attempted to reproduce the cognitive mechanisms of the human brain by developing artificial neural networks (NNs) [161, 162, 163, 164]. Since then, the number of available models and their applications has grown significantly (see Fig. 5.1.1). The types of ML tasks can be grouped into three main categories:

1. Supervised learning – predicts the output based on labelled input data (features).
 - a) Classification – predicts categorical labels (e.g. ‘cat’, ‘dog’). In the case of binary classification (classification with only two classes), typically one of the labels (classes) is of particular interest and such a label is referred to as positive label, and analogously the other one is called negative.
 - b) Regression – predicts values of a continuous target, e.g. energy of a particle.
2. Unsupervised learning – learns the structure of the data based on unlabelled input.
 - a) Clustering – looks for groups (clusters) of data points, based on their similarities and differences.
 - b) Dimensionality reduction – applies a transformation to the data, preserving as much information as possible, while shrinking the number of features.
3. Reinforcement learning – puts an agent in an interactive environment, where it learns by trial and error. The agent receives positive or negative feedback each time it performs an action. The learning consists in maximization of the cumulative reward (positive feedback from the environment) by the agent. The resulting strategy of actions to be taken in a particular state is called the policy.

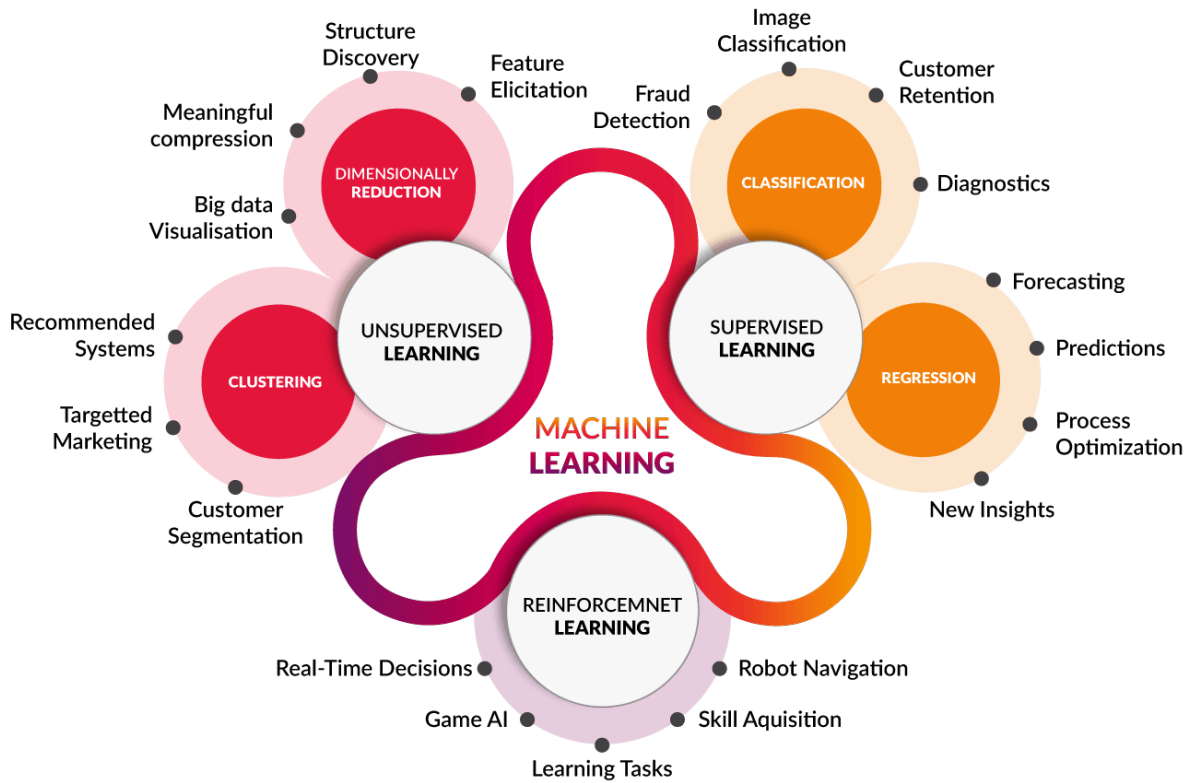


FIGURE 5.1.1.: Diagram depicting main types of machine learning methods and some of their applications. Taken from [165].

The presented categorisation of ML is in fact not the only one in use. Another way to divide machine learning models is by their architecture, with the two main types:

1. Deep learning – the model is a neural network with multiple layers of neurons. The exact number of layers required for the NN to be considered deep is as a matter of fact somewhat fluid, however within this work, the threshold of 2 layers was adopted.
2. Shallow learning – by construction, anything which is not considered ‘deep’: single-layer NNs and other types of models, e.g. support vector machines [165, 166, 167].

In this chapter, application of supervised shallow learning (with an exception of multi-layer perceptron, see Sec. 5.1.2) to regression tasks is presented. In Sec. 5.3.1.1 a single best-performing model was identified and used throughout the entire chapter to address each of the considered problems.

5.1.1. General workflow

In all machine learning tasks, there is a common set of steps, which have to be completed to obtain useful results:

1. Collecting the data (in the case of this work, from the MC simulation).
2. Data preprocessing:
 - a) Handling issues like (partially) missing data points, noise, or inconsistencies in the data.

- b) Scaling the features and weights to make them more convenient to work with for the models. Too large values or too wide value ranges can lead to numerical problems in most ML algorithms.
 - c) Splitting the data into the train, validation, and test sets, typically reserving the majority of the samples for the training. The difference between the validation and the test dataset is that the model is tuned on the validation set, while the test set is only used for the final results. This means that the test data does not influence the training of the model in any way and hence, allows for an unbiased evaluation of the model performance.
3. Finding the optimal model for the task. This may include both researching available options and directly comparing performance of models.
 4. Training and validating the model performance.
 5. Tuning the internal parameters of the model, called hyperparameters (for instance: learning rate). It should be undoubtedly done at the very end, since it involves repeated re-training, while scanning for the optimal combination of hyperparameters and is hence computationally intensive.
 6. Evaluation of the results — it is verified, whether the model can generalise well, i.e. if it can work well also on the data it has not seen before (the test data).

In practice, many of the steps require re-iteration upon completion of the other ones. For example, the hyperparameter tuning involves multiple training and validation steps, and preliminary validation results can often lead to modifications, e.g. in- or exclusion of certain models.

5.1.2. Considered models

In this work, the task was the regression of KM3NeT detector observables, based on the CORSIKA MC, which is a type of supervised learning. To this end, a variety of ML algorithms available in the scikit-learn library [168] and outside it [169, 170] were tested. They can be grouped into several categories:

1. Linear models: they assume that the reconstructed target $y_{\text{pred},i}$ for i -th sample is merely a linear combination of n features $x_i = (x_{1,i}, \dots, x_{n,i})$:

$$y_{\text{pred},i} = c_{0,i} + c_{1,i} \cdot x_{1,i} + \dots + c_{n,i} \cdot x_{n,i},$$

where $c_i = (c_{0,i}, \dots, c_{n,i})$ are constant coefficients, which must be fitted.

- a) Linear — an implementation of the least squares algorithm. It minimizes the sum of squared residuals:

$$\min_c \left[\sum_{i=1}^m (y_{\text{true},i} - y_{\text{pred},i})^2 \right],$$

where $y_{\text{true},i}$ and $y_{\text{pred},i}$ are the true and predicted (reconstructed) values respectively.

- b) Ridge — modifies Linear by adding a penalty term:

$$\min_c \left[\sum_{i=1}^m (y_{\text{true},i} - y_{\text{pred},i})^2 + \alpha \cdot \sum_{i=0}^m \sum_{j=0}^n c_{j,i}^2 \right],$$

to prevent too large linear coefficients. The regularisation parameter $\alpha \geq 0$ controls the strength of coefficient shrinking.

- c) **ARD** — stands for Automatic Relevance Determination. It is a type of Bayesian regression, where the regularisation parameters are not fixed, but tuned to the data presented to the model. In the particular case of ARD, the priors on c_i are drawn from a Gaussian distribution, with zero mean and standard deviation λ_i :

$$p(c_i | \lambda_i) = \mathcal{N}(c_i | 0, \lambda_i),$$

where $\mathcal{N}(\mu, \sigma)$ is the Gauss distribution (often called normal distribution) with a mean μ and standard deviation σ .

- d) **Lasso** (least absolute shrinkage and selection operator) — a linear model designed to estimate sparse coefficients (i.e. most of them will be just zero). It does so by minimising:

$$\min_c \left[\frac{1}{2n_{\text{samples}}} \sum_{i=1}^m (y_{\text{true},i} - y_{\text{pred},i})^2 + \alpha \cdot \rho \sum_{i=0}^m \sum_{j=0}^n c_{j,i} \right].$$

- e) **ElasticNet** — a combination of Lasso and Ridge, allowing to learn a sparse model with only few non-zero coefficients, while keeping the regularisation properties of Ridge. The minimised function is:

$$\min_c \left[\frac{1}{2m} \sum_{i=1}^m (y_{\text{true},i} - y_{\text{pred},i})^2 + \alpha \cdot \rho \sum_{i=0}^m \sum_{j=0}^n c_{j,i} + \frac{\alpha \cdot (1 - \rho)}{2} \sum_{i=0}^m \sum_{j=0}^n c_{j,i}^2 \right].$$

- f) **Lars** (least-angle regression) — a regression algorithm developed specifically for data with high dimensionality. It iterates over the following steps:

- i. Initialise all the coefficients to zero: $c_{j,i} = 0$.
- ii. Find the feature $x_{j,i}$ with the strongest correlation to corresponding $y_{\text{true},i}$.
- iii. Increase $c_{j,i}$ in the direction of the sign of correlation with $y_{\text{true},i}$. Stop when some other feature $x_{k,i}$ has the same correlation with $y_{\text{true},i} - y_{\text{pred},i}$ as $x_{j,i}$ has.
- iv. Increase $c_{j,i}, c_{k,i}$ in their joint least squares direction, until some other feature x_l has as much correlation with $y_{\text{true},i} - y_{\text{pred},i}$ as they do.
- v. Do the same for $c_{j,i}, c_{k,i}, c_{l,i}$
- vi. Carry on until all features are included in the model with non-zero coefficients.

- g) **LassoLars** v a combination of Lasso and Lars approaches.

- h) **LassoLarsIC** — a version of LassoLars, which uses the Akaike information criterion (AIC) as minimisation objective, computed as:

$$AIC = m \cdot \log \left(2\pi \frac{\sum_{i=1}^m (y_{\text{true},i} - y_{\text{pred},i})^2}{m - n} \right) + m + n,$$

where n is the number of features and m is the number of samples.

- i) `OrthogonalMatchingPursuit` — implements the orthogonal matching pursuit (OMP) algorithm [171], designed to work with sparse data. It approximates the optimal solution for a fixed number of $c_{j,i} \neq 0$, by default: $0.1 \cdot n$.
- j) `SGD` (Stochastic Gradient Descent) — makes use of the stochastic gradient descent [167] method to train the model (minimise the given objective function). In principle, it can attempt to solve a number of different minimisation problems. Here, the Ridge regularisation was used.
- k) `PassiveAggressive` — the algorithm starts by initialising all the $c_{j,i}$ coefficients to zero, to then learn them one by one. After each prediction, a loss is applied instantaneously:

$$\ell_\epsilon(y_{\text{true},i} - y_{\text{pred},i}) = \begin{cases} 0 & \text{if } |y_{\text{true},i} - y_{\text{pred},i}| \leq \epsilon \\ |y_{\text{true},i} - y_{\text{pred},i}| - \epsilon & \text{otherwise} \end{cases},$$

where $\epsilon > 0$ controls the accuracy [172]. The loss is applied by modifying the coefficients from the current iteration t :

$$c_{t+1} = c_t + \text{sign}(y_{\text{true}} - y_{\text{pred},t}) \frac{\ell_\epsilon(y_{\text{true},i} - y_{\text{pred},i})}{\sum_{i=1}^m x_{t,i}^2 + \frac{1}{2C}} x_t,$$

where $C > 0$ is the aggressiveness parameter. This is carried out until coefficients of all features were set.

- l) `Robust regressors`: try to fit a model on corrupt data (e.g. containing outliers). Three of such algorithms were used:
 - i. `RANSAC` (RANDOM SAMPLE CONSENSUS) — iteratively fits a model to random subsets of datapoints identified as inliers. The inliers are picked by computing the residuals $y_{\text{true},i} - y_{\text{pred},i}$ and comparing them against a residual threshold parameter ϵ , requiring $|y_{\text{true},i} - y_{\text{pred},i}| < \epsilon$ [173].
 - ii. `TheilSen` — it is characterised by robustness against multivariate outliers, owing to the use of spatial median (a multi-dimensional generalisation of the median) [174].
 - iii. `HuberRegressor` — it suppresses the outliers by assigning them lower coefficients. The minimised function is

$$\min_{c,\lambda} \left[\sum_{i=1}^m \left(\lambda + \lambda \cdot H_\epsilon \left(\frac{y_{\text{true},i} - y_{\text{pred},i}}{\lambda} \right) \right) + \alpha \sum_{i=0}^m \sum_{j=0}^n c_{j,i}^2 \right],$$

where

$$H_\epsilon(z) = \begin{cases} z^2 & \text{if } |z| < \epsilon \\ 2\epsilon|z| - \epsilon^2 & \text{otherwise} \end{cases},$$

with a fixed ϵ parameter, acting as a threshold for classification as in- or outlier, similarly as for `RANSAC` [175].

- 2. `Neighbours-based models`: they ‘memorise’ the data they have been trained on, often in a transformed form. Based on this memory, they allow assigning new datapoints to already existing clusters.

- a) KNeighbors — an implementation of the k -nearest neighbours algorithm (kNN), which predicts the target based on the interpolation of the k nearest neighbours [176]. The distance definition is in general adjustable, but the one used in this work was the standard Euclidean distance.
3. Neural networks: consist of artificial neurons, mimicking the function of the human brain, as described in Sec. 5.1.
 - a) MLP (multi-layer perceptron) — one of the most simple NN architectures. It consists of three or more layers: one input representing the features, one output representing the target, and at least one non-linear hidden layer. In this thesis, a MLP with 3 hidden layers with 100, 50 and 25 neurons was used. Each neuron in the hidden layer transforms the values from the previous layer as a weighted sum.
4. Decision Trees: models, which predict their target based on a set of decision rules, learned from the training data. One can think of a decision tree as a piecewise constant approximation of the problem. Each split of the decision tree is evaluated in terms of its quality, i.e. how much it will improve the prediction.
5. Ensemble methods: they put together predictions of multiple base estimators to improve the robustness of results. There are two main approaches:
 - a) Averaging — base estimators are built independently, sometimes even in parallel, and their results are averaged. This helps to reduce the variance of the final result.
 - i. RandomForest — creates a 'forest' of decision trees, built from samples of the training data drawn with replacement. Here, the randomisation not only reduces variance, but also prevents overfitting (see Sec. 5.1.3), which is a common issue of single decision trees [177].
 - ii. ExtraTrees — extremely randomized trees model goes even further in randomisation than RandomForest, sacrificing the control over bias to decrease the variance. Instead of looking for the most discriminative split thresholds, they are picked randomly for each considered feature and the best of those becomes the next split [178].
 - iii. Bagging — a form of meta-estimator, which adds an additional layer of averaging. It creates several separate instances of a chosen estimator (in the case of this work, ExtraTrees), and produces a combined prediction out of those [179].
 - b) Boosting: here, the base estimators are built in sequence and they attempt to reduce the bias of the final result.
 - i. AdaBoost — fits a sequence of single estimators (learners), e.g. decision trees, on different variants of the training data. The data is modified by applying weights to training samples at each so-called boosting stages. The initial weights are set to a constant value, but in the next iterations the weights are reduced for well-predicted and increased for incorrectly predicted samples. This forces the learners to focus on the problematic cases, which were missed in the previous stage. The final prediction is obtained by weighted majority vote or sum of all estimators [180, 181].
 - ii. Gradient Boosted Decision Trees (GBDT) — a boosting algorithm able to work with any chosen differentiable loss function. The name of the model comes from the

fact that at each boosting stage a decision tree is fit on the negative gradient the loss function. This means that each consequent tree attempts to improve on the prediction of the previous one. The base estimator for GBDT is always a decision tree, unlike AdaBoost where it is merely a popular choice. [182]

- iii. LightGBM — a highly optimised implementation of a GBDT developed by Microsoft [170]. The model is particularly efficient in working with large datasets, since it works not directly on samples, but on their histograms. In addition, LightGBM makes use of two novel techniques. The first one is gradient-based one-side sampling (GOSS) — it allows to selectively compute the information gain using only the data with large gradients. The second method is exclusive feature bundling (EFB), which is in essence a type of feature selection. It bundles together mutually exclusive features (such features will rarely be $\neq 0$ at the same time), allowing to reduce the dimensionality of the problem.
- iv. XGBoost (Extreme Gradient Boosting) — a competitor of LightGBM, with a preference for growing deeper trees with more leaves. It also does not histogram the data. This is reflected in strong performance, but for the price of inferior memory efficiency and speed (see Fig. 5.3.4 and 5.3.5), which can pose problems for larger datasets [169].
- v. HistGradientBoosting — is a scikit-learn [168] implementation of the gradient boosting machine algorithm, inspired by LightGBM. It has a smaller number of hyperparameters, which makes it potentially easier to tune.

To limit the number of potential permutations while tuning the performance, it was decided to pick a single best model early on and apply it to each of the tasks. The model selection is described in Sec. 5.3.1.1.

5.1.3. Performance assessment

Inspection of learning curves of the models is a great way to pinpoint evident issues early on. Learning curves can display either the score (maximised during training) or the loss function (minimised during training) versus the number of training examples (events) seen by the model. Sketches of a few possible cases are shown in Fig. 5.1.2. Underfitting means that the model is not able to learn the training dataset. If the validation score maintains the ascending trend (Fig. 5.1.2a), adding more training examples may be beneficial. Otherwise, a change or modification of the model to increase its complexity may be advisable. In the case of a good fit (Fig. 5.1.2b), adding further training data will not yield any significant gain and may actually lead to overfitting and hence, a loss of generalisability. The characteristic trait of a learning curve of an overfitted model (Fig. 5.1.2c) is the deflection point in the validation score, after which it starts to decrease.



FIGURE 5.1.2.: Comparison of the three basic behaviours of the learning curves.

To evaluate how well a trained estimator (model) performs, a set of metrics has to be defined. Here, only the relevant metrics will be discussed, for a more complete overview see e.g. [168, 167, 183]. To judge if a regression attempt was successful, one should first look at the correlation plot between the true and predicted values of a target (see e.g. Fig. 5.3.2). There is a variety of metrics for goodness of a regression [184, 166]. In this work, two were used:

1. The (weighted) Pearson correlation coefficient:

$$c(y_{\text{true}}, y_{\text{pred}}) = \frac{\sum_i w_i (y_{\text{true},i} - \bar{y}_{\text{true}}) (y_{\text{pred},i} - \bar{y}_{\text{pred}})}{\sqrt{\sum_i w_i (y_{\text{true},i} - \bar{y}_{\text{true}})^2 \sum_i w_i (y_{\text{pred},i} - \bar{y}_{\text{pred}})^2}}, \quad (5.1.1)$$

where y_{true} are the true, and y_{pred} are the predicted values of a random variable, for which the correlation is tested. Consequently, \bar{y}_{true} and \bar{y}_{pred} are their respective mean values. The weight w_i is the event weight w_{event} for the i -th event.

2. The (weighted) R^2 -score, called the coefficient of determination:

$$R^2(y_{\text{true}}, y_{\text{pred}}) = 1 - \frac{\sum_i w_i (y_{\text{true}} - y_{\text{pred}})^2}{\sum_i w_i (y_{\text{true}} - \bar{y}_{\text{true}})^2}. \quad (5.1.2)$$

One should note that Eq. 5.1.2 does allow negative values, despite having a square in its symbol. Such values indicate that the regression is performing worse than just using the mean value ($R^2 = 0$ would imply $y_{\text{pred}} = \bar{y}$). Both the Pearson correlation coefficient and the coefficient of determination are quoted in all the correlation plots and 1D distributions in Sec. 5.3 and 5.4.

5.2. Monte Carlo samples used

As indicated in Sec. 5.1.1, the training data was obtained from the CORSIKA simulation. The results presented in the following sections are based on the MC produced for ARCA115, ARCA6, ORCA115, and ORCA6 (for more details see Sec. 5.3 and A.1). In each case, the same set of features, targets, and weights has been extracted. In fact, the very same features were used both for the multiplicity and energy reconstruction (Sec. 5.4 and 5.3). All the available features, along with the three considered targets are displayed in Fig. 5.2.1 in the form of a correlation matrix. The

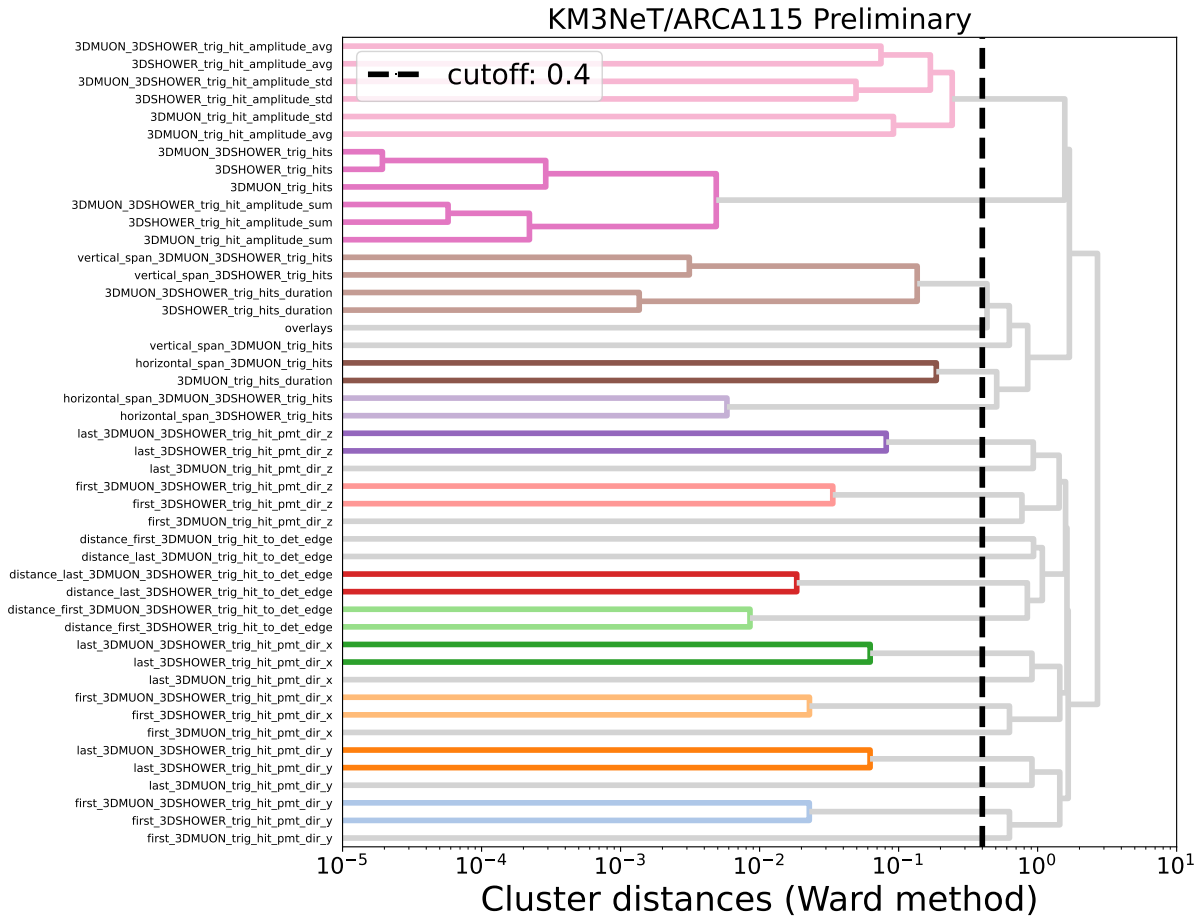


FIGURE 5.2.2.: Visualisation of feature clustering in form of a dendrogram plot, showing *cluster distances* obtained by computing Ward’s linkage based on the correlation matrix in Fig. 5.2.1 [185]. The cutoff for clusters was picked manually to be 0.4. The image was produced using the ARCA115 CORSIKA MC. The dendrograms for the other three detector configurations may be found in Sec. A.5.2.

5.2.1. Preprocessing

Before the analysis could be carried out, the datasets for the four detector configurations were carefully put together. The procedure was as follows:

1. The whole dataset was split into a train, validation, and test set in proportions 64:16:20. Due to the nature of CORSIKA simulation weighting (see Eq. 4.2.3), the events from a single run could not be divided. Instead, entire runs were split between the samples. To avoid accidental mixing of events from different datasets, the datasets were stored in separate files.
2. Features were transformed to resemble normally distributed data with a mean of 0 and a variance of 1 (using the StandardScaler utility implemented in scikit-learn framework[168]). Feature scaling is a necessity for a number of ML models, which would otherwise either perform very badly or in some cases run into complete failure.

3. The sample weights (event weights to be used for training, validation, and testing) were computed in two variants: unscaled w_{event} (as in Eq. 4.2.3), and scaled according to:

$$w_{\text{scaled}} = \frac{\log_{10} w_{\text{event}} + \max(|\log_{10} w_{\text{event}}|) \cdot 1.01}{\max(|\log_{10} w_{\text{event}}|)}, \quad (5.2.1)$$

motivated by the fact that their value range spans from roughly 10^{-10} up to 10^{14} , which could cause problems for some models, similarly to unscaled features with large dynamic ranges. The $\max(|\log_{10} w_{\text{event}}|)$ terms ensure that the resulting scaled weights w_{scaled} have positive values.

5.2.2. Summary of datasets

After preprocessing and splitting the CORSIKA MC, the following datasets were used for the reconstruction tasks:

TABLE 5.2.1.: Size summary of the datasets used to train the ML models.

Detector	Training set [# events]	Validation set [# events]	Test set [# events]
ARCA115	14 374 415	3 598 133	4 489 177
ARCA6	3 894 293	974 371	1 215 552
ORCA115	15 439 946	3 857 715	4 825 073
ORCA6	6 154 895	1 539 988	1 923 475

5.3. Reconstruction of energy

The energy reconstruction is described first, although the methodology for multiplicity reconstruction was very similar. Most of the intermediate results are only presented for ARCA115 for the sake of readability, however the exactly same procedure was followed for each of the four detector configurations.

5.3.1. Bundle energy

The idea to reconstruct the muon bundle energy was inspired by the available official KM3NeT reconstruction. The performance of the muon energy reconstruction code JMuon (see Sec. 4.3.5) is shown in Fig. 5.3.1. Here it has to be noted that JMuon was designed to reconstruct a single muon track per event. Hence, an evaluation of its performance in the case of single muon events was included in Fig. 5.3.1b. Such events were selected by requiring the true multiplicity equal to 1. The goal of this work was to predict the bundle energy, as the JMuon reconstruction seemed not to deliver satisfactory results. Even an untuned ML result (Fig. 5.3.2) was clearly performing better than the standard reconstruction (JMuon), which became even more evident in Fig. 5.3.3.

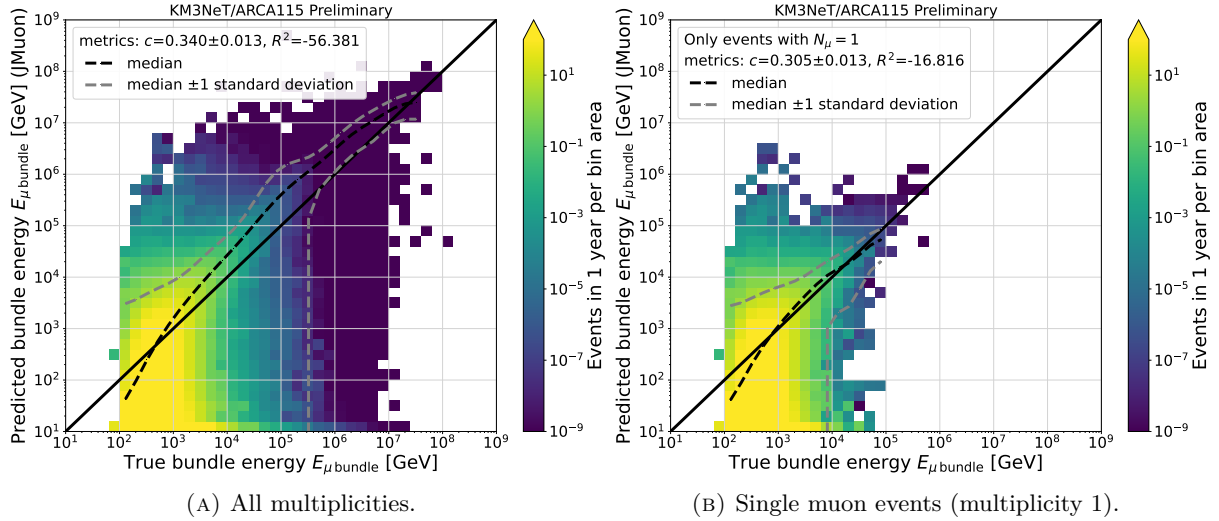


FIGURE 5.3.1.: Comparison of the energy predicted by the JM3uon reconstruction and true bundle energy. The reconstruction was applied to ARCA115 CORSIKA MC. Plots for the remaining configurations (ARCA6, ORCA115, ORCA6) may be found in Sec. A.4.

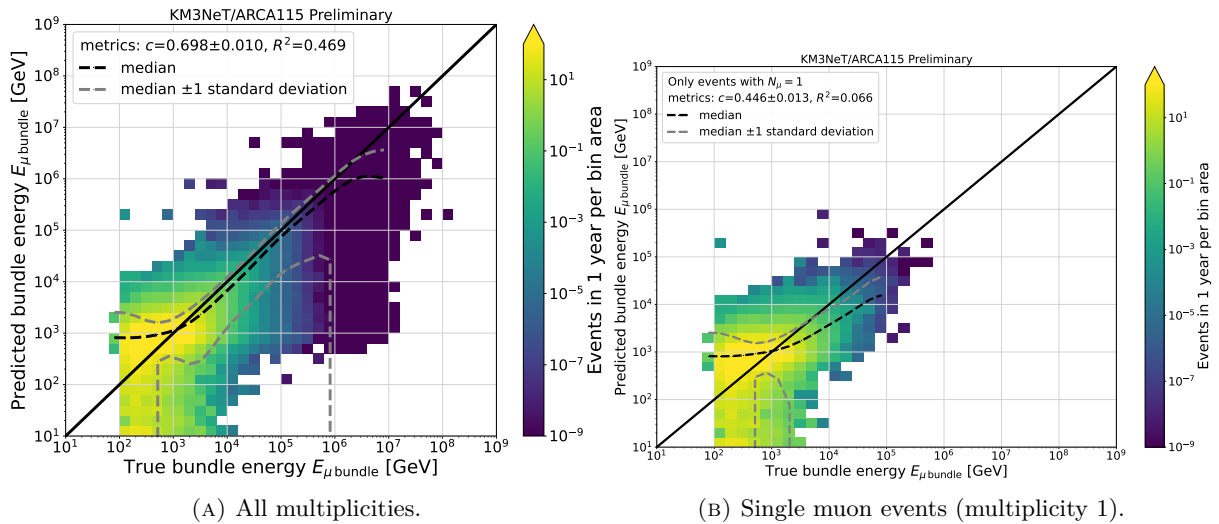


FIGURE 5.3.2.: Comparison of predicted and true bundle energy for the LightGBM reconstruction. The reconstruction was applied to ARCA115 CORSIKA MC.

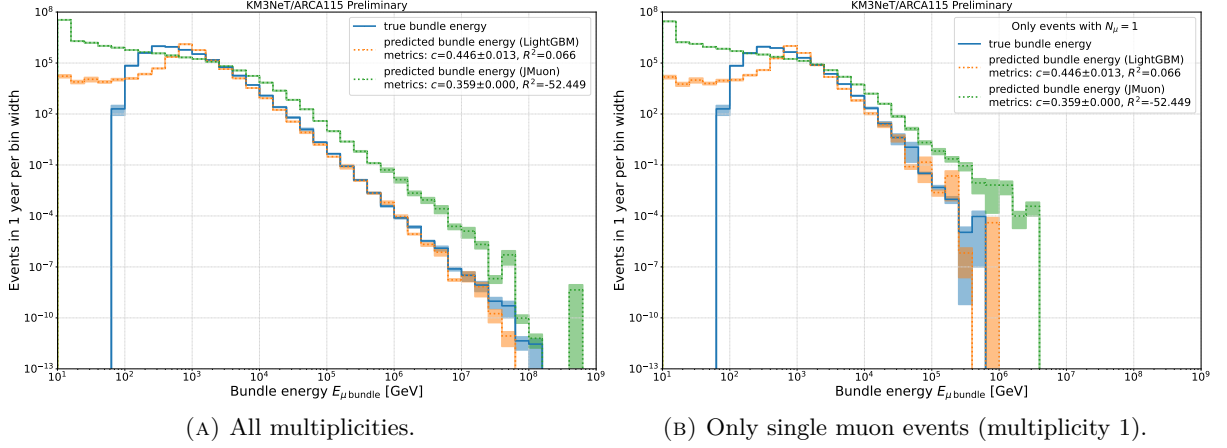


FIGURE 5.3.3.: Comparison of predicted and true distributions of bundle energy for the JMuon and LightGBM reconstruction, applied to ARCA115 CORSIKA MC. Corresponding plots for the remaining configurations (ARCA6, ORCA115, ORCA6) may be found in Sec. A.4. The error bands were computed using Eq. A.2.1.

5.3.1.1. Choice of the best model

The best model was picked from a wide range of candidates, briefly introduced in Sec. 5.1.2 and listed in Fig. 5.3.4 and 5.3.5. All estimators were trained using a fraction of the ARCA115 training data (50 000 events out of 14 374 415 at hand; see Tab. 5.2.1) and evaluated on the full validation set. This was dictated by the memory and execution time limitations.

It was presumed that the best model would outperform the others, regardless of the detector configuration, or available training data. Furthermore, an assumption was made that the same learner would be the best both for the muon bundle energy and for the primary energy. This is well-grounded, as the bundle energy is the primary energy reduced by the interactions in the shower prior to the arrival of the muons at the can. Moreover, it was presupposed that the full validation dataset was sufficient to compare the performance reliably. The models were compared in terms of the obtained Pearson correlation coefficient c and the coefficient of determination R^2 (see Sec. 5.1). In addition, their execution times on an Intel i5-2400 CPU were measured. Since a number of estimators (MLP, KNeighbors, ARD, PassiveAggressive, TheilSen, Lars, LassoLars, LassoLarsIC, and OrthogonalMatchingPursuit; see Sec. 5.1.2) did not support sample weights at all, they were trained unweighted (equivalent to training with all weights equal to 1). In the case of the remaining models, it was possible that training with scaled or unscaled weights (see Sec. 5.2.1) could yield better results (and neither is intrinsically wrong). Hence, each estimator supporting weights was trained twice: with scaled and with unscaled weights, and the better of the two results was used. The values of the metrics were always computed using the unscaled flux weights, since they provide an approximation of what may be expected from the experimental data.

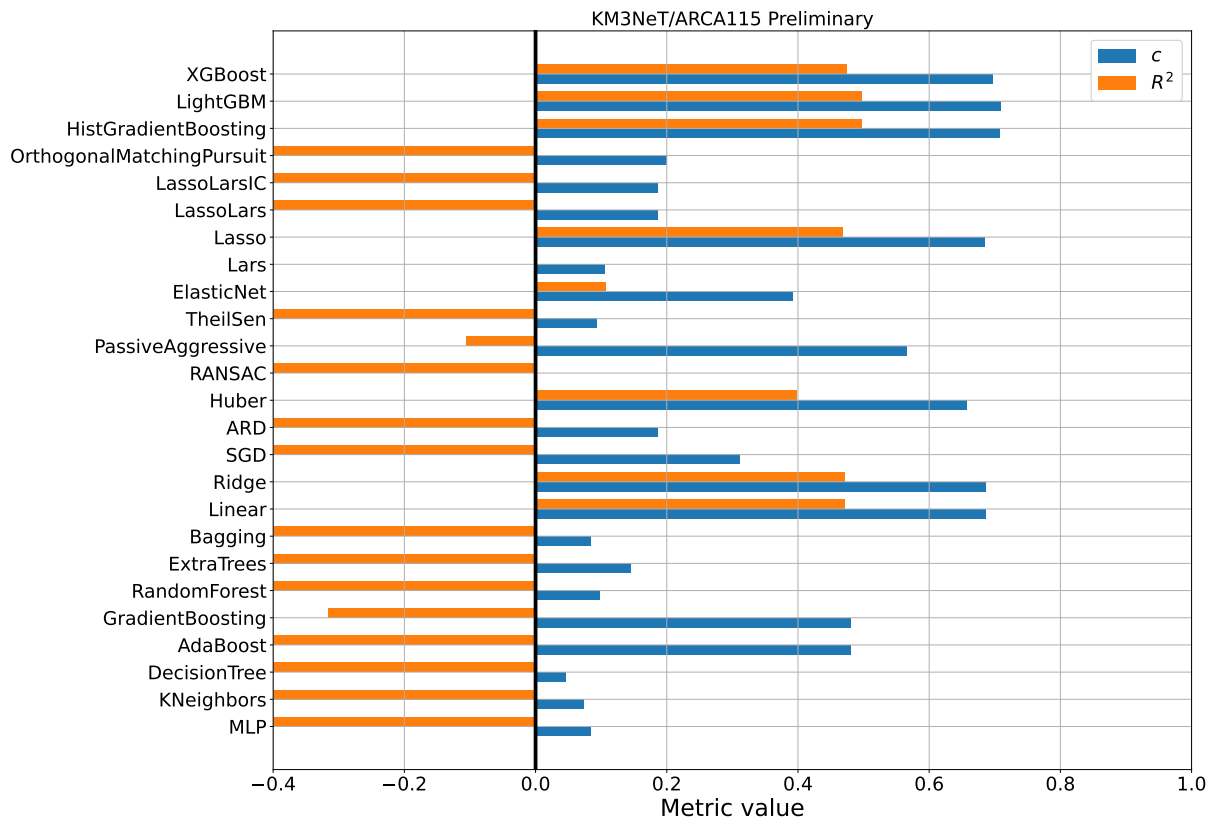


FIGURE 5.3.4.: Performance comparison of selected models in terms of correlation c and R^2 -score (for both metrics 1.0 is the perfect score).

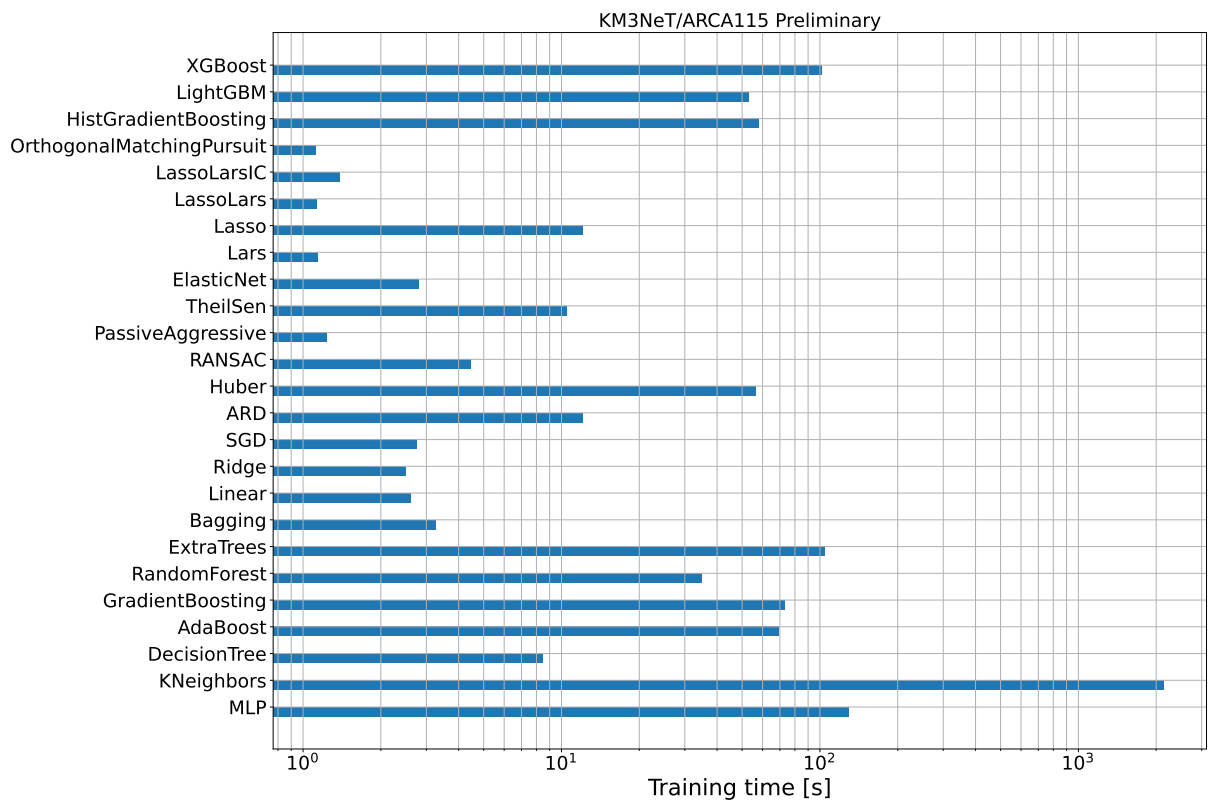


FIGURE 5.3.5.: Performance comparison of selected models in terms of execution speed.

The results are compiled in Fig. 5.3.4, and the winner was LightGBM. It achieved the best regression metrics, while remaining the fastest among the three best models, beating XGBoost and HistGradientBoosting (Fig. 5.3.5). This was possible, among the other factors, thanks to its approach of internally histogramming the data and working on the histogram counts, rather than on individual events [170]. In this entire chapter, LightGBM was used as the default model for all regression tasks.

5.3.1.2. Inspection of learning

As mentioned in Sec. 5.1.3, checking the learning curve of the model is an important step in assuring the correctness of the results. The learning curves of LightGBM training for the bundle energy regression task are presented in Fig. 5.3.6. As may be seen, the model was still slightly underfitting (see Fig. 5.1.2), however the improvement with adding more training data was rather slow and the cost of simulating more events would be substantial. When learning on small samples of the training dataset, one can see very rapid changes in the scores: this is an expected behaviour. The model was hardly able to generalise (negative validation score) because it was exposed to too little examples. Relatively small samples of the dataset had low chance of being representative for the complete one. As the training sample size grew above 10^4 , the training started to converge to a score of around 0.5. The final result was further improved by hyperparameter tuning (see Sec. A.5.4).

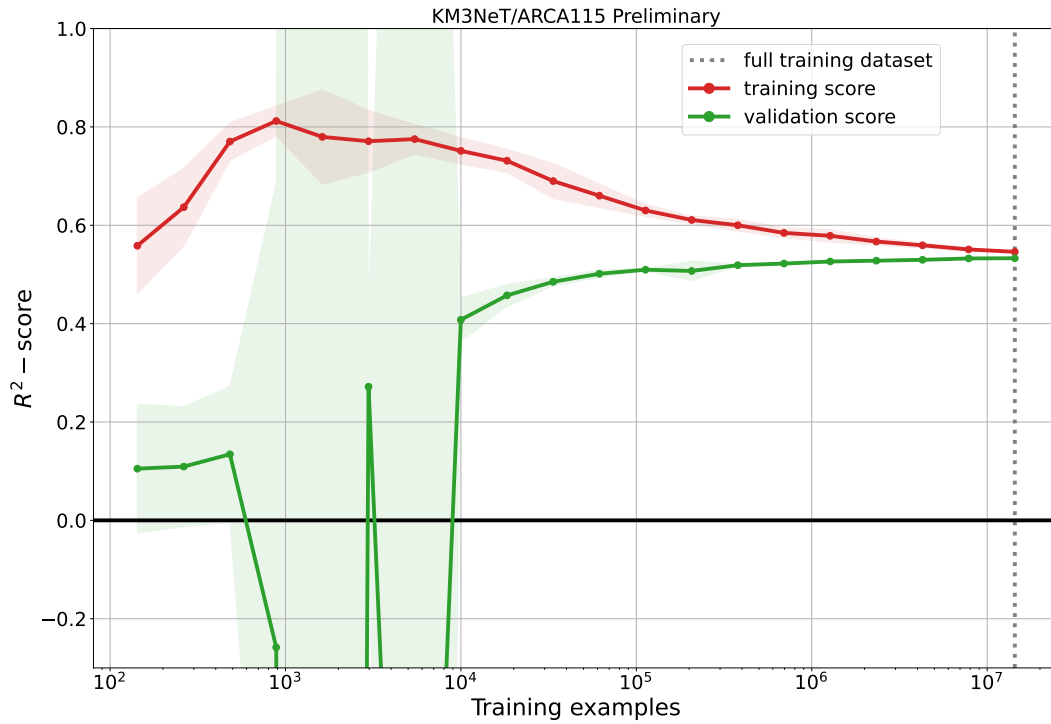


FIGURE 5.3.6.: R^2 -scores for the training and validation sets as function of the number of seen training examples. The reconstruction was applied to ARCA115 CORSIKA MC. The R^2 metric values were computed taking into account the unscaled event weights. For each point, the training was performed 7 times on a randomly selected part of the training dataset, each time with a different random seed. The solid line with dots represents the median of the score and the surrounding band — one standard deviation. The validation score was computed using the entire validation dataset each time.

5.3.1.3. Feature importances

This section investigates the profitability of restricting the features in use to only the most important ones, as hinted in Sec. 5.2. Fig. 5.3.7 visualises how essential each of the features was. The features, which boost the resulting R^2 -score the most have been selected by applying a cutoff on the feature importance, requiring a positive importance for each such feature. In addition, only one feature with the highest importance was picked out of each cluster (the colour coding corresponds to Fig. 5.2.2). The features selected in this manner are listed in Tab. 5.3.1. The importance was dominated by 3DMUON_3DSHOWER_trig_hits, which is the number of hits triggered by both the 3DMuon and 3DSHOWER trigger algorithms, followed by 3DSHOWER_trig_hits, 3DMUON_trig_hits, and overlays (see Sec. 4.3.3).

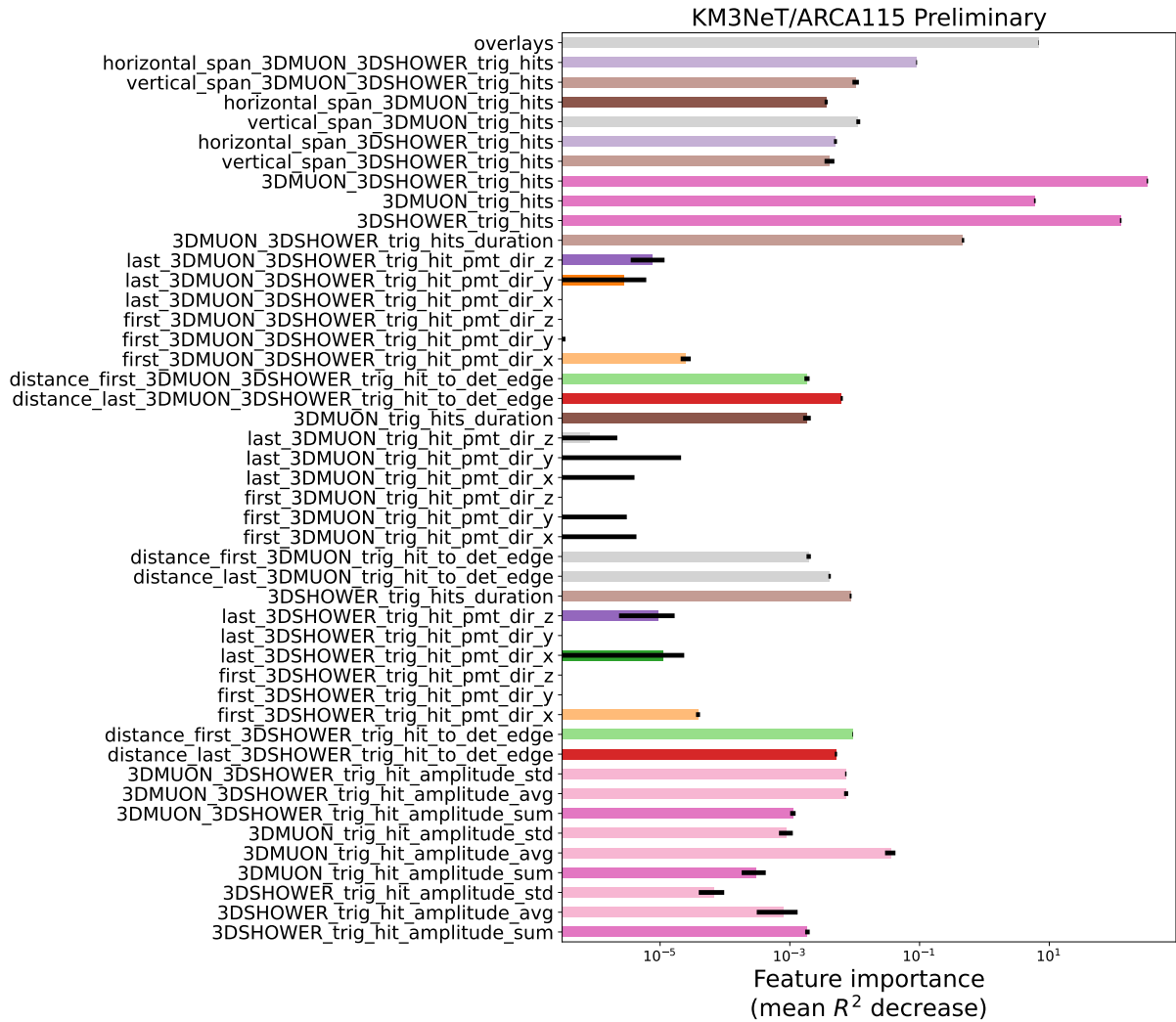


FIGURE 5.3.7.: Feature importance plot, showing how much each feature contributes to training. The figure has been obtained by performing 10 permutations for each feature to ensure a stable result. The standard deviation for each feature is denoted by a black bar. The colour coding of features is consistent with Fig. 5.2.2 to show the clusters, and their most important members. Feature importance plots for the other detector configurations are gathered in Sec. A.5.3.

TABLE 5.3.1.: Features selected by feature importance and clustering (see Fig. 5.3.7 and 5.2.2).
For description of individual features, refer to Sec. A.5.1.

Feature	Importance \pm 1 standard deviation
distance_first_3DMUON_trig_hit_to_det_edge	0.0020 ± 0.0001
horizontal_span_3DMUON_trig_hits	0.0036 ± 0.0002
distance_last_3DMUON_trig_hit_to_det_edge	0.0041 ± 0.0002
distance_last_3DMUON_3DSHOWER_trig_hit_to_det_edge	0.0063 ± 0.0002
distance_first_3DSHOWER_trig_hit_to_det_edge	0.0093 ± 0.0001
vertical_span_3DMUON_trig_hits	0.0114 ± 0.0008
3DMUON_trig_hit_amplitude_avg	0.0359 ± 0.0065
horizontal_span_3DMUON_3DSHOWER_trig_hits	0.0900 ± 0.0016
3DMUON_3DSHOWER_trig_hits_duration	0.47 ± 0.02
overlays	6.84 ± 0.06
3DMUON_3DSHOWER_trig_hits	325 ± 8

A comparison of performance with and without feature selection is presented in Fig. 5.3.8. The results do not differ much, however the number of selected features was only 11, as compared against 46 without the selection. The training time was reduced from 3 min 19 s down to 38.8 s, and the the R^2 -score improved by 0.2%, while the correlation coefficient worsened only by 0.1%. Fig. 5.3.8c shows the result if only the most important feature (3DMUON_3DSHOWER_trig_hits) was used. It confirms that the energy measurement is in essence equivalent to counting the hits caused by the muons. However, both metrics were noticeably worse, which meant that the additional information provided by the other features does make a difference. Lastly, Fig. 5.3.8d shows the outcome if features with negative or null importance (see Fig. 5.3.7) were not used. In this case not only the learning was faster (1 min 59 s), due to bringing the number of features down to 35, but also both the correlation and R^2 improved. Since the ultimate deciding factor here was not the code speed, but rather the achieved scores, the feature selection using only the positive-importance features was adopted.

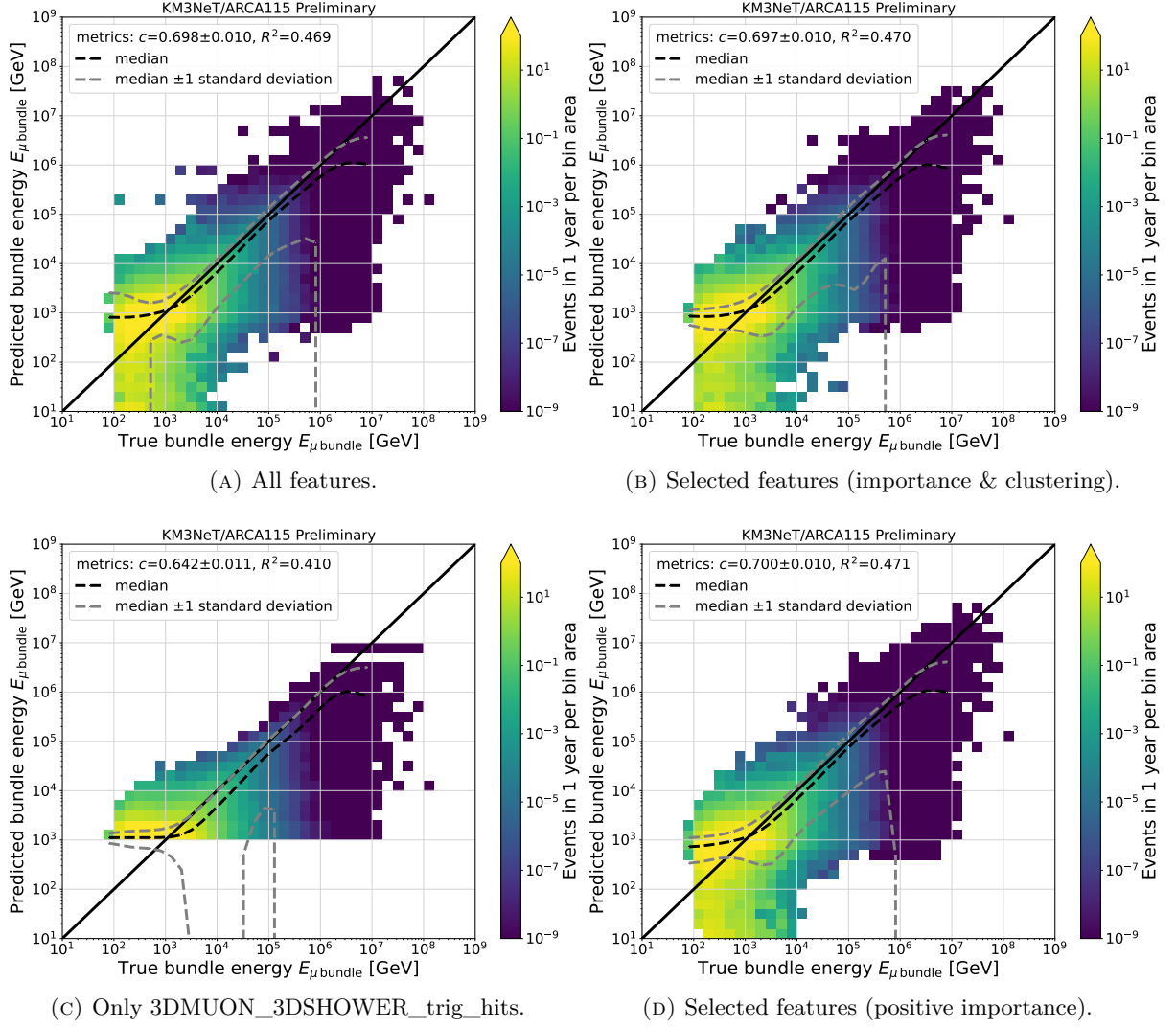


FIGURE 5.3.8.: Predicted bundle energy plotted against the MC truth with and without feature selection. Both the correlation c and R^2 -score values were computed bin-wise.

5.3.1.4. Results

The final outcome of muon bundle energy reconstruction is shown in Fig. 5.3.9. For this result, LightGBM with tuned hyperparameters from Tab. A.5.3 has been used. In the previous sections, all the steps were only shown for ARCA115, with the intent of making the description of the procedure clearer. The same procedure was carried out for each of the detector configurations. From the point of view of data vs MC comparisons (Chap. 6), it is encouraging to see that the shape of the distribution is retained above $E_{\text{bundle}} \sim 1$ TeV for each of the detector configurations (see Fig. 5.3.10). The performance of LightGBM-based regression clearly outperforms JMuoN in the whole range of energies.

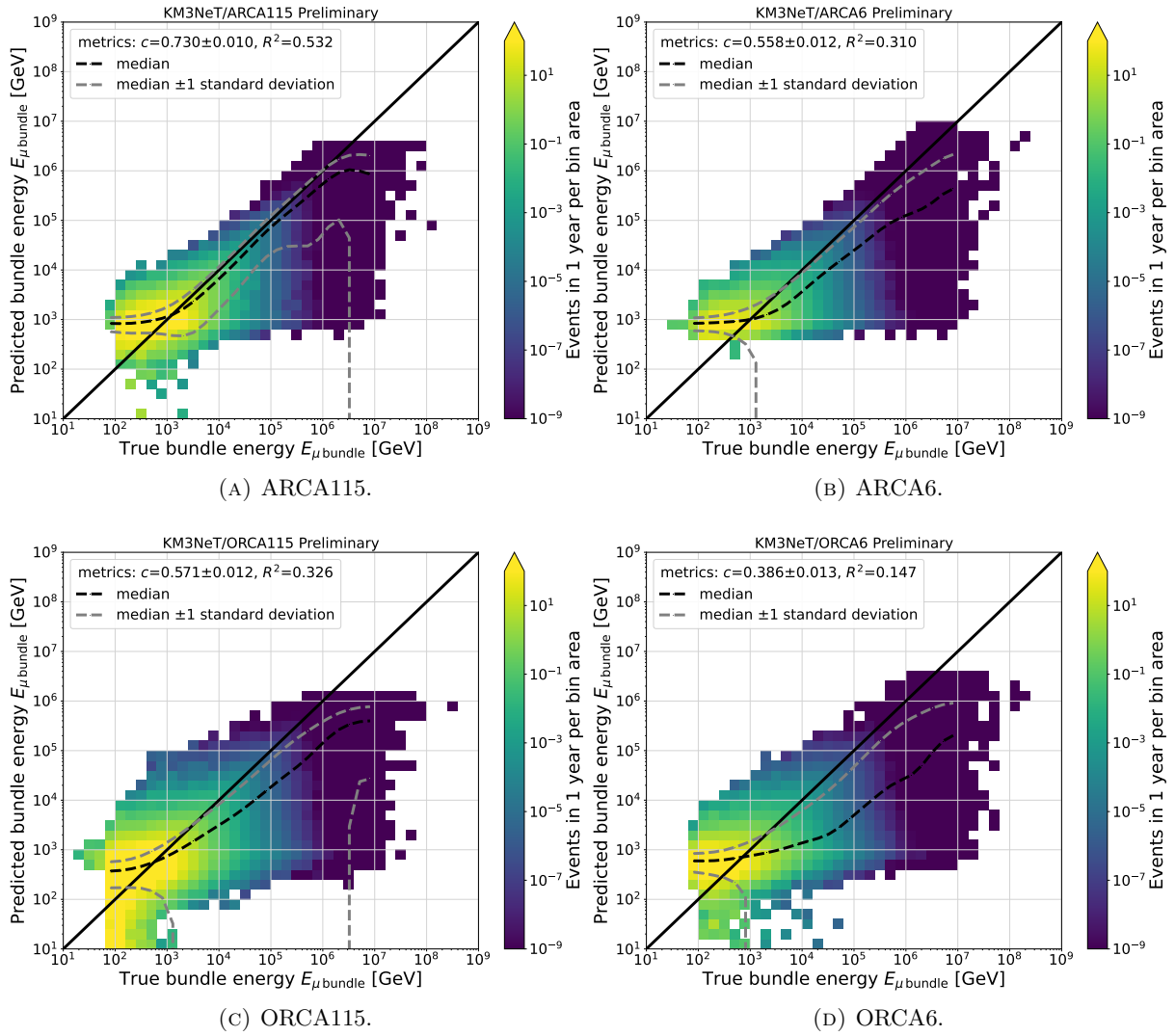


FIGURE 5.3.9.: Comparison of muon bundle energy reconstructed with LigthGBM against the true value. Both the correlation c and R^2 -score values were computed on the bin values, not individual events.

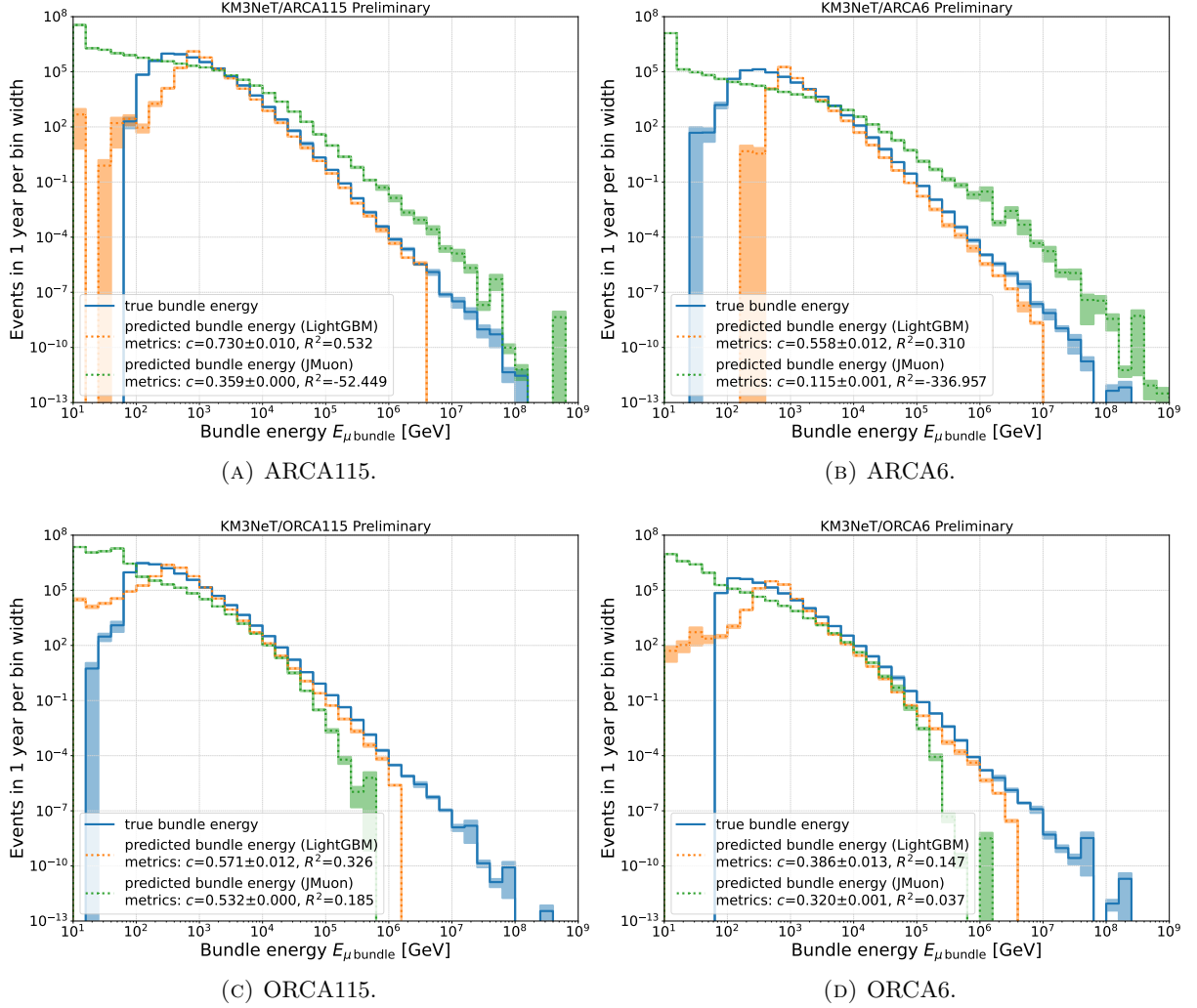


FIGURE 5.3.10.: Comparison of muon bundle energy reconstructed with LigthGBM against the true value in 1D. The error bands were computed using Eq. A.2.1.

5.3.2. Total primary energy

The results obtained for bundle energies encouraged an attempt at reconstructing the energy of the primary nucleus as well. The very same method has been adopted. In this case, there was no standard reconstruction to compare against. Given the very close relation between the bundle energy and the primary energy, neither separate model selection, nor feature selection, nor hyperparameter tuning was performed, and the results from Sec. 5.3.1 were directly adopted.

The primary energy reconstruction described within this section, concerns the total energy of the primary nucleus $E_{\text{prim}} \cdot A$, which should not be confused with the energy per nucleon E_{prim} , used as the CORSIKA input (see Sec. A.1.1). The results are shown in Fig. 5.3.11 and 5.3.12. The predictions are clearly less accurate than for the bundle energy — both metric values are much lower compared to Fig. 5.3.9a. This was expected, since the reconstruction was forced to predict the energy of the parts of the shower, which did not make it to the detector at all. Having this in mind, the obtained reconstruction is in fact extraordinary. Above the predicted primary energy of

few PeV, with some difference between the detector configurations, the quality of the reconstruction seems to be good enough to allow for CR-related studies.

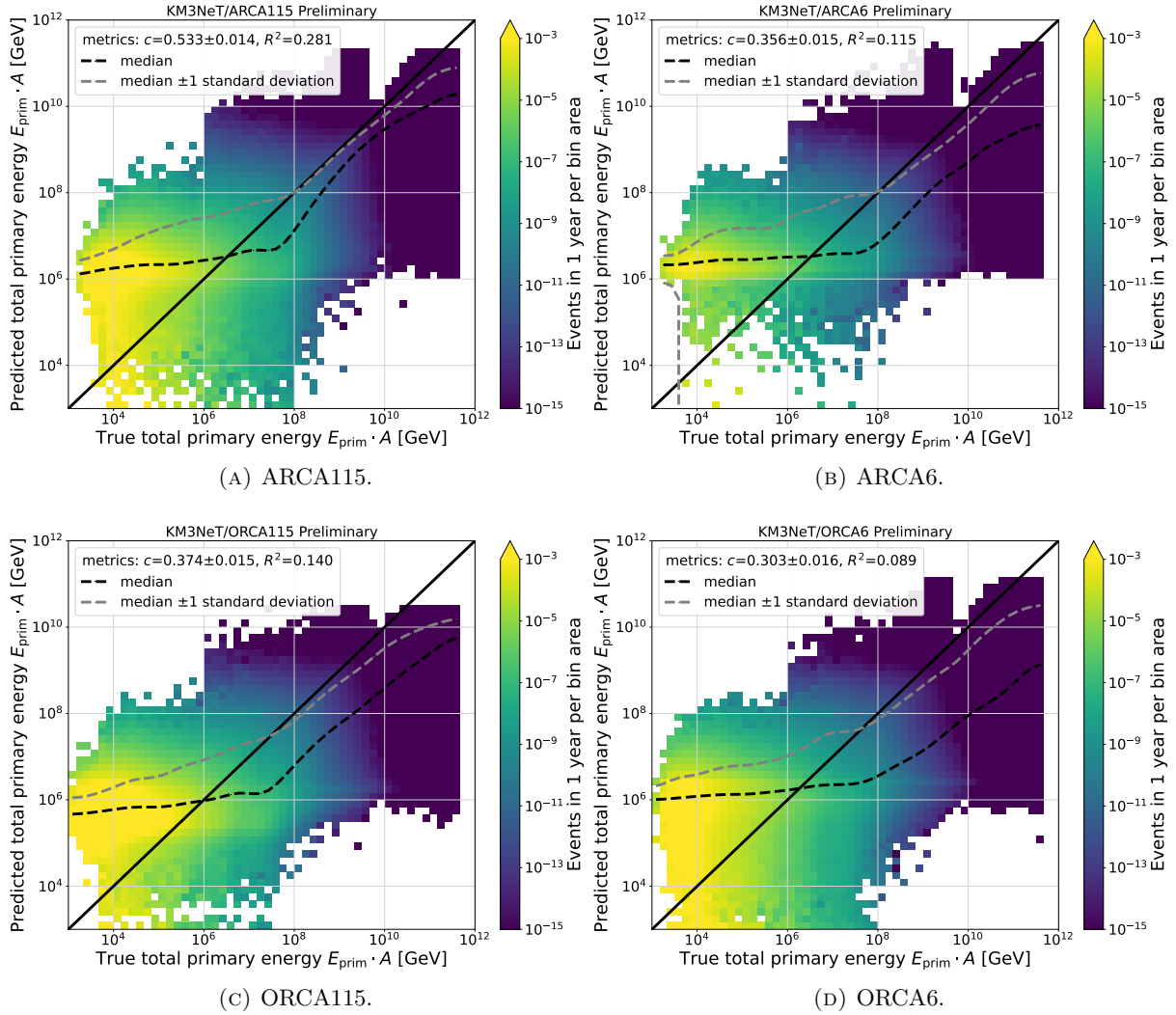


FIGURE 5.3.11.: Comparison of total primary energy reconstructed with the LighGBM model against the true value. The lower grey dashed lines are not visible, because their values are negative.

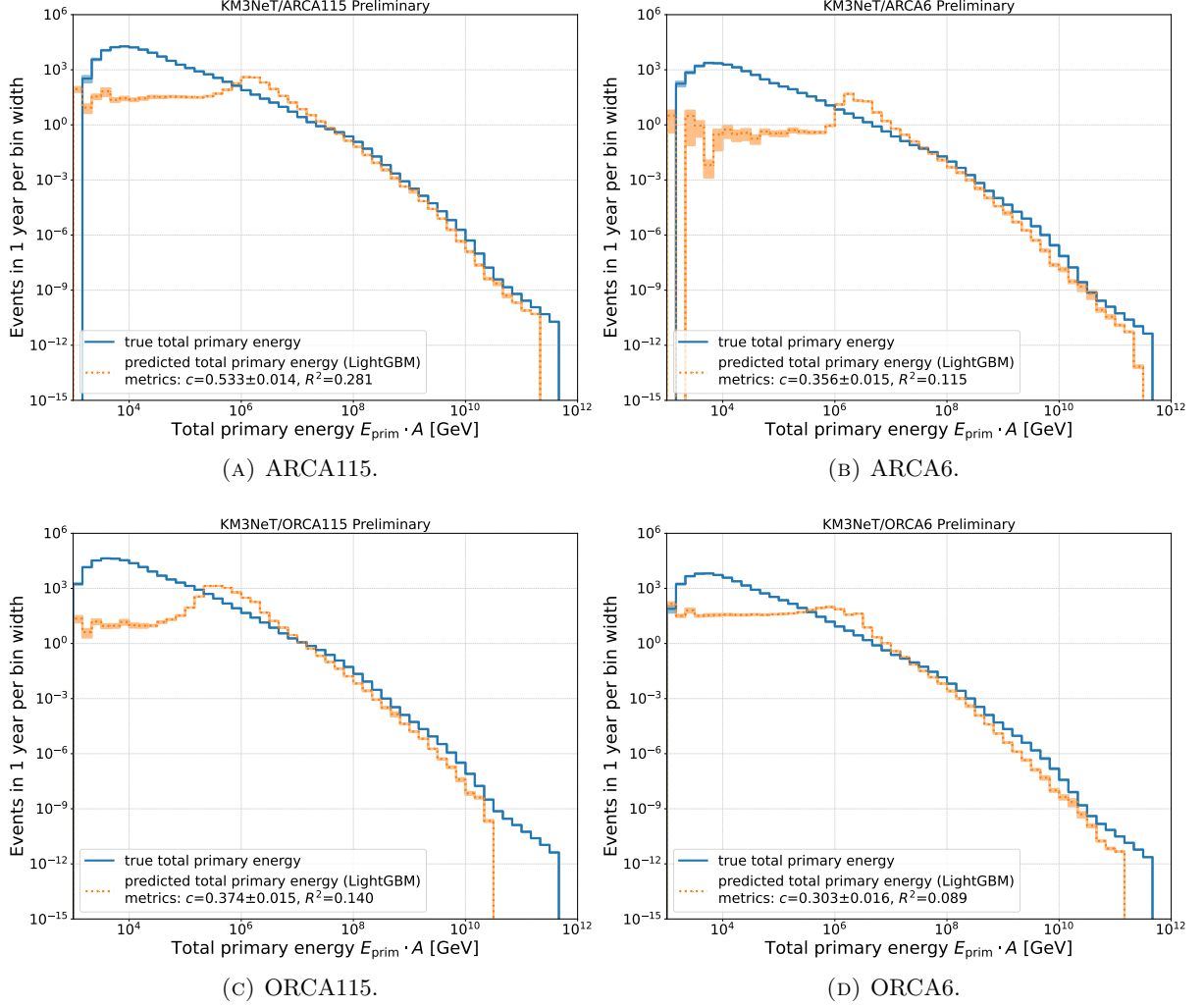


FIGURE 5.3.12.: Comparison of total primary energy reconstructed with the LigthGBM model against the true value in 1D. The error bands were computed using Eq. A.2.1.

5.4. Reconstruction of multiplicity

Reconstruction of individual tracks in multi-track events is a complex task, in the case of extensive air showers often practically impossible without a very fine-grained detector. However, as is demonstrated in this section, reconstruction of the number of muon tracks was possible using machine learning algorithms. The result of the procedure in Sec. 5.3.1.1 was adopted for the estimator selection, given the similarity of the reconstruction task and the same set of used features. Hence, in the following, LightGBM has been used as the default model.

5.4.1. Muon selection

Not every muon can be reliably counted. There are certain cases, when the muon might produce very few, or even no hits in the detector whatsoever. They are sketched in Fig. 5.4.1 and condense into two categories:

1. Energetic — low-energy muon emits less light and may just stop.

2. Spatial — light from the muon that is too far may not reach the optical modules.

It has to be noted that the muons created by ν_μ interactions are neglected here, as the muon-only MC was used. This is well justified, since the neutrino-induced muon flux contributes to less than 1% of the overall muon flux, even at a depth of ARCA [186]. In fact, there are other secondaries (e.g. Σ , Λ , p , n , π^\pm , K^\pm), which reach the sea level, and could contribute to the muon flux at the KM3NeT detectors. However, their contribution to the total flux is of the order of 2.7 % (evaluated using the CORSIKA datasets used within this chapter), and was hence neglected.

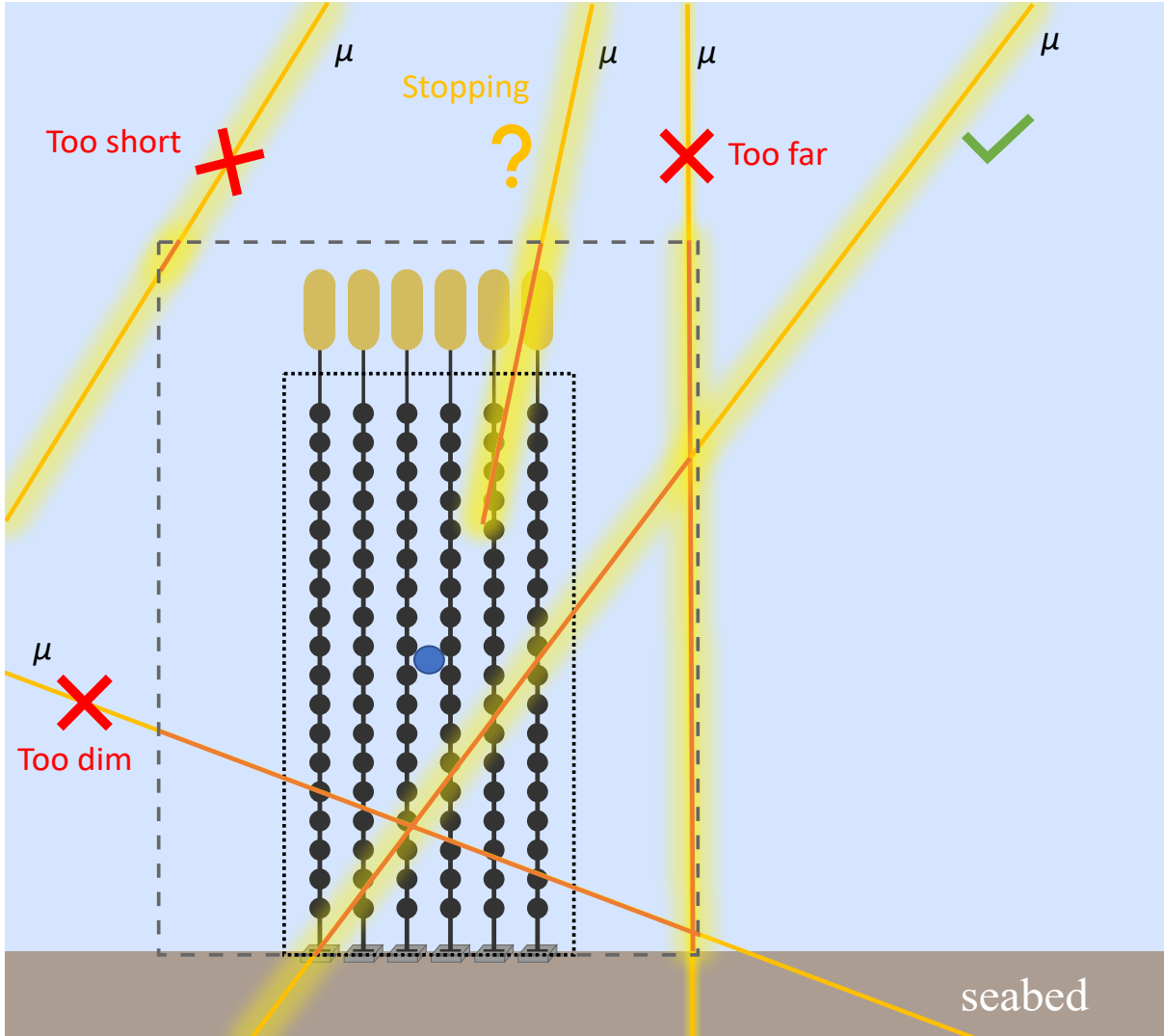


FIGURE 5.4.1.: Sketch of various cases potentially relevant for the muon selection.

Based on these considerations and having a standard single muon track reconstruction (JMuon) at hand, a set of three control plots (see Fig. 5.4.2, 5.4.3, and 5.4.4) was devised. They show the reconstruction quality of JMuon, which is quantified in terms of the likelihood parameter \mathcal{L} , as a function of:

- muon energy E_μ ,
- minimum distance of the muon track from the can centre $d_{\mu-\text{can center}}^{\text{min}}$ (blue dot in Fig. 5.4.1): only vertical muons with $\cos\theta > 0.95$ (θ is the true zenith angle of the muon, and $\cos\theta = 1.0$ is perfectly vertical) are considered,

- muon pathlength L_μ under assumption of a straight line track (neglecting the scattering), determined after fixing the $d_{\mu\text{-can center}}^{\min}$ value, and thus, the volume of interest.

For all three listed variables, only events with true muon multiplicity $N_\mu = 1$ were used. The motivation was to ensure that each likelihood value \mathcal{L} would correspond to a single muon. Moreover, in the case of $d_{\mu\text{-can center}}^{\min}$ (Fig. 5.4.3), only vertical ($\cos\theta > 0.95$) muons were investigated. The muon direction was fixed along the vertical axis of the detector for two reasons. Firstly, the statistics of horizontal single muon events in the Monte Carlo was insufficient. The second reason was the intention to simplify the problem and look only for one value of maximal allowed distance from the optical modules d_{\max} , both in horizontal, and vertical direction. Such an approach resulted in a cylindrical volume of interest, with radius $r = r_{\text{det}} + d_{\max}$, and height $h = h_{\text{det}} + d_{\max}$, where r_{det} and h_{det} are the radius and height of the smallest cylinder enclosing the instrumented volume (the detector). The value of d_{\max} (see Tab. 5.4.1) was decided based on the $d_{\mu\text{-can center}}^{\min}$ plot (Fig. 5.4.3) for each of the detector configurations. In the described approach, differences in the inter-DOM and inter-DU spacings, and due to inclination other than horizontal or vertical were neglected.

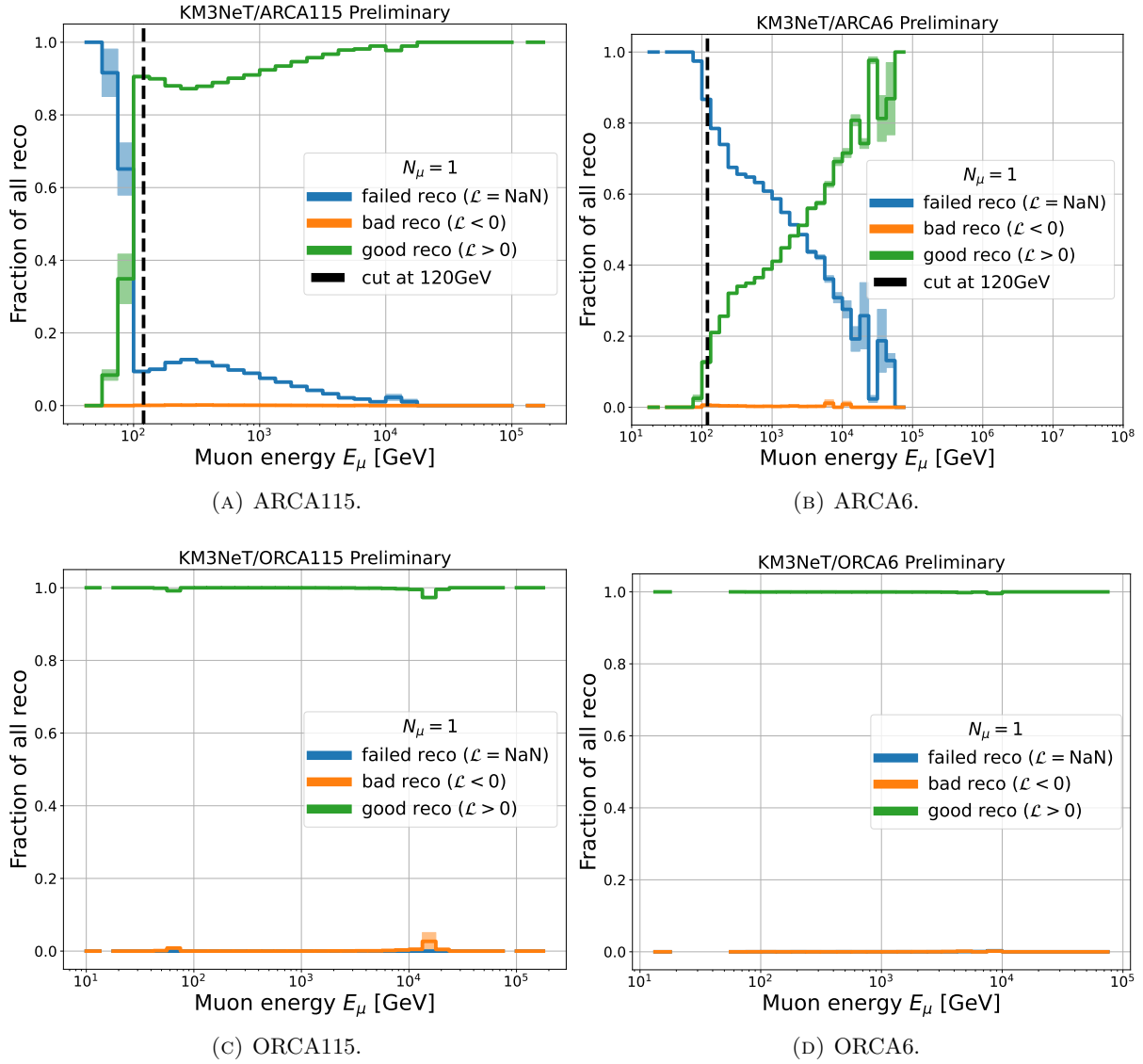


FIGURE 5.4.2.: Fractions of good ($\mathcal{L} > 0$), bad ($\mathcal{L} < 0$), and completely failed ($\mathcal{L} = \text{NaN}$) reconstructions as function of E_μ . Only single muon events (multiplicity $N_\mu = 1$) were used, and the reconstruction algorithm was JMuon. Plots are shown for different detector configurations, and have the energy cut indicated by a black dashed line (if applicable).

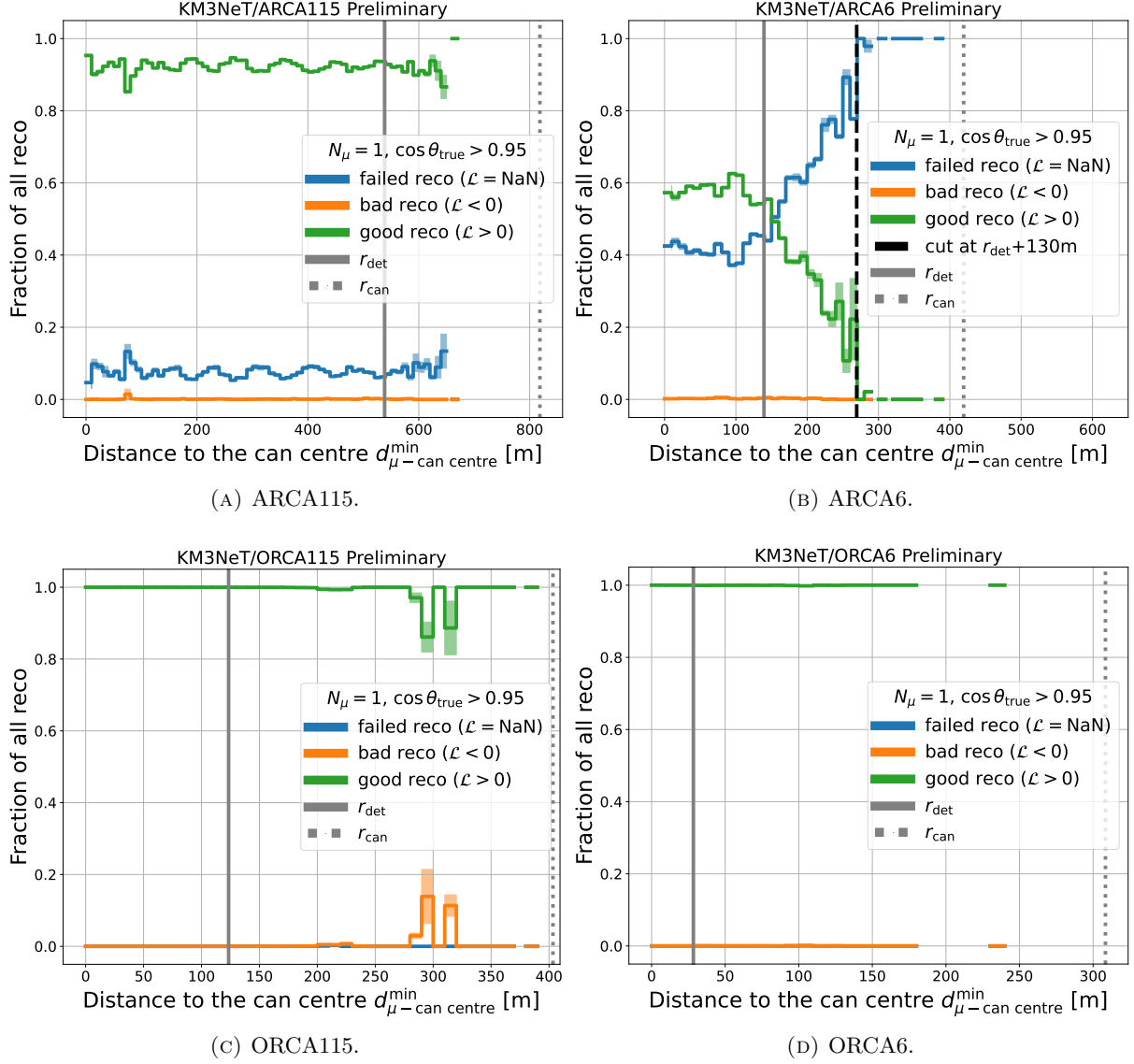


FIGURE 5.4.3.: Fractions of good ($\mathcal{L} > 0$), bad ($\mathcal{L} < 0$), and completely failed ($\mathcal{L} = \text{NaN}$) reconstructions as function of $d_{\mu-\text{can centre}}^{\text{min}}$. Only vertical ($\cos\theta_{\text{true}} > 0.95$) single muon events (multiplicity $N_{\mu} = 1$) were used, and the reconstruction algorithm was JMuon. Plots are shown for different detector configurations, and have the distance cut indicated by a black dashed line (if applicable).

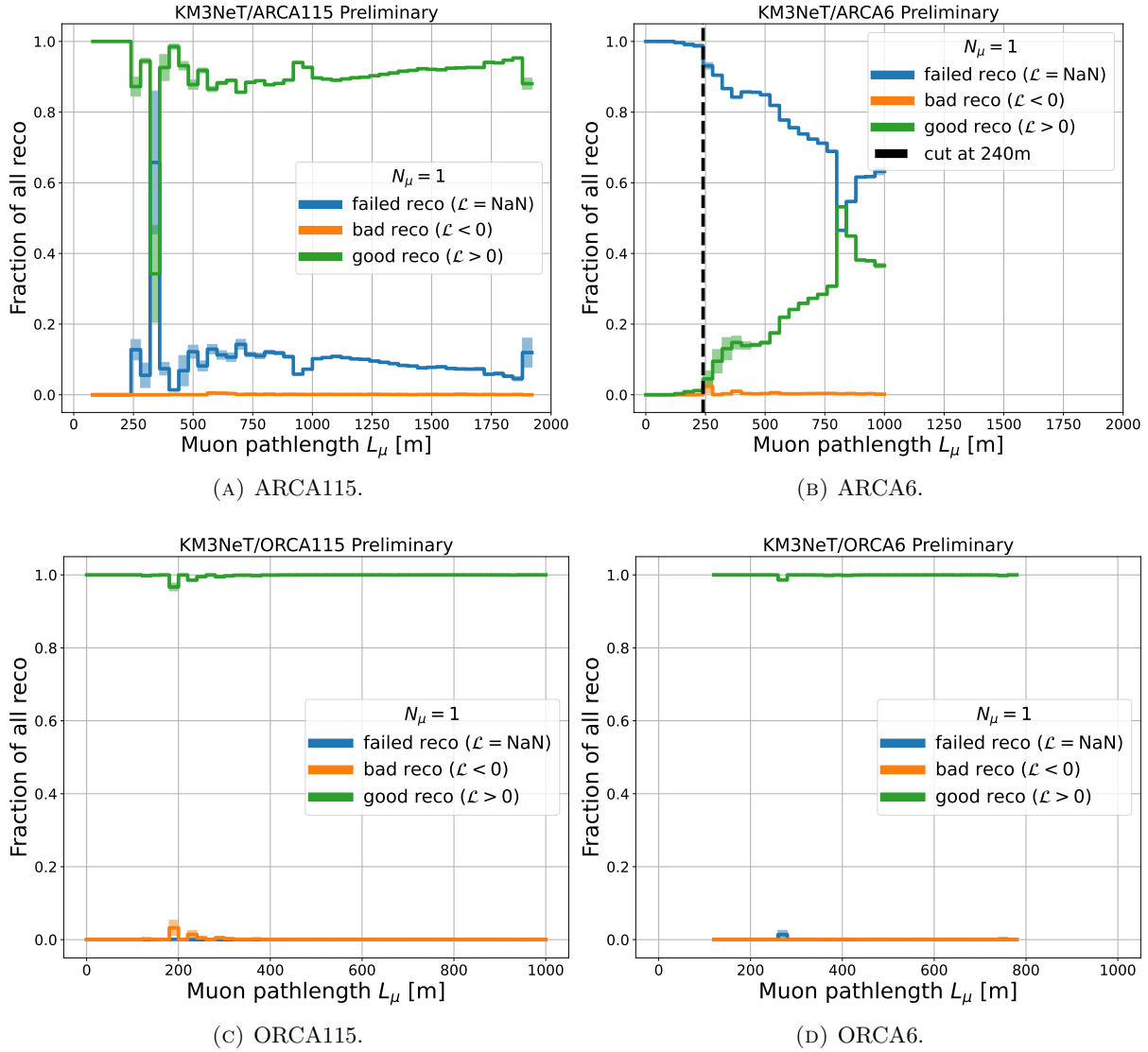


FIGURE 5.4.4.: Fractions of good ($\mathcal{L} > 0$), bad ($\mathcal{L} < 0$), and completely failed ($\mathcal{L} = \text{NaN}$) reconstructions as function of muon pathlength L_μ . Only single muon events (multiplicity $N_\mu = 1$) were used, and the reconstruction algorithm was JMuon. Plots are shown for different detector configurations, and have the pathlength cut indicated by a black dashed line (if applicable).

The muon selections for the muon multiplicity reconstruction were derived from Fig. 5.4.2, 5.4.3, and 5.4.4, and were compiled in Tab. 5.4.1. Somewhat expected, no cuts seemed to be needed for ORCA (thanks to much denser instrumentation than ARCA), therefore the energy cut has been set to 1 GeV, which is the expected lower threshold for the reconstruction, according to [2]. An alternative approach could have been the energy threshold matching the point, where the LightGBM bundle energy starts to fail (see Sec. 5.3.1.4) or to set a certain cutoff at the difference between the true energy and JMuon prediction, however neither of the two was adopted. The energy cut for ARCA was the same regardless of the configuration, and for ARCA6, additional spatial cuts were found to be beneficial. Those selections were applied by default in the following sections.

TABLE 5.4.1.: Selection of muons to be counted when computing the multiplicity for different detector configurations.

Detector	Minimal E_μ [GeV]	d_{\max} [m]	Minimal L_μ [m]
ARCA115	120	—	—
ARCA6	120	269.4	240
ORCA115	1	—	—
ORCA6	1	—	—

5.4.2. Verification of the muon selection

The effect of introducing the muon selection (see Sec. 5.4.1) was the modification of the target for the reconstruction. Instead of predicting the true number of all muons in an event, the model attempted to evaluate the true number of all muons meeting the selection criteria (Tab. 5.4.1) in an event. This number is smaller or equal than the one without selection, and there were events for which such multiplicity with muon selection was equal to zero. The impact of the muon selection was demonstrated on ARCA6, as there, it is expected to be most pronounced. As one may see in Fig. 5.4.5, the selection improves both metric values. After inspection of the bottom-left part of Fig. 5.4.5b, it is evident that the reconstruction struggled with $N_\mu = 0$ events, mostly betting for $N_\mu = 1$. True multiplicity 0 cases were relatively rare ($< 0.4\%$ of all events), while not counting barely visible muons clearly boosted the overall LightGBM’s performance. The muon selection was used as the default in all further sections.

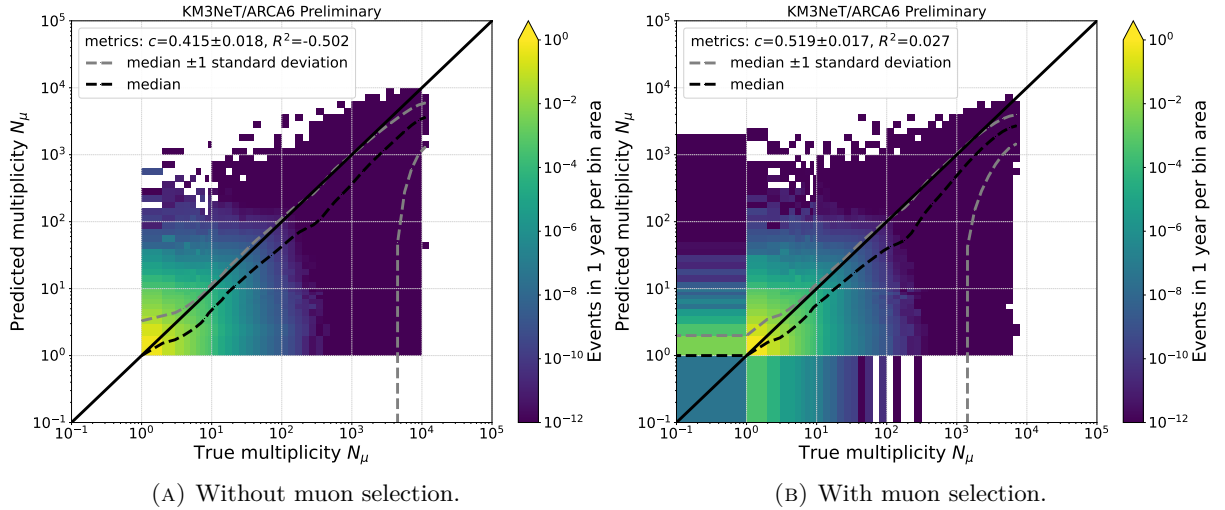


FIGURE 5.4.5.: Predicted muon multiplicity plotted against the MC truth with and without muon selection. In each of the cases, the LightGBM model was trained on features selected according to results of Sec. 5.4.3. Both the correlation c and R^2 -score values were computed on the bin values, not individual events.

5.4.3. Feature importances

Feature importances for the multiplicity reconstruction have been studied analogously to Sec. 5.3. The result is shown in Fig. 5.4.6 and 5.4.7. The same behaviour has been observed — the most profitable selection was the one picking only features with positive importance, hence the other selections were not included in Fig. 5.4.7. The correlation coefficient c has in fact slightly worsened, however within the statistical uncertainty, while the R^2 -score improved by 8 %. Interestingly, in this particular case the feature selection also purged the events falsely reconstructed as $N_\mu = 0$. However, this is not a general rule, as one can see in Sec. 5.4.5.

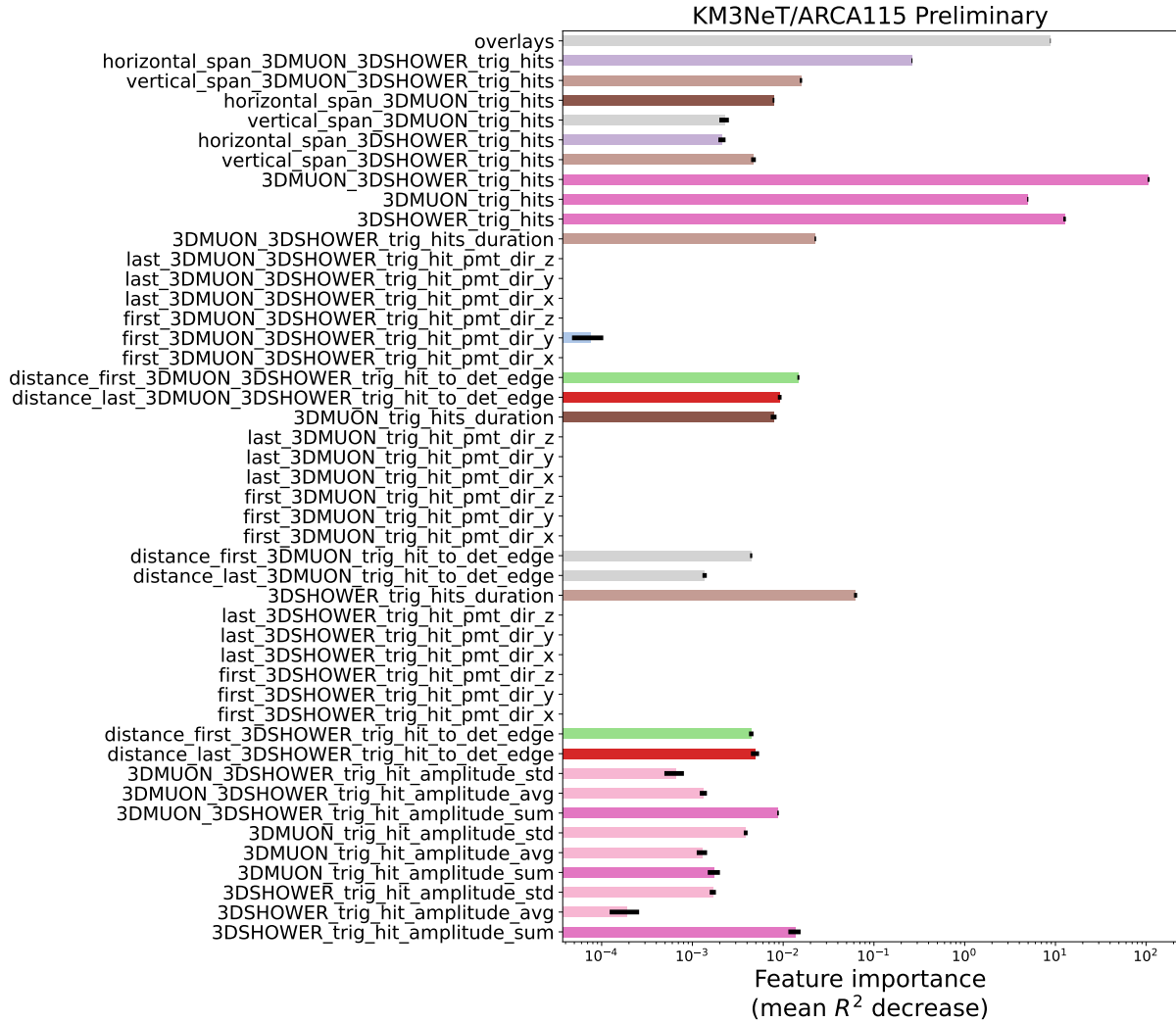


FIGURE 5.4.6.: Feature importance plot, showing how much each feature contributed to the training. The figure has been obtained by performing 10 permutations on a trained model to ensure a stable result. The standard deviation for each feature is denoted by a black bar. The colour coding of features is consistent with Fig. 5.2.2 to show the feature clusters and their most important members. Feature importance plots for the other detector configurations were gathered in Sec. A.5.3.

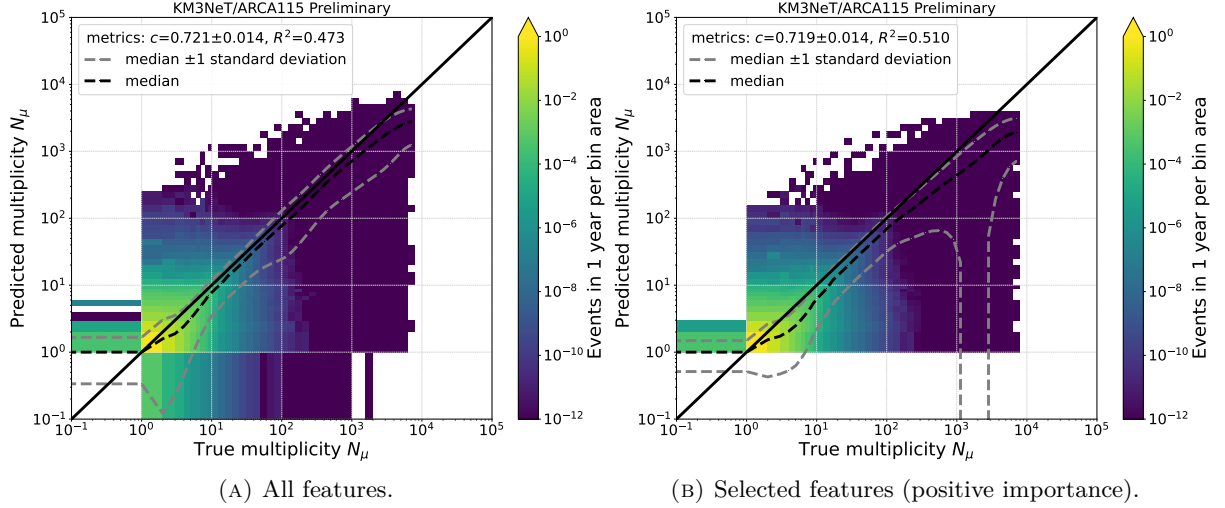


FIGURE 5.4.7.: Predicted muon multiplicity plotted against the MC truth with and without feature selection. Both the correlation and R^2 -score values were computed on the bin values, not individual events.

5.4.4. Hyperparameter tuning

The LightGBM hyperparameters have been tuned in the same way as for the energy reconstruction. The resulting parameter values are documented in Tab. A.5.3.

5.4.5. Results

Using the parameters from Tab. A.5.3, the final results were computed and are presented in Fig. 5.4.8 and 5.4.9. The best reconstruction was achieved for ARCA115, which would indicate that apparently a detector with larger instrumented volume has an advantage over the same number of DOMs packed into a more dense configuration (ORCA). This should not come as a surprise, when one considers e.g. how the muon trackers around the ATLAS detector are designed: they are the most sparsely instrumented part of the detector [187]. This is a direct consequence of the fact that a typical muon signature in a detector is an elongated track (although muons can and sometimes do produce particle showers!). The effect of improved performance upon adding additional DOMs is evident for both ARCA and ORCA. Fig. 5.4.9 demonstrates very good reproduction of the shape of the muon multiplicity distributions in the low and intermediate N_μ range (except for multiplicity 0), with a growing underprediction towards higher values of multiplicity.

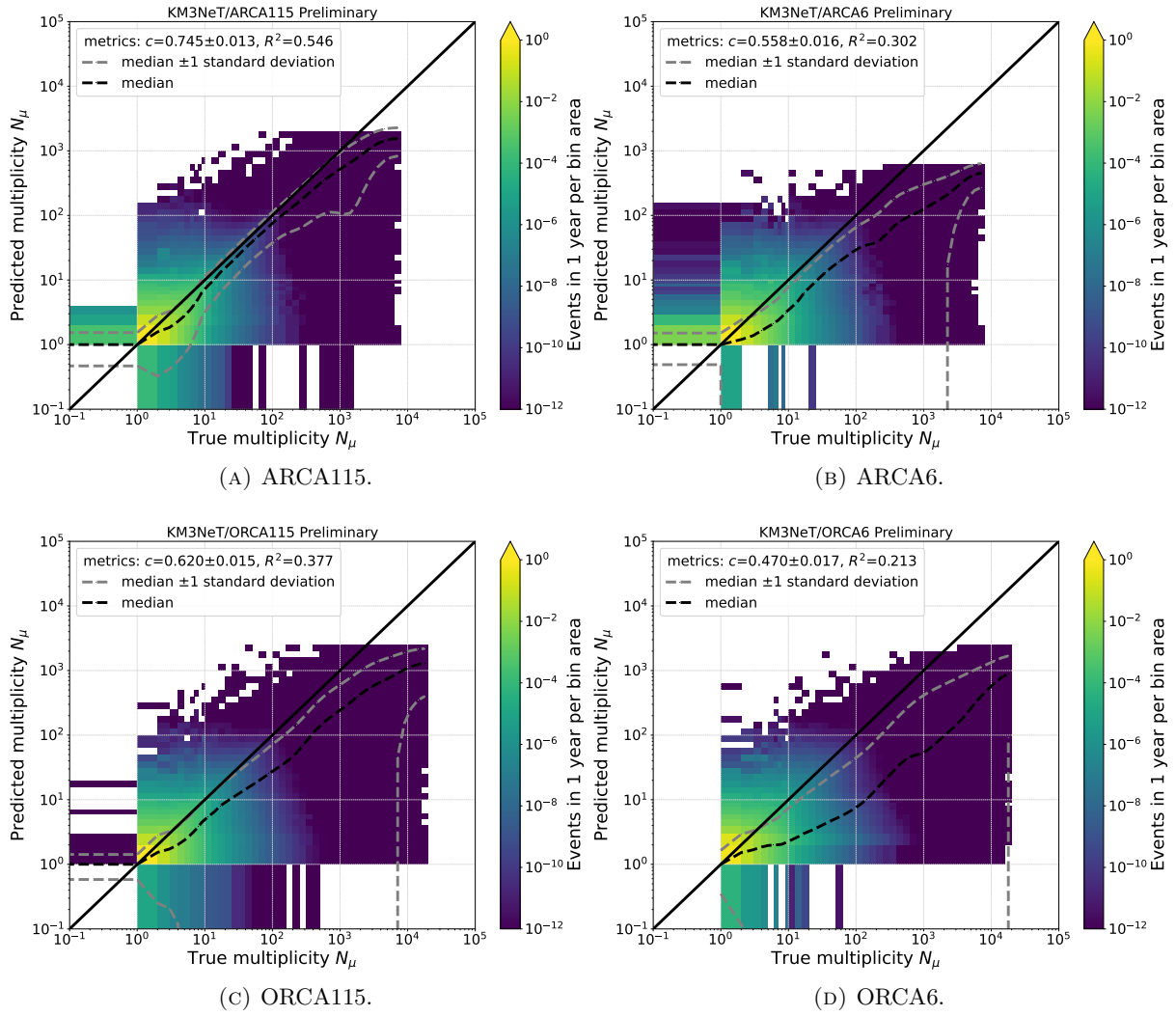


FIGURE 5.4.8.: Comparison of muon multiplicity reconstructed with the LigthGBM model against the true value. Both the correlation and R^2 -score values were computed on the bin values, not individual events.

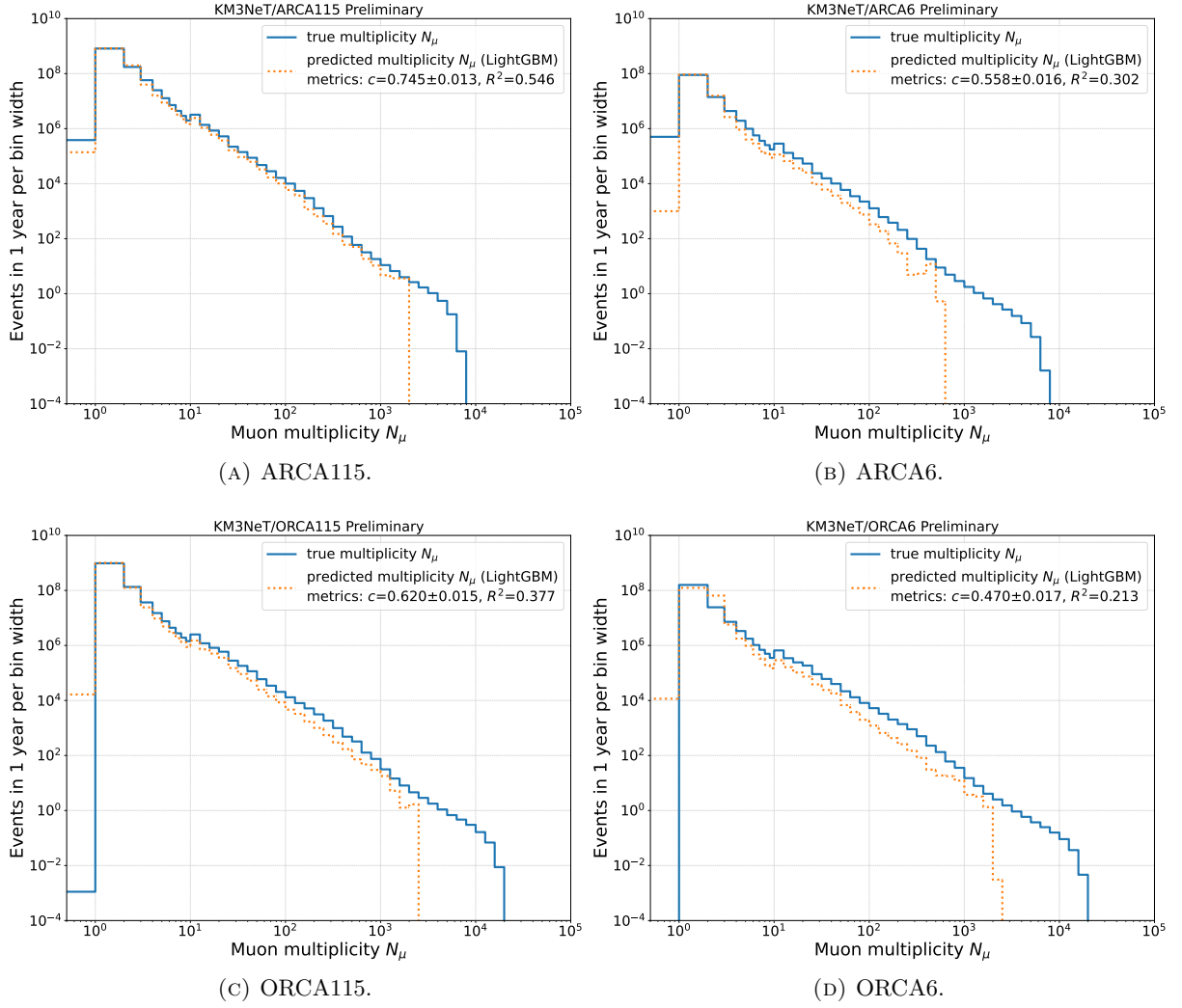


FIGURE 5.4.9.: Comparison of muon multiplicity reconstructed with the LighGBM model against the true value in 1D. Both the correlation and R^2 -score values were computed on the bin values, not individual events.

6. Muon rate measurement with KM3NeT detectors

This chapter is devoted to the comparison of the simulated MC and experimental data for a number of KM3NeT detector configurations, listed in the next section. A comparison of data against the Monte Carlo simulation is the ultimate test of the reliability of the MC. The outcomes are shown in terms of weighted distributions of reconstructed observables. The author has published earlier results of the data vs MC comparisons in [13, 11, 12, 14]. For the most recent ones (ARCA6, ORCA6), he has evaluated the systematic uncertainties on the event weights (Sec. 6.2), except for the two incorporated from the work of A. Romanov [148], and prepared an event quality selection (Sec. 6.3). In addition, the energy and multiplicity reconstruction described in Chap. 5 were applied to ARCA6 and ORCA6 data. The systematic uncertainties were combined with statistical uncertainty according to Eq. A.2.2 for simulated events from the CORSIKA MC productions prepared by the author of this dissertation.

6.1. Simulated samples and experimental data

At the time of compiling this thesis, data and MC for several detector configurations of both ARCA and ORCA were available. The datasets used in this chapter are listed in Tab. 6.1.1. From the indicated run ranges, the selected ones corresponding to particularly stable data taking periods were used.

TABLE 6.1.1.: Available data and MC simulations.

Detector	data/MUPAGE			CORSIKA		
	Runs	Dates	Livetime [d]	Code version	$n_{\text{generated showers}}$	E_{prim} range
ARCA2	5009 - 5408	23.12.2016 - 08.03.2017	57.71	v7.6400	$2.5 \cdot 10^9$	1 TeV–1 EeV
ARCA6	9635 - 10286	12.05.2021 - 10.09.2021	113.63	v7.7410	$1.44 \cdot 10^{10}$	1 TeV–8 EeV
ORCA1	2867 - 3250	09.11.2017 - 13.12.2017	33.77	v7.6400	$2.5 \cdot 10^9$	1 TeV–1 EeV
ORCA4	5378 - 7219	01.07.2019 - 25.01.2020	188.17	v7.6400	$2.5 \cdot 10^9$	1 TeV–1 EeV
ORCA6	7231 - 9264	27.01.2020 - 07.01.2021	328.38	v7.7410	$1.44 \cdot 10^{10}$	1 TeV–8 EeV

CORSIKA MC each time was generated in non-rbr mode, i.e. with averaged PMT parameters and trigger settings (see Sec. 4.3.4). This means that the muon flux simulated with CORSIKA is averaged over time. For MUPAGE, depending on the detector configuration, both simulations in rbr (ARCA2, ORCA1, ORCA4) and in non-rbr mode (ARCA6, ORCA6) were used.

6.2. Systematic uncertainty study

The goal of the study described here was to estimate the systematic uncertainty on the atmospheric muon bundle rate. The systematics were included event-wise, as in Eq. A.2.2, hence the sought quantity was the uncertainty on event weight as function of the primary energy: $\Delta w(E_{\text{prim}})$. The following five sources of systematic uncertainty were considered in this work:

1. Primary cosmic ray flux models.
2. High-energy hadronic interaction models.
3. Seasonal differences in the atmospheric density profile.
4. Spread of the PMT efficiency.
5. Varying light absorption length.

The methods by which individual uncertainties were evaluated are explained in the following subsections. The last 3 listed uncertainties were evaluated separately for KM3NeT/ARCA and KM3NeT/ORCA.

There were a number of sources of systematic uncertainty, which were neglected in this study:

1. The Earth's magnetic field strength variations: see Sec. A.1.3.
2. Atmospheric density models: due to lack of recent models, satisfying the requirements of CORSIKA simulations for KM3NeT (see Sec. A.1.2).
3. Primary CR flux composition (see Sec. 6.2.1).
4. Low-energy hadronic interaction models: they have marginal influence on the CORSIKA results, as they are only used below 80 GeV in air [5]. In the case of KM3NeT, muons with energies of 80 GeV and extremely unlikely to reach even the top of ORCA (see Sec. A.1.4).
5. Differences in the run settings, which were averaged out in the non-rbr MC simulations. Based on MUPAGE studies in [148], the difference between the rbr and non-rbr MC is on the order of $\sim \pm 5\%$.

The obtained uncertainties are shown collectively in Fig. 6.2.1.

6.2.1. Primary cosmic ray flux models

The uncertainty coming from the differences between the predictions of the total CR primary flux ϕ_{CR} by the different models, was estimated directly based on those flux predictions. This was the most natural way to evaluate it, as the event weights are computed using the CR flux (see Eq. 4.2.2). The total (all-nuclei) flux was used, since this is precisely what is indirectly observed by KM3NeT by looking at the atmospheric muon bundles. One could try to infer the underlying composition of primary CRs, however as demonstrated in [9], it is no trivial task. The uncertainty related to the unknown underlying primary CR composition was neglected in this work and the composition as in the default primary CR flux model: GST3, was assumed.

The uncertainty on the event weight was estimated using:

$$\Delta w_{\text{cr}}|_{\text{upper}} = \frac{\phi_{\text{CR}}(E_{\text{prim}})|_{\text{max}} - \phi_{\text{CR}}(E_{\text{prim}})|_{\text{default}}}{\phi_{\text{CR}}(E_{\text{prim}})|_{\text{default}}} \cdot 100\% \quad (6.2.1)$$

and

$$\Delta w_{\text{cr}}|_{\text{lower}} = \frac{\phi_{\text{CR}}(E_{\text{prim}})|_{\text{default}} - \phi_{\text{CR}}(E_{\text{prim}})|_{\text{min}}}{\phi_{\text{CR}}(E_{\text{prim}})|_{\text{default}}} \cdot 100\%. \quad (6.2.2)$$

The considered CR flux models included: GST3 (default), GST4, H3a, H4a, cH3a, and cH4a [127, 131, 132]. Models like poly-gonato or ZS [128, 188, 133, 130] were excluded from the evaluation, as they are clearly outdated and do not describe the CR flux above the knee.

6.2.2. High-energy hadronic interaction models

The uncertainty due to the modelling of the HE hadronic interactions was computed based on a set of dedicated CORSIKA mini-productions. The mini-productions were processed in the same way as the mass production, used for the development of the event reconstruction in Chap. 5 and analysis in Chap. 7. The only differences were:

- zenith angle fixed to 0° (vertically downgoing events only),
- fixed primary energies were sampled: 1, 2, 3, 6, 20, 60, 200 TeV and 2 PeV (instead of a continuous spectrum),
- the total number of generated showers per primary: $1.11 \cdot 10^7$,
- each of the mini-productions was done for a different HE hadronic interaction model: EPOS LHC (v3400), SIBYLL 2.3d, or QGSJET II-04.

The first two changes were introduced to minimize the fluctuations related to the sampling itself. The second and third also aimed at reducing the required computational resources. Fixing the zenith relies on the assumption that the uncertainty only weakly depends on the direction, as compared to the energy. This has been verified for single muons using the simplified simulation using [189], with the result of sub-percent variation of muon flux due to varying the zenith angle. The uncertainty on the event weight was evaluated in an analogous manner as in Sec. 6.2.1:

$$\Delta w_{\text{had}}|_{\text{upper}} = \frac{f_{\text{surv}}(E_{\text{prim}})|_{\text{max}} - f_{\text{surv}}(E_{\text{prim}})|_{\text{default}}}{f_{\text{surv}}(E_{\text{prim}})|_{\text{default}}} \cdot 100\%, \quad (6.2.3)$$

$$\Delta w_{\text{had}}|_{\text{lower}} = \frac{f_{\text{surv}}(E_{\text{prim}})|_{\text{default}} - f_{\text{surv}}(E_{\text{prim}})|_{\text{min}}}{f_{\text{surv}}(E_{\text{prim}})|_{\text{default}}} \cdot 100\%, \quad (6.2.4)$$

where $f_{\text{surv}} = \frac{N_{\text{survived}}}{N_{\text{generated}}}$ is the fraction of showers surviving until the sea level and the default model is SIBYLL 2.3d. At the sea level, the shower content is already dominated by the muons and neutrinos, with a contribution of only $\sim 2.7\%$ from the hadrons (based on the CORSIKA mass production). For this reason, the selection of the hadronic interaction model could be assumed to be irrelevant for the transport of muons from the sea to the can.

6.2.3. Atmospheric density profiles

The values of $\Delta w_{\text{atm}}|_{\text{upper}}$ and $\Delta w_{\text{atm}}|_{\text{lower}}$, related to different atmospheric density profiles were calculated exactly in the same way, as in Sec. 6.2.2, but with the HE hadronic interaction model fixed to SIBYLL 2.3d and for the following atmosphere fits:

- evaluated at ARCA in summer (June),
- evaluated at ARCA in winter (December),
- evaluated at ORCA in summer (June),
- evaluated at ORCA in winter (December),
- evaluated for a prediction averaged between ARCA and ORCA and over a time period of 2 years (default).

The first four were taken from [190] and the fifth one is the same as in Sec. A.1.2.

For the ARCA result, only the averaged and the ARCA summer and winter atmosphere fits were used. Analogously, for ORCA the considered atmosphere fits were the averaged one and the ones for ORCA summer and winter.

6.2.4. Photomultiplier tube efficiency

The uncertainty related to the variations in PMT efficiencies was adapted from the study performed by A. Romanov [148]. There, muon bundle rates were compared using MUPAGE simulations with PMT efficiencies set to the nominal value or to the nominal value modified by $\pm 10\%$. The result was an uncertainty of $\Delta w_{\text{pmt}} \pm 5\%$ for ORCA6 and $\Delta w_{\text{pmt}} \pm 20\%$ for ARCA6. The difference between the detectors stems from the higher density of instrumentation with PMTs of the ORCA telescope. The effect of the detector size was neglected and the uncertainty for ORCA6 was assumed to be the same as for ORCA115. Analogously, the one for ARCA6 was set equal to ARCA115 as well.

6.2.5. Light absorption length

The same study by A. Romanov mentioned in Sec. 6.2.4 encompassed the comparison of MUPAGE simulation results with varied absorption length of light in seawater. In this case, the absorption length was varied by $\pm 10\%$, following the results from [151]. The obtained uncertainties were $\Delta w_{\text{abs}} = \pm 5\%$ for ORCA6 and $\Delta w_{\text{abs}} = \pm 15\%$ for ARCA6, again with the difference between the two coming from different detector geometries. In ORCA light has shorter path to travel between the DOMs, and hence ORCA is less affected by the uncertainty due to the light absorption. The uncertainty for ORCA115 was taken to be the same as for ORCA6 and for ARCA115 the same as ARCA6.

6.2.6. Combined results

The final result on systematic uncertainty was obtained by adding the five contributions in quadrature:

$$\Delta w_{\text{sys}} = \sqrt{(\Delta w_{\text{had}})^2 + (\Delta w_{\text{cr}})^2 + (\Delta w_{\text{atm}})^2 + (\Delta w_{\text{pmt}})^2 + (\Delta w_{\text{abs}})^2}, \quad (6.2.5)$$

where had, cr, atm, pmt, and abs stand for uncertainties related to HE hadronic interaction models, primary CR flux models, atmospheric seasonal density variations, PMT (see Sec. 3.1.2) efficiency

and light absorption length, respectively. The result of combining the uncertainties is displayed in Fig. 6.2.1, separately for ARCA and ORCA.

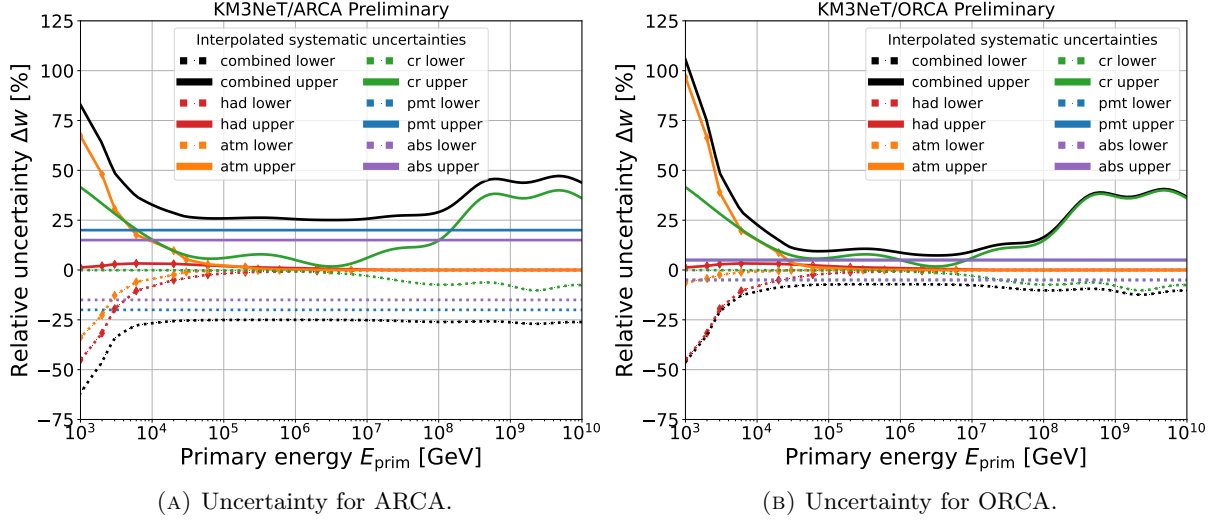


FIGURE 6.2.1.: Interpolated relative systematic uncertainties for ARCA and ORCA. Both individual contributions and the combined uncertainties are plotted. The upper uncertainties are shown as solid lines and the lower uncertainties: as dashed lines. The square points indicate the sampled energies, over which the interpolation was done. There was no interpolation for cr, pmt and abs.

As one may note in Fig. 6.2.1, there is a plateau of minimal systematic uncertainty for both KM3NeT/ARCA and KM3NeT/ORCA in the range of primary energies between 10 TeV and 100 PeV. Nevertheless, the minimal uncertainties are still large, on the order of 25 % for ARCA and 10 % for ORCA. The low-energy regime is mostly dominated by the atmospheric uncertainty. This can be intuitively understood in the following way: the varying atmospheric density profiles result in different first interaction heights and also different total atmosphere thicknesses that have to be traversed (see Sec. A.1.2). For a very low-energy shower it may be critical for reaching the sea-level. Here it must be stressed that what is meant are muons from such a shower reaching the sea: neutrinos easily travel even longer distances. It has been verified that below 10 TeV, the mean survival rate of showers starts to vary considerably between showers starting at different heights. The difference between events that start above and below 24 km reaches 50 % at $E_{\text{prim}} = 1$ TeV. The difference in what and how many particles are produced in the hadronic interactions can also become crucial for the survival of air showers. For this reason the hadronic uncertainty also rises at low primary energies. This only happens for the lower hadronic uncertainty, since SIBYLL 2.3d tends to produce on average more low-energy muons, which are able to reach the sea.

At the highest energies, the atmospheric and hadronic uncertainties become irrelevant, since the events are energetic enough to reach the sea, regardless of the starting point, atmospheric density or the interactions undergone along the way. However, what does become important are the uncertainties related to the primary CR flux modelling. This is a limitation imposed by the insufficient experimental data in this regime, as the CR flux drops sharply with increasing energy. Similarly, the cosmic ray flux uncertainty at the lowest energies results from the limited experimental data at lowest energies at the time of design of the models. Admittedly, there is one more recent,

data-driven model: Global Spline Fit (GSF) [191], which was not considered in this work and could be included in future extensions. The upper cosmic ray flux uncertainty is larger than the lower one due to the choice of the GST3 as the default CR flux model.

The results from Fig. 6.2.1 have been included in the ARCA6 and ORCA6 plots in Sec. 6.4 and in results in Chap. 7.

6.3. Event quality selection

The comparison of experimental data against MC simulations typically requires purging the datasets of the following two classes of events:

1. Generally poorly reconstructed, e.g. low-energy muons, skimming the outer parts of the can. Such μ may produce little to none detectable photons (see the discussion in Sec. 5.4.1).
2. Not included in the standard KM3NeT MC productions:
 - a) pure noise events: events containing solely environmental background due to ^{40}K radioactive decays in seawater (see Sec. 4.3.4) and electronics noise [2],
 - b) events related to hardware malfunctions, e.g. sparking DOMs (DOMs with a short-circuit) or afterpulses (additional delayed signal, which occurs after the main response of the PMT to a detected photon) [123, 115, 117].

This section is dedicated to the quality selection further used in Sec. 6.4 for the most recent detector configurations: ARCA6 and ORCA6. The cut on JMuon likelihood \mathcal{L} was performed for both detectors, as \mathcal{L} is a generic quantity evaluating the feasibility of reconstruction of an event. Undoubtedly, it would be more optimal to have a separate, dedicated measure of the ML reconstruction uncertainty, similarly to what was done in [9]. Nevertheless, the employed cuts improved the data vs MC agreement for low-level variables, as demonstrated in the following two subsections.

The event quality selection, applied in Sec. 6.4.1.2 and 6.4.2.3, is a combination of the minimum likelihood cut ($\mathcal{L} > 50$ for ARCA and $\mathcal{L} > 280$ for ORCA, see Sec. 6.3.1 and 6.3.2) and reconstruction reliability cuts, summarized in Tab. 6.3.1.

TABLE 6.3.1.: Lower prediction reliability bounds for different observables reconstructed by JMuon and the ML models, based on results from Chap. 5 and Sec. A.4. In the case of ORCA115 JMuon energy reconstruction, no limit could be set based on the available CORSIKA datasets, however 1 GeV was taken as the expected lowest achievable energy with ORCA [2].

Reconstruction	Observable	ARCA115	ARCA6	ORCA115	ORCA6
JMuon	$\cos(\theta_{\text{zenith}})$	-	-	-	-
	Energy	10 GeV	1 TeV	1 GeV	60 GeV
ML	Bundle energy E_{bundle}	1 TeV	1 TeV	400 GeV	600 GeV
	Total primary energy $A \cdot E_{\text{prim}}$	6 PeV	8 PeV	3 PeV	5 PeV
	Multiplicity N_{μ}	1	1	1	1

6.3.1. ARCA6

In this section, selected trigger-level observables for ARCA6 are shown to investigate the effect of the cut on the JMuon likelihood \mathcal{L} . The adopted cut value was $\mathcal{L} = 50$, which followed the previous ARCA6 data analysis work [56]. It can be verified by looking at Fig. 6.3.1, that such a selection indeed focuses on a region with better agreement between the data and MC.

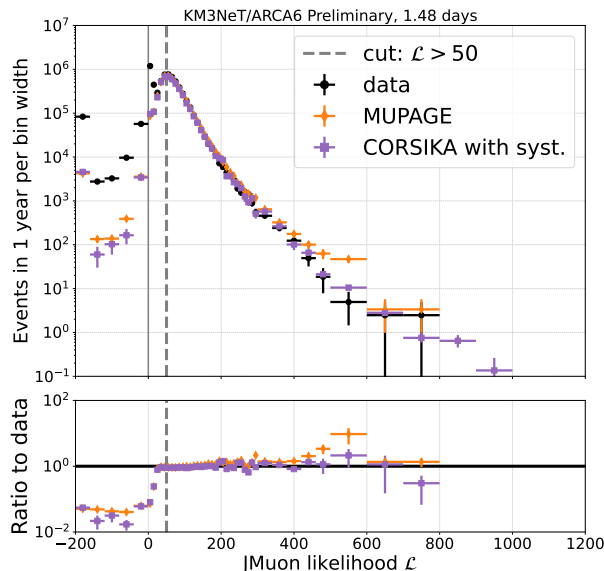


FIGURE 6.3.1.: The comparison of the distributions of the JMuon likelihood \mathcal{L} for ARCA6 data and MC simulations.

The first investigated trigger-level quantity was the number of hits passing the requirements of both the 3DMuon and 3DShower trigger, which was picked as the most important feature for the reconstruction in Sec. 5.3.1.3. The comparison of experimental and simulated data is presented in Fig. 6.3.2. Both MCs were generated with averaged PMT parameters and trigger settings (in non-rbr mode, see Sec. 4.3.4). In addition, the distributions of the duration of events with hits triggered by both 3DMuon and 3DShower were plotted in Fig. 6.3.3.

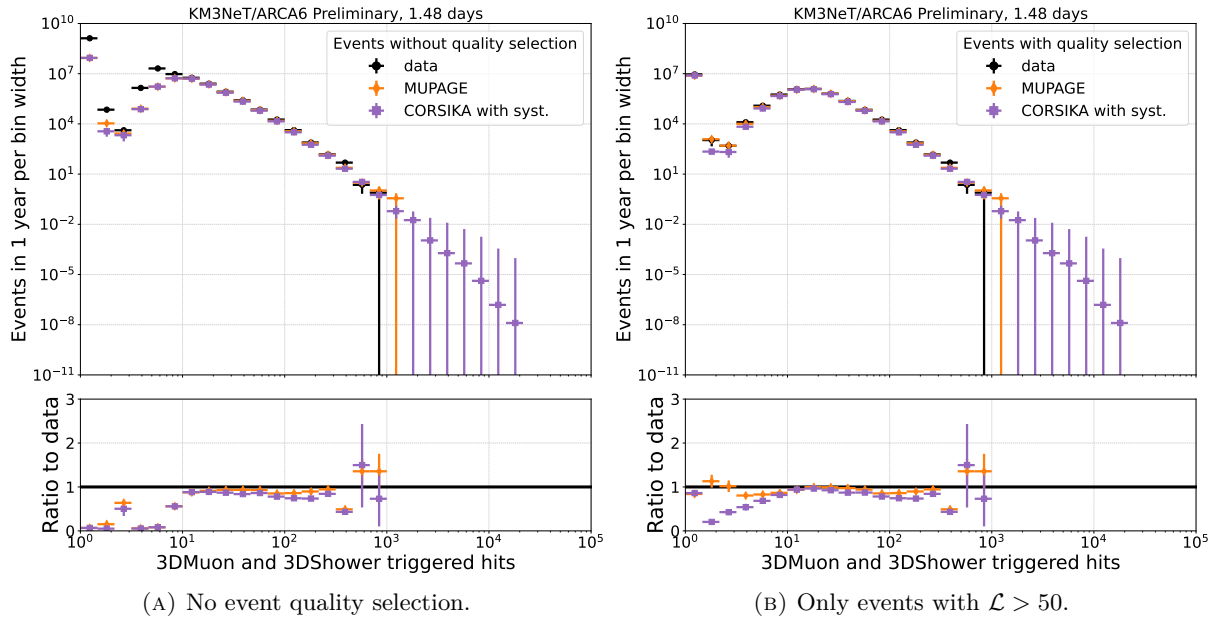


FIGURE 6.3.2.: The comparison of the distributions of the number of hits triggered by the 3DMuon and 3DShower triggers for ARCA6 data and MC simulations.

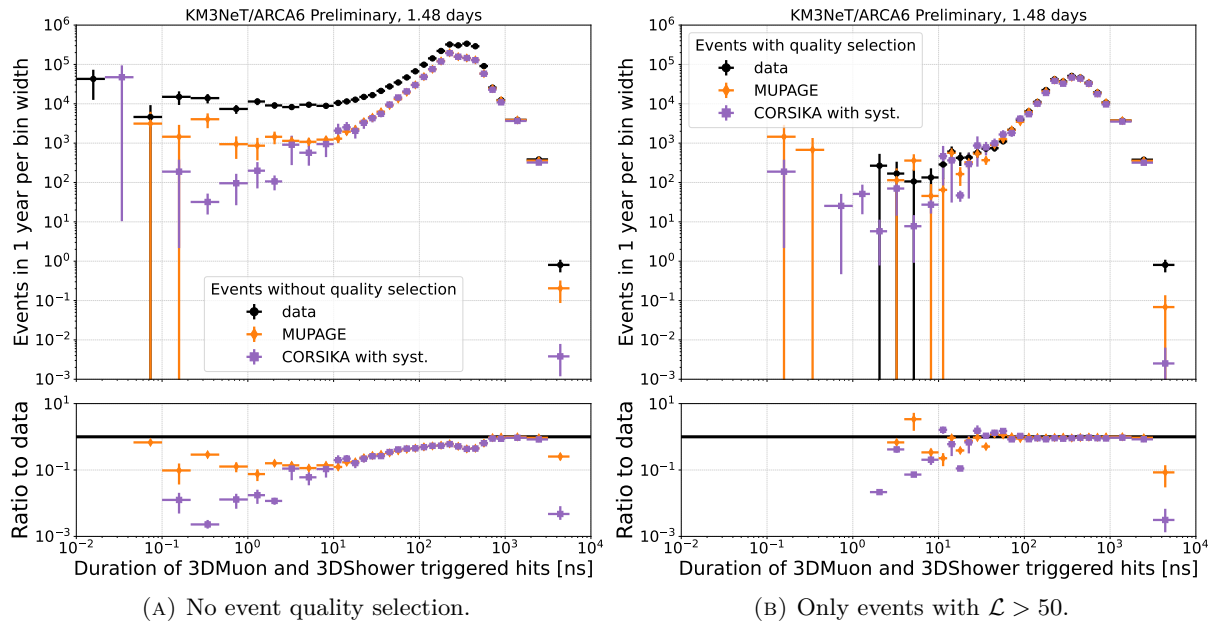


FIGURE 6.3.3.: The comparison of the distributions of the duration of hits triggered by the 3DMuon and 3DShower triggers for ARCA6 data and MC simulations.

As demonstrated on examples of Fig. 6.3.2 and 6.3.3, the agreement of the trigger-level variables clearly improved after applying the cut on the JMuon likelihood. It has to be noted that such variables are entirely independent of the JMuon reconstruction, since they are computed at trigger level (see Sec. 4.3). This leads to a conclusion that the likelihood is an effective proxy of the ‘reconstructability’ of an event. In other words, it measures the feasibility of reconstruction of an event, with a caveat that it is somewhat biased towards the JMuon reconstruction. The applied

quality cut mostly rejects the sub-ns events with few triggered hits, which are indeed expected to be more challenging to reconstruct. Such short events are dominated by the pure noise, which is not included in the simulations, hence the surplus of the experimental data over the MC.

6.3.2. ORCA6

In this section, a set of plots for ORCA6, analogous to the ones from Sec. 6.3.1 is presented. The likelihood cut for ORCA6 was fixed at $\mathcal{L} = 280$.

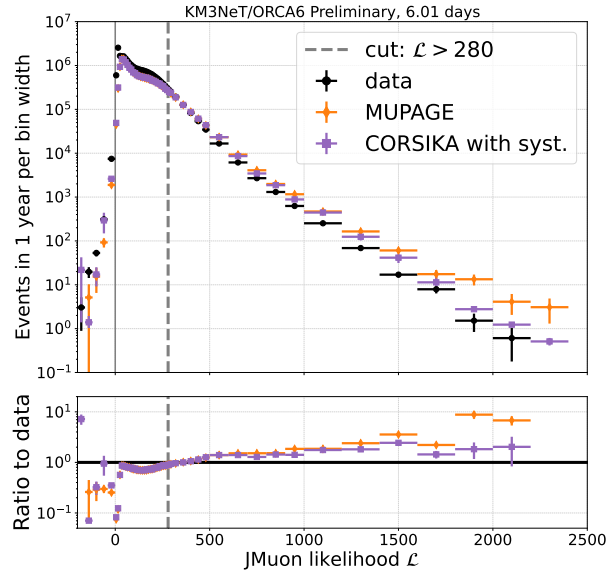


FIGURE 6.3.4.: The comparison of the distributions of the JMMuon likelihood \mathcal{L} for ORCA6 data and MC simulations.

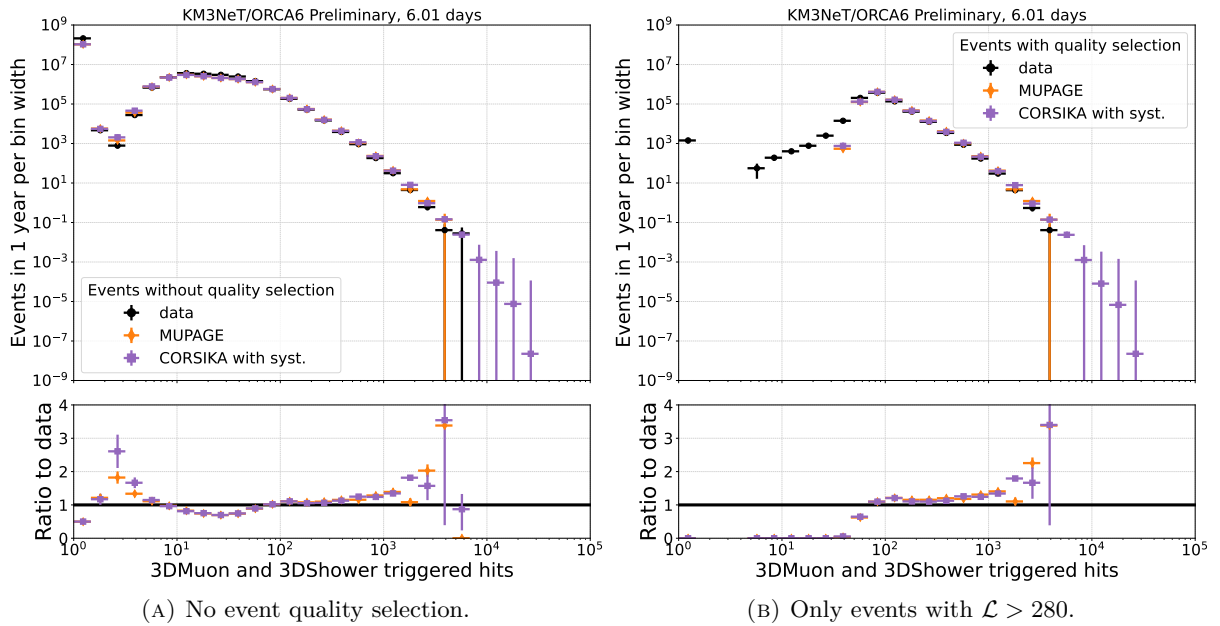


FIGURE 6.3.5.: The comparison of the distributions of the number of hits triggered by the 3DMuon and 3DShower triggers for ORCA6 data and MC simulations.

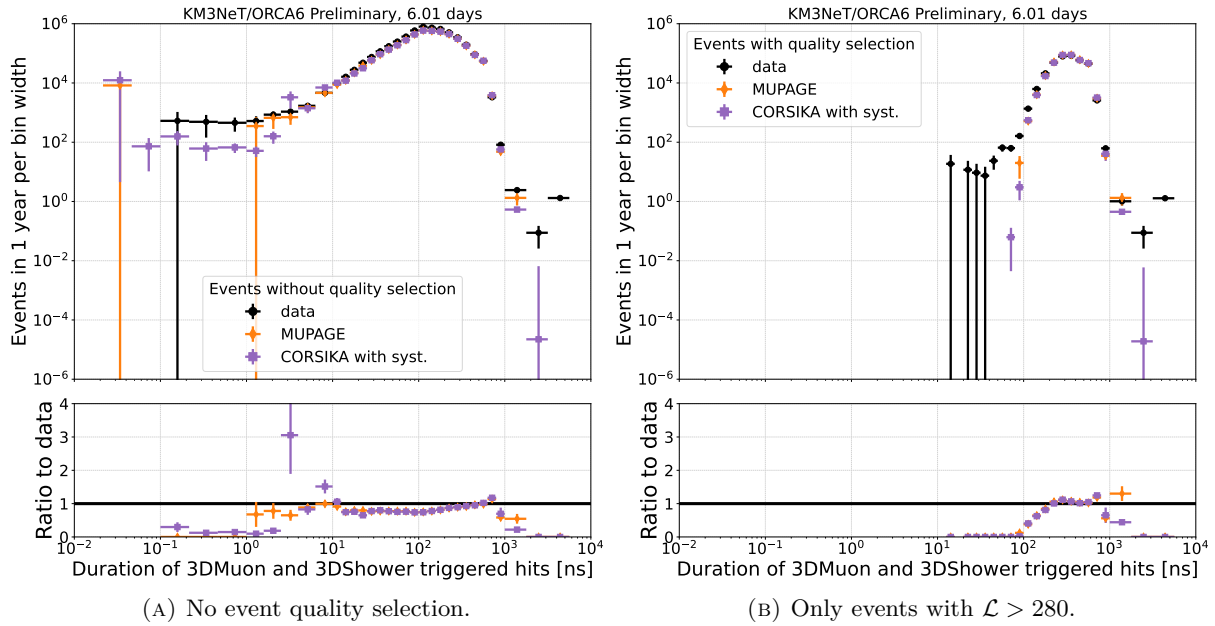


FIGURE 6.3.6.: The comparison of the distributions of the duration of hits triggered by the 3DMuon and 3DShower triggers for ORCA6 data and MC simulations.

As clear already from Fig. 6.3.4, the agreement between the data and MC simulations for ORCA6 still required significant improvement. Both MUPAGE and CORSIKA simulations have shown consistent behaviour, however their ratio to experimental data did not settle around 1 at high \mathcal{L} values, as was the case for ARCA6. One of the known factors causing the difference between the experimental data and MC simulation were the differences between the rbr (data) and non-rbr (MC) processing modes, which were larger than for ARCA6. This is tied to generally less stable data taking of ORCA6. The much stricter cut at $\mathcal{L} = 280$ was introduced to remedy these problems to some extent. As one can see, most of the rejected events are again ones with few triggered hits and short duration.

With the quality of results in mind, the ORCA6 data was not used in Chap. 7. Nevertheless, the comparison of reconstructed observables is still shown in Sec. 6.4.2.3. The exact reasons for the observed discrepancies are still under close investigation within the KM3NeT Collaboration. They were certainly at least partially connected with hardware issues, which have affected the stability of ORCA6 data taking. Recovery and replacement of the faulty DUs is foreseen during the upcoming ORCA sea campaigns (rounds of deployment of further DUs and other hardware). In parallel, there are ongoing efforts to improve the entire KM3NeT simulation chain. The work of this thesis, in particular the developments in the gSeaGen code (see Sec. A.3), has been a significant contribution in this area.

6.4. Comparisons of data and Monte Carlo simulations

In the following, selected ARCA and ORCA experimental data sets were compared against the MUPAGE and CORSIKA muon simulations. To minimize the influence of the seasonal variations on the experimental data, the runs covering the full available periods of data taking were used both

for the data and MUPAGE simulation (if using the rbr simulation). The seasonal variations of the muon flux observed by ANTARES, which was located near the ORCA site, were on the order of 2 % [23]. The systematic uncertainties have been included only in the most recent results: for ARCA6 and ORCA6. The results for ARCA2, ORCA1, and ORCA4 have been published prior to completion of the systematic uncertainty study and were hence not modified [13, 11, 12, 14]. The primary CR flux model assumed for CORSIKA MC weighting was GST3 [127], as mentioned in Sec. 4.1.1.

6.4.1. KM3NeT/ARCA

In this section, comparisons of measured and simulated distributions of different reconstructed muon bundle observables for ARCA2 and ARCA6 were collected. ARCA2 and ARCA6 are the intermediate configurations of the ARCA detector with 2 and 6 installed DUs respectively.

6.4.1.1. ARCA2

For the ARCA2 configuration, reconstructed muon bundle direction (average muon $\cos\theta_{\text{zenith}}$) and energy (sum of E_{μ}) distributions were compared between experimental data, MUPAGE and CORSIKA, using the datasets indicated in Tab. 6.1.1. No cuts have been applied.

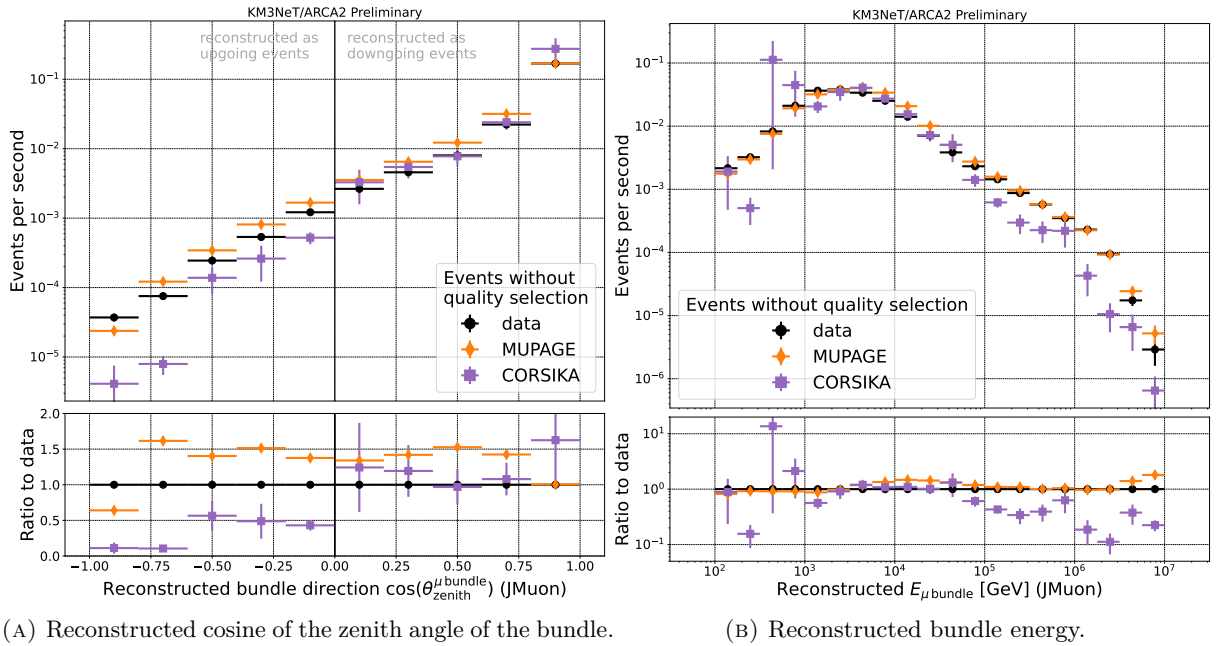


FIGURE 6.4.1.: The muon bundle rates for the ARCA2 detector. The data and MUPAGE samples both have the livetimes of about 20 d. The plots have been published in [13, 11, 12].

Results presented in Fig. 6.4.1 are one of the very first KM3NeT muon measurements and have been an invaluable proof of concept for the detector operation and the validity of KM3NeT simulations. At the same time, the observed discrepancies were a clear sign, where further improvement was needed. In the zenith plot (Fig. 6.4.1a), the events reconstructed as upgoing ($\cos\theta_{\text{zenith}}^{\mu \text{ bundle}} < 0$) are

in fact muons for which the direction was flipped by JMuon (possibly with a very small contribution of actual upgoing events from neutrino interactions in the data). A number of possible causes of the clear underprediction of the data by CORSIKA at higher energies (Fig. 6.4.1b) have been identified and were discussed in [13, 11, 12]. Notably, one of the underlying issues was solved by improving the propagation of muons through water with gSeaGen (some of these developments are described in Sec. A.3).

6.4.1.2. ARCA6

For the ARCA6 results, the selected runs corresponded to a livetime of 1.46 days. It may seem small at first, however it has to be noted that this translates to 3 013 982 events, out of which all were reconstructed by the ML-based reconstruction and 287 553 by JMuon. The used runs were intentionally picked to be separated by possibly large periods of time, to ensure at least partial averaging out of the seasonal variations of the muon flux. For CORSIKA, the ARCA6 test dataset from Sec. 5.2.2 was used. An event quality selection from Sec. 6.3.1 has been applied to both MCs and to the data.

The standard JMuon reconstruction results are presented in Fig. 6.4.2. The agreement between data and MC in zenith has improved with respect to ARCA2 results, however most of the upgoing events were still misreconstructed downgoing ones, as in Sec. 6.4.1.1. The reconstructed energy distributions in Fig. 6.4.2b match well below few TeV. As one can verify in Fig. A.4.4a, this is in fact a region, where JMuon prediction largely underestimates the true energy. Above TeV energies, both CORSIKA and MUPAGE underestimate the data. MUPAGE is closer to the experimental data, since it was tuned on the KM3NeT data from earlier detector configurations. For CORSIKA, the behaviour is consistent with results reported in Sec. 6.4.1.1, however the ratio is closer to one than it was for ARCA2. This is an improvement directly resulting from optimisation of the gSeaGen code, especially in terms of muon propagation (see Sec. A.3). MUPAGE, on the other hand, displays a different behaviour than it did in Fig. 6.4.1b. This stems from the fact that MUPAGE simulation in non-rbr mode was used for ARCA6, while for ARCA2 it was in rbr mode. This points out that there is a need for run-by-run simulations, especially in the case of intermediate KM3NeT detector configurations, which typically do not collect data for much longer than a year before next detection units are deployed. The caveat here is that more detailed simulations with CORSIKA in rbr mode are simply not feasible, due to enormous computational cost. This was addressed in [148], where the MUPAGE parametrization was tuned to the CORSIKA simulation produced within this work.

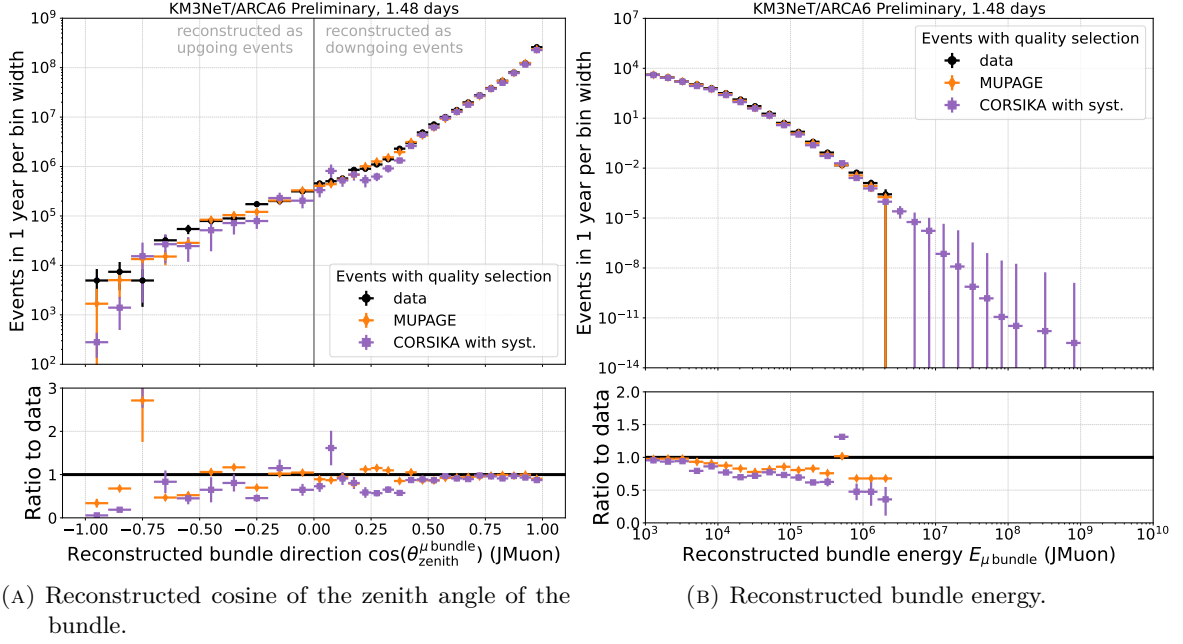


FIGURE 6.4.2.: The muon bundle rates for the ARCA6 detector as function of the direction and energy reconstructed by JMuon

Another open question is, whether the JMuon energy reconstruction, which is developed under a hypothesis of a single muon track is a suitable tool for reconstruction of high-energy muon bundles. On one hand, muons in EAS are highly collinear due to very forward production, on the other hand it is highly unlikely to encounter an EeV shower producing a bundle with multiplicity equal to one. An alternative was provided by the energy reconstruction developed within this work (see Chap. 5). The results of the LightGBM-based reconstruction applied to the experimental data, MUPAGE, and CORSIKA MC is shown in Fig. 6.4.3. The reconstructed bundle energy in Fig. 6.4.3a does not reach as high values as the JMuon energy reconstruction in Fig. 6.4.2b. This is expected, since LightGBM reconstruction tends to underpredict the true energy, especially at higher energies (see Sec. 5.3.1). In Fig. 6.4.3a, the energy prediction can be trusted above few TeV (see Fig. 5.3.9). The underestimation of the data by the MC simulations is consistent between Fig. 6.4.3a and 6.4.2b, hence such a behaviour cannot be attributed to the reconstruction. It implies that there is a need for more accurate modelling of CR air showers.

The total primary energy reconstruction behaves in a similar manner to the bundle energy reconstruction, as the two quantities are tightly related. According to Fig. 5.3.11, the primary energy prediction offers sensible (under-)predictions above 10 PeV. The GZK cutoff value of 50 EeV has been marked in Fig. 6.4.3b to guide the eye [79]. As one may note, the data does not reach near that point, hence it is not possible to draw any conclusion yet. The CORSIKA simulation extends beyond 50 EeV, however the GZK cutoff is not implemented in any way in the CORSIKA MC (nor in MUPAGE).

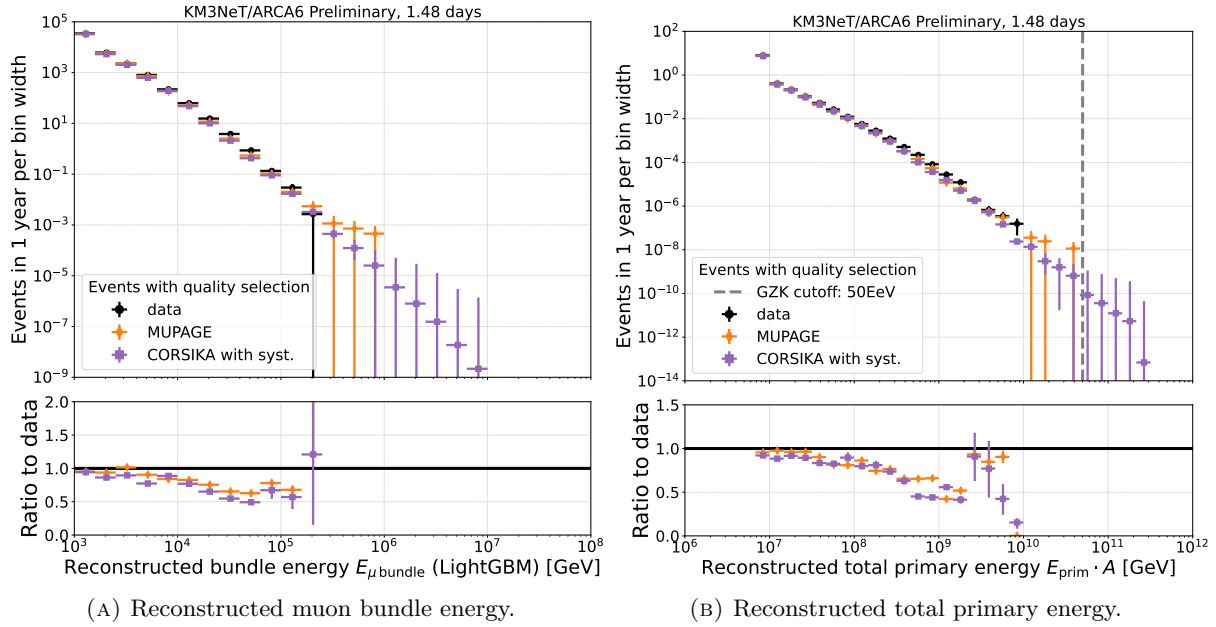


FIGURE 6.4.3.: ML-based energy reconstruction results for the ARCA6 detector.

The multiplicity reconstructed in Fig. 6.4.4 is the one with muon selection, as in Sec. 5.4.5. The MUPAGE simulation generally tends to better match the data, which is expected as it was tuned on ORCA4 data. Both simulations struggle to accurately describe the data for bundles with more than 10 muons. This is again an indication that further work in CR shower simulations is required.

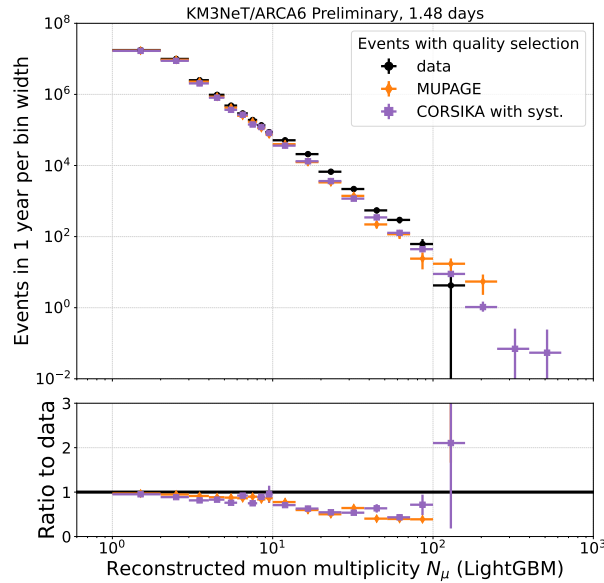


FIGURE 6.4.4.: ML-based multiplicity reconstruction result the ARCA6 detector.

6.4.2. KM3NeT/ORCA

Here, the results of data vs MC comparisons for ORCA1, ORCA4, and ORCA6 were gathered. Analogous to Sec. 6.4.1, ORCA1, ORCA4, and ORCA6 are the intermediate ORCA configurations with 1, 4, and 6 installed DUs respectively.

6.4.2.1. ORCA1

In the case of the ORCA1, no energy reconstruction has been performed, as this was one of the earliest detector configurations. The reconstructed zenith angle is shown in Fig. 6.4.5. A very similar behaviour was observed as for ARCA2 (Fig.6.4.1a). In this case no cuts have been applied.

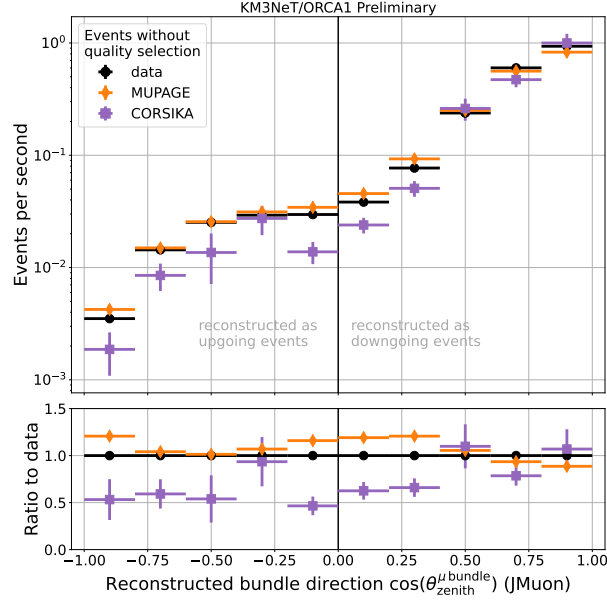


FIGURE 6.4.5.: The muon bundle rates as a function of the reconstructed cosine of the zenith angle of the bundle for the ORCA1 detector. The data and MUPAGE samples both have the livetimes of about 24 days. The plot has been published in [13].

6.4.2.2. ORCA4

The JMuon reconstruction of zenith and energy for ORCA4 with no cuts applied is presented in Fig.6.4.6. The agreement between the data and both Monte Carlos for the downgoing muons has significantly improved with respect to the ORCA1 result, which can be attributed to advances in both simulation and reconstruction software. Interestingly, here MUPAGE seems to overestimate the high-energy event rate (see Fig. 6.4.6b). The excess of upgoing events in data is most probably due to pure noise events, as e.g. in Fig. 6.4.2a.

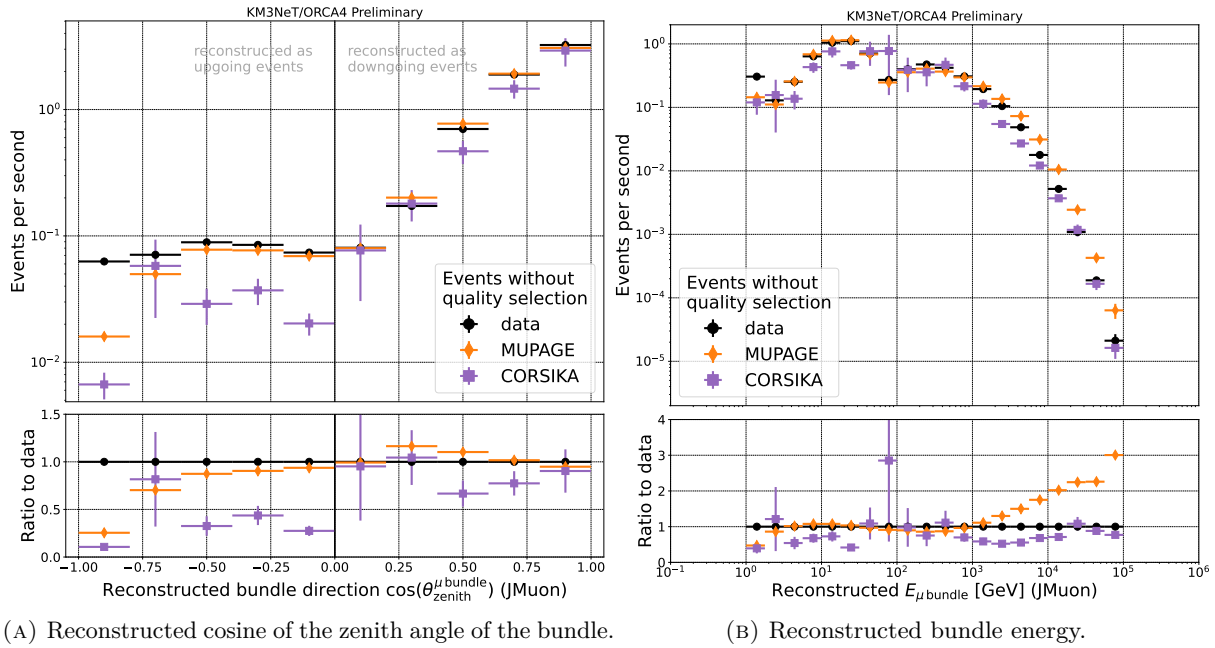


FIGURE 6.4.6.: The muon bundle rates for the ORCA4 detector. The data and MUPAGE samples both have the livetimes of about 10 days. The plots have been published in [11, 12, 14].

6.4.2.3. ORCA6

The ORCA6 results were derived using a subsample of the runs from Tab. 6.1.1 with a livetime of 6.01 days. The runs were selected sparsely, analogously to what was done for ARCA6 in Sec. 6.4.1.2. This was equivalent to 4 574 887 events reconstructed with LightGBM and 4 571 428 with JMuon). Here, the reconstruction failure rate of JMuon is noticeably lower, compared with ARCA6 (Sec. 6.4.1.2), owing to more dense instrumentation of ORCA. Regarding CORSIKA, the ORCA6 test dataset from Sec. 5.2.2 was used. The event quality selection from Sec. 6.3.2 has been applied to both MCs and to the data.

Distributions of zenith and energy for ORCA6 as reconstructed by JMuon can be found in Fig. 6.4.7. The stricter cut on likelihood seems to have eliminated the upgoing pure noise events. Given the challenges noted in Sec. 6.3.2, the agreement between the simulated and measured direction of showers is remarkably good. It has also improved with respect to results for ORCA1 and ORCA4. It might come as a surprise that in Fig. 6.4.7b both simulations seem to overpredict the experimental data, which was only the case for MUPAGE in earlier results. However, upon inspection of Fig. A.4.6a one has to conclude that for ORCA6 the JMuon energy reconstruction results are simply not reliable above 3 TeV. Such a problem does not occur for LightGBM-based reconstruction (see Fig. 5.3.9), hence one may claim that it is related to the inaccuracy of JMuon in reconstruction of muon bundle energies. In Fig. 6.4.8a, the experimental data and simulations match well up to about 20 TeV and there is a large excess of data over the CORSIKA MC above 200 TeV, however confirming it with a larger collected (and simulated for MUPAGE) livetime would be preferable. The observed excess seems to be much larger than statistical fluctuations, even including potential

unidentified sources of systematic uncertainty. The region, where it occurs, roughly matches where the contribution from the prompt muon component is expected, however at this stage it would be premature to draw any conclusions, given the remaining challenges in the simulation of atmospheric muons.

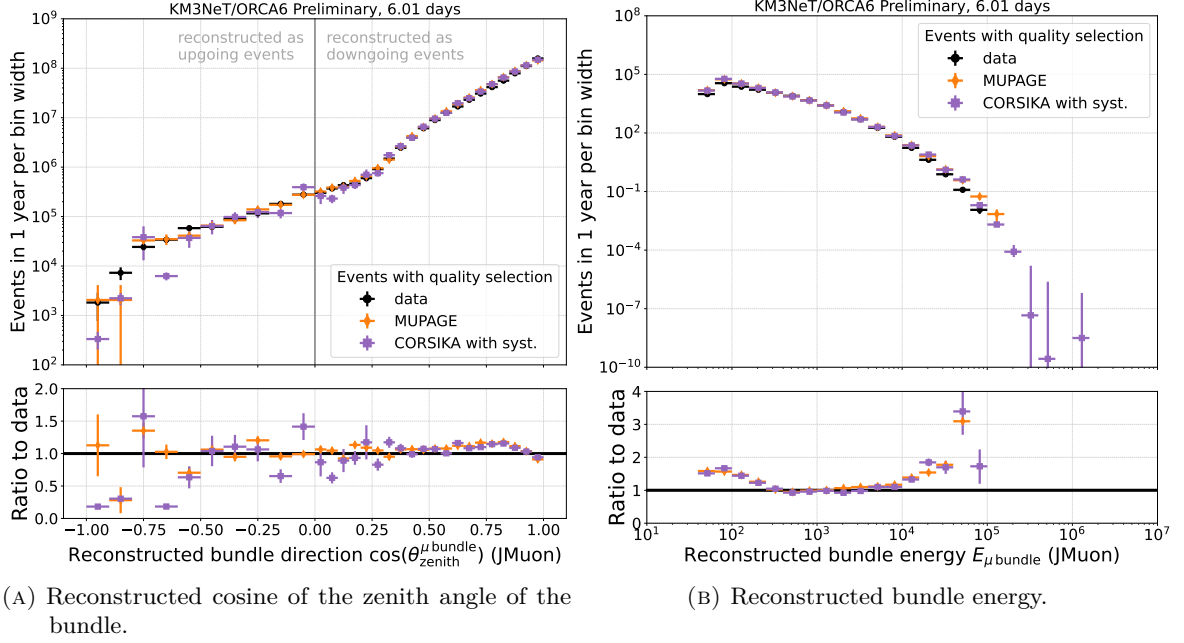


FIGURE 6.4.7.: The muon bundle rates for the ORCA6 detector as function of the direction and energy reconstructed by JMuon.

The total primary energy reconstruction in Fig. 6.4.8b yielded results consistent to the ones for ARCA6 in Fig. 6.4.3b, also demonstrating an excess at high energies, as one would expect after seeing Fig. 6.4.8a. For ORCA6 data, there is a single data point at the GZK cutoff value, unlike for ARCA6. It is the first such a measurement with KM3NeT detectors, and it still remains to be verified with a more conclusive dataset. As was already noted when discussing the ARCA6 results, neither CORSIKA nor MUPAGE implements the GZK cutoff directly.

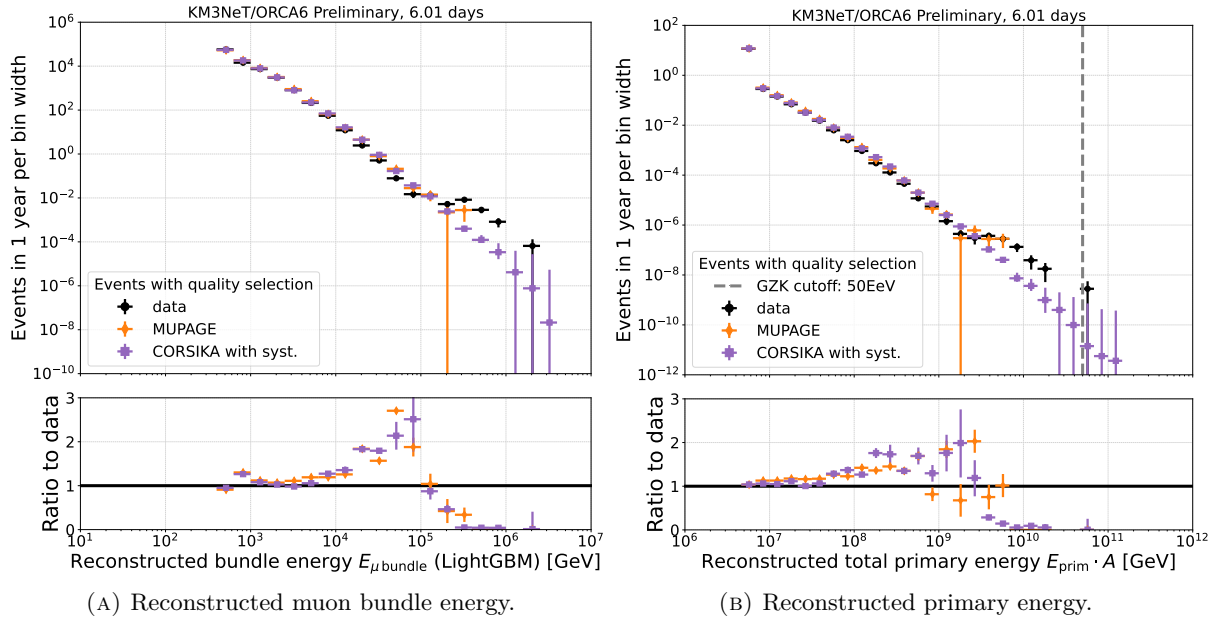


FIGURE 6.4.8.: ML-based energy reconstruction results the ORCA6 detector.

The excess of the data over the simulations observed for the energy reconstructions is present in the reconstructed multiplicity as well (Fig. 6.4.9). This is expected, as bundle energy and muon multiplicity are strongly correlated observables, especially at high energies: the value of Pearson correlation coefficient is around 0.7 for true and 0.9 for reconstructed variables. Despite the poor agreement above multiplicity 10, both MUPAGE and CORSIKA seem to be reproducing the experimental data quite well at low multiplicities, which could be owed to the dense instrumentation of ORCA.

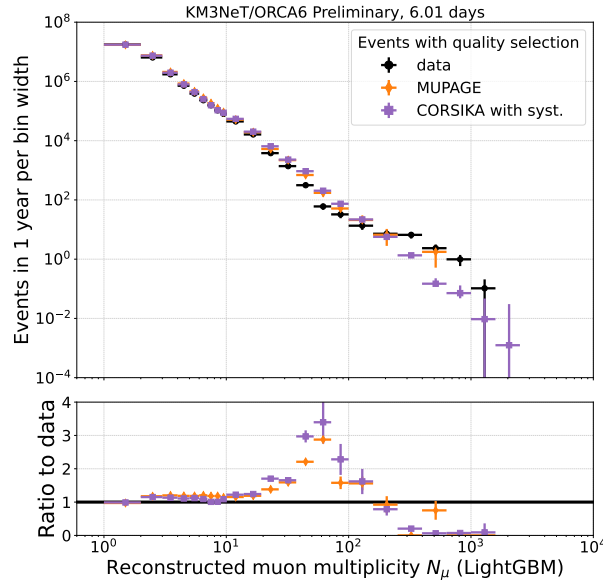


FIGURE 6.4.9.: ML-based multiplicity reconstruction result the ORCA6 detector.

6.5. Summary

A clear progress has been made in quality of the KM3NeT atmospheric muon simulations. Still, further improvements in the simulation software are necessary for a reliable measurement of the prompt muon flux (see Chap. 7) or to determine, whether the KM3NeT indeed observe the GZK cutoff [78]. It may be anticipated that by the time of completion of KM3NeT/ARCA and KM3NeT/ORCA construction, such measurements will be possible.

The underprediction of the high-energy muon rates by the Monte Carlo simulations is not unique to KM3NeT. It was seen by a number of experiments and a term ‘Muon Puzzle’ was coined for it [192]. One of the possible explanations for this can be a larger than currently predicted prompt muon flux (see Chap. 7). What is novel here is also the fact that the excess is also visible in muon multiplicity (admittedly, not a completely independent channel). The excess is more pronounced in the ORCA6 results as compared to ARCA6 mainly due to 6 times larger lifetime. There are also the factors of shallower depth at which ORCA is located (additional boost of collected statistics) and its smaller size, which allows to collect less data in the same time, however their impact is not as large.

The measurement of the all-nuclei primary CR flux was demonstrated to be possible, even with intermediate configurations of the KM3NeT detectors. The total primary energy reconstruction has yielded sensible results, although burdened with large, partially irreducible, inaccuracy related to the information loss as the shower propagates and loses energy.

7. Sensitivity of KM3NeT detectors to the prompt muon flux

This chapter presents the study investigating the potential of KM3NeT detectors to observe the **prompt** muon flux. The general scheme of the analysis is presented in Fig. 7.0.1. The analysis starts with definitions of the hypotheses and how they should be tested. Consequently, signal **SIG** and background **BGD** are defined, based on studying the properties of available CORSIKA MC simulation. Afterwards, distributions of reconstructed observables, split into containing either pure **BGD** or **BGD** with **SIG** are investigated. By computing the test statistic from them, a set of cuts that will maximize the sensitivity is procured (defining the so-called ‘critical region’). Next, expected significances as function of the data taking time and **prompt** flux normalisation are computed using the selected region. After inserting the experimental data, the **prompt** muon rate fit or a limit on this rate is obtained.

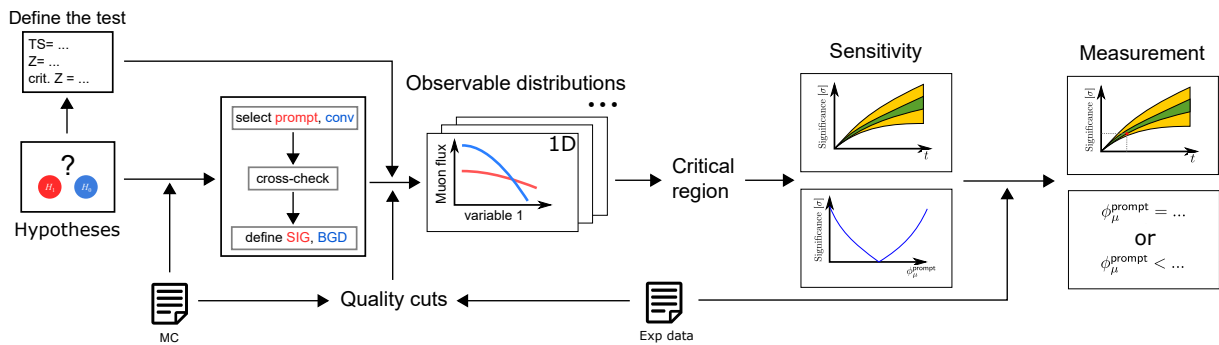


FIGURE 7.0.1.: The outline of the analysis.

The hypotheses of this analysis were:

- null hypothesis H_0 : the atmospheric muon flux consists solely of **conventional** muons.
- alternate hypothesis H_1 : the atmospheric muon flux is a combination of **prompt** and **conventional** contributions.

The following study evaluated the capability of KM3NeT/ARCA and KM3NeT/ORCA to reject H_0 by performing a significance test. The discovery level of significance was set at $Z_{\text{discovery}} = 5\sigma$. The exact formulation of the test may be found in Sec. 7.4, after the MC-based definitions of signal **SIG** and background **BGD**. The sensitivity results in this chapter were derived for ARCA115 and ORCA115 (complete building blocks) and ARCA6 and ORCA6 (already available data, see Tab. 5.2.1). Since the agreement between the ARCA6 and ORCA6 data and simulations in Chap. 6 was not yet sufficient to claim good description of the non-sensitive region, no measurement was performed.

7.1. Separation of conventional and prompt muons

As pointed out in Sec. 2.4, **conventional** and **prompt** are two distinct muon categories with their characteristic properties. These differences can be utilized to separate the two contributions to the atmospheric muon flux in the CORSIKA MC. In practice, one can either look at the parent particles or at where in the shower the muon was produced. Here, the first is used for the definition and the latter helps to gain a better understanding of the sample and to cross-validate the results (see Sec. 7.2).

7.1.1. Parent particles

Each secondary particle in CORSIKA has two parent particles assigned: a mother and a grandmother. This is the case regardless of the actual number of parent particles of the muon. It is possible to distinguish between the **conventional** and **prompt** muons by setting a threshold on lifetimes of the parent particles. In the case of this analysis, the lifetime of K_S^0 was selected as a reference point. Every parent particle, which decays on average faster than K_S^0 is declared **prompt** (see Sec. A.6.2), following the approach in [105]. The simulated contributions of muons with particular parent particles are shown in Fig. 7.1.1. As expected, the muon rates are dominated by **conventional** muons produced by π^\pm and K^\pm mothers (see Sec. 2.4). It has to be stressed that even if a grandmother particle is short-lived (**prompt**), it can still lead to a production of a **conventional** muon, if the mother particle is **conventional** or if there are other interactions in between. To keep track of the latter, CORSIKA introduces interaction counters (see Sec. 7.1.2).

By further inspection of Fig. 7.1.1b, it is not uncommon that a nucleus is saved as the grandmother particle. This may happen in two cases:

1. When there is no other parent particle between the primary and the mother particle of the muon. This implies that either the primary nucleus will be saved as the grandmother particle, or the muon will be saved as its own mother particle, if it underwent scattering on its way (see Fig. 7.1.1a).
2. If the incident nucleus (or an air particle) is fragmented and a new nucleus is formed (in the dedicated CORSIKA simulation produced for this analysis, only p , He , C , O and Fe nuclei are used as primaries, see Sec. 4.1.1.2 and Tab. A.1.2).

In the second scenario, the new nucleus may produce a particle cascade, leading to the production of a muon. However, production of such intermediate nuclei implies that only a fraction of the original primary energy is available, meaning that the produced muons may have worse chance to reach the detector.

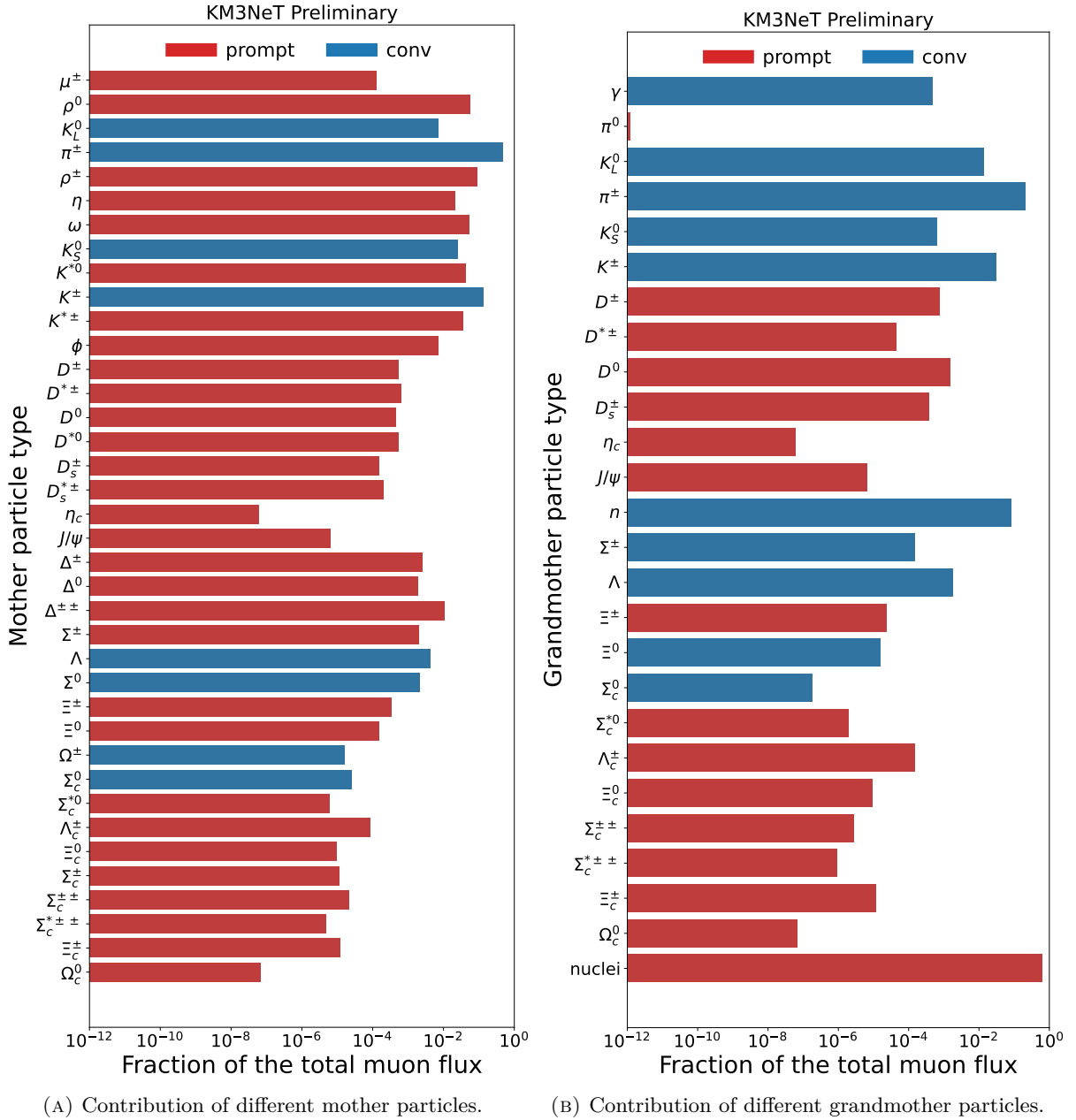


FIGURE 7.1.1.: Contributions of different parent particles in the CORSIKA simulation at sea level. The particles and anti-particles were counted together. The parent particles that may potentially result in a **prompt** muon are coloured red and the ones that will only produce **conventional** muons are coloured blue.

7.1.2. Parent particle generations

A muon may have more than just two parent particles, however only the two most recent ones are stored in the CORSIKA7 output. In the case of EeV showers, the average number of muon parents is ~ 8 and can be even 15 [193]. Saving all of them could be highly inefficient, given that a single EeV primary CR may often produce thousands of muons. Not to mention that the number of secondaries from EM cascades, simulated by CORSIKA as well is even larger (by several orders of

magnitude). This is the main motivation for the introduction of interaction counters in CORSIKA. From the point of view of this analysis, the relevant ones are:

- hadronic interaction counter h , encoding the number of hadronic interactions and/or decays,
- electromagnetic (EM) interaction counter e , summarizing the number of e^\pm interactions (including emission of low- E particles),

where the only desired value of the latter is 0 (see Tab. 7.1.1 and Sec. A.6.3). The CORSIKA output stores EM and hadronic interaction counters of the muon (e_μ, h_μ) and its mother particle ($e_{\text{mother}}, h_{\text{mother}}$). More details on the CORSIKA counters can be found in [5]. The hadronic interaction counter h is typically incremented by 1 after each interaction or decay, however there are exceptions to this rule [5, 194]. The incrementation scheme is presented below, with the channels that contribute to the **prompt** muon flux marked with ■:

- +0:
 - $\Delta \rightarrow p + \pi$
 - $\Delta \rightarrow n + \pi$
 - $K^* \rightarrow K + \pi$
 - $\rho^0 \rightarrow \pi^+ + \pi^-$
 - $\rho^\pm \rightarrow \pi^\pm + \pi^0$ ■ (through π^0)
 - $\omega \rightarrow \pi^+ + \pi^- (+\pi^0)$ ■ (through π^0)
 - $\omega \rightarrow \pi^0 + \gamma$ ■ (through π^0)
 - other short-lived resonances ■
- +1:
 - hadron + air \rightarrow hadron + X ■
 - γ + air \rightarrow hadron + X
 - γ + air $\rightarrow \rho^0$ (+ recoil nucleus)
 - γ + air $\rightarrow \omega$ (+ recoil nucleus)
 - γ (+ air) $\rightarrow \mu^+ \mu^-$
 - all hadronic decays except π^\pm :
 - * π^0, η ■
 - * K^\pm, K_S^0, K_L^0
 - * all strange baryons ■
 - * all charmed hadrons ■
 - π^\pm if its hadronic interaction counter $h_{\pi^\pm} \geq 49$
- +31: (but clipped at 99)
 - $D \rightarrow \mu + X$ ■
 - other charmed mesons ■
- +51:
 - $\pi^\pm \rightarrow \mu^\pm + \nu_\mu$ (if $h_{\pi^\pm} < 49$, otherwise +1)

- +500:
 - μ pair production
 - photonuclear interaction in μ history

7.1.3. Definition of a prompt muon

The definition of what would be considered a **prompt** muon in the CORSIKA simulation was constructed with the intent to retain as much control over the particle history as possible. For this reason, the muons with more than two parent particles were excluded, making use of the hadronic and electromagnetic generation counters (see Sec. 7.1.2). The criteria for a muon to be considered **prompt** are summarized in Tab. 7.1.1. Every muon, which does not meet those, is by construction declared **conventional**. The muons with **prompt** grandmother and muon mother were rejected, motivated by the fact that in the MC they are produced only far away from the shower start (see Fig. A.6.4).

TABLE 7.1.1.: Parent particle and generation counter combinations for **prompt** muons.

Grandmother	Mother	h_{mother}	h_{μ}	EM counters (e_{μ} and e_{mother})
primary	muon	1	1	0
primary	prompt	≤ 2	≤ 2	
prompt	prompt	2	32	
		3	33	

7.2. Control plots for the selection

To ensure that the selection of **conventional** and **prompt** muons proposed in Tab. 7.1.1 is reasonable, a number of sanity checks were performed. They are discussed in this section.

7.2.1. Muon arrival time

The time distribution could potentially reveal a distinct feature coming from the **prompt** contribution. If so, it would allow for an event-by-event detection of the showers containing **prompt** muons. However, after inspecting a number of events, examples of which are shown in Fig. 7.2.1, it became clear that it is not feasible. **Prompt** muons are typically not really the leading muons in the bundle, understood as being the first to arrive. They arrive at around the same time as most of the **conventional** ones do. In some cases there are a few muons arriving earlier than the rest, but they are **conventional**. This can be understood by considering the fact that muons, which are produced early on, but e.g. in decays of π^{\pm} or K^{\pm} , are still considered **conventional**. The lifetime of a particle is only the average time after which the particle is expected to decay. The low probability of a sooner decay can be compensated by the huge amount of produced **conventional** muons, exceeding the numbers of **prompt** muons by orders of magnitude.

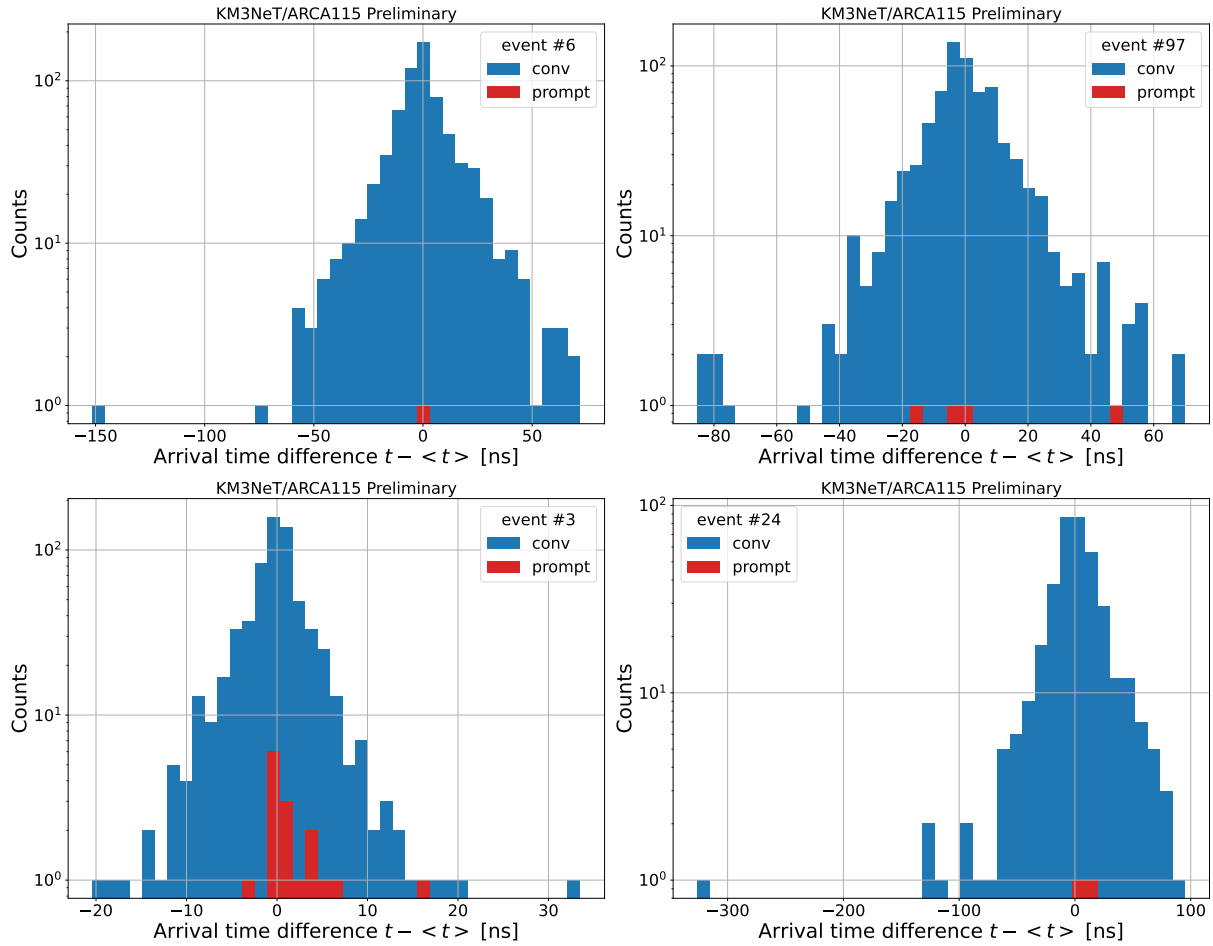


FIGURE 7.2.1.: Distributions of the arrival time difference, where for each muon the average arrival time is subtracted. The arrival time is defined as the time since the first interaction of the primary to the arrival of a muon at the ARCA115 can. In the top row there are two examples of events started by proton primaries and the showers shown in the bottom row were caused by iron primaries. Each plot is an unweighted histogram of a single muon bundle event at the can level. The events from the EeV sub-production were intentionally picked here, to increase the chance of observing **prompt** muons.

A cross-check of the range of observed values can be done by estimating the time it takes a muon, travelling at nearly the speed of light in vacuum c , to reach the detector. The minimal and maximal observed first interaction heights are ~ 3 km and ~ 500 km (see Fig. A.1.2) above the sea level. From the sea surface, there are ~ 2 km or ~ 3 km left to the ORCA and ARCA detector respectively. By dividing those distances by c , one arrives at travel time estimates in the range 0.01-2 ms. The absolute values of the arrival times used to compute the time differences in Fig. 7.2.1 were between 0.39 and 2.38 ms, which is in good agreement with the estimated time.

7.2.2. Muon energy share

Since **prompt** muons are expected to have systematically higher energies, it means that they should typically take up a bigger portion of the initial available energy (E_{prim}). This was tested and the outcome is shown in Fig. 7.2.2. As one may see, even though the **prompt** curve does not exceed

the [conventional](#) one, it does indeed have a flatter slope towards higher energy fractions. The multi-peak structure of the distribution is a result of superposition of contributions from different primary nuclei, with the biggest energy share belonging to hydrogen (proton) primaries.

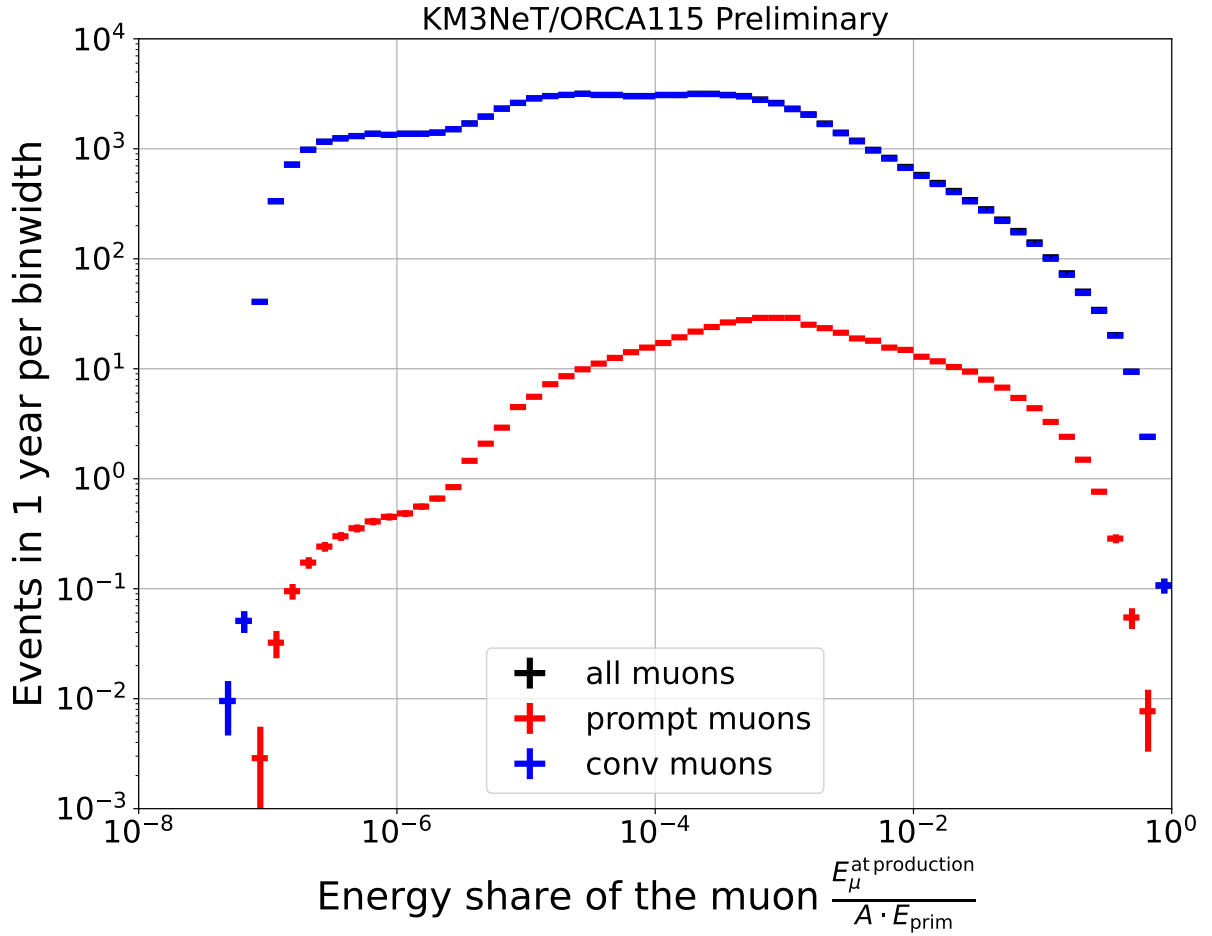


FIGURE 7.2.2.: Distribution of the fraction of the original total primary energy held by the muon when it was created. A is the atomic mass number (the number of nucleons) and E_{prim} is the primary energy per nucleon. The plot was produced for muons reaching the ORCA115 detector. The error bands were computed using Eq. [A.2.1](#) and marked with shaded rectangles (mostly very small, but there is e.g. a larger one on the left edge of the [conv](#) distribution).

7.2.3. Muon production point

The average distance travelled by the parent particle before decaying $\langle d \rangle$ may be estimated knowing the particle type and its energy. The basic formula is:

$$\langle d \rangle = v \cdot \tau, \quad (7.2.1)$$

where v is the particle's velocity and τ – its lifetime in the lab reference frame. Since EAS produce highly energetic particles, travelling at speeds close to the speed of light in vacuum, the time dilation effect has to be taken into account:

$$\tau = \gamma\tau_0, \quad (7.2.2)$$

where $\gamma = \frac{1}{\sqrt{1-(\frac{v}{c})^2}} = \frac{E}{m_0c^2}$, m_0 is the rest mass, and τ_0 is the lifetime in the rest frame. Inserting into Eq. 7.2.1 and rearranging gives the final formula:

$$\langle d \rangle = \frac{\sqrt{E^2 - m_0^2c^4}}{m_0c^2} \cdot c\tau_0. \quad (7.2.3)$$

In Tab. 7.2.1, a few examples were calculated to get a feeling for the possible range of values. As one may note, they are spread over many orders of magnitude.

TABLE 7.2.1.: Examples of average distances travelled by 4 different parent particles before decaying. The energies are roughly the lower and upper bound for what can be expected. The particles with $E < 10^3$ GeV will seldom produce a μ that can reach the detector and particles with $E > 10^8$ GeV are produced extremely rarely.

	E [GeV]	m_0 [$\frac{\text{MeV}}{c^2}$]	τ_0 [s]	$\langle d \rangle$ [m]
π^\pm	10^3	139.57	$2.60 \cdot 10^{-8}$	$5.58 \cdot 10^4$
	10^8			$2.15 \cdot 10^9$
D_s^+	10^3	1968.34	$5.04 \cdot 10^{-13}$	0.08
	10^8			$7.60 \cdot 10^3$
η_c	10^3	2983.90	$2.06 \cdot 10^{-23}$	$2.07 \cdot 10^{-12}$
	10^8			$2.07 \cdot 10^{-7}$
K_S^0	10^3	497.61	$8.95 \cdot 10^{-11}$	53.92
	10^8			$5.39 \cdot 10^6$

The distributions of the distance between the first interaction of the primary and the creation of the muon $d_{\mu \text{ prod}}$ are depicted in Fig. 7.2.3. Even though the **prompt** muons do not necessarily arrive in the detectors first (see Sec. 7.2.1), they are less likely to be produced far from the first interaction of the primary nucleus. This is a consequence of defining the **prompt** muons as the ones created in decays of parent particles with particularly short lifetimes (see Sec. 7.1). The upper limit of $d_{\mu \text{ prod}} \approx 300$ km is below the expected maximal distances for π^\pm and K_S^0 from Tab. 7.2.1. However, it is fully consistent both with Fig. A.1.2 and with the bounds of the simulation geometry: for maximally horizontal showers (at 87° from the zenith in the CORSIKA simulation used in this work), the distance could be at most 2155.31 km. Even if not for this limitation, Tab. 7.2.1 gives only rough estimates, not taking into account energy losses and deflection of the trajectory during particle propagation.

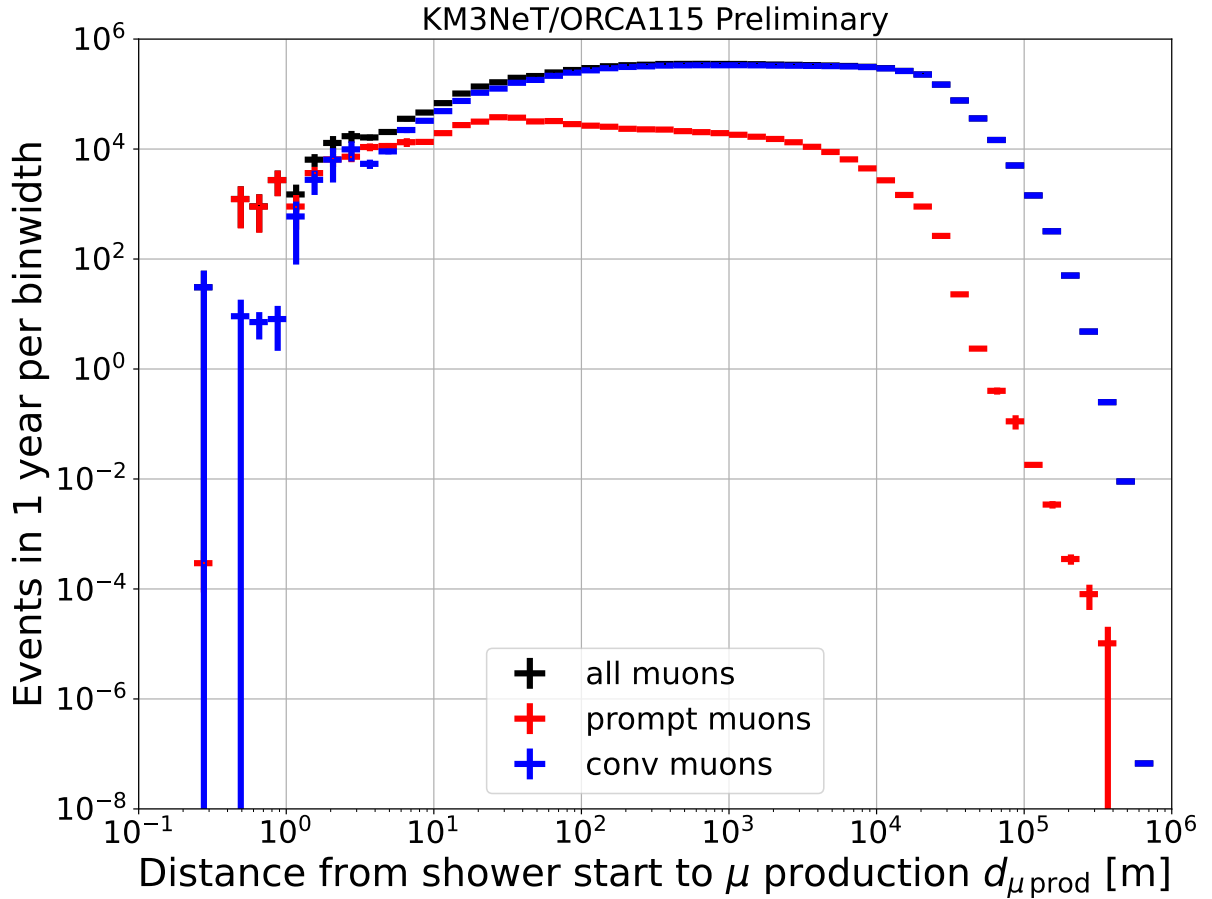


FIGURE 7.2.3.: Distributions of distance from the first interaction point of a primary to the point at which a muon was created $d_{\mu\text{prod}}$. The plot was produced for muons at sea level, which were part of showers reaching the ORCA115 detector. This means that muons stopping before reaching ORCA115 were included. The error bars were computed using Eq. A.2.1.

In Sec. A.6.3, a complete set of $d_{\mu\text{prod}}$ plots, cross-checking the **prompt** muon definition in Tab. 7.1.1 may be found.

7.3. Definition of signal and background

Up to this point, a distinction was made between **prompt** and **conventional** muons. However, as was very clearly demonstrated in Chap. 5 and 6, the observed events consist only partially of single muons. Therefore, the signal and background in this analysis must be defined in terms of entire showers, not individual muons. Consequently, three categories of events (showers observed at the detectors) were introduced:

- **TOTAL** – all showers,
- **SIG** – showers with at least 1 **prompt** muon (not directly used for the hypothesis test),
- **BGD** – showers with 0 **prompt** muons (100% **conventional**).

Since **prompt** and **conventional** components were simulated together in CORSIKA MC, they share a common phase-space. When selecting shower for **BGD**, a part of the simulated muon rate is

discarded. To compensate for this, **BGD** had to be reweighted (for **TOTAL** it was not necessary). The motivation for this was that for the null hypothesis H_0 , **BGD** constitutes the entirety of the muon flux and the MC prediction should be adapted accordingly. The details of reweighting are discussed in the following subsection.

7.3.1. Reweighting of background

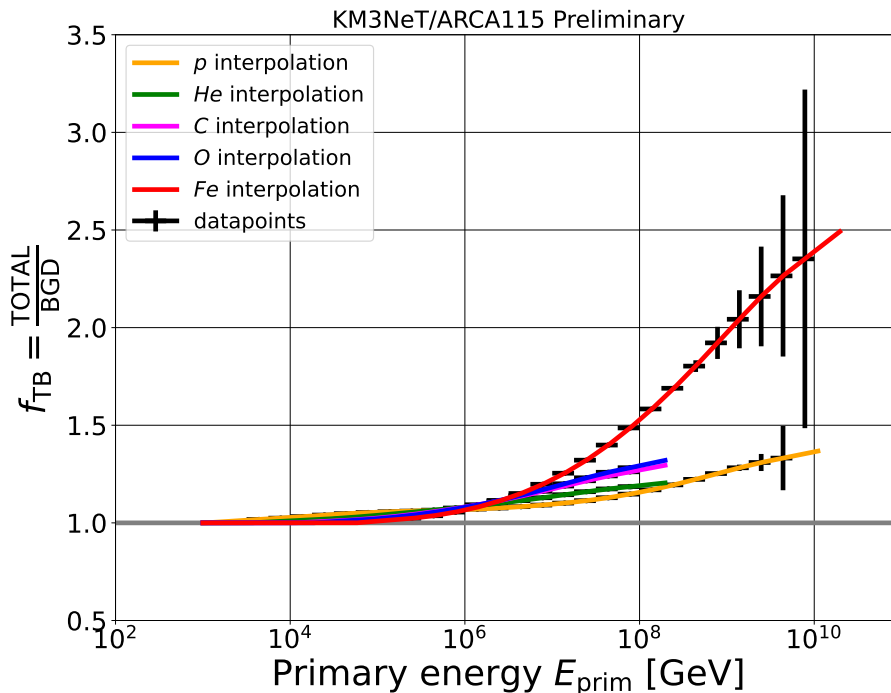


FIGURE 7.3.1.: Interpolated fraction of all generated events to the number of **BGD** events as a function of the primary type and energy. The values were computed for ARCA115 at reconstruction level.

The **SIG** events were discarded and thus, not all generated showers were used, which had to be reflected in the weights. In principle, the goal was to obtain such a distribution of **BGD**, as if it was simulated alone. The number of discarded events (‘taken away’ by **SIG**) is a function of the primary type and energy E_{prim} , as are the event weights themselves. A ratio between the number of events falling into the **TOTAL** category divided by the number of **BGD** events $f_{\text{TB}}(\text{prim}, E_{\text{prim}})$ is plotted in Fig. 7.3.1. The final weight for **BGD** was computed as:

$$w_{\text{BGD}} = w_{\text{event}}(\text{prim}, E_{\text{prim}}) \cdot f_{\text{TB}}(\text{prim}, E_{\text{prim}}), \quad (7.3.1)$$

where $w_{\text{event}}(\text{prim}, E_{\text{prim}})$ are the event weights (see Eq. 4.2.3) that would be used for **TOTAL**. The f_{TB} in Fig. 7.3.1 was evaluated from unweighted **TOTAL** and **BGD** distributions at reconstruction level under assumption that the ratio does not change significantly from the generation level (which is not directly accessible). An ideal solution would be a separate MC simulation without the **prompt** contribution, however it was not possible with CORSIKA v7.7410 for technical reasons. For every detector configuration, a common f_{TB} evaluated using the ARCA115 dataset was used, as it had

the smallest uncertainty on the values at high energies. It was verified that the f_{TB} interpolations obtained using the other datasets produce consistent results.

7.4. Significance test

The test of the background-only hypothesis H_0 (defined in the beginning of this chapter) performed in this analysis followed the procedure proposed in [195, 196, 197, 198]. It was based on the profile likelihood ratio for Poisson-distributed measurements. The assumption that the measurements followed Poisson statistics was justified, since the measured quantity was the number of observed muon bundles, which is an example of a counting experiment. The function q_0 , used to maximize the power of the null hypothesis test of an analysis, is often referred to as the test statistic (TS). The TS used in this analysis was:

$$q_0 = \begin{cases} 2 \cdot \left[N_{\text{TOTAL}} \cdot \ln \left(\frac{N_{\text{TOTAL}} \cdot (N_{\text{BGD}} + \sigma_{\text{BGD}}^2)}{N_{\text{BGD}}^2 + N_{\text{TOTAL}} \cdot \sigma_{\text{BGD}}^2} \right) - \frac{N_{\text{TOTAL}}^2}{\sigma_{\text{BGD}}^2} \cdot \ln \left(1 + \frac{\sigma_{\text{BGD}}^2 (N_{\text{TOTAL}} - N_{\text{BGD}})}{N_{\text{BGD}} \cdot (N_{\text{BGD}} + \sigma_{\text{BGD}}^2)} \right) \right] & \text{for } N_{\text{TOTAL}} \geq N_{\text{BGD}} \\ 0 & \text{for } N_{\text{TOTAL}} < N_{\text{BGD}} \end{cases}, \quad (7.4.1)$$

where N_{TOTAL} and N_{BGD} are the expected numbers of TOTAL and BGD events respectively and σ_{BGD} is the uncertainty on BGD. In the case of a measurement on experimental data, N_{TOTAL} is equal to the number of measured events. In the sensitivity study, the CORSIKA MC was used as the Asimov dataset [198]. The value of σ_{BGD} was computed in quadrature from the statistical and systematic uncertainty:

$$\sigma_{\text{BGD}} = \sqrt{(\sigma_{\text{BGD}}^{\text{stat}})^2 + (\sigma_{\text{BGD}}^{\text{syst}})^2}. \quad (7.4.2)$$

The systematic uncertainty $\sigma_{\text{BGD}}^{\text{syst}}$ was evaluated using the method described in Sec. 6.2, i.e. it included the uncertainty due to different HE hadronic interaction models, CR flux models, seasonal variations of the atmosphere, PMT efficiency, and light absorption in seawater. Since the histograms were weighted, the error $\sigma_{\text{BGD}}^{\text{stat}}$ is not a square root of N_{BGD} (see Sec. A.2.1). The derivation of Eq. 7.4.1 may be found in [195, 196]. Following those references, the median significance may be found by using the asymptotic approximation (Wilks' theorem [199]):

$$Z = \sqrt{q_0}. \quad (7.4.3)$$

7.4.1. Scaling with time and prompt normalisation

The TS was always computed for a certain time period and **prompt** muon flux normalisation $\phi_{\text{prompt } \mu}$. The event rates themselves were treated as constant in time (averaged over seasonal variations), which was a necessary approximation when using very computationally intensive CORSIKA simulations. The yearly variations were neglected (see Sec. A.1.2). These simplifying assumptions allowed to scale q_0 obtained from the MC. Based on Sec. A.2.1, the values of each bin and their errors could be scaled with time t as follows:

$$N(t) = \left(\frac{t}{t_{\text{nom}}}\right) \cdot \sum_i w_i = \left(\frac{t}{t_{\text{nom}}}\right) \cdot N(t_{\text{nom}})$$

$$\Delta N(t) = \sqrt{\left(\frac{t}{t_{\text{nom}}}\right) \sum_i w_i^2} = \sqrt{\frac{t}{t_{\text{nom}}}} \cdot \Delta N(t_{\text{nom}}),$$

where $t_{\text{nom}} = 1$ year is the nominal time. This, after inserting into Eq. 7.4.1, leads to:

$$q_0(t) = \left(\frac{t}{t_{\text{nom}}}\right) \cdot q_0(t_{\text{nom}}). \quad (7.4.4)$$

Scaling by the **prompt** muon flux normalisation is effectively a scaling of **SIG** and thus only affects **TOTAL**, not **BGD**:

$$N_{\text{SIG}}(\phi_{\text{prompt } \mu}) = \left(\frac{\phi_{\text{prompt } \mu}}{\phi_{\text{prompt } \mu}^{\text{nom}}}\right) \cdot \sum_i w_i = \left(\frac{\phi_{\text{prompt } \mu}}{\phi_{\text{prompt } \mu}^{\text{nom}}}\right) \cdot N_{\text{SIG}}(\phi_{\text{prompt } \mu}^{\text{nom}}),$$

where $\phi_{\text{prompt } \mu}^{\text{nom}}$ is the nominal **prompt** muon flux normalisation and is equal to the flux predicted by the CORSIKA MC. This time, Eq. 7.4.1 did not simplify to a compact formula as for the time scaling. One can see it by substituting $N_{\text{TOTAL}} = N_{\text{SIG}} + N_{\text{BGD}}$ in the case of $N_{\text{TOTAL}} \geq N_{\text{BGD}}$:

$$q_0 = 2 \cdot \left[(N_{\text{SIG}} + N_{\text{BGD}}) \cdot \ln \left(\frac{(N_{\text{SIG}} + N_{\text{BGD}}) \cdot (N_{\text{BGD}} + \sigma_{\text{BGD}}^2)}{N_{\text{BGD}}^2 + (N_{\text{SIG}} + N_{\text{BGD}}) \cdot \sigma_{\text{BGD}}^2} \right) - \frac{(N_{\text{SIG}} + N_{\text{BGD}})^2}{\sigma_{\text{BGD}}^2} \cdot \ln \left(1 + \frac{\sigma_{\text{BGD}}^2 \cdot N_{\text{SIG}}}{N_{\text{BGD}} \cdot (N_{\text{BGD}} + \sigma_{\text{BGD}}^2)} \right) \right].$$

There is no possibility for the flux scaling factors to cancel out, since only N_{SIG} undergoes scaling. Nevertheless, this posed merely an inconvenience, not a real technical problem for the computation.

7.5. Selection of the critical region

The critical region is a part of the considered phase-space, in which the sensitivity of the hypothesis test is the greatest. This section demonstrates the procedure for choosing the optimal critical region.

To perform the same selection on the MC simulation and on experimental data, it was necessary to restrict to the observables reconstructed in the detector. The considered phase-space was 3-dimensional: zenith, energy, and multiplicity. The distributions of each of the variables, together with corresponding TS values for each bin are plotted in Fig. 7.5.1, 7.5.2, and 7.5.3. In those figures, only events meeting the quality criteria outlined in Sec. 6.3 were included. Following the convention from Chap. 5, only the plots for ARCA115 are shown. The zenith distribution has been rejected as not particularly useful, due to negligible difference between **TOTAL** and **BGD**, resulting TS values consistent with zero in every bin (see bottom panel of Fig. 7.5.1).

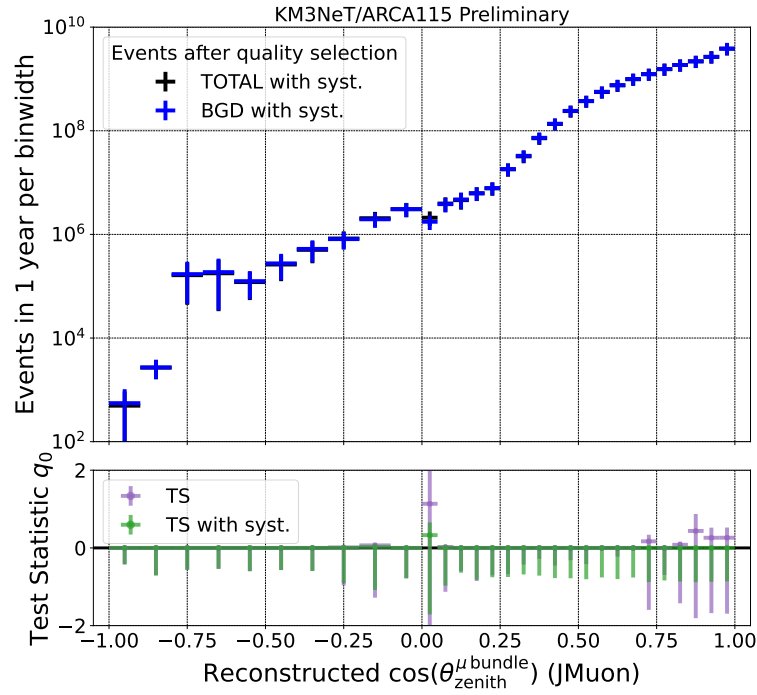


FIGURE 7.5.1.: Distributions of reconstructed zenith for ARCA115 events passing the quality selection from Sec. 6.3. The TS values were computed according to Eq. 7.4.1 for each bin. The histograms and TS values are shown computed with and without the systematic uncertainties.

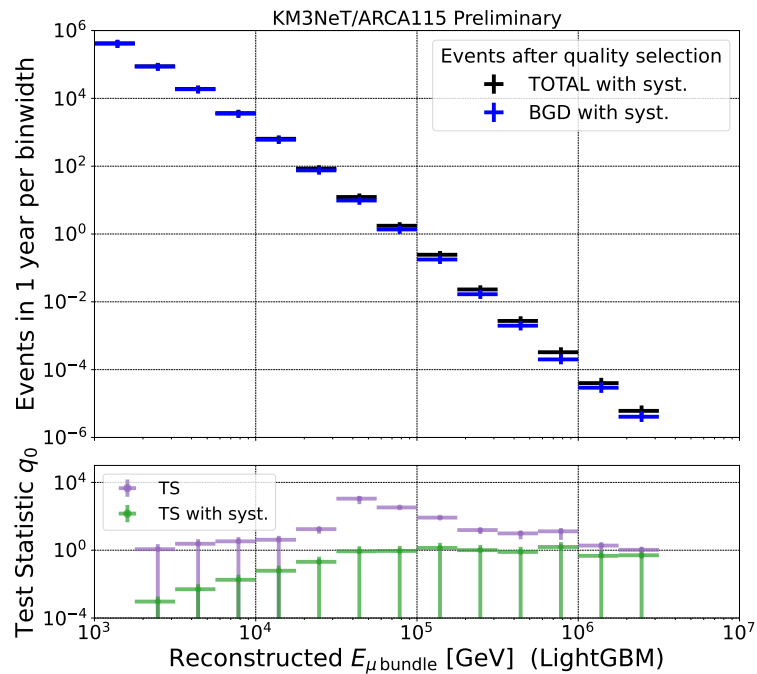


FIGURE 7.5.2.: Distributions of reconstructed muon bundle energy for ARCA115 events passing the quality selection from Sec. 6.3. The TS values were computed according to Eq. 7.4.1 for each bin. The histograms and TS values are shown computed with and without the systematic uncertainties.

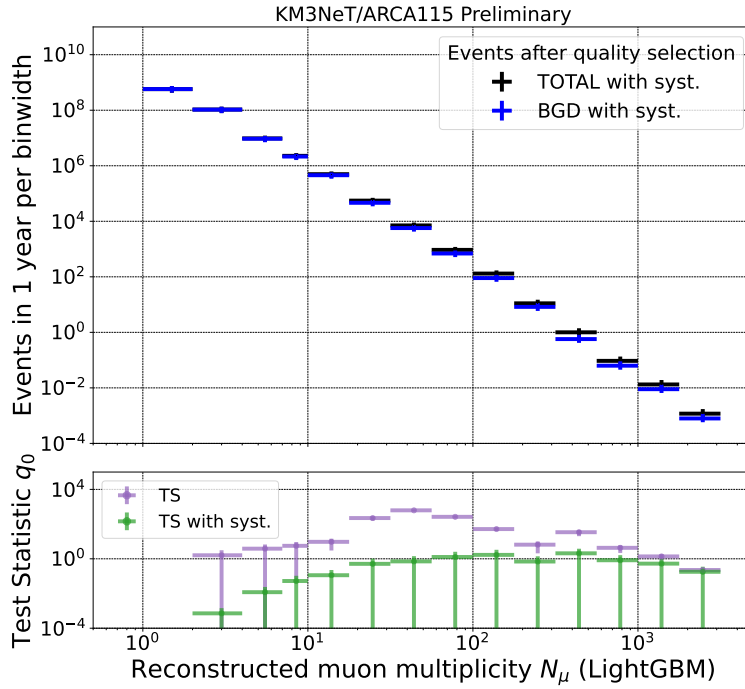


FIGURE 7.5.3.: Distributions of reconstructed multiplicity for ARCA115 events passing the quality selection from Sec. 6.3. The TS values were computed according to Eq. 7.4.1 for each bin. The histograms and TS values are shown computed with and without the systematic uncertainties.

The plots in Fig. 7.5.1, 7.5.2, and 7.5.3 already roughly indicate, what could be a reasonable critical region. However, a more direct optimization approach has been adopted to determine its boundary. A range of minimum reconstructed bundle energy $E_{\text{bundle}}^{\text{min}}$ and minimum reconstructed muon multiplicity N_μ^{min} values has been scanned, investigating the impact on the resulting significance. Such scans for ARCA115 and ORCA115 are shown in Fig. 7.5.4, and for the remaining detector configurations (ARCA6 and ORCA6 respectively), the same values were used, as summarized in Tab. 7.5.1. Applying identical critical regions, regardless of the detector configuration, aimed at ensuring the comparability of results. No upper bounds on energy and multiplicity were set, as it was found that they do not boost the power of the hypothesis test. The difference between KM3NeT/ARCA and KM3NeT/ORCA in Tab. 7.5.1 is compliant with the expectations coming from the detector geometries. ARCA as the larger detector, dedicated to study of higher energies, requires a higher value of $E_{\text{bundle}}^{\text{min}}$, whereas the more densely instrumented ORCA is sensitive to lower energies. ORCA is located shallower than ARCA and hence observes events with systematically larger multiplicities (see Fig. 5.4.9), which is reflected in the larger value of N_μ^{min} .

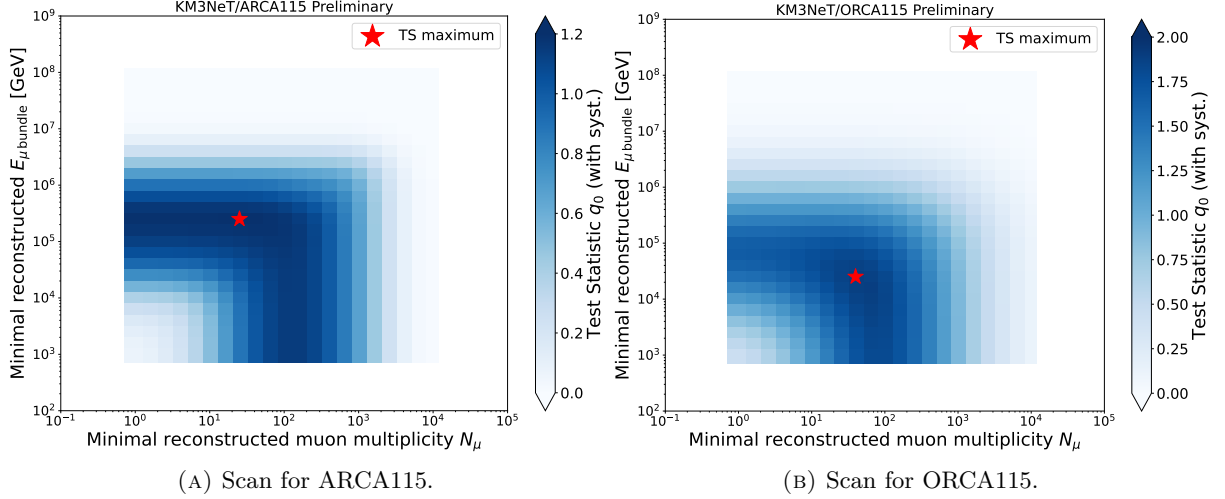


FIGURE 7.5.4.: Scans over minimal energy and multiplicity, identifying the optimal selection of the critical region. The significance computed with the systematic uncertainties was maximized and the maximum is denoted with the red star. The obtained data was smoothed by convolving it with a Gaussian kernel to minimize the impact of statistical fluctuations on the selection of the critical region.

TABLE 7.5.1.: Lower bounds of the critical regions for each of the considered detector configurations.

Detector	$E_{\text{bundle}}^{\text{min}}$	N_{μ}^{min}
ARCA115	251 TeV	25
ARCA6	251 TeV	25
ORCA115	25 TeV	40
ORCA6	25 TeV	40

A potential refinement of the analysis presented in this chapter could be a non-rectangular critical region, introduced either by specifying a two-dimensional function of E_{bundle} and N_{μ} or by computing the TS on a grid of very fine bins. Both approaches could lead to a boost of the power of the test, however they bear a risk of producing over-tuned results, especially with overly dense binning. For this reason, a robust single-bin method was used here. A further alternative would be direct classification of events as **SIG** and **BGD**. This has been attempted, however the developed classifier strongly underestimated **BGD**, which could compromise the entire analysis. For this reason, such an approach was disqualified.

7.6. Sensitivity results

In this section, the final results of the analysis are presented. Sensitivity to exclude the null hypothesis H_0 was expressed in terms of expected median significance, computed from the TS using Eq. 7.4.3. The sensitivities of ARCA115, ARCA6, ORCA115, and ORCA6 detectors are shown in Fig. 7.6.1. Naturally, the complete building blocks are more sensitive, since they collect more data and can reconstruct the events with better precision. A comparison of the results of this analysis

against the results obtained by IceCube using data from approximately 2 years of operation was included as well [200]. However, it has to be taken with a grain of salt, given the vast differences in the analysis methods and in the experimental setups, to name a few:

1. The definition of the **prompt** component:
 - a) IceCube (IC) analysis: **prompt** flux prediction obtained by reweighting the CORSIKA MC, assuming it to be purely **conventional** (which is a crude approximation). The reweighting followed the, somewhat outdated, ERS model [201].
 - b) This analysis: direct **prompt** muon flux prediction from CORSIKA.
2. The HE hadronic interaction model:
 - a) IC analysis: SIBYLL 2.1.
 - b) This analysis: SIBYLL 2.3d.
3. Observables used:
 - a) IC analysis: reconstructed energy and direction of the most energetic muon in the bundle.
 - b) This analysis: reconstructed muon bundle energy and reconstructed number of visible muons.
4. IceCube is located shallower than ARCA and ORCA, which means that it measures a larger muon flux, than the KM3NeT detectors.
5. The DOM and string (equivalent of a DU in KM3NeT) spacing in IceCube is different than in KM3NeT.
6. The total photo-cathode areas of the PMTs for IceCube is roughly 261 m^2 , while for one KM3NeT building block it is 292.5 m^2 .
7. IceCube did not consider the CR flux models as a source of the systematic uncertainty. Instead, they have provided separate significance values for the assumptions of different models – this is what the error bars in Fig. 7.6.1a were derived from.

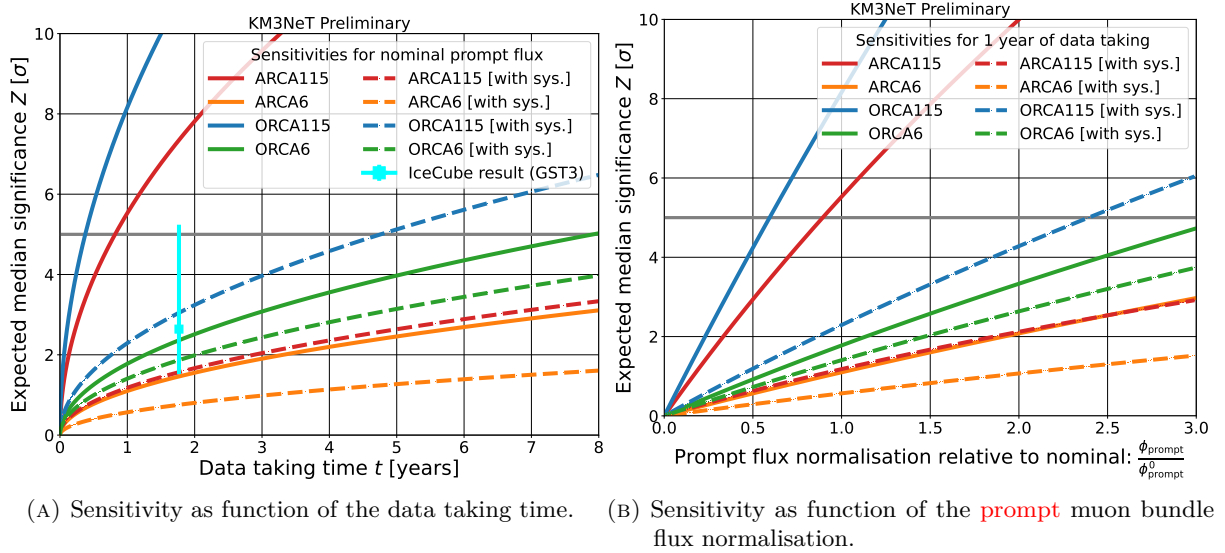


FIGURE 7.6.1.: Sensitivities of different detector configurations to the **prompt** muon bundle signal (as defined in Sec. 7.3). The solid lines were computed only with the statistical uncertainty and the dashed ones: with the total uncertainty, including the systematics from Sec. 6.2. The IceCube result was taken from [200] and was obtained for the GST3 CR flux model and livetime of 645.4 d, while the error bar shows the variation for different CR flux models.

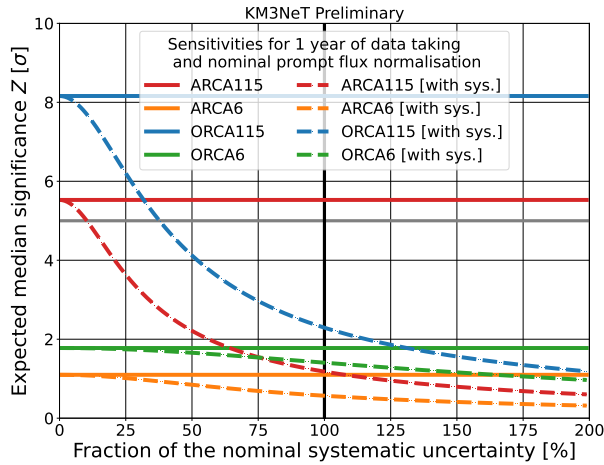


FIGURE 7.6.2.: Sensitivities of different detector configurations to the **prompt** muon bundle signal (as defined in Sec. 7.3). The solid lines were computed only with the statistical uncertainty and the dashed ones: with the total uncertainty, including the systematics from Sec. 6.2. The systematic uncertainty was then varied as function of the fraction of the nominal value.

The predictions of Fig. 7.6.1 look rather optimistic for KM3NeT, despite the evident strong limitation by systematic uncertainties. It is expected that by the time of completion of ARCA and ORCA the uncertainties related to the HE hadronic interactions will be reduced, thanks to advances in theoretical models [202, 203, 204]. The scale of improvement is hard to predict and will largely depend on the availability of complementary measurements. The most anticipated data are the oxygen runs at LHC [205, 206, 207]. Accumulation of new data from experiments measuring

the cosmic rays directly might shrink the uncertainty related to the CR flux modelling as well [208, 209]. In fact, already the incorporation of the currently available experimental data into newer models should provide a significant improvement in this regard. Upon inspection of Fig. 7.6.1a, even in the worst case: with unchanged uncertainties, KM3NeT/ORCA should be able to exclude the BGD-only scenario at 5σ in about 5 years. As demonstrated in Fig. 7.6.2, the same may be achieved in just 1 year if the systematic uncertainty can be shrunk to 37% of the current level.

The most crucial systematic uncertainties for this analysis are the ones related to: CR flux models, PMT efficiencies, and light absorption length (see Sec. 6.2.6). The first relies on primary CR measurements by other experiments and corresponding theoretical advancements [75, 93, 210]. The current efforts focus on improving the understanding of the primary CR spectrum at the ankle (see Fig. 2.3.1) and beyond, which is highly relevant for this work. To make a rough prediction of the capability of the full KM3NeT detectors, let us assume that by the time of completion of ARCA and ORCA, the CR flux model uncertainty would be reduced by 50%. The uncertainties due to PMT efficiencies and light absorption length were evaluated by A. Romanov in [148] as function of the zenith angle, leading to constant value estimates in Sec. 6.2.6. The zenith distributions are dominated by the low-energy events, hence the same uncertainties in the energy range most relevant for this work may in fact be lower. To investigate this, an updated study with larger high-energy statistics would be needed. This is feasible, as the study can be done with MUPAGE, as was the original one. Let us suppose that the uncertainties would be at $\sim 70\%$ of the original values and that the resulting total uncertainty (together with the 50% reduction of the CR flux model uncertainty) would be $\sim 60\%$ of the nominal one. This would imply a discovery at 5σ in less than 2 years with ORCA115 and in about 6 years with ARCA115. For ORCA6 and ARCA6 the same could be achieved in approximately 10 and 51 years respectively, which clearly illustrates the benefit of having larger detector configurations. Such a long timescale is certainly not the fate of KM3NeT, since as of August 2023, the currently installed configurations are already ARCA19 and ORCA16.

One should note that the sensitivity for ARCA is indicated for 1 building block (ARCA115), yet the complete detector will consist of two such blocks, doubling the amount of collected data. From Eq. 7.4.3 and 7.4.4 it follows that the corresponding significance will be $\sqrt{2}$ times larger. Furthermore, the results of ARCA and ORCA may in principle be combined and the data collected with intermediate configurations of both detectors could be put to use as well. Producing such a result during the construction phase of KM3NeT will surely present an exciting technical challenge.

8. Conclusions

This chapter contains a brief summary of this thesis and some thoughts on possible improvements and extensions.

8.1. Summary

The work of this thesis revolved around few main points: CORSIKA simulation (Chap. 4, Sec. 4.1.1 and A.3), ML-based muon bundle observable reconstruction (Chap. 5, Sec. A.5), comparisons of experimental data against the Monte Carlo simulations (Chap. 6), and the **prompt** muon analysis (Chap. 7 and Sec. A.6). They are all briefly recapitulated in the following sections.

8.1.1. CORSIKA Monte Carlo production

The procurement of the CORSIKA simulation for KM3NeT detectors has proven to be a complex and challenging task for a number of reasons. Obtaining reasonable results and covering the entire phase space of interest required careful selection of inputs. The simulation settings had to be iteratively adjusted after generating the test productions, e.g. to evaluate the optimal energy thresholds. Some inputs, for instance the Earth's magnetic field strength or the atmosphere layer parameters had to be first estimated from or fitted to a model, which should meet certain specifications (see Sec. 4.1.1.2). Even after finalising all the settings, running the CORSIKA MC still posed a challenge in terms of the required computing power, storage, and bookkeeping effort. The process was partially automated, yet still manual scrutiny was, and will most likely remain a necessity.

The CORSIKA simulation produced for this work has already found use in a number of analyses within the KM3NeT collaboration and is expected to continue to contribute to the scientific success of KM3NeT. The applications of the CORSIKA MC outside of this work included reconstruction of muon bundle properties, measurement of the primary CR flux composition, tuning of the MUPAGE code, classification of muons stopping inside the KM3NeT detectors, and more [9, 148, 10, 211].

8.1.2. Muon bundle reconstruction

As was shown in Chapters 5–7, the ML-based muon bundle property reconstruction has yielded valuable results. Even the regression of the total primary energy was successful, despite the intrinsic loss of large portion of the original information about the shower. This opens a window to interesting analysis possibilities from the point of view of the CR physics. After improving the agreement between the data and MC, the KM3NeT datapoints could be included in the primary CR spectrum (Fig. 2.3.1). The ML bundle energy reconstruction has proven to be a much better description of

reality, than the traditional JMuon reconstruction designed under single muon hypothesis. The reconstruction of muon multiplicity was the first such reconstruction performed for an underwater neutrino telescope. It allowed to boost the power of the hypothesis test in Chap. 7 by rejecting the less sensitive phase space.

8.1.3. Data vs simulation comparisons

Chap. 6 has demonstrated that even very early KM3NeT detector configurations, like ORCA1 and ARCA2, were not merely a proof of concept. They were already capable of delivering physically sound results. In addition, thanks to the development of dedicated reconstruction, the first measurements of muon multiplicity and total primary energy with an underwater neutrino telescope were performed on ARCA6 and ORCA6 data. By comparing the outcomes for different detector configurations, one can note clear progress in the description of the data. It was achieved by both advancing the detector construction, and significant improvements in simulation and reconstruction software. A consistent picture emerges from looking at the data: the high-energy and high-multiplicity muon bundle rates are severely underestimated by the simulations. This is consistent with observations of other experiments and indicates that there is a need for further work in modelling of hadronic interaction models [192].

8.1.4. Prompt muon analysis

The sensitivities obtained for ARCA115 and ORCA115 (Sec. 7.6) predict a bright future for KM3NeT. Even the results for ARCA6 and ORCA6 look encouraging, although the detectors in these configurations have been in operation for too short (each for less than a year). To provide a definite confirmation, whether the **prompt** muon flux component is present in the atmospheric muon flux or not, more data will be needed. Currently, the strongest limitation to the sensitivity comes from large systematic uncertainties (Sec. 6.2.6). The comparison against experimental data for ARCA6 and ORCA6 suggests that there is indeed an excess of high-energy and high-multiplicity events. However, a reliable measurement will require further work on improving the simulations to accurately describe the data in the insensitive region of the phase space.

The comparison with the IceCube results suggests that it also has a great potential to confirm the existence of the **prompt** muon flux component. In fact, with more than 10 years of accumulated livetime, IceCube is most probably already able to make a significant measurement, or at least set a strong upper limit on the **prompt** muon flux. The only hindrance may be the need for a dedicated simulation.

8.2. Outlook

There is a number of routes that have been followed in this thesis, yet there are even more that have been not. Some of those are listed and grouped topically in the following sections.

8.2.1. CORSIKA Monte Carlo production

In the case of the CORSIKA simulation, one could think of a number of improvements. There are CR flux models, which require other CR primaries than the ones simulated for this work (p , He , C , O , Fe) [132, 131, 128, 191]. Such a model could in principle also be used as the default one for the analysis. However, adding more primaries would considerably increase the computational cost of the CORSIKA MC, since one must produce sufficient statistics for each of the primaries.

Producing a rbr CORSIKA simulation would certainly be extremely valuable for a number of analyses. However, it would be a costly endeavour, perhaps not even feasible. Besides the need to generate sufficient statistics for each run, the atmosphere fit (see Sec. A.1.2) should ideally be redone for each run, or at least each month, since the atmospheric conditions vary seasonally.

The propagation of muon bundles simulated with CORSIKA has been fully integrated into gSeaGen. However, those muons often come mixed with neutrinos, and they remain to be included in the implementation. Notably, such a combined simulation of μ and ν would be necessary to carry out a self-veto study for KM3NeT [212].

Already with the current CORSIKA7 simulation, di-muon production from the Drell-Yan processes [213] could be studied closer by finding muons with common parent particles.

A MC production with CORSIKA8 [150], once it is officially released, would be invaluable for cross-checking the CORSIKA7 results. In particular, the new feature allowing to simulate showers across different media would enable a direct validation of the gSeaGen code. Furthermore, CORSIKA8 is expected to provide much more detailed particle history information and a more flexible atmosphere modelling.

8.2.2. Muon bundle reconstruction

The reconstruction of muon bundle observables developed in Sec. 5 is in principle extensible to other detector configurations beyond ARCA6 and ORCA6. It requires processing the existing CORSIKA MC for the desired detector configuration to be able to train the estimator. For instance, processing a MC for ORCA4 could allow a direct comparison with the deep learning muon multiplicity reconstruction developed in parallel to this work by S. Reck [9].

Besides extending to other detector configurations, reconstruction of further muon bundle observables listed in Sec. 2.3.3 could certainly be attempted. To this end, it might be beneficial to consider including additional information in the training. In this work, each feature was a single number per event, however the spatial and temporal distributions of hits are in principle accessible. Furthermore, complementary data could be extracted from the other sensors besides the PMTs, which are already installed in the DOMs [123]. The technical challenge would be how to deal with such irregular and highly multidimensional data in an efficient manner. In a broader perspective, a step towards diversifying the collected information could be an extension of the KM3NeT detectors, e.g. by installing a (sea-)surface detector array above ARCA or ORCA (or both), similarly to IceTop array above IceCube [214].

The muon selection, described in Sec. 5.4.1 could be further refined, perhaps without relying on the likelihood from the classical reconstruction (JMuon). Instead, a direct measure of reconstruction

confidence, similar to what was done by S. Reck in [9] could be used. The approximation of cylindrical symmetry of the detector in the geometric part of the selection could have compromised the results to some extent, especially for ORCA (see Fig. 3.2.4). Hence, the performance could profit from developing a more robust approach the performance.

8.2.3. Data vs simulation comparisons

An obvious extension of the comparisons of experimental data and simulations would be to include datasets from newer detector configurations. This could allow to include more runs, resulting in a longer total livetime, preferably sampled from a period of 1 year or longer. This is crucial from the point of view of studying the seasonal variations in the muon rates (or averaging them out accurately). In addition, the agreement between the data and MC could be improved by applying a stricter event selection, utilising more of the available low-level information.

From the MC side, there are still ongoing efforts to improve the light simulation, which are most relevant for ORCA and should be included in the CORSIKA production when possible. As mentioned in Chap. 6, pure noise is currently not included in the official simulations, it was evaluated only in standalone studies. Adding it could foster the event selection and improve the understanding of the observed discrepancies when comparing MC against the data.

8.2.4. Systematic uncertainties

Most of the systematic uncertainties evaluated in Sec. 6.2 could be either reduced by improvement of modelling, or refined through more detailed studies.

The first category includes the total CR flux uncertainty due to differences between the models, which can be expected to shrink as a result of new direct CR measurements and theoretical advancements. Similarly, the next generation of HE hadronic interaction models is in the making. They will benefit from oxygen runs at LHC [205, 206, 207], which are crucial for better understanding of interactions in the atmosphere. The uncertainty related to the density variations of the atmosphere itself may be reduced by generating separate CORSIKA productions with dedicated atmosphere fits. This could be done both for the ARCA and ORCA locations, and for different months.

The uncertainty evaluation related to the light absorption length in water and the PMT efficiency would surely benefit from larger statistics, allowing to express the uncertainty as the function of the energy. What is more, the PMT efficiency study should be preferably done on a simulation in rbr mode (see Sec. 4.3.4), since the PMT parameters can vary from run to run.

Along with reducing the leading uncertainties, the neglected ones mentioned in Sec. 6.2 should ideally be included.

8.2.5. Prompt muon analysis

The **prompt** muon analysis could be refined in a number of ways. The sensitivity could unquestionably benefit from a combination of ARCA and ORCA results. Moreover, the results from intermediate KM3NeT detector configurations could in principle be consolidated. Another way to

boost the sensitivity would be including more observables, for instance the muon bundle diameter, or time spread of the event.

Selection of the critical region is an aspect of the analysis, which could use further investigation. In the earlier phases of this work, direct classification into **SIG** and **BGD** was attempted, although with unsatisfactory results. The contribution of **BGD** was largely underestimated in this approach, which could lead to a false discovery. To avoid it, this approach was abandoned. An alternative would be more complex critical region boundary, either defined by a function, or by binning in energy and multiplicity. The latter might require additional caution, not to tune the selection of the binning to statistical fluctuations. This is a real risk due to lower statistics available for high-energy (and multiplicity) events.

By default, MUPAGE does not simulate the μ flux consistent with **BGD**. However, there may be a way around this. Following the success of the MUPAGE tuning on CORSIKA in A. Romanov's work [148], one could attempt a specialized tuning of MUPAGE on the **BGD**-only CORSIKA. This would not only allow for easier generation of considerable statistics of pure **BGD** simulation, but also to produce a rbr MC with the tuned MUPAGE.

The discrimination between **prompt** and **conventional** muons could be made more precise with CORSIKA8 [150]. It will come with more complete particle history, including exact numbers of interactions, which will remove the ambiguity in the case of longer particle genealogies.

A very natural extension of the analysis would be to study the sensitivity of KM3NeT to the **prompt** neutrinos, however this will require implementing propagation of ν simulated with CORSIKA, as mentioned in Sec. 8.2.1. Another possible variation of the analysis could investigate the sensitivity to the presence of heavy quarks (c , s , t , b) in the atmospheric flux. Such a heavy-quark component is in fact partially overlapping with the **prompt** definition. It is more inclusive, since secondaries with one heavy and other light parent particles would still be counted as contributing to the heavy flux. For **prompt** muons, a single **conventional** parent particle was already excluding such a secondary μ (or ν , if we consider the proposed extension). It was verified, that excluding the absence of charmed and heavier hadrons in observed EAS is indeed easier than excluding the **conventional**-only scenario. This alternative approach was not pursued further, since currently the main hindrance to any measurement is the accuracy of simulations (see Chap. 6), which was thoroughly addressed in this work.

A. Appendix

In this chapter, all the supplementary materials for the thesis have been gathered.

A.1. CORSIKA

This section contains miscellaneous information concerning the CORSIKA MC production.

A.1.1. Simulation inputs

The CORSIKA production, on which all the results of Chap. 5, the ARCA6 and ORCA6 results in Chap. 6, and the entire analysis in Chap. 7 are based, was ran with CORSIKA v7.7410 [8]. Tab. A.1.1 summarises the compilation options, which were common for all sub-productions: TeV_low, TeV_high, PeV, and EeV. The sub-production naming refers roughly to simulated E_{prim} ranges, as can be verified in Tab. A.1.1, which details all the relevant CORSIKA settings used in the simulation.

TABLE A.1.1.: Compilation settings used for CORSIKA. The complete list of possible options is documented in [5].

	Value	Description
main options	SIBYLL-2.3d [109]	HE hadronic interaction model
	URQMD-1.3cr [136]	LE hadronic interaction model
	VOLUMEDET	non-flat (volume) detector geometry
additional options	CURVED	Earth's curvature is accounted for
	PYTHIADIR	particle decays are handled by PYTHIA [106]
	EHISTORY	parent particle information for muons is saved in the output
	NEUTRINO	ν 's from π , K , and μ decays are tracked explicitly (but without interaction)
	CHARM	charmed particle and τ lepton production is enabled
	UPWARD	upward (or nearly horizontal) particles are not discarded
	LPM	LPM effect [215] is simulated

TABLE A.1.2.: Simulation settings used for CORSIKA.

Prod	Setting	Value	Param name
TeV_low	Primaries used	p, He, C, O, Fe	-
TeV_high		p, He, C, O, Fe	
PeV		p, He, C, O, Fe	
EeV		p, Fe	
all	Primary codes	14, 402, 1206, 1608, 5626 (p, He, C, O, Fe)	PRMPAR
TeV_low	Generated showers per file	$1.5 \cdot 10^7$ (p) 10^7 (He) $5 \cdot 10^6$ (C) $5 \cdot 10^6$ (O) $5 \cdot 10^6$ (Fe)	NSHOW
TeV_high		$6 \cdot 10^6$ (p) $4 \cdot 10^6$ (He) $1.5 \cdot 10^6$ (C) $1.5 \cdot 10^6$ (O) $4 \cdot 10^5$ (Fe)	
PeV		$4 \cdot 10^4$ (p) $4 \cdot 10^4$ (He) $2.5 \cdot 10^4$ (C) $2.5 \cdot 10^4$ (O) $2 \cdot 10^4$ (Fe)	
EeV		100	
TeV_low	E_{prim} range	$400 < \frac{E_{\text{prim}}}{\text{GeV}} < 2 \cdot 10^4$ (p) $1.6 \cdot 10^3 < \frac{E_{\text{prim}}}{\text{GeV}} < 2 \cdot 10^4$ (He) $4.8 \cdot 10^3 < \frac{E_{\text{prim}}}{\text{GeV}} < 6 \cdot 10^4$ (C) $6.4 \cdot 10^3 < \frac{E_{\text{prim}}}{\text{GeV}} < 8 \cdot 10^4$ (O) $2.24 \cdot 10^4 < \frac{E_{\text{prim}}}{\text{GeV}} < 3 \cdot 10^5$ (Fe)	ERANGE
TeV_high		$6 \cdot 10^3$ (p) $1 \cdot 10^4$ (He) $3 \cdot 10^4$ (C) $< \frac{E_{\text{prim}}}{\text{GeV}} < 1.1 \cdot 10^6$ $3 \cdot 10^4$ (O) $1 \cdot 10^5$ (Fe)	
PeV		$1.1 \cdot 10^6 < \frac{E_{\text{prim}}}{\text{GeV}} < 0.9 \cdot 10^8$	
EeV		$0.9 \cdot 10^8 < \frac{E_{\text{prim}}}{\text{GeV}} < \begin{matrix} 4.0 \cdot 10^9 \text{ (p)} \\ 8.0 \cdot 10^9 \text{ (Fe)} \end{matrix}$	
TeV_low	E_{prim} spectrum slope	-3.0	ESLOPE
TeV_high		-3.5, -3.0, -3.0, -3.0, -2.5 (p, He, C, O, Fe)	
PeV		-2.0	
EeV		0.0	
TeV_low	Primary zenith angle range	75 (p) 75 (He) $0 < \frac{\theta}{\text{deg}} < 60$ (C) 60 (O) 65 (Fe)	THETAP
TeV_high		$0 < \frac{\theta}{\text{deg}} < 87$	
PeV		$0 < \frac{\theta}{\text{deg}} < 87$	
EeV		$0 < \frac{\theta}{\text{deg}} < 87$	
all	Azimuth angle range	$180 < \frac{\phi}{\text{deg}} < 180$	PHIP

all	Observation level	0 cm (sea level)	OBSLEV
all	Starting altitude	$0 \frac{\text{g}}{\text{cm}^2}$	FIXCHI
all	Magnetic field	$B_x = 25.2179 \mu\text{T}, B_z = 38.4848 \mu\text{T}$	MAGNET
all	Flags for hadronic interactions and fragmentation	0 0 0 0 0 2	HADFLAG
all	Energy cuts (hadrons/nuclei, μ , e , γ)	(300, 300, 10^3 , 10^3) GeV	ECUTS
all	Atmosphere fit	0	ATMOD
		(1750000, 4500000, 7300000, 10130000, 12500000) cm	ATMLAY
		-58.44897651964439, 0.5019792446185176, -0.014658740225644349, -4.286764182377298e-05, 0.0030020492001918493	ATMA
		1071.309922924368, 1380.8205315315772, 450.1250293064572, 5714.833843117572, -38.86175122739144	ATMB
		865209.9870960491, 622615.8339434739, 790046.9277382238, 599218.1788640362, -141350551294.98242	ATMC
all	Additional information on ν	T	NUADDI
all	Additional information on μ	T	MUADDI
all	μ multiple scattering angle	T	MUMULT
all	EM interaction flags	F T	ELMFLG
all	Multiple scattering step length factor	1	STEPFC
all	Outer radius for NKG lateral density distribution	200.E2	RADNKG
all	Longitudinal distribution, step size, fit, out	F 10 F F	LONGI
all	Cut on γ factor for printout	10^4	ECTMAP
all	Max number of printed events	1	MAXPRT

The parameters in Tab. A.1.2 were optimised for a simulation of atmospheric muon fluxes at ARCA and ORCA detectors. The atmosphere fit (see Sec. A.1.2) and magnetic field model were averaged between the two detector locations and also over the time (seasonal and yearly variations). The EeV sub-production was only ran for proton and iron primaries, since only those have a non-negligible contribution to the all-nuclei CR flux in the GST3 model, which assumes the composition, as shown in Fig. A.1.1. For more details, see the following sections.

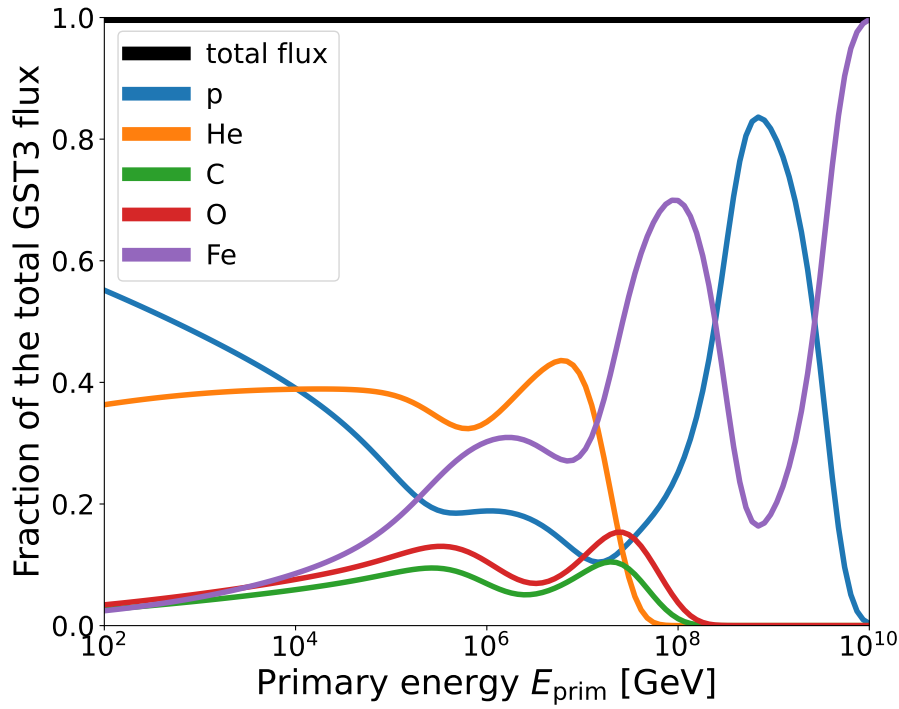


FIGURE A.1.1.: Primary CR composition assumed in the GST3 CR flux model [127].

A.1.2. Fit of the atmosphere

The range of the atmospheric heights (altitudes) h relevant for the fit has been determined from the first interaction height H_{int} distribution (Fig. A.1.2). It was concluded that a fit should reproduce the model of the atmosphere at least till ~ 70 km, which was the limit of validity (within $\pm 5\%$) of the previously used fit [190]. The fit had to cover the lower altitudes as well, to ensure CORSIKA propagates the showers down to the sea level ($h = 0$ km) through a realistic approximation of the atmosphere. The maximum extent of the atmosphere in CORSIKA is 112.8 km and above, the density is clipped to zero by the code, regardless of the actual fit range [5]. The NRLMSIS-2.0 model was well suited here, since it covers the heights up to thousands of km, unlike e.g. the GDAS model, supplied together with CORSIKA, which only goes up to $h = 25$ km [145, 5]. A further advantage of NRLMSIS-2.0 was the flexibility of choice of any geographical location of the detector, which was fixed in the predefined models within CORSIKA.

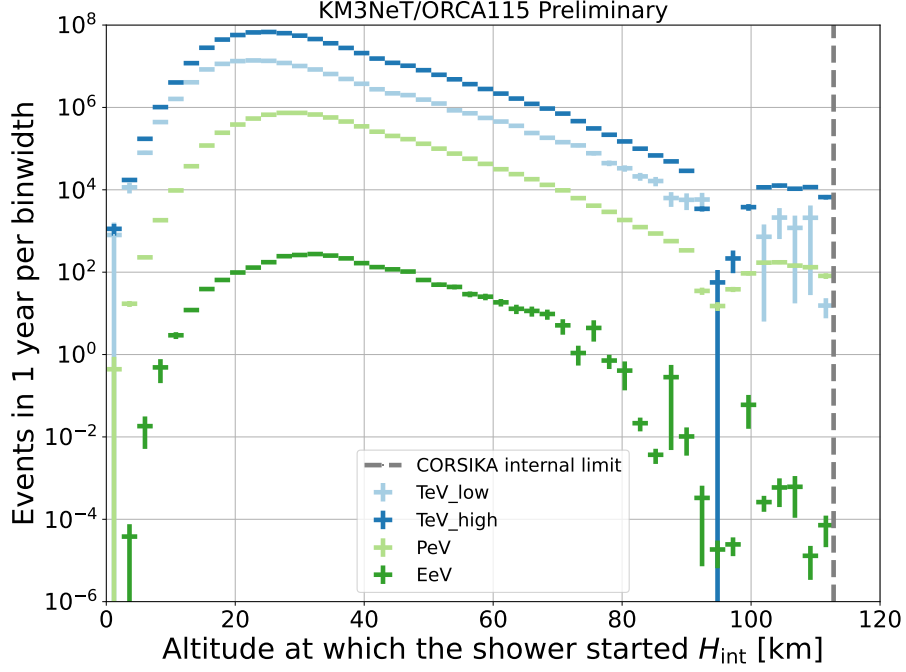


FIGURE A.1.2.: Distributions of the first interaction height H_{int} of CORSIKA showers for different sub-productions (see Tab. A.1.2). Using the weighted simulation (see Sec. 4.2), the expected numbers of events in ORCA115 after 1 year of data taking were estimated. The dip and peak structures above 90 km stem from the fact that the simulation already used the fit from Fig. A.1.10. The fit overpredicts the density at highest altitudes, leading to premature start of some showers.

The NRLMSIS-2.0 model does not directly predict the atmospheric thickness $T(h_0)$ at a certain height, which is the input required by CORSIKA. Instead, it provides an estimate of the density of the atmosphere at a fixed location and time, which can be recalculated into atmospheric thickness (see Fig. A.1.3) by integrating over the atmosphere above the height of interest h_0 :

$$T(h_0) = \int_{h_0}^{h_{\text{max}}} \rho dh, \quad (\text{A.1.1})$$

where h_{max} is the height at which the atmosphere is assumed to end (have negligible density). When computed numerically, the integral becomes a sum over a histogram with very fine steps (in this case 1 m) and the atmosphere has to be clipped at a certain point. The range of altitudes interesting from the point of view of CORSIKA simulations for KM3NeT extends up to ~ 113 km, however it is most important to cover the low altitudes around 20-40 km (see Fig. A.1.2). Fig. A.1.4 demonstrates the effect of varying the h_{max} parameter. The clipping point was picked to be $h_{\text{max}} = 1600$ km, which ensures that up to 112.8 km the model prediction is within 0.0005% from the unclipped case, in Fig. A.1.4 approximated by $h_{\text{max}} = 5000$ km.

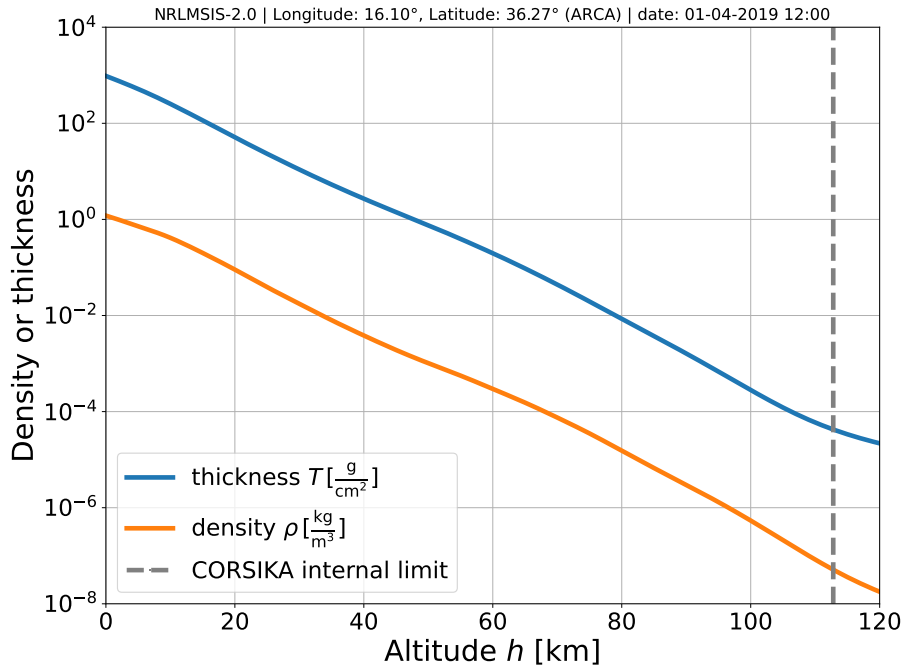


FIGURE A.1.3.: Atmospheric density and thickness as a function of height above the ARCA site, according to NRLMSIS-2.0.

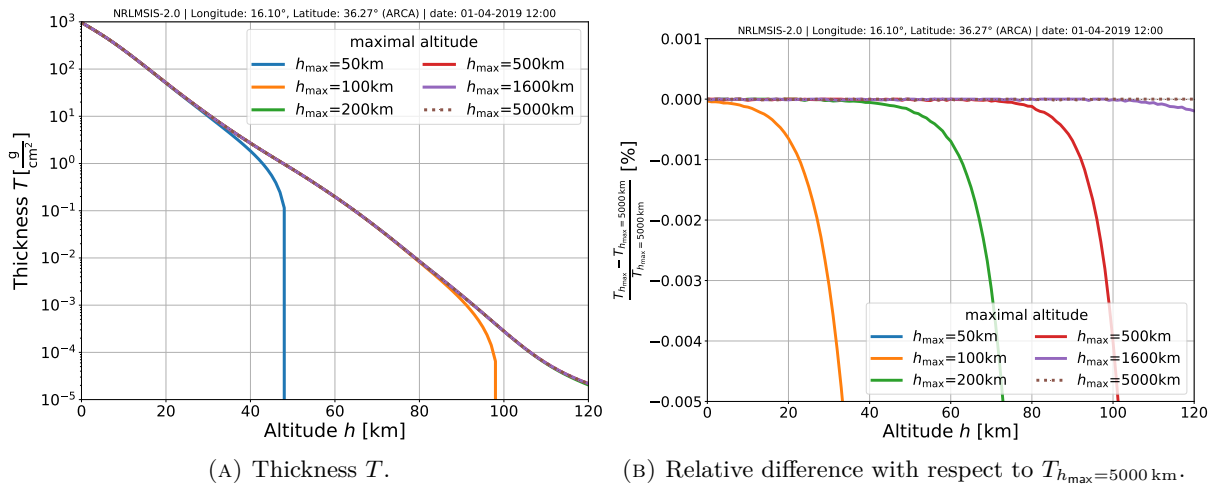


FIGURE A.1.4.: Atmospheric thickness as function of height computed for different h_{\max} values. The location is at the ARCA site.

There is in fact an older atmospheric density model: NRLMSISE-00 [216], which was a predecessor of NRLMSIS-2.0. NRLMSISE-00 was used in the KM3NeT CORSIKA test simulations, prior to this work. The relative difference between the two is between 1% and 18 %, depending on the altitude (see Fig. A.1.5). The NRLMSIS-2.0 was a significant upgrade of NRLMSISE-00, addressing a number of issues [146]:

1. Thermospheric densities were fully coupled to the entire temperature profile from the ground to the exosphere, while in NRLMSISE-00 they were treated independently from the lower layers of the atmosphere.

2. Upper thermosphere in the model was tuned to better match new satellite mass density measurements.
3. Many new temperature measurements in the mesosphere, stratosphere, and troposphere have been included.
4. A number of new atomic oxygen and hydrogen measurements in the mesosphere were added.

Not all changes are listed, however the changes in NRLMSIS-2.0 are mostly focused on altitudes below 100 km [146], which are the most relevant ones for the CORSIKA simulations in this thesis.

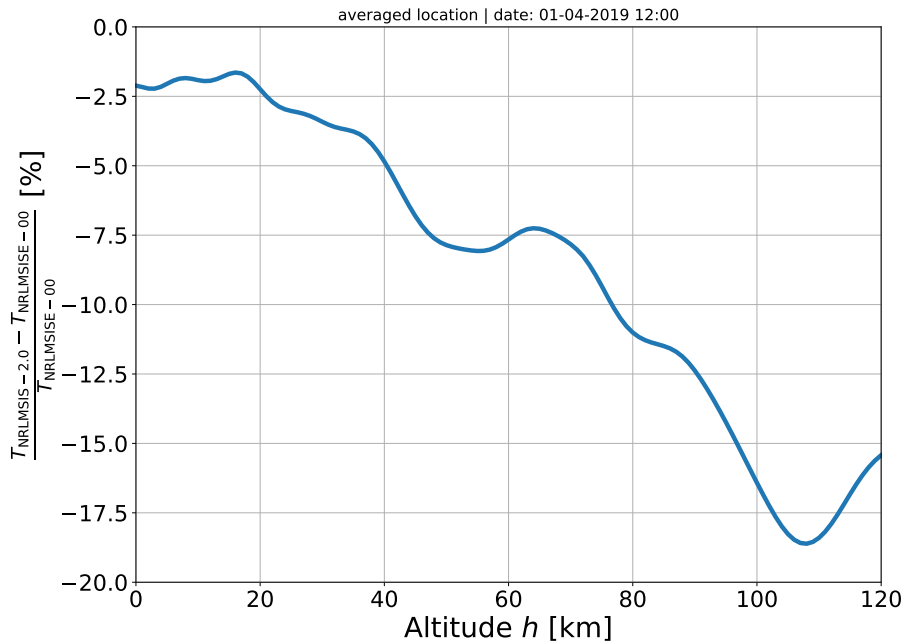


FIGURE A.1.5.: Ratio of atmospheric thickness of NRLMSIS-2.0 and NRLMSISE-00 to their average, at ARCA site.

An important issue to investigate were the variations in model predictions depending on the chosen location and time. The comparison of the atmosphere at ARCA and ORCA sites, along with ANTARES x, Baikal GVD, IceCube and Super-Kamiokande (SK) sites added for comparison [AMANDA=000026IC, 23, 57, 217, 50], is shown in Fig. A.1.6. An interesting observation from Fig. A.1.6 is that the differences between the atmospheric properties of both KM3NeT sites and Baikal and SK seem to be rather small at the considered altitudes. This indicates that these two experiments could potentially share a CORSIKA MC production with KM3NeT if there are not other factors preventing it (e.g. the magnetic field strength). The same conclusion is certainly true for ANTARES, however its case is more trivial, as it was (the detector was dismantled on 12.02.2022) located very close to ORCA. IceCube on the other hand, due to its unique location at the geographic South Pole, has noticeably different atmospheric thickness, which seems to be prone to larger variations with height.

Seasonal variations in muon flux have already been measured by the IceCube and ANTARES experiments to be about 10 % and 2 % respectively [53, 217, 23]. Monthly atmosphere variability predicted by NRLMSIS-2.0 is shown in Fig. A.1.7 and the thickness varies up to $\sim \pm 10\%$ at around 70 km above the sea level. However, one should refrain from a conclusion that the expected

variation in the muon flux will also be on the order of 10 %. As was shown in Fig. A.1.2, most of the showers typically start at ~ 30 km, where the thickness varies by about 6 %. The seasonal changes may in fact shift the peak of the H_{int} distribution, since there will be a bigger or smaller slant depth before reaching a certain height. Generally, the lower the first interaction happens, the better is the chance for the shower to reach the sea surface, and hence the higher muon flux can be expected. Neutrino flux should be less affected, since neutrinos do not lose energy on their way. There is typically much less difference between the days of a single month. In Fig. A.1.8, one can see that the variations are below 1 % in the range of interest. Stronger effects may be seen in hourly changes, associated with the day-night cycle, as shown in Fig. A.1.9. The effect is the strongest at very high altitudes, higher than the typical first interaction height (see Fig. A.1.2). For this reason, the effect on the total atmospheric muon flux may be hard to measure. The yearly differences were not plotted, however they are very small, of the order of 0.01 %.

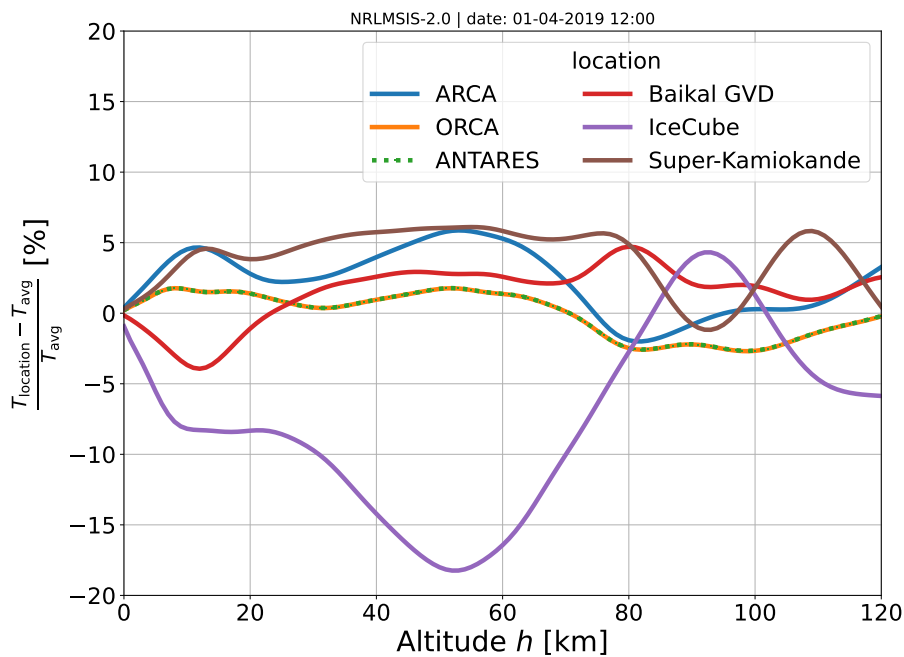


FIGURE A.1.6.: Ratio of atmospheric thickness computed at ARCA, ORCA, and other experimental sites from Fig. 3.1.1 to their average, plotted as function of the height. IceCube atmosphere clearly stands out from the other ones at low altitudes and it is a real effect of the different atmospheric conditions at the geographic South Pole [217, 53].

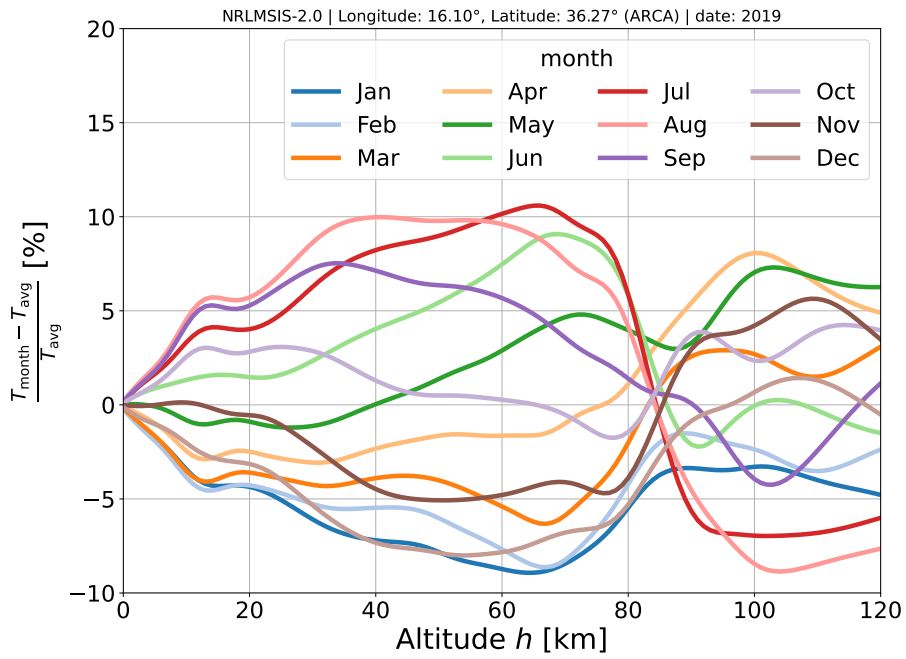


FIGURE A.1.7.: Ratio of atmospheric thickness for different months in 2019 to their average. The choice of the year was made only such that it overlaps with the actual data taking by KM3NeT detectors. The result is shown for the ARCA location.

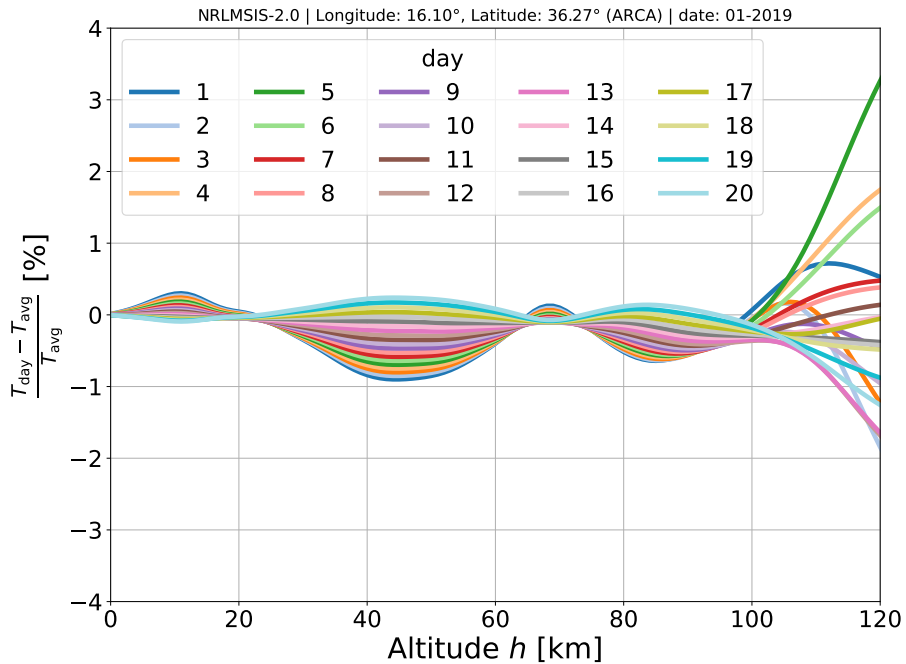


FIGURE A.1.8.: Ratio of atmospheric thickness for individual days of January 2019 to their average. The result is shown for the ARCA location. The day-to-day changes in the atmospheric density are rather negligible (however, they accumulate into the monthly variations, which are not).

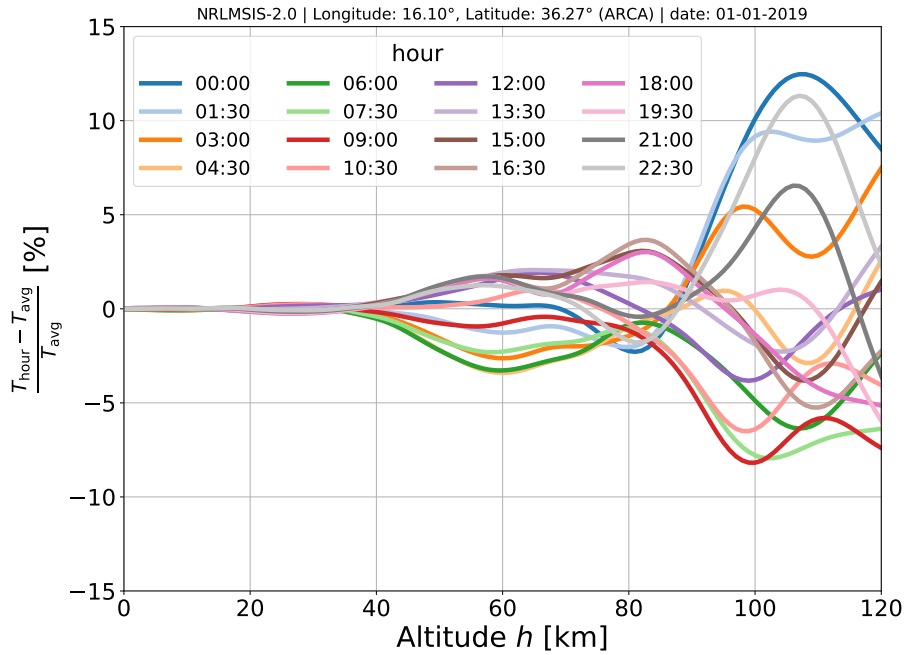


FIGURE A.1.9.: Ratio of atmospheric thickness for individual hours to their average on 01.01.2019. The result is shown for the ARCA location. The hourly changes in the atmosphere, especially at higher altitudes are much stronger than the daily variations (Fig. A.1.8). This is connected with the day-night cycle and the corresponding heating and cooling of the atmosphere, which affects the density.

The fit of the NRLMSIS-2.0 model has been performed on the prediction averaged over the time (period from 01.04.2019 to 01.04.2020, with a step of 1 hour) and location (ARCA and ORCA sites). Each of the 5 CORSIKA atmosphere layers (see Eq. 4.1.2 and 4.1.3) was fitted separately. Each of the fits was bound at least from one side by the requirement that the layers should connect exactly. The resulting fit, presented in Fig. A.1.10, is stable and within $\pm 5\%$ around the average thickness from the model up to 99 km. This is a significant improvement with respect to the previously used fit, which was stable within $\pm 5\%$ only up to 70 km [190]. The fit parameters are reported in Tab. A.1.2 as ‘Atmosphere fit’.

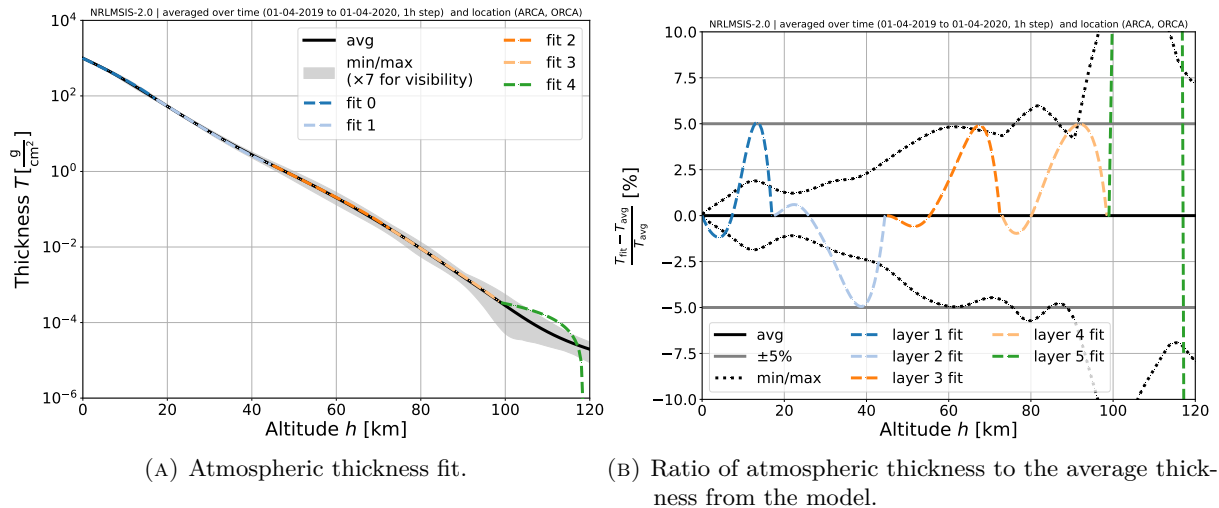


FIGURE A.1.10.: Atmospheric thickness fit performed for 5 CORSIKA layers (colour-coded). The avg stands for the average thickness, as predicted by NRLMSIS-2.0 and min/max indicates the corresponding possible extremal values when varying the location and time. The horizontal grey bands indicate the $\pm 5\%$ validity interval.

A.1.3. Magnetic field strength

The mean Earth's magnetic field strength used for CORSIKA simulations was estimated using the International Geomagnetic Reference Field (IGRF) [218]. CORSIKA requires the north and east components of the magnetic field (B_x and B_z respectively) as input. The values $B_x = 25.2179 \mu\text{T}$ and $B_z = 38.4848 \mu\text{T}$ were computed for the location in between the ARCA and ORCA sites: (40.825214° N, 10.442726° E), and averaged over the year 2019. It was also checked that, according to IGRF model, the yearly variations in the magnetic field components are at most of the order of $\pm 6\%$, which allows for rather stable results, regardless of the date used.

A.1.4. Benchmarking and energy thresholds

Here, a number of tests performed on CORSIKA MC are highlighted. Their main purpose was to optimise the settings in Tab. A.1.2, and assess the feasibility of CORSIKA mass production with the computational resources available within The KM3NeT Collaboration.

The impact of the minimal electron and photon energies E_e^{\min} and E_γ^{\min} was checked to be of little importance for CORSIKA muon simulations and set to 1 TeV. Varying each by two orders of magnitude only results in at most 5 % difference in expected muon rate at sea level, and at can level the effect was even weaker.

The muon and hadron/nuclei energy thresholds play a much more important role in KM3NeT CORSIKA simulations. The threshold for hadrons/nuclei in practice has turned out to be equivalent to a threshold on neutrino energy, hence in the following it is referred to as E_ν^{\min} . The choice of the minimal muon energy E_μ^{\min} was dictated by the muon range in seawater and the shortest possible distance to the can, which is the vertical distance from the sea surface to the top of the can of ORCA: $d_{\min} = 2440\text{m} - 476.5\text{m} = 1963.5\text{m}$. Muon range estimation, produced along with the other results from Sec. A.3.1, is shown in Fig. A.1.11. Based on this result, the value of $E_\mu^{\min} = 300 \text{ GeV}$

was adopted. Since muon neutrinos can produce only muons with smaller energies than their own, the same cut was used for E_ν^{\min} .

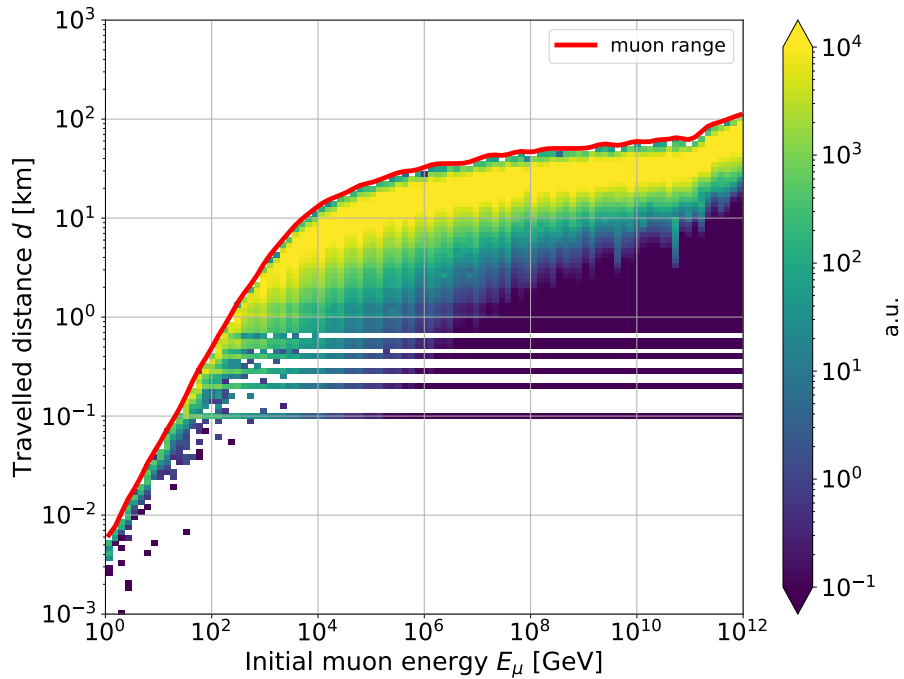


FIGURE A.1.11.: Distance d travelled by muons in seawater as a function of their initial energy E_μ . The red line is the maximum of the histogram increased by half of the standard deviation and is an estimate of the muon range in seawater. The horizontal lines in the histogram are an artefact of the fact that the muon positions were recorded every 100 m (or after stopping, but this did not contribute to the effect; see Sec. A.3.1).

A.1.4.1. Surviving shower fraction

The first investigated issue was the success rate of showers as a function of the primary energy E_{prim} . The results shown in Fig. A.1.12 indicate that the E_ν^{\min} is slightly more constraining than E_μ^{\min} , which is related to the much smaller probability of interaction for neutrinos, compared against muons (in fact, in CORSIKA simulation ν are not interacted at all, only tracked). Thus, even very low-energy neutrinos make it to the sea level, which is not true for muons, losing energy on their way. One may also note that showers with $E_{\text{prim}} \gtrsim 1$ PeV almost always survive.

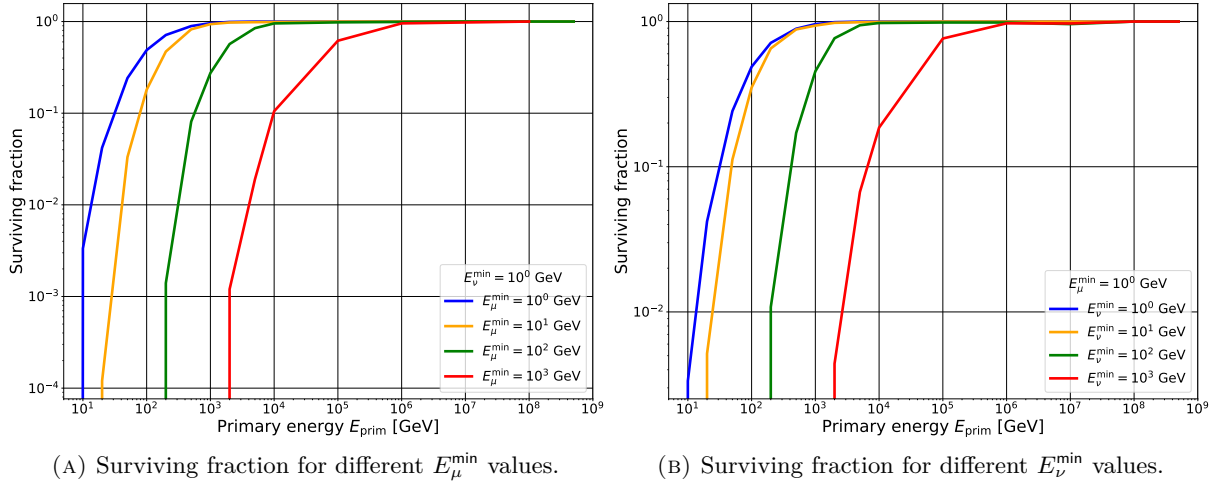


FIGURE A.1.12.: Fraction of the generated showers, producing particles reaching the sea level.

A.1.4.2. Storage and CPU time

Next, the storage and the time needed to produce a certain number of events at sea have been investigated. All the performance checks were performed on Intel(R) Xeon(R) CPU E5-2680 v2 @ 2.80GHz with 126GB RAM. As visible in Fig. A.1.13 and A.1.14, both required CPU time and disk space seem to have one global minimum (naturally, shifting with the energy thresholds). Beyond a certain E_{prim} range around this minimum, the simulation seems if not completely impossible, then at least very challenging. The increase in required resources is particularly dramatic towards lower energies, as there, the chance to produce secondaries that can possibly reach the sea diminishes rapidly. On the other hand, the atmospheric muon and neutrino fluxes peak at low energies, which means it is extremely important to properly simulate that region. This has been one of the motivations for splitting up the originally defined TeV sub-production into two, more fine-tuned ones: TeV_low and TeV_high (see Tab. A.1.2).

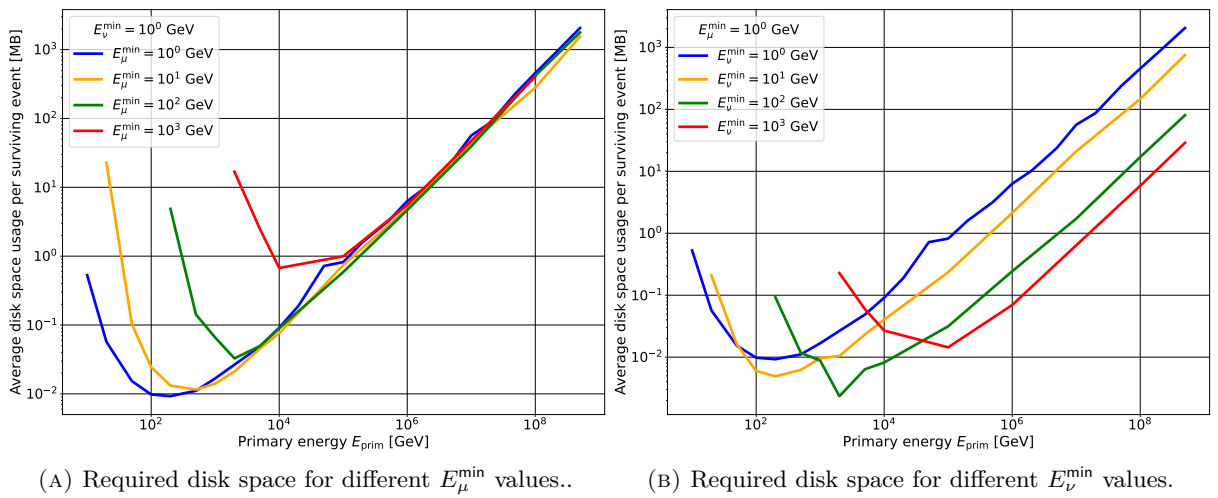


FIGURE A.1.13.: Storage per successful event that is required to store CORSIKA files as a function of the primary energy.

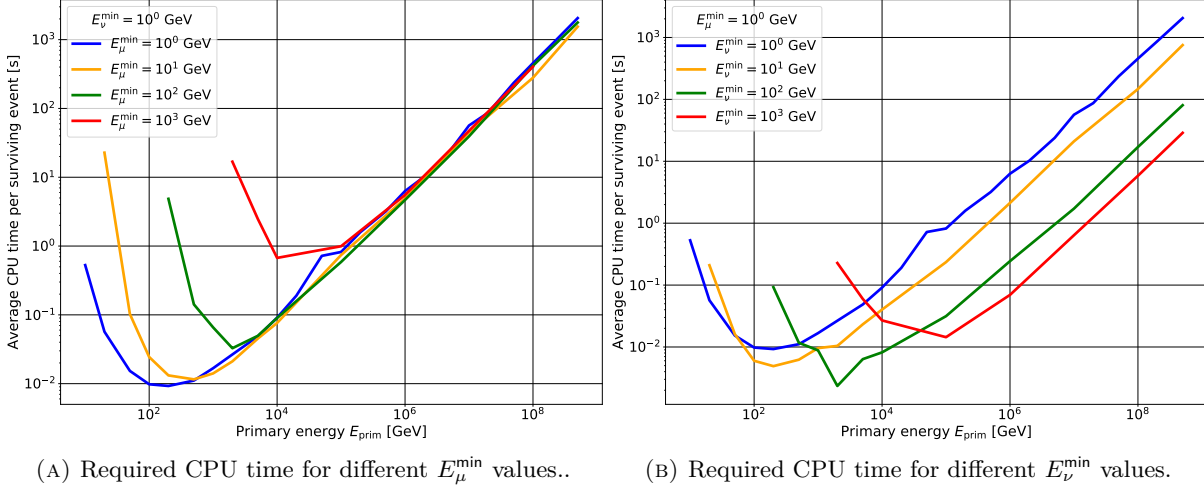


FIGURE A.1.14.: CPU time per successful event that is required to process CORSIKA files as a function of the primary energy.

A.2. Formulae

This section gathers the derivations of some of the equations used throughout this thesis.

A.2.1. Errors for the weighted histograms

The value of each bin in the weighted histogram is given by

$$N_i = \sum_j w_{ij},$$

where w_{ij} is the weight of the j -th event, falling into the i -th bin. The error of this quantity is related to its variance:

$$\Delta N_i = \sqrt{\text{Var} \left(\sum_j w_{ij} \right)} = \sqrt{\sum_j \text{Var} (w_{ij})} = \sqrt{\sum_j w_{ij}^2}. \quad (\text{A.2.1})$$

The systematic uncertainties can be included by modifying the event weights:

$$\Delta N_i = \sqrt{\sum_j [w'_{ij}]^2} = \sqrt{\sum_j [w_{ij} \cdot (1 + \Delta w_{\text{syst},j})]^2}, \quad (\text{A.2.2})$$

where $\Delta w_{\text{syst},j}$ is evaluated for the j -th event according to the results from Sec. 6.2.6.

A.2.2. The shortest distance between a point and a line

The result of this derivation was applied to a number of tasks within this thesis, notably during the implementation of a more accurate calculation of event weights in gSeaGen (see Sec. A.3.2). The general vector formula for the point-line distance is:

$$d = \frac{|(\vec{x}_0 - \vec{x}_1) \times (\vec{x}_0 - \vec{x}_2)|}{|\vec{x}_2 - \vec{x}_1|},$$

where \vec{x}_0 is the point and \vec{x}_1 and \vec{x}_2 lie on the line [219]. By expanding into versor notation:

$$\begin{aligned} d &= \frac{|[(x_0 - x_1)\hat{x} + (y_0 - y_1)\hat{y} + (z_0 - z_1)\hat{z}] \times [(x_0 - x_2)\hat{x} + (y_0 - y_2)\hat{y} + (z_0 - z_2)\hat{z}]|}{\sqrt{(x_2 - x_1)^2 + (y_2 - y_1)^2 + (z_2 - z_1)^2}} = \\ &= \frac{|[(y_0 - y_1)(z_0 - z_2) - (z_0 - z_1)(y_0 - y_2)]\hat{x} + [(z_0 - z_1)(x_0 - x_2) - (x_0 - x_1)(z_0 - z_2)]\hat{y} + [(x_0 - x_1)(y_0 - y_2) - (y_0 - y_1)(x_0 - x_2)]\hat{z}|}{\sqrt{(x_2 - x_1)^2 + (y_2 - y_1)^2 + (z_2 - z_1)^2}} = \\ &= \frac{|[y_0 z_0 - y_0 z_2 - y_1 z_0 + y_1 z_2 - z_0 y_0 + z_0 y_2 + z_1 y_0 - z_1 y_2]\hat{x} + [z_0 x_0 - z_0 x_2 - z_1 x_0 + z_1 x_2 - x_0 z_0 + x_0 z_2 + x_1 z_0 - x_1 z_2]\hat{y} + \dots}{\sqrt{(x_2 - x_1)^2 + (y_2 - y_1)^2 + (z_2 - z_1)^2}} \\ &= \frac{.. + [x_0 y_0 - x_0 y_2 - x_1 y_0 + x_1 y_2 - y_0 x_0 + y_0 x_2 + y_1 x_0 - y_1 x_2]\hat{z}|}{\sqrt{(x_2 - x_1)^2 + (y_2 - y_1)^2 + (z_2 - z_1)^2}} = \\ &= \frac{\sqrt{[y_0(z_1 - z_2) + z_0(y_2 - y_1) + y_1 z_2 - z_1 y_2]^2 + [z_0(x_1 - x_2) + x_0(z_2 - z_1) + z_1 x_2 - x_1 z_2]^2 + [x_0(y_1 - y_2) + y_0(x_2 - x_1) + x_1 y_2 - y_1 x_2]^2}}{\sqrt{(x_2 - x_1)^2 + (y_2 - y_1)^2 + (z_2 - z_1)^2}} \end{aligned}$$

The fact that one point on the trajectory line and the directional cosines $\cos \theta_{x,y,z}$ are known allowed to write down the following relations:

$$\begin{cases} x_2 = x_1 + \cos \theta_x \cdot |\vec{v}| \cdot t \\ y_2 = y_1 + \cos \theta_y \cdot |\vec{v}| \cdot t \\ z_2 = z_1 + \cos \theta_z \cdot |\vec{v}| \cdot t \end{cases}, \quad (\text{A.2.3})$$

where \vec{v} is the velocity vector of a particle, trajectory of which is approximated by the line, and t is the time duration of its travel. In this case, the choice of $|\vec{v}| \cdot t$ was completely arbitrary and, in fact, this factor would cancel out in the further simplification. Thus, for convenience, it was picked to be $|\vec{v}| \cdot t = 1$, simplifying the above equation to:

$$\begin{cases} x_2 = x_1 + \cos \theta_x \\ y_2 = y_1 + \cos \theta_y \\ z_2 = z_1 + \cos \theta_z \end{cases}. \quad (\text{A.2.4})$$

Using Equation A.2.4 and shorthand notation: $\cos \theta_i = c_i$ ($i = x, y, z$), one could simplify the expression for d as:

$$\begin{aligned} d &= \sqrt{\frac{[-y_0 c_z + z_0 c_y + y_1(z_1 + c_z) - z_1(y_1 + c_y)]^2 + [-z_0 c_x + x_0 c_z + z_1(x_1 + c_x) - x_1(z_1 + c_z)]^2 + [-x_0 c_y + y_0 c_x + x_1(y_1 + c_y) - y_1(x_1 + c_x)]^2}{c_x^2 + c_y^2 + c_z^2}} = \\ &= \sqrt{\frac{[-y_0 c_z + z_0 c_y + y_1 c_z - z_1 c_y]^2 + [-z_0 c_x + x_0 c_z + z_1 c_x - x_1 c_z]^2 + [-x_0 c_y + y_0 c_x + x_1 c_y - y_1 c_x]^2}{c_x^2 + c_y^2 + c_z^2}} = \end{aligned}$$

$$= \sqrt{\frac{[(y_1 - y_0)c_z + (z_0 - z_1)c_y]^2 + [(z_1 - z_0)c_x + (x_0 - x_1)c_z]^2 + [(x_1 - x_0)c_y + (y_0 - y_1)c_x]^2}{c_x^2 + c_y^2 + c_z^2}} =$$

and finally, using the basic property of directional cosines, i.e. $c_x^2 + c_y^2 + c_z^2 = 1$, the final formula for the shortest point-line distance reads:

$$d = \sqrt{[(y_1 - y_0)c_z + (z_0 - z_1)c_y]^2 + [(z_1 - z_0)c_x + (x_0 - x_1)c_z]^2 + [(x_1 - x_0)c_y + (y_0 - y_1)c_x]^2}. \quad (\text{A.2.5})$$

A.2.3. Intersection of a point and a sphere

Following the derivation in [220], the line-sphere intersection can be found by solving the following quadratic equation for $d_{\text{intersect}}$:

$$0 = a \cdot d_{\text{intersect}}^2 + b \cdot d_{\text{intersect}} + c.$$

The coefficients are:

$$\begin{aligned} a &= (x_2 - x_1)^2 + (y_2 - y_1)^2 + (z_2 - z_1)^2, \\ b &= 2 \cdot [(x_2 - x_1) \cdot (x_1 - x_s) + (y_2 - y_1) \cdot (y_1 - y_s) + (z_2 - z_1) \cdot (z_1 - z_s)], \\ c &= x_s^2 + y_s^2 + z_s^2 + x_1^2 + y_1^2 + z_1^2 - 2 \cdot [x_s x_1 + y_s y_1 + z_s z_1] - r^2, \end{aligned}$$

where (x_1, y_1, z_1) and (x_2, y_2, z_2) are two arbitrary points along the line, (x_s, y_s, z_s) is the centre of the sphere, and r is the radius of the sphere. Switching to the usual KM3NeT convention, using the directional cosines (see Sec. A.2.2), the second point can be picked to be: $(x_2, y_2, z_2) = (x_1 + c_x, y_1 + c_y, z_1 + c_z)$. Such a choice, together with locating the centre sphere at the origin of the coordinate system: $(x_s, y_s, z_s) = (0, 0, 0)$, allows to simplify the coefficients to:

$$\begin{aligned} a &= (\cancel{x_1} + c_x \cancel{-x_1})^2 + (\cancel{y_1} + c_y \cancel{-y_1})^2 + (\cancel{z_1} + c_z \cancel{-z_1})^2 = c_x^2 + c_y^2 + c_z^2 = 1, \\ b &= 2 \cdot [(\cancel{x_1} + c_x \cancel{-x_1}) \cdot (x_1 - 0) + (\cancel{y_1} + c_y \cancel{-y_1}) \cdot (y_1 - 0) + (\cancel{z_1} + c_z \cancel{-z_1}) \cdot (z_1 - 0)] = 2 \cdot [c_x x_1 + c_y y_1 + c_z z_1], \\ c &= 0 + 0 + 0 + x_1^2 + y_1^2 + z_1^2 - 2 \cdot [0 \cdot x_1 + 0 \cdot y_1 + 0 \cdot z_1] - r^2 = x_1^2 + y_1^2 + z_1^2 - r^2. \end{aligned}$$

The first point (x_1, y_1, z_1) can be then any known point lying on the line.

A.3. gSeaGen

This section contains a more detailed description of selected developments in the gSeaGen code performed for this work.

A.3.1. Muon lateral deflection in water

While investigating possibilities to improve the gSeaGen code, lateral deflection of muons in seawater was studied. The result in Fig. A.3.1 was obtained by using gSeaGen with PROPOSAL as muon propagator and shooting μ vertically downwards through 10000 km of seawater until they stopped. Such a geometry allowed to conveniently compute the lateral deflection as $R_\mu = \sqrt{x^2 + y^2}$ and ensured that all the muons would have enough space to stop. Muon energy range between 1 GeV and 1 ZeV (10^{12} GeV) was scanned, with 1000 muons generated per sampled energy. The μ deflection R_μ was saved every 100 m, or after the muon stopped. For the largest muon energies, the longest distances travelled were slightly more than 100 km. The geometrical limit for the travelled distance in CORSIKA simulation for KM3NeT is about 66 km and can be derived using the maximum depth (ARCA site depth: $d_{\max} = 3450\text{m}$) and the maximum allowable zenith angle of 87° (see Tab. A.1.2).

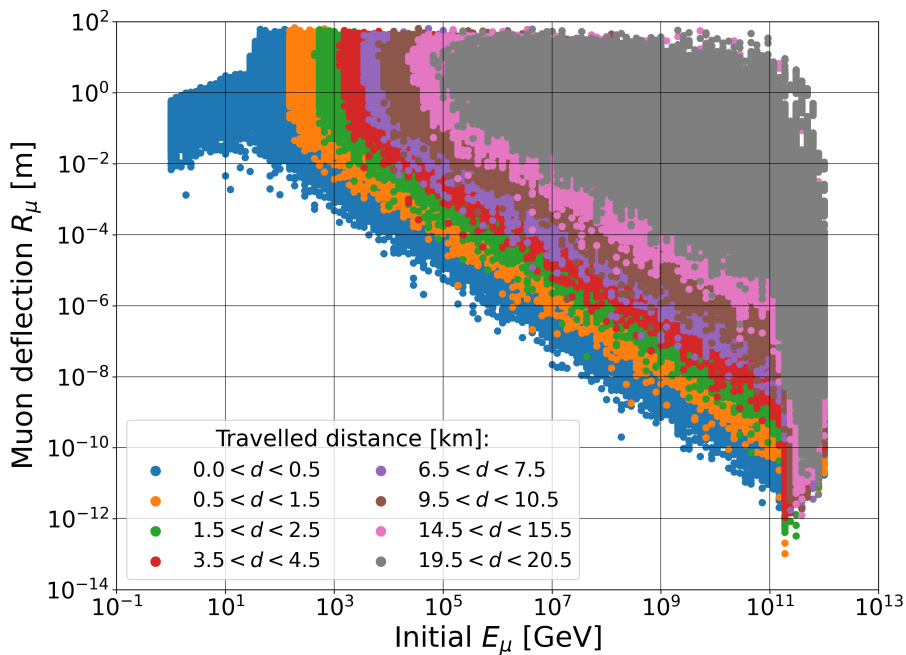


FIGURE A.3.1.: Lateral deflection of muons R_μ as a function of their initial energy E_μ and distance d travelled in seawater.

Fig. A.3.1 is very rich in physics. The vertical left edges for different travelled distances demonstrate that a certain minimal energy is required for a muon to be able to travel a particular distance. The upper limit on the lateral deflection seems to be roughly 100 m, almost regardless of initial muon energy. An exception from this is the initial E_μ region 1-50 GeV, where the dominating energy loss source is ionisation. At higher energies, radiative energy losses start to dominate and generally, μ energy losses increase sharply. As initial E_μ increases, smaller radial (lateral) deflections are possible for fixed travelled distances, which is a result of muons having stronger Lorentz boosts and the fact that high-momentum particles are just harder to deflect. It is reflected in the downward slope in Fig. A.3.1. The falling upper edge of the distribution for $19.5 < \frac{d}{\text{km}} < 20.5$ is not special, the ones for other distributions are simply buried underneath. The reason for such falling edges is

the very same as for the log-log-linear slope on the bottom of the distributions: for high-energy muons big lateral deflections are just less likely.

It was possible to fit the maximal deflections linearly in log-log scale as function of E_μ in the range from 10^2 GeV to 10^8 GeV, which is the relevant range for gSeaGen. The fitting function was:

$$R_\mu^{\max}(E_\mu) = 10^{a_{E_\mu} \cdot \log_{10}(E_\mu) + b_{E_\mu}} \text{ m}, \quad (\text{A.3.1})$$

where a_{E_μ} and b_{E_μ} are the fit parameters. Instead of the maximum value of the energy bin, the mean value incremented by 10 standard deviations was used as the maximal deflection: $R_\mu^{\max} = R_\mu^{\text{avg}} + 10 \cdot R_\mu^{\text{std}}$. The reasoning behind this was that the maximal values tend to scatter more and the standard deviation gives a more smooth result. In addition, the R_μ^{\max} was set up to slightly exceed the sampled datapoints, in order to compensate for the finite sample size. Examples of fits are shown in Fig. A.3.2. Moreover, the dependence of R_μ^{\max} on the travelled distance d was successfully parametrised as well. It turned out that the fit parameters a_{E_μ} and b_{E_μ} from the E_μ -dependent fit changed linearly (in appropriate scales) with distance, as shown in Fig. A.3.3. The corresponding fitting function for the $a_{E_\mu}(d)$ fit was

$$a_{E_\mu}(d) = a_{\text{dist}} \cdot \log_{10}(d) + b_{\text{dist}}, \quad (\text{A.3.2})$$

and for $b_{E_\mu}(d)$:

$$b_{E_\mu}(d) = a_{\text{dist}} \cdot d + b_{\text{dist}}. \quad (\text{A.3.3})$$

Inserting Eq. A.3.2 and A.3.3 and the fit parameters from Fig. A.3.3 into Eq. A.3.1 allowed for a swift computation of the maximal expected deflection for each individual muon as:

$$R_\mu^{\max}(E_\mu, d_{\max}) = 10^{[\log_{10}(\frac{d_{\max}}{\text{m}}) \cdot 0.67971202 - 3.07154976] \cdot \log_{10}(\frac{E_\mu}{\text{GeV}}) - 753778.571 \cdot \frac{d_{\max}}{\text{m}} + 3.97088084} \text{ m}, \quad (\text{A.3.4})$$

where $d_{\max} = \frac{\text{site depth}}{\cos \theta}$. It was confirmed that simulating more muons at highest energies (and hence maximal travelled distances) caused more a_{E_μ} and b_{E_μ} points to align along the distance-dependent fit. However, propagation of such energetic muons was computationally intensive and further extension of the fit range was not needed. After concluding the study, Eq. A.3.4 was implemented in muon propagation routine of gSeaGen, which was used in the CORSIKA MC productions used within this thesis.

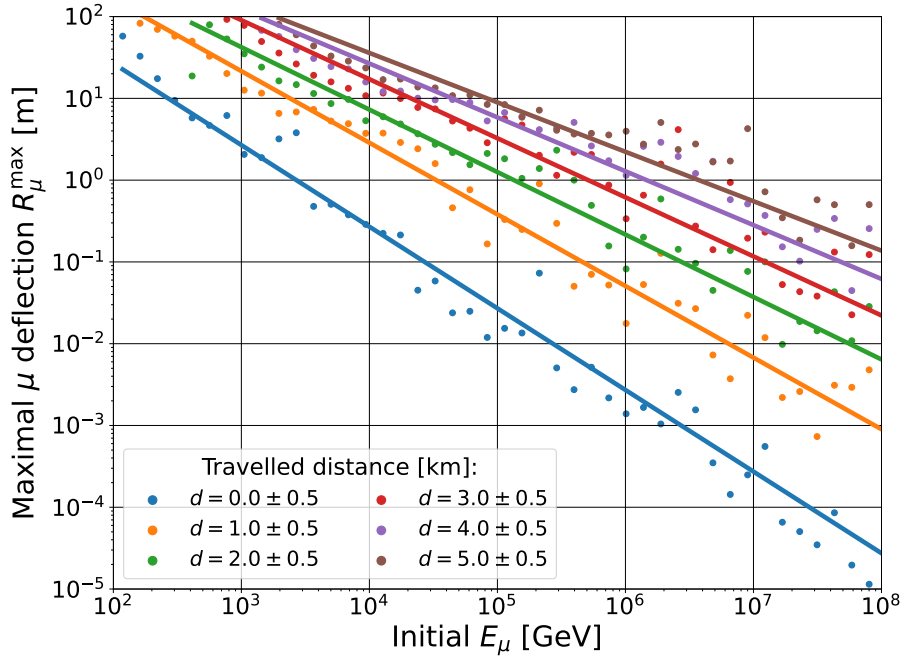
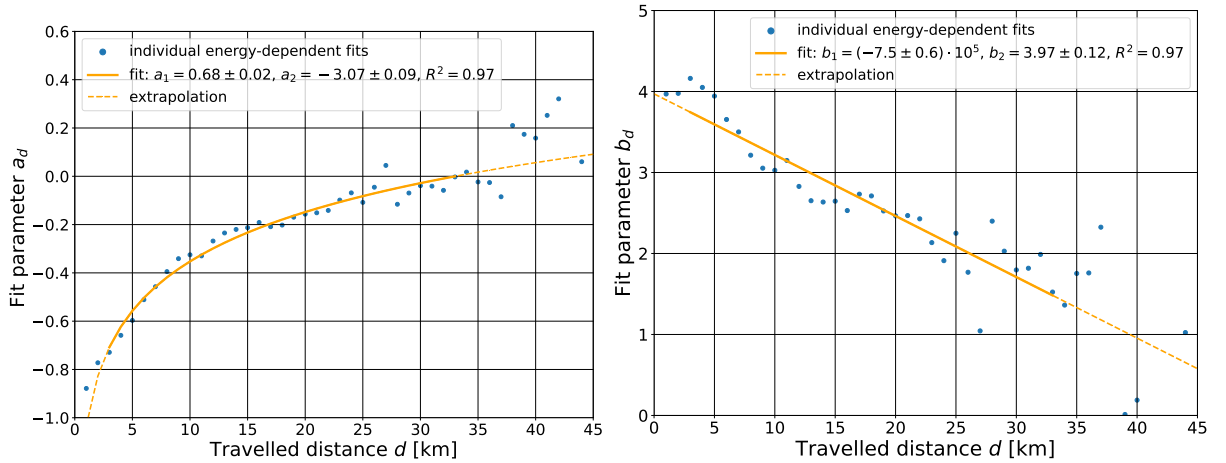


FIGURE A.3.2.: Maximal lateral muon deflections fitted as a function of E_μ . The fits were based on Eq. A.3.1.



(A) Dependence of the fit parameter a_{E_μ} on the distance (B) Dependence of the fit parameter b_{E_μ} on the distance.

FIGURE A.3.3.: Energy-dependent fit parameters of the maximal lateral muon deflection fitted as functions of travelled distance.

A.3.2. Computation of DistaMax

DistaMax is a measure of the lateral size of the CORSIKA shower used in gSeaGen. It is the maximal lateral distance of a muon in the shower to the primary trajectory line, evaluated at the sea level, before the muon propagation through water (see Fig. A.3.4). DistaMax is computed at sea level, because it is used in the propagation routine itself. The lateral distance Dista for each muon is simply the shortest distance from the muon position to the primary trajectory and is computed from Eq. A.2.5. To take into account the fact that muons scatter on their way to the

can, $Dista$ of each muon is increased by an estimate of how far could it laterally deflect, given its energy and the distance it has to travel (Eq. A.3.4). It is important to note that only muons that have sufficient range (energy) to reach the can are considered in the evaluation of $DistaMax$, to avoid an overestimation. The muons below the range threshold are not propagated at all.

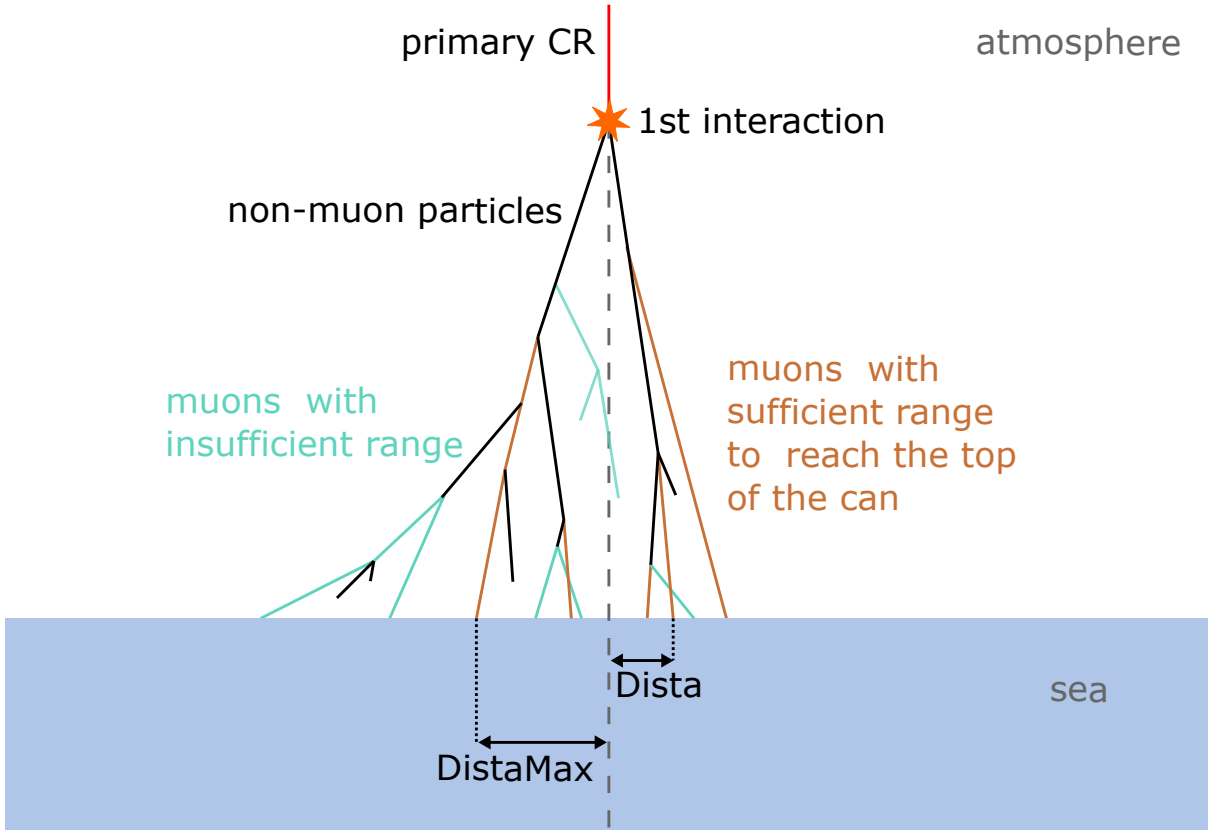


FIGURE A.3.4.: Sketch demonstrating the meaning of $Dista$ and $DistaMax$. A vertical shower has been drawn for simplicity.

A.3.3. Reorientation of CORSIKA showers

The way for gSeaGen to ensure that an event will hit the detector is by moving it around, such that its trajectory (inferred from the direction before propagation) will cross the detector volume. As a vital part of this work, a fundamental rework of CORSIKA shower re-orientation in gSeaGen was performed. Previously, the showers were only horizontally shifted in the x - y plane, assuming a flat geometry. Here, a more accurate approach was introduced, taking into account the curvature of the Earth. It was identified to play a significant role for the horizontal showers, where the differences between the flat and curved scenarios could reach hundredths of meters.

The geometry of the problem was assumed to be symmetric around the z axis, going through the centre of the Earth and the centre of the can (see Fig. A.3.5). The Earth's shape was approximated as a perfect sphere with radius $R_{Earth} = 6371.315$ km, matching the CORSIKA simulation [5]. This allowed to arbitrarily rotate showers around the Earth without changing the physics of an event (keeping the same altitude). The only requirement for the rotation was that the shower trajectory, evaluated from the initial position and direction of the primary, should intersect the can. When processing a CORSIKA output file, the initial shower position is always at the sea level at $(0, 0, D)$

(• violet point in Fig. A.3.5), where D is the depth at which the detector is located. The origin of the coordinate system is located at the centre of the base of the can (see Sec. 4.3.2). The shower in its original orientation will not intersect the can unless it happens to be vertical, hence it has to be rotated. In addition, including such a random rotation is necessary to avoid a directional bias in the simulation.

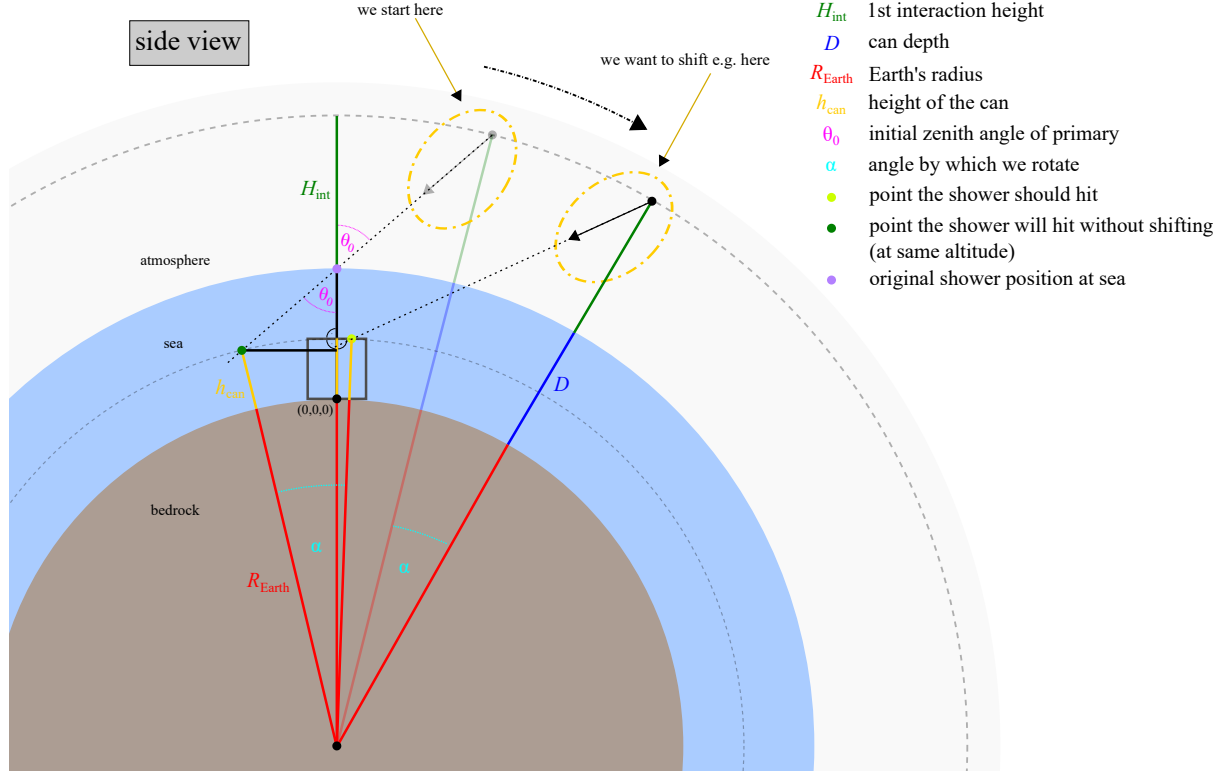


FIGURE A.3.5.: Side view of the geometry of rotating the shower. It could be either $x - y$ or $x - z$ plane, since the problem was assumed to be completely symmetric around the z axis.

A.3.3.1. Computation of the required rotation

To evaluate the rotation matrix M , required for a shower trajectory to intersect a given point • ($x_{\text{can}}, y_{\text{can}}, z_{\text{can}}$), one must follow the steps:

1. The point • (x_p, y_p, z_p), where the initial primary trajectory intersects with the sphere of radius $r = R_{\text{Earth}} + z_{\text{can}}$, centred on the centre of the Earth (see Fig. A.3.5) must be found. It is sufficient to find the distance to that point, since the direction $(c_x^p, c_y^p, c_z^p) = (c_x^{\text{sea}}, c_y^{\text{sea}}, c_z^{\text{sea}})$ is already known (here the shorthand notation for directional cosines from Sec. A.2.2 is used). Using the result from Sec. A.2.3, the sought distance $d_{\text{intersect}}$ is the solution to the quadratic equation:

$$0 = a \cdot d_{\text{intersect}}^2 + b \cdot d_{\text{intersect}} + c$$

with the coefficients:

$$a = 1, \tag{A.3.5}$$

$$b = 2 \cdot (c_x^p x_1 + c_y^p y_1 + c_z^p z_1), \quad (\text{A.3.6})$$

$$c = x_1^2 + y_1^2 + z_1^2 - r^2, \quad (\text{A.3.7})$$

where (x_1, y_1, z_1) can be set to $\bullet (x_{\text{sea}}, y_{\text{sea}}, z_{\text{sea}})$, i.e. the original shower position at sea. There are in general two solutions for $d_{\text{intersect}}$:

$$d_{\text{intersect}} = \frac{-b \pm \sqrt{b^2 - 4ac}}{2a}, \quad (\text{A.3.8})$$

however only the smaller distance is of interest, as the larger one is to the intersection point on the other side of the sphere approximating the Earth. Thus, after inserting Eq. A.3.5, A.3.6, A.3.7, and $r = R_{\text{Earth}} + z_{\text{can}}$ into Eq. A.3.8, the solution is:

$$d_{\text{intersect}} = -(c_x^p x_{\text{sea}} + c_y^p y_{\text{sea}} + c_z^p z_{\text{sea}}) \pm \sqrt{(c_x^p x_{\text{sea}} + c_y^p y_{\text{sea}} + c_z^p z_{\text{sea}})^2 - [x_{\text{sea}}^2 + y_{\text{sea}}^2 + z_{\text{sea}}^2 - (R_{\text{Earth}} + z_{\text{can}})^2]}. \quad (\text{A.3.9})$$

Using the obtained distance from $(x_{\text{sea}}, y_{\text{sea}}, z_{\text{sea}})$, the intersection point can be computed as:

$$\begin{pmatrix} x_p \\ y_p \\ z_p \end{pmatrix} = \begin{pmatrix} x_{\text{sea}} + c_x^p \cdot d_{\text{intersect}} \\ y_{\text{sea}} + c_y^p \cdot d_{\text{intersect}} \\ z_{\text{sea}} + c_z^p \cdot d_{\text{intersect}} \end{pmatrix} \quad (\text{A.3.10})$$

2. After the $\bullet (x_p, y_p, z_p)$ was found, the next step is to determine a rotation necessary to move it to $\bullet (x_{\text{can}}, y_{\text{can}}, z_{\text{can}})$.

a) First, the axis of rotation described by a vector \vec{a} must be identified. If the vectors pointing from the origin of the coordinate system (centre of the Earth) to (x_p, y_p, z_p) and $(x_{\text{can}}, y_{\text{can}}, z_{\text{can}})$ will be denoted as \vec{u} and \vec{v} respectively, then \vec{a} will be a vector orthogonal to them (see Fig. A.3.6). The orthogonal vector can be found from the cross-product:

$$\vec{a} = \vec{u} \times \vec{v} = \begin{bmatrix} y_p z_{\text{can}} - z_p y_{\text{can}} \\ z_p x_{\text{can}} - x_p z_{\text{can}} \\ x_p y_{\text{can}} - y_p x_{\text{can}} \end{bmatrix}.$$

For the rotation, the versor (unit vector) \hat{a} must be computed:

$$\hat{a} = \frac{\vec{a}}{\|\vec{a}\|} = \begin{bmatrix} a_x \\ a_y \\ a_z \end{bmatrix} = \frac{1}{\sqrt{(y_p z_{\text{can}} - z_p y_{\text{can}})^2 + (z_p x_{\text{can}} - x_p z_{\text{can}})^2 + (x_p y_{\text{can}} - y_p x_{\text{can}})^2}} \begin{bmatrix} y_p z_{\text{can}} - z_p y_{\text{can}} \\ z_p x_{\text{can}} - x_p z_{\text{can}} \\ x_p y_{\text{can}} - y_p x_{\text{can}} \end{bmatrix}.$$

b) The second step is finding $\sin \alpha$ and $\cos \alpha$ by using:

$$\sin \alpha = \frac{\|\vec{u} \times \vec{v}\|}{\|\vec{u}\| \cdot \|\vec{v}\|} = \frac{\|\vec{a}\|}{\|\vec{u}\| \cdot \|\vec{v}\|}$$

and

$$\cos \alpha = \frac{\|\vec{u} \cdot \vec{v}\|}{\|\vec{u}\| \cdot \|\vec{v}\|}.$$

c) Finally, the rotation matrix M can be computed, as all the elements are known:

$$M = \begin{bmatrix} \cos \alpha + a_x^2(1 - \cos \alpha) & a_x a_y(1 - \cos \alpha) - a_z \sin \alpha & a_x a_z(1 - \cos \alpha) + a_y \sin \alpha \\ a_y a_x(1 - \cos \alpha) + a_z \sin \alpha & \cos \alpha + a_y^2(1 - \cos \alpha) & a_y a_z(1 - \cos \alpha) - a_x \sin \alpha \\ a_z a_x(1 - \cos \alpha) - a_y \sin \alpha & a_z a_y(1 - \cos \alpha) + a_x \sin \alpha & \cos \alpha + a_z^2(1 - \cos \alpha) \end{bmatrix}. \quad (\text{A.3.11})$$

Derivation of Eq. A.3.11 may be found in Sec. 9.2 of [221]. Matrix M can be applied both to position and direction vectors:

$$\begin{bmatrix} x \\ y \\ z \end{bmatrix}_{\text{rotated}} = M \begin{bmatrix} x \\ y \\ z \end{bmatrix},$$

$$\begin{bmatrix} c_x \\ c_y \\ c_z \end{bmatrix}_{\text{rotated}} = M \begin{bmatrix} c_x \\ c_y \\ c_z \end{bmatrix}.$$

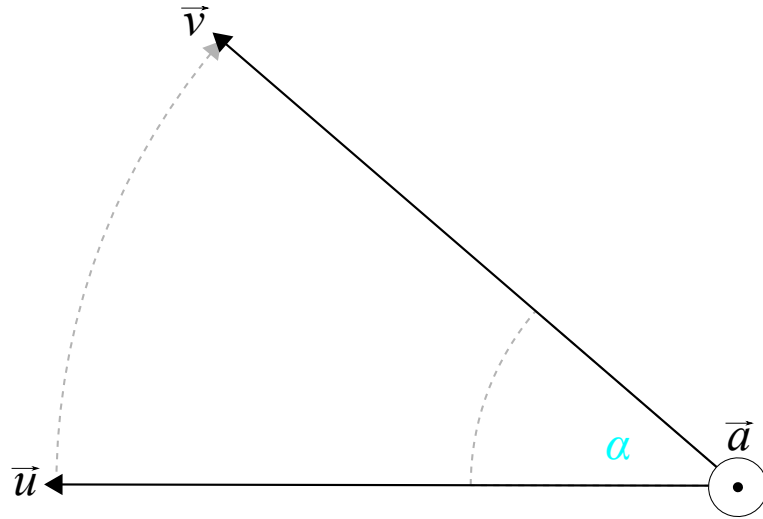


FIGURE A.3.6.: Sketch of the vector \vec{u} rotated by an angle α around an axis of rotation, described by an orthogonal vector \vec{a} .

A.3.3.2. Rotation of showers around the Earth

The procedure of reorienting the CORSIKA showers is multi-staged:

1. The primary direction rotated such that the trajectory intersects the middle of the can: $(0, 0, \frac{h_{\text{can}}}{2})$ is computed:

$$\begin{bmatrix} c_{x,\text{mid}} \\ c_{y,\text{mid}} \\ c_{z,\text{mid}} \end{bmatrix} = M_{\text{mid}} \cdot \begin{bmatrix} c_{x,\text{sea}} \\ c_{y,\text{sea}} \\ c_{z,\text{sea}} \end{bmatrix},$$

where h_{can} is the height of the can and M_{mid} is computed according to Sec. A.3.3.1.

2. The surface of the can is increased by DistaMax (see Sec. A.3.2) by adding it in projection to the can radius and height to account for lateral spread of the muons due to the scattering.

3. A point on the enlarged surface of the can is randomly picked. The code selects, whether the point will be on the top cap, or on the side of the can. The probability to land on either of the two is weighted by the top and side areas of the can (extended by DistaMax) A_{top} and A_{side} , projected onto the plane perpendicular to $[c_x^{\text{mid}}, c_y^{\text{mid}}, c_z^{\text{mid}}]$.
 - a) If the top area is selected: a random point is drawn from the circle of radius $r_{\text{can}} + \text{DistaMax} \cdot c_x^{\text{mid}}$.
 - b) If the side area is selected: a random point is drawn from half the cylinder side of radius $r_{\text{can}} + \text{DistaMax} \cdot c_x^{\text{mid}}$ and height $h_{\text{can}} + \text{DistaMax} \cdot \sqrt{1 - (c_x^{\text{mid}})^2}$. Only one half of the side is used because the shower does not ‘see’ the whole can side. This half is subsequently rotated to face the incoming primary.
4. When the point on the increased can surface $(x_{\text{can}}, y_{\text{can}}, z_{\text{can}})$ is selected, the rotation matrix M is computed for that point, following Sec. A.3.3.1.
5. The rotation by M is applied to both positions and directions of all tracks in an event: primary, muons (which will be propagated), and their parent particle tracks, containing additional information on the muon history [194]. The final effect is a coherent rotation of the entire shower around the Earth.

A.4. Performance of JMuon reconstruction

Supplementary plots showing the results of JMuon reconstruction are gathered here.

A.4.1. Zenith reconstruction

In this section, the performance of JMuon in the zenith reconstruction is briefly shown. Fig. A.4.1 shows how accurate the reconstruction is and in Fig. A.4.3 one can see that the shape of the true distribution is mostly reconstructed well, but only for cosines above 0.5. The events reconstructed as upgoing ($\cos(\theta_{\text{zenith}}^{\mu \text{ bundle}}) < 0$) are true downgoing events with their direction erroneously flipped by JMuon. The performance of the reconstruction improves dramatically if a quality cut on the JMuon likelihood \mathcal{L} is applied, as demonstrated in Fig. A.4.2.

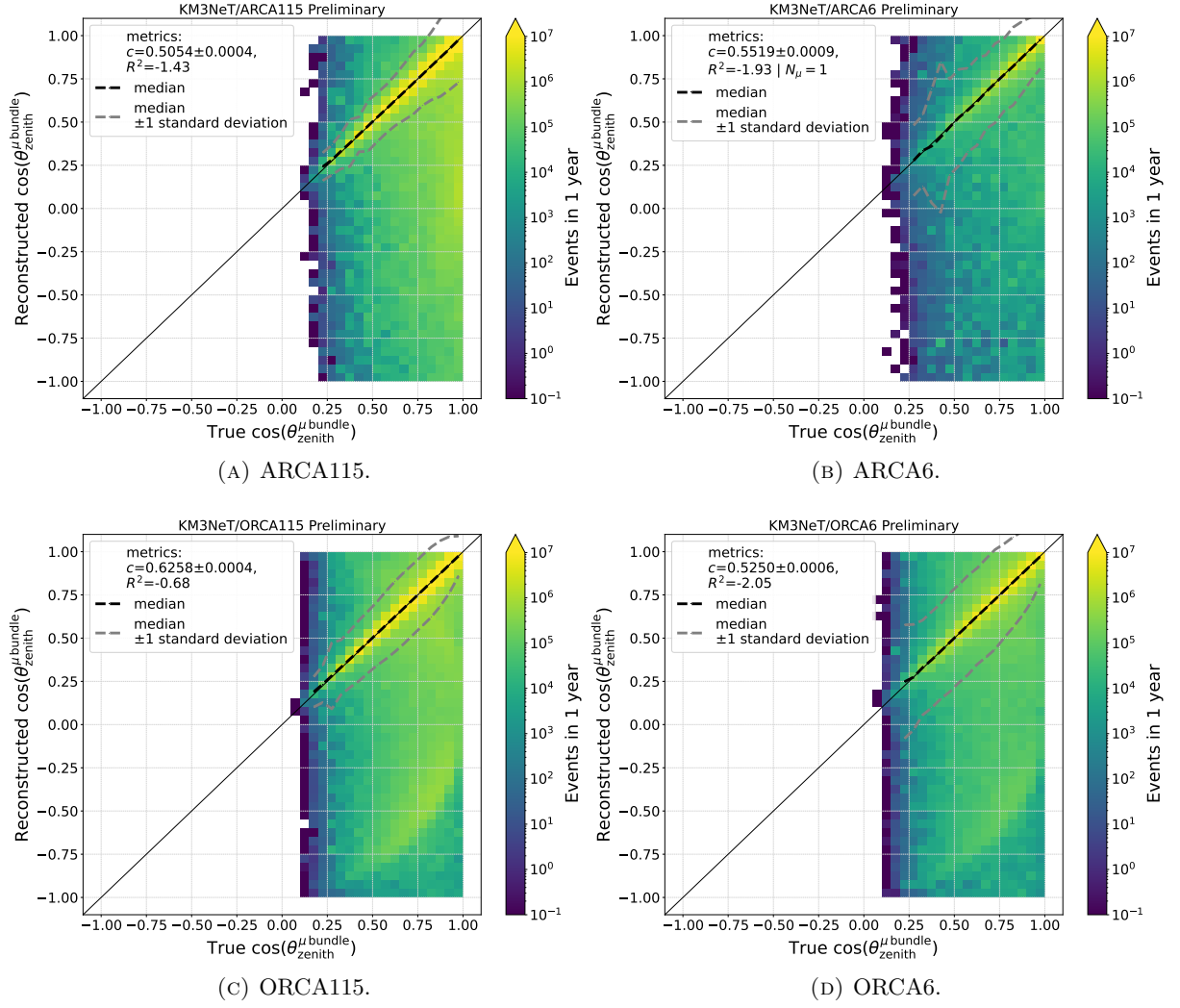


FIGURE A.4.1.: Performance of JMuon for different detector configurations, shown in terms of true vs reconstructed cosines of the zenith angles of muon bundles simulated with CORSIKA.

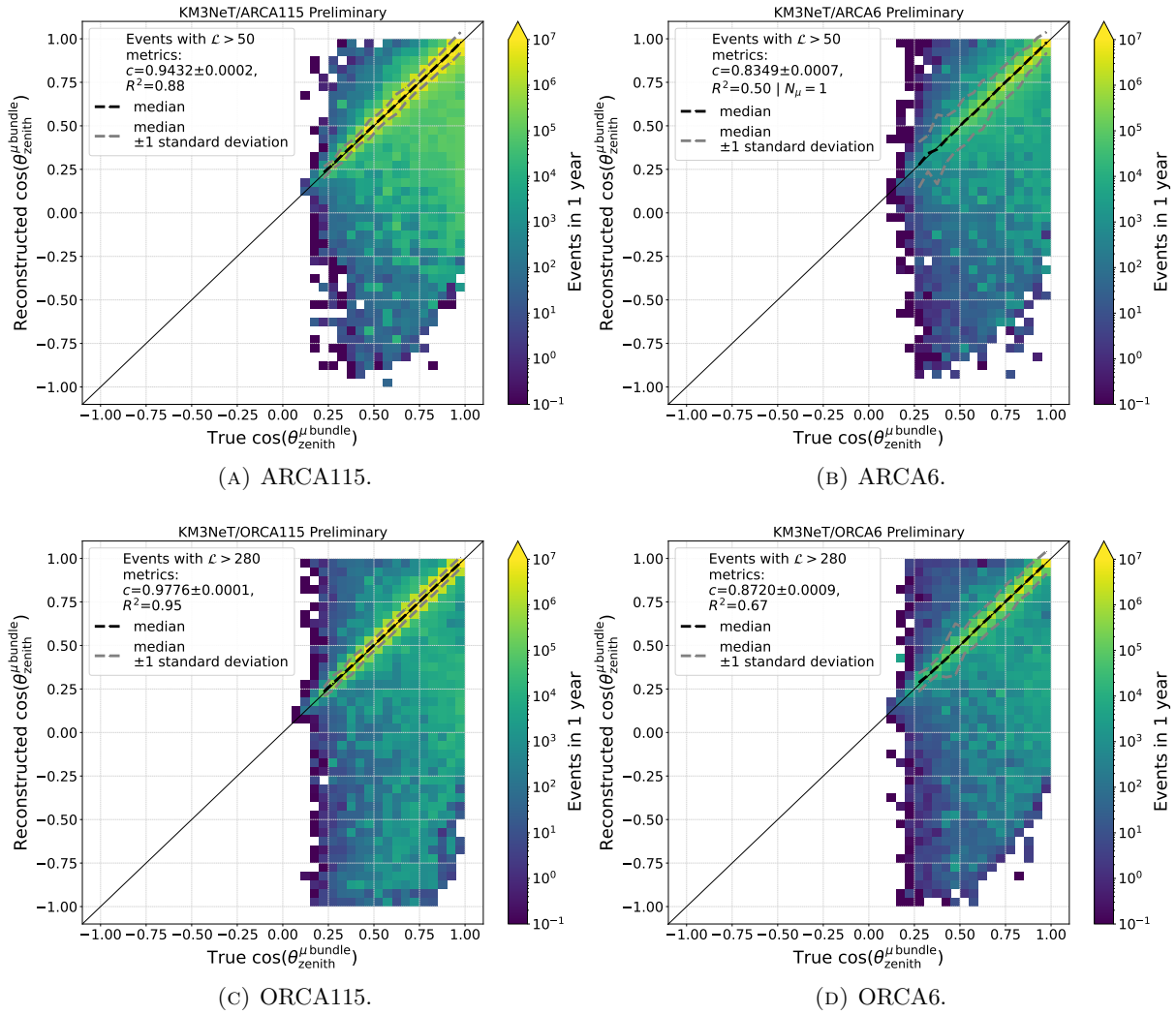


FIGURE A.4.2.: Performance of JMuon for different detector configurations, shown in terms of true vs reconstructed cosines of the zenith angles of muon bundles simulated with CORSIKA. The plots show the performance on the selected high-quality events (by cutting of the JMuon likelihood \mathcal{L}).

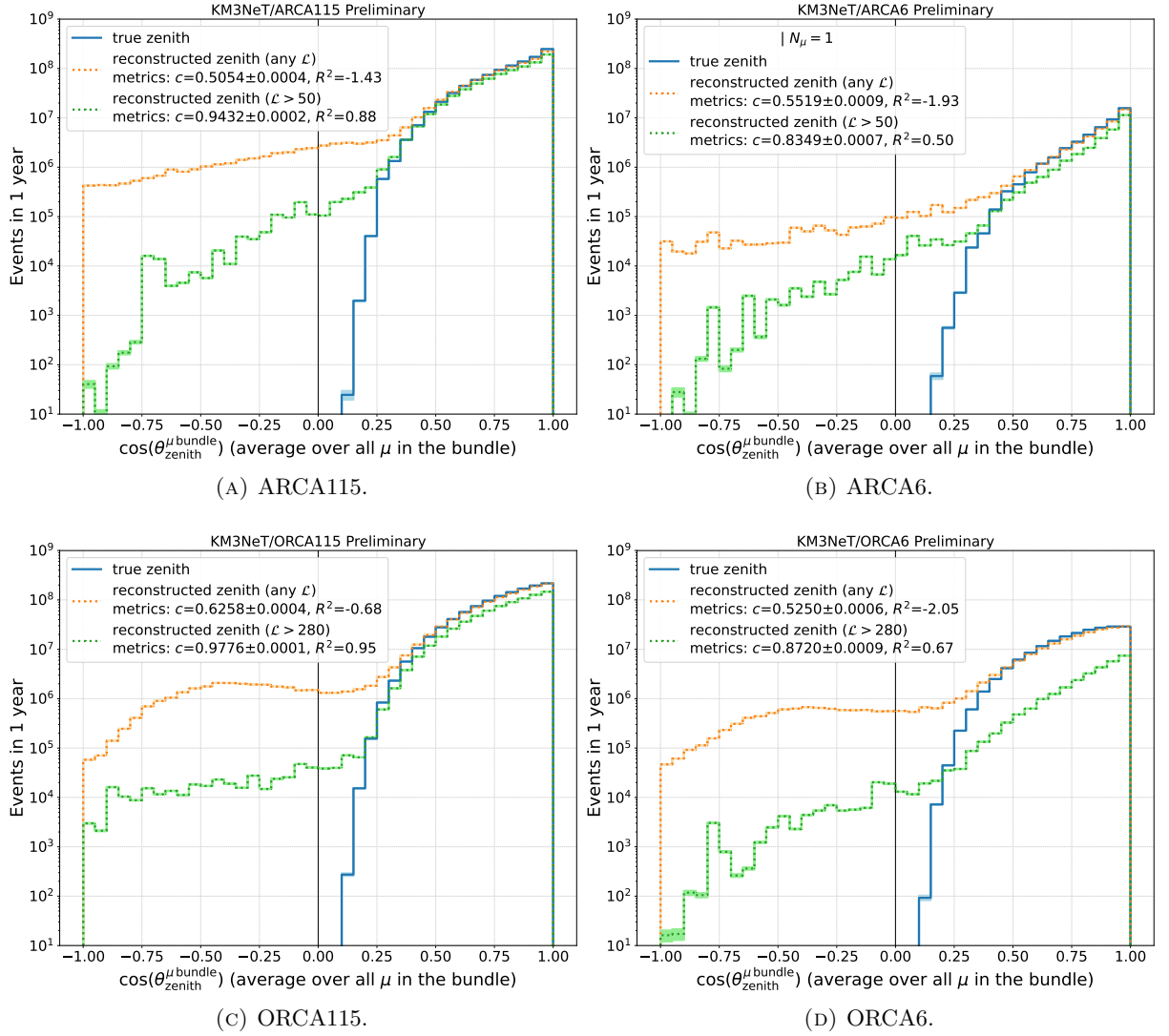


FIGURE A.4.3.: Performance of JMuon shown in terms 1D distributions of cosines of the zenith angles of muon bundles simulated with CORSIKA. The green histogram is obtained by cutting of the JMuon likelihood \mathcal{L} .

A.4.2. Energy reconstruction

Here, the results of applying JMuon to the muon bundle energy reconstruction task are presented. Since they have been partially shown in Sec. 5.3.1, only the 2D plots for ARCA6, ORCA115 and ORCA6 are displayed in Fig. A.4.4, A.4.5, and A.4.6 respectively.

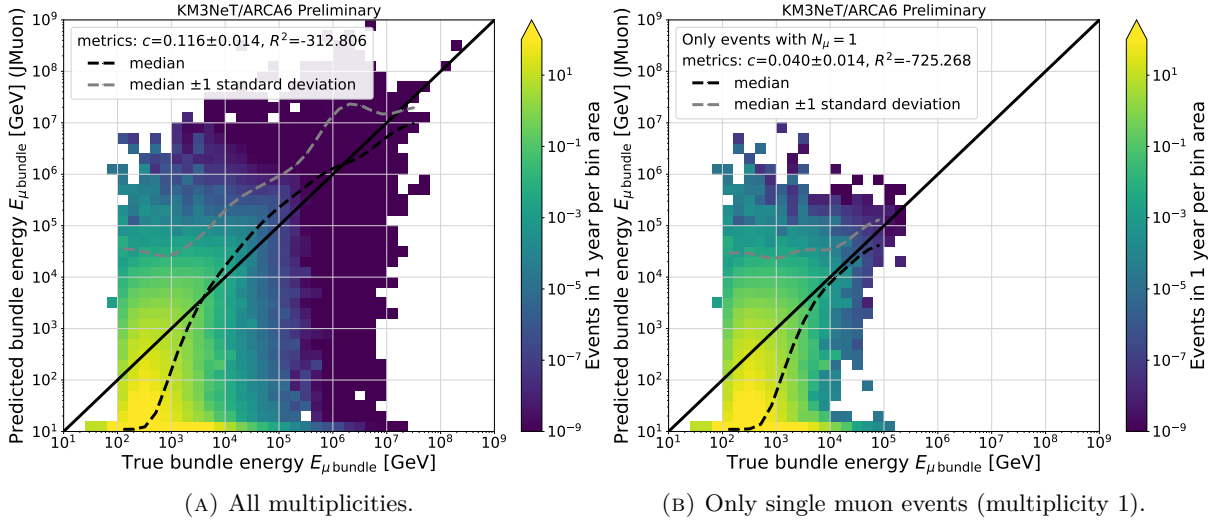


FIGURE A.4.4.: Comparison of predicted and true bundle energy for the JMuon reconstruction. The reconstruction was applied on CORSIKA MC for ARCA6.

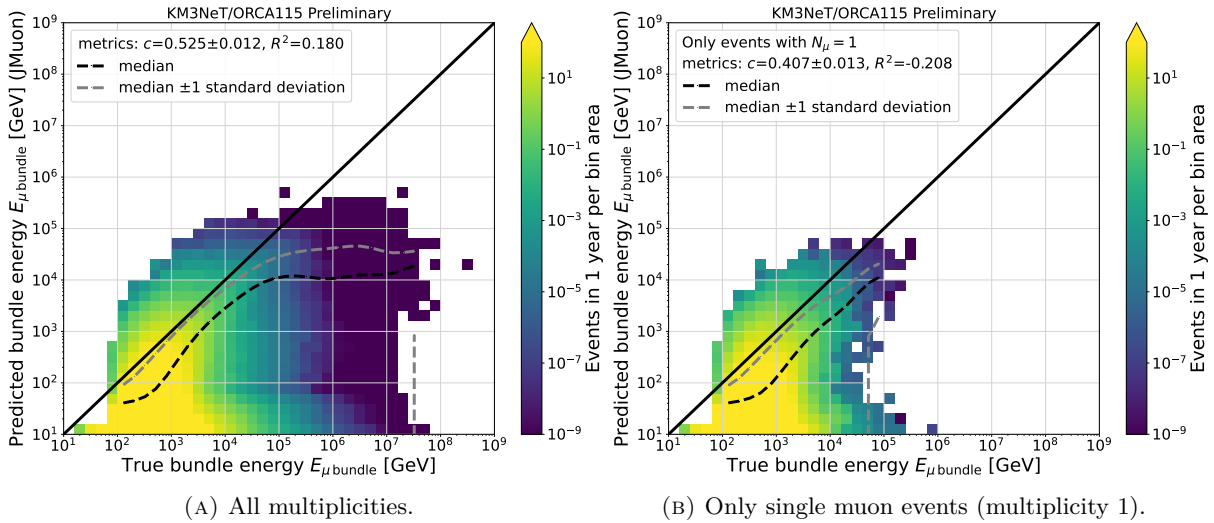


FIGURE A.4.5.: Comparison of predicted and true bundle energy for the JMuon reconstruction. The reconstruction was applied on CORSIKA MC for ORCA115.

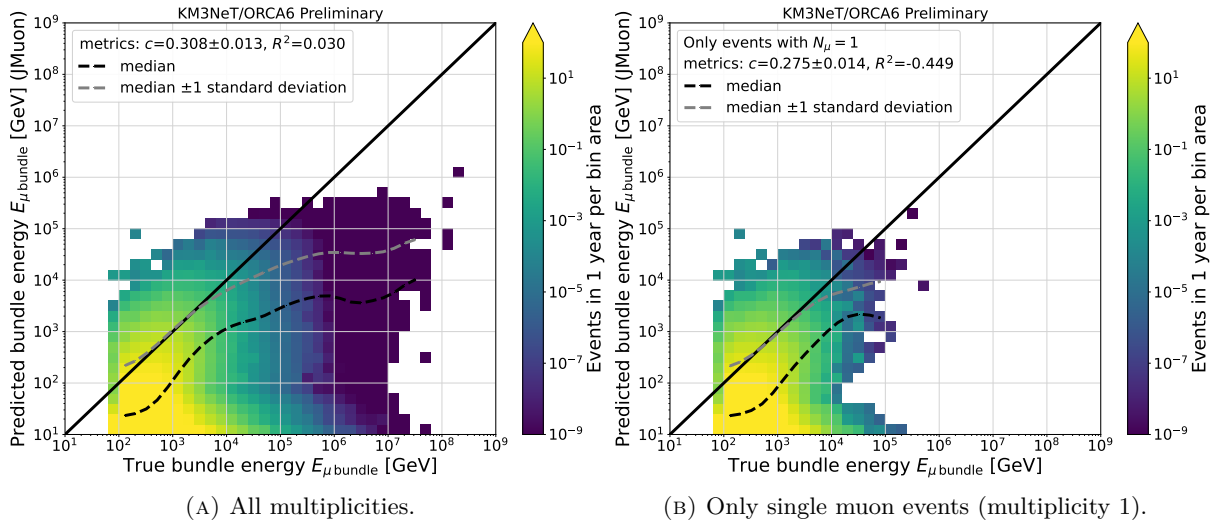


FIGURE A.4.6.: Comparison of predicted and true bundle energy for the JMuon reconstruction. The reconstruction was applied on CORSIKA MC for ORCA6.

A.5. Muon bundle reconstruction

The supplementary material for Chap. 5 is gathered in this section.

A.5.1. List of used features

Here, each of the features used in Chap. 5 is briefly described, using the following abbreviations and nomenclature:

- ToT – time over threshold. Time over which a PMT voltage exceeded a certain threshold value (differs between the PMTs). The motivation for using a threshold is noise reduction.
- Hit – a PMT is said to have a hit when its voltage exceeds the set threshold (equivalently, when ToT > 0). Each hit has a position and a direction, which correspond to the location of the PMT and the direction, which it is facing. The hit time is the time at which the threshold was exceeded.
- 3DMUON and 3DSHOWER are the dedicated track and shower triggers, as mentioned in Sec. 4.3.4. There can also be events, where both triggers were activated. In such a case they will be marked as 3DMUON_3DSHOWER.
- c_x , c_y , c_z are the directional cosines along x , y and z axes respectively. Here, the movement of the optical modules in water is not taken into account.
- Avg – average value.
- Std – standard deviation.
- Edge of the detector – an edge of the smallest enclosing cylinder around the installed DUs.

TABLE A.5.1.: Summary of all available features for the reconstruction of muon bundle properties.

Feature	Description
3DSHOWER_trig_hit_amplitude_sum	sum of 3DSHOWER hit amplitudes
3DSHOWER_trig_hit_amplitude_avg	avg 3DSHOWER hit amplitude
3DSHOWER_trig_hit_amplitude_std	std of 3DSHOWER hit amplitudes
3DMUON_trig_hit_amplitude_sum	sum of 3DMUON hit amplitudes
3DMUON_trig_hit_amplitude_avg	avg 3DMUON hit amplitude
3DMUON_trig_hit_amplitude_std	std of 3DMUON hit amplitudes
3DMUON_3DSHOWER_trig_hit_amplitude_sum	sum of 3DMUON_3DSHOWER hit amplitudes
3DMUON_3DSHOWER_trig_hit_amplitude_avg	avg 3DMUON_3DSHOWER hit amplitude
3DMUON_3DSHOWER_trig_hit_amplitude_std	std of 3DMUON_3DSHOWER hit amplitudes
distance_last_3DSHOWER_trig_hit_to_det_edge	distance between the last 3DSHOWER hit and the edge of the detector
distance_first_3DSHOWER_trig_hit_to_det_edge	distance between the first 3DSHOWER hit and the edge of the detector
first_3DSHOWER_trig_hit_pmt_dir_x	c_x of the first 3DSHOWER hit
first_3DSHOWER_trig_hit_pmt_dir_y	c_y of the first 3DSHOWER hit
first_3DSHOWER_trig_hit_pmt_dir_z	c_z of the first 3DSHOWER hit
last_3DSHOWER_trig_hit_pmt_dir_x	c_x of the last 3DSHOWER hit
last_3DSHOWER_trig_hit_pmt_dir_y	c_y of the last 3DSHOWER hit
last_3DSHOWER_trig_hit_pmt_dir_z	c_z of the last 3DSHOWER hit
3DSHOWER_trig_hits_duration	time difference between the last and first 3DSHOWER hit
distance_last_3DMUON_trig_hit_to_det_edge	distance between the last 3DMUON hit and the edge of the detector
distance_first_3DMUON_trig_hit_to_det_edge	distance between the last 3DMUON hit and the edge of the detector
first_3DMUON_trig_hit_pmt_dir_x	c_x of the first 3DMUON hit
first_3DMUON_trig_hit_pmt_dir_y	c_y of the first 3DMUON hit
first_3DMUON_trig_hit_pmt_dir_z	c_z of the first 3DMUON hit
last_3DMUON_trig_hit_pmt_dir_x	c_x of the last 3DMUON hit
last_3DMUON_trig_hit_pmt_dir_y	c_y of the last 3DMUON hit
last_3DMUON_trig_hit_pmt_dir_z	c_z of the last 3DMUON hit
3DMUON_trig_hits_duration	time difference between the last and first 3DMUON hit
distance_last_3DMUON_3DSHOWER_trig_hit_to_det_edge	distance between the last 3DMUON_3DSHOWER hit and the edge of the detector

distance_first_3DMUON_3DSHOWER_trig_hit_to_det_edge	distance between the first 3DMUON_3DSHOWER hit and the edge of the detector
first_3DMUON_3DSHOWER_trig_hit_pmt_dir_x	c_x of the first 3DMUON_3DSHOWER hit
first_3DMUON_3DSHOWER_trig_hit_pmt_dir_y	c_y of the first 3DMUON_3DSHOWER hit
first_3DMUON_3DSHOWER_trig_hit_pmt_dir_z	c_z of the first 3DMUON_3DSHOWER hit
last_3DMUON_3DSHOWER_trig_hit_pmt_dir_x	c_x of the last 3DMUON_3DSHOWER hit
last_3DMUON_3DSHOWER_trig_hit_pmt_dir_y	c_y of the last 3DMUON_3DSHOWER hit
last_3DMUON_3DSHOWER_trig_hit_pmt_dir_z	c_z of the last 3DMUON_3DSHOWER hit
3DMUON_3DSHOWER_trig_hits_duration	time difference between the last and first 3DMUON_3DSHOWER hit
3DSHOWER_trig_hits	total number of 3DSHOWER hits
3DMUON_trig_hits	total number of 3DMUON hits.
3DMUON_3DSHOWER_trig_hits	total number of 3DMUON_3DSHOWER hits
vertical_span_3DSHOWER_trig_hits	the largest vertical distance between two 3DSHOWER hits
horizontal_span_3DSHOWER_trig_hits	the largest horizontal distance between two 3DSHOWER hits
vertical_span_3DMUON_trig_hits	the largest vertical distance between two 3DMUON hits
horizontal_span_3DMUON_trig_hits	the largest horizontal distance between two 3DMUON hits
vertical_span_3DMUON_3DSHOWER_trig_hits	the largest vertical distance between two 3DMUON_3DSHOWER hits
horizontal_span_3DMUON_3DSHOWER_trig_hits	the largest horizontal distance between two 3DMUON_3DSHOWER hits
overlays	number of overlaid triggers in an event

A.5.2. Correlation matrices and dendrograms

The correlation matrices for ARCA6, ORCA115 and ORCA6 are shown in Fig. [A.5.1](#), [A.5.2](#), and [A.5.3](#). The corresponding dendrograms are plotted in Fig. [A.5.4](#), [A.5.5](#), and [A.5.6](#).

KM3NeT/ARCA6 Preliminary

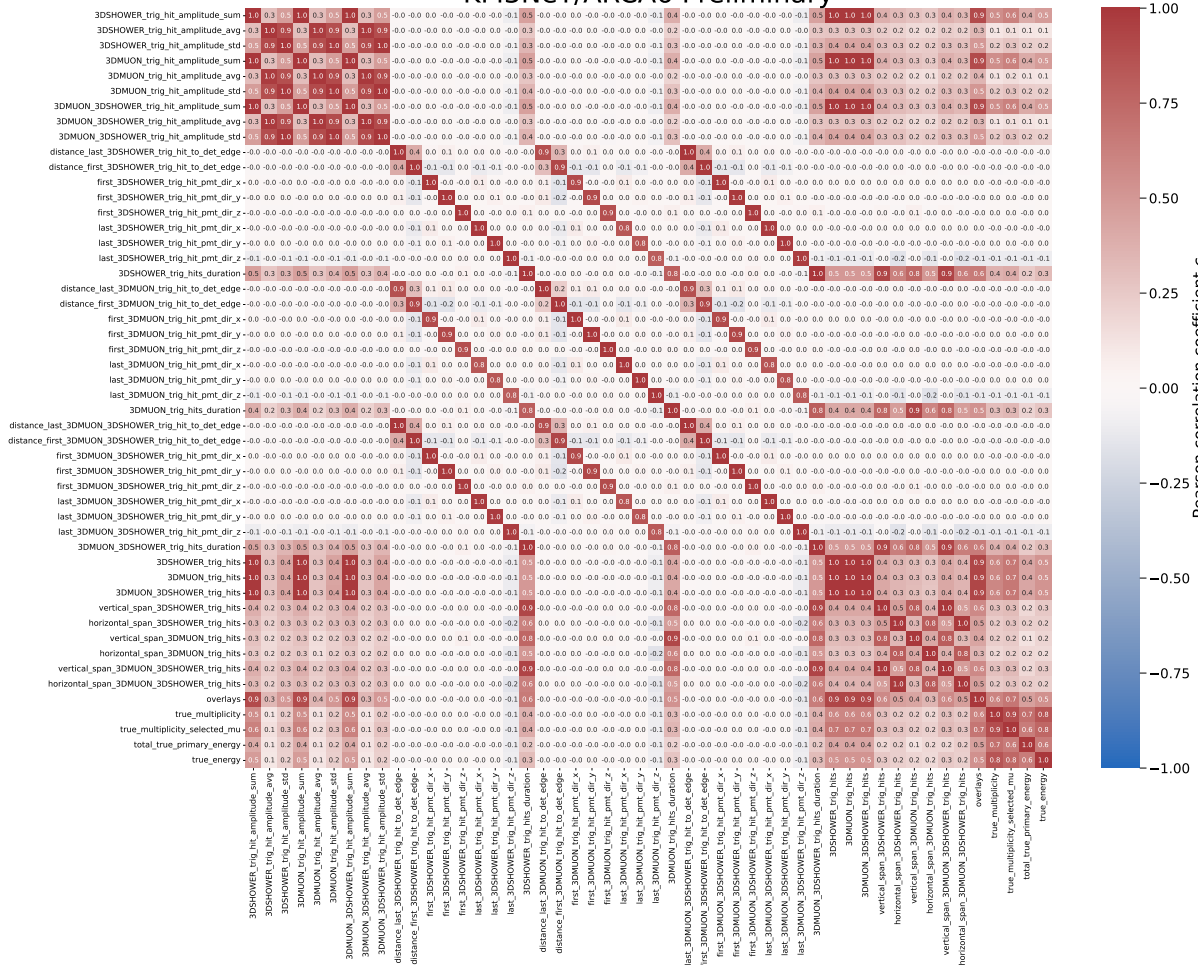


FIGURE A.5.1.: Correlation matrix with all features and potential targets for ARCA6.

KM3NeT/ORCA115 Preliminary

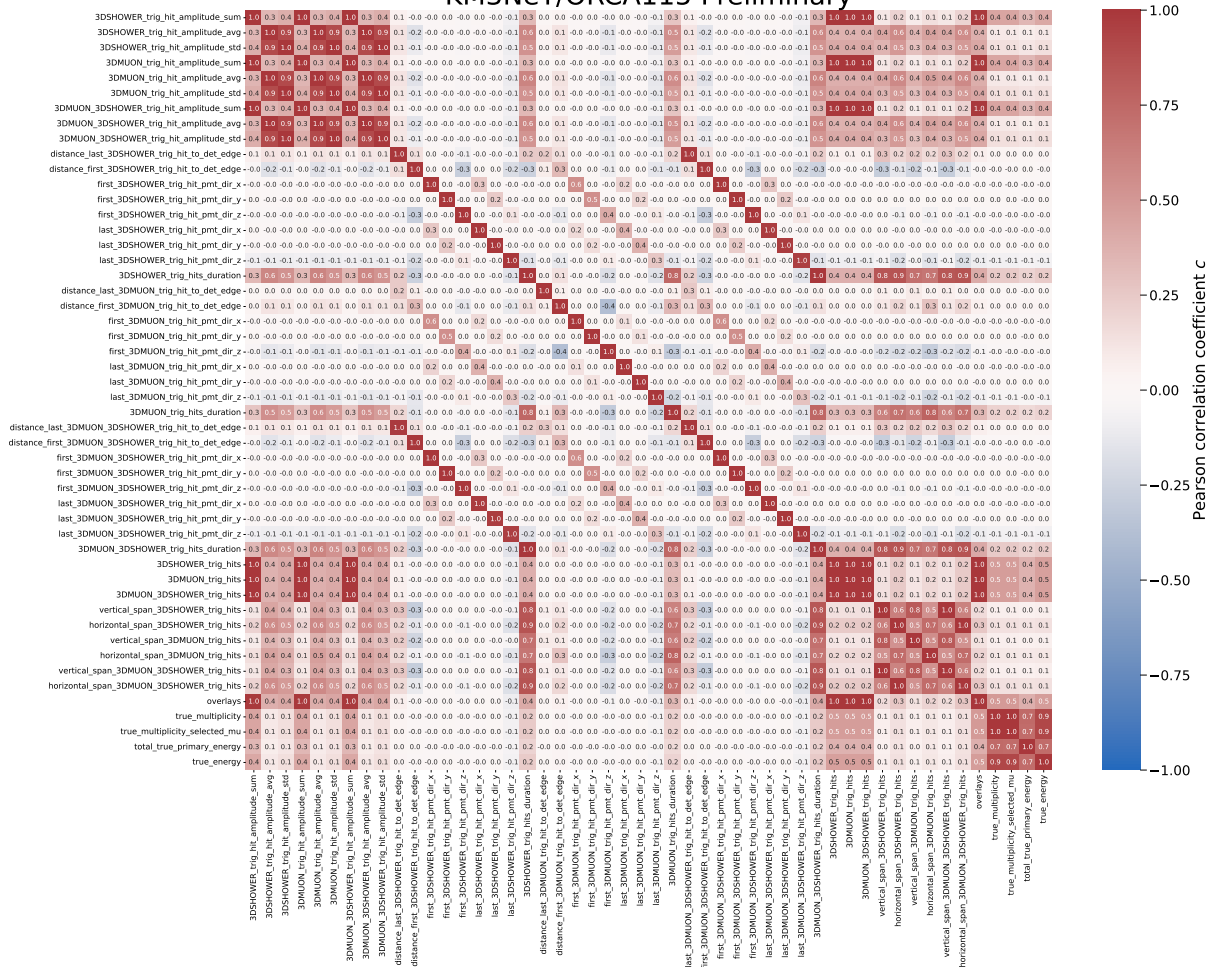


FIGURE A.5.2.: Correlation matrix with all features and potential targets for ORCA115.

KM3NeT/ORCA6 Preliminary



FIGURE A.5.3.: Correlation matrix with all features and potential targets for ORCA6.

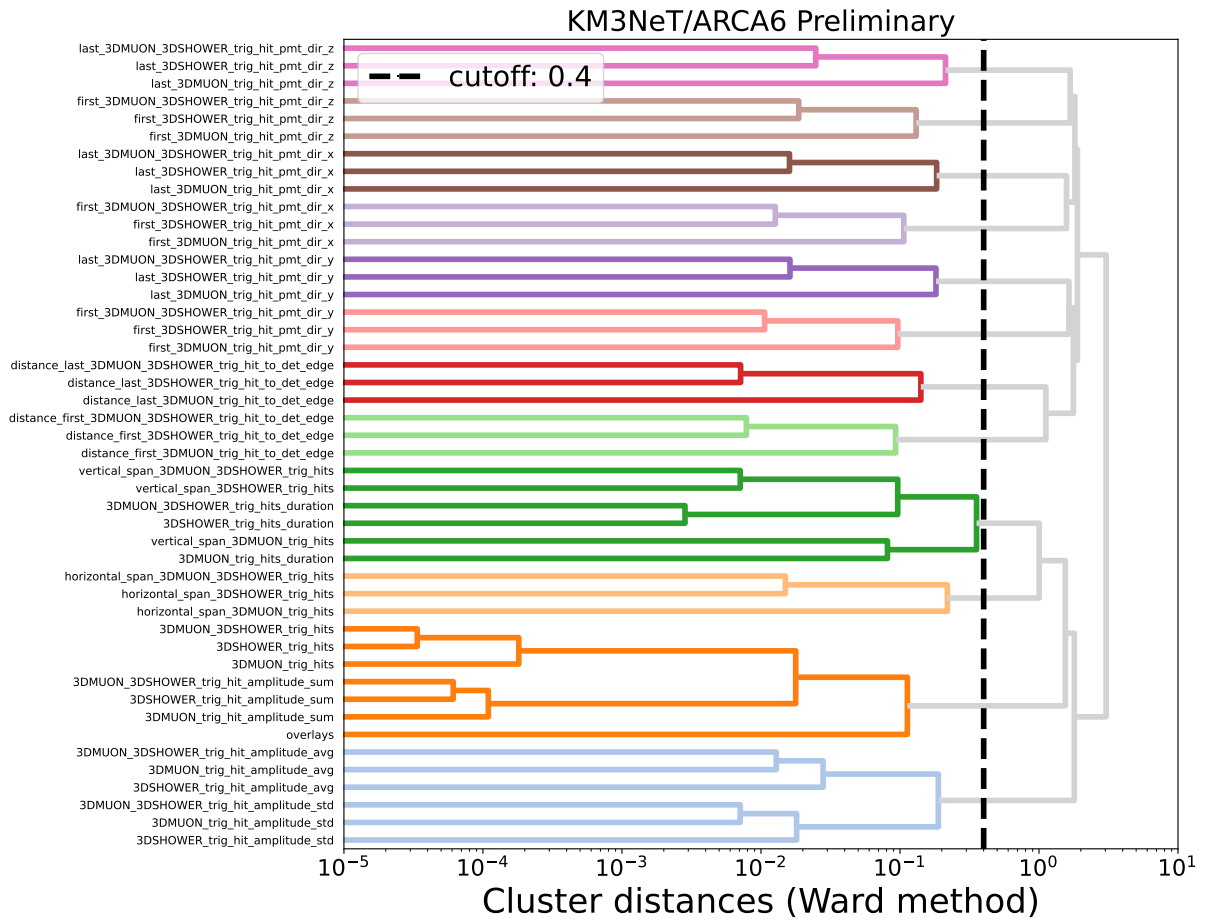


FIGURE A.5.4.: Dendrogram showing the clustering of features for ARCA6.

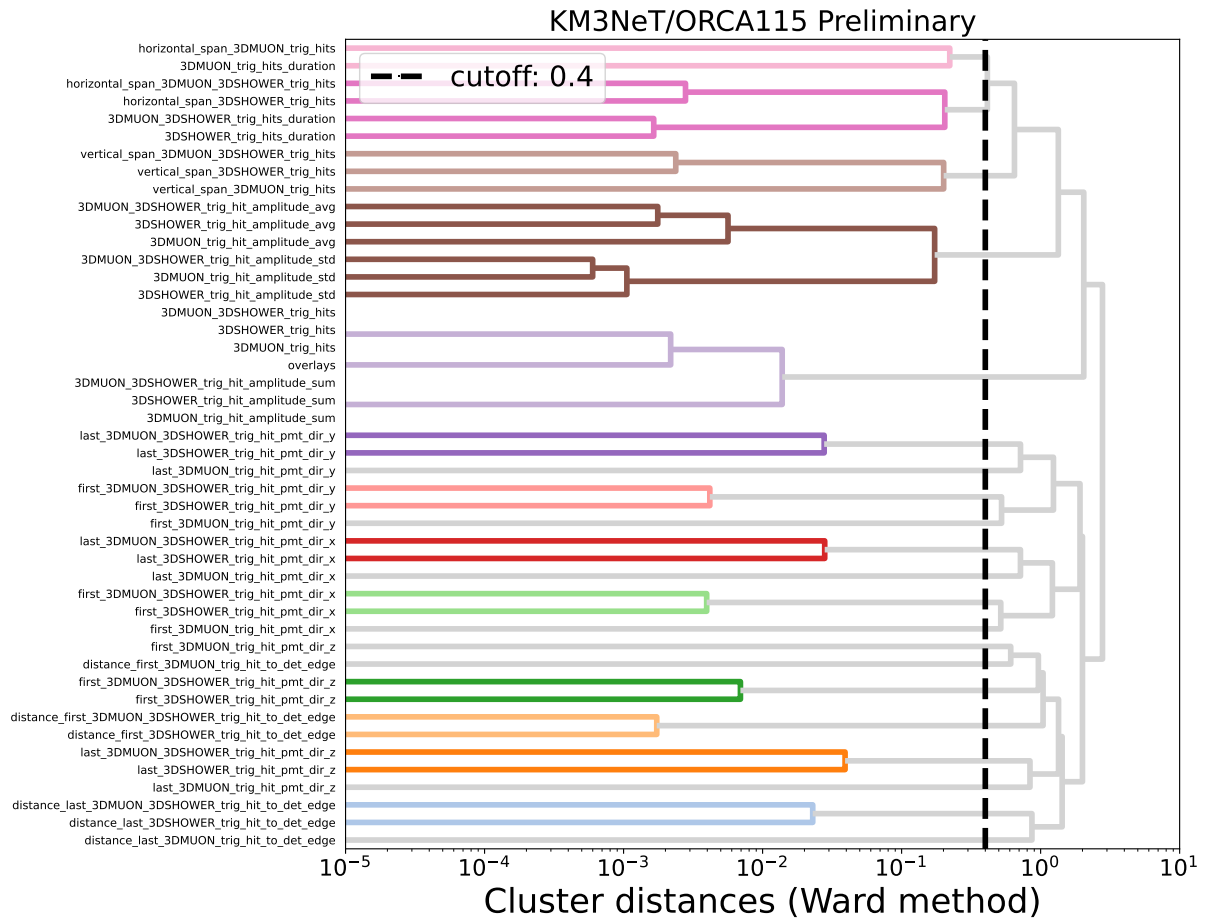


FIGURE A.5.5.: Dendrogram showing the clustering of features for ORCA115.

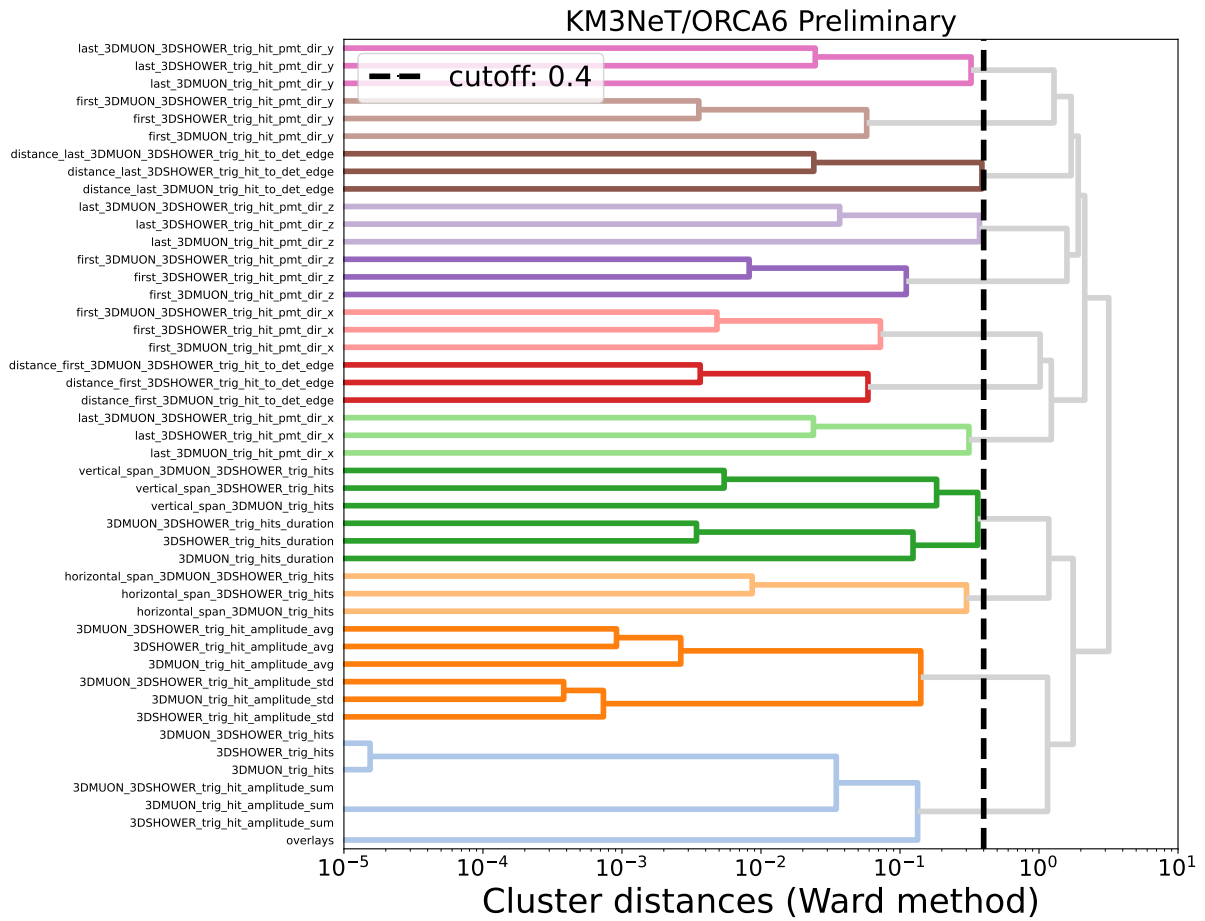


FIGURE A.5.6.: Dendrogram showing the clustering of features for ORCA6.

A.5.3. Feature importances

Feature importances for energy and multiplicity reconstructions are compiled in this section. For each of the detector configurations (ARCA6, ORCA115, ORCA6), the first one is for the energy, and the second one is for the multiplicity reconstruction. All the importances were computed on untuned LightGBM.

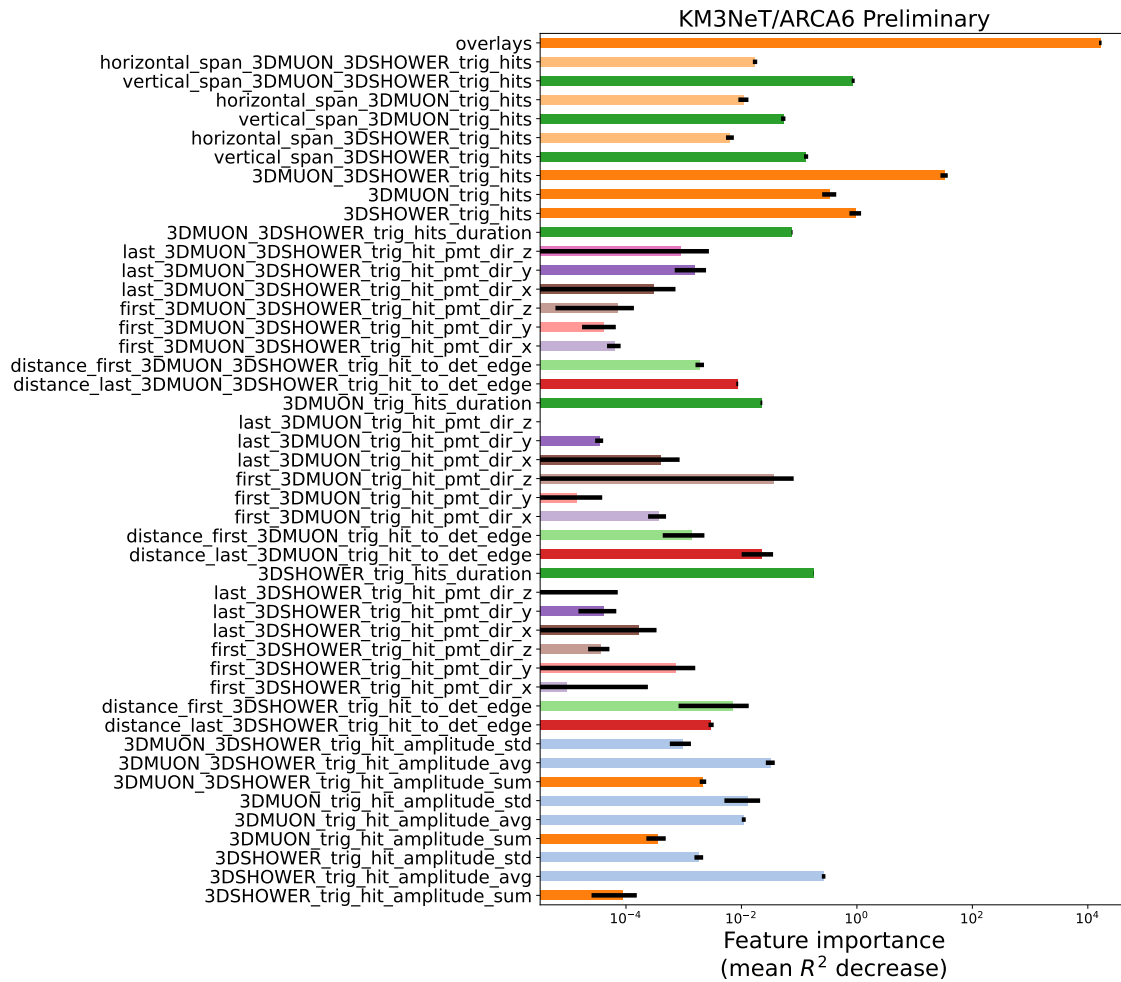


FIGURE A.5.7.: Feature importance for ARCA6 for the energy reconstruction.

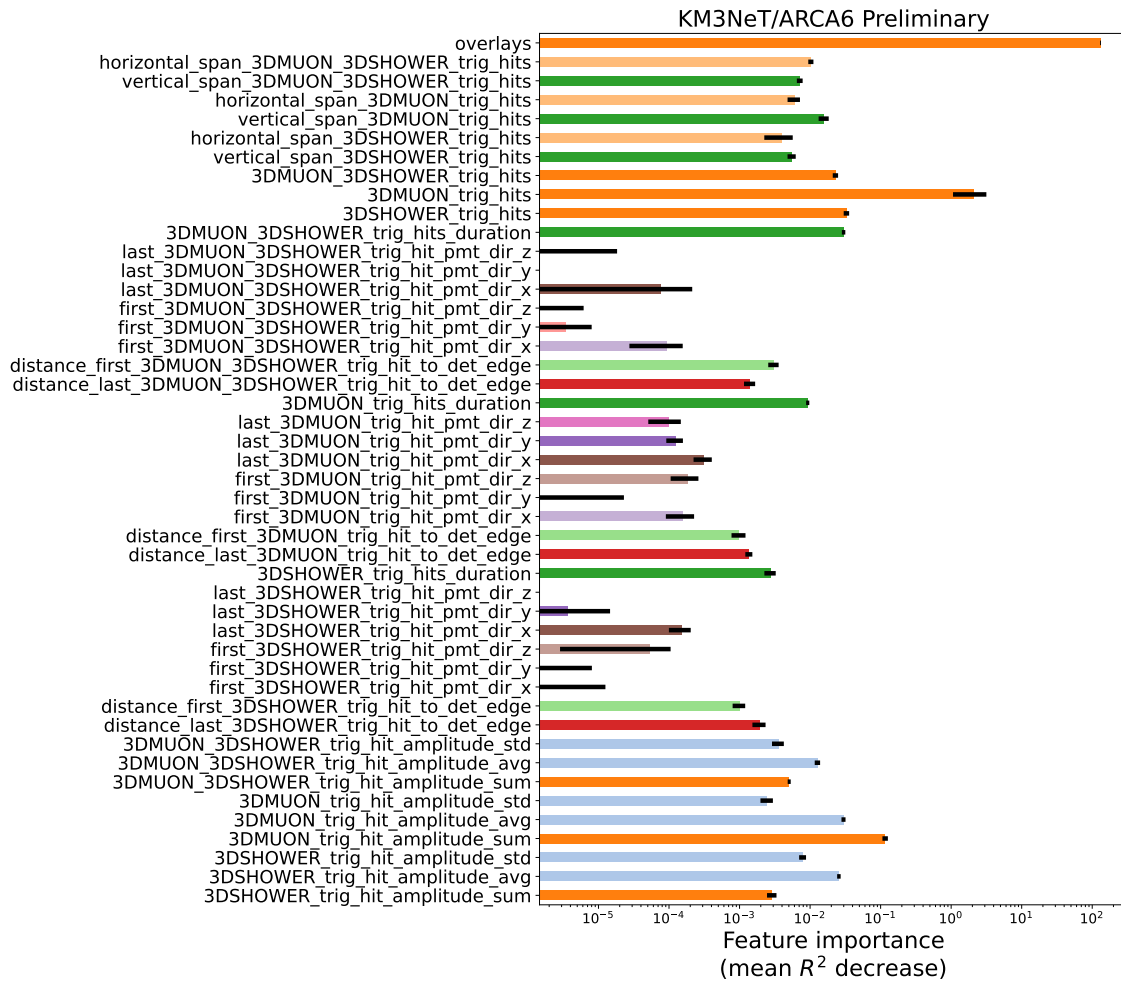


FIGURE A.5.8.: Feature importance for ARCA6 for the multiplicity reconstruction.

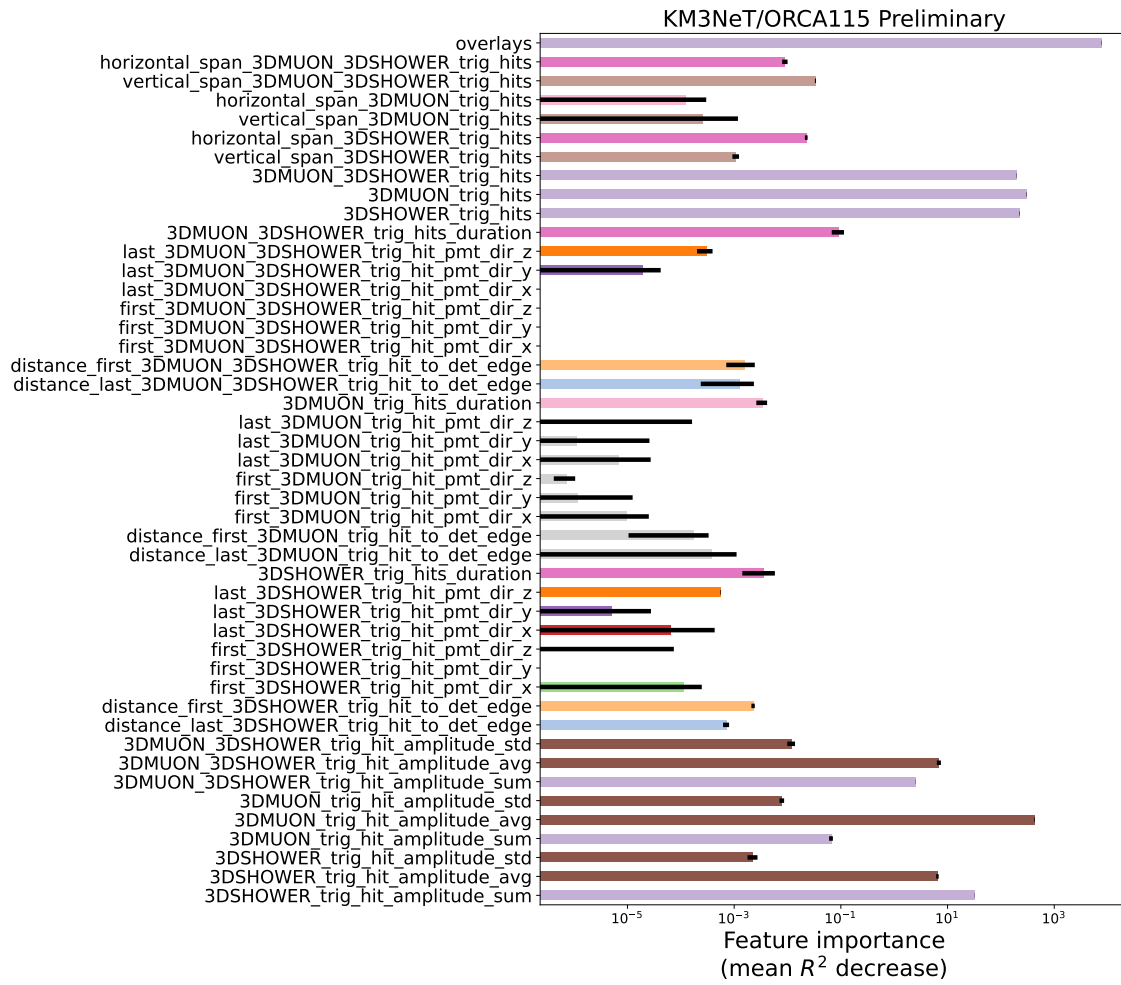


FIGURE A.5.9.: Feature importance for ORCA115 for the energy reconstruction.

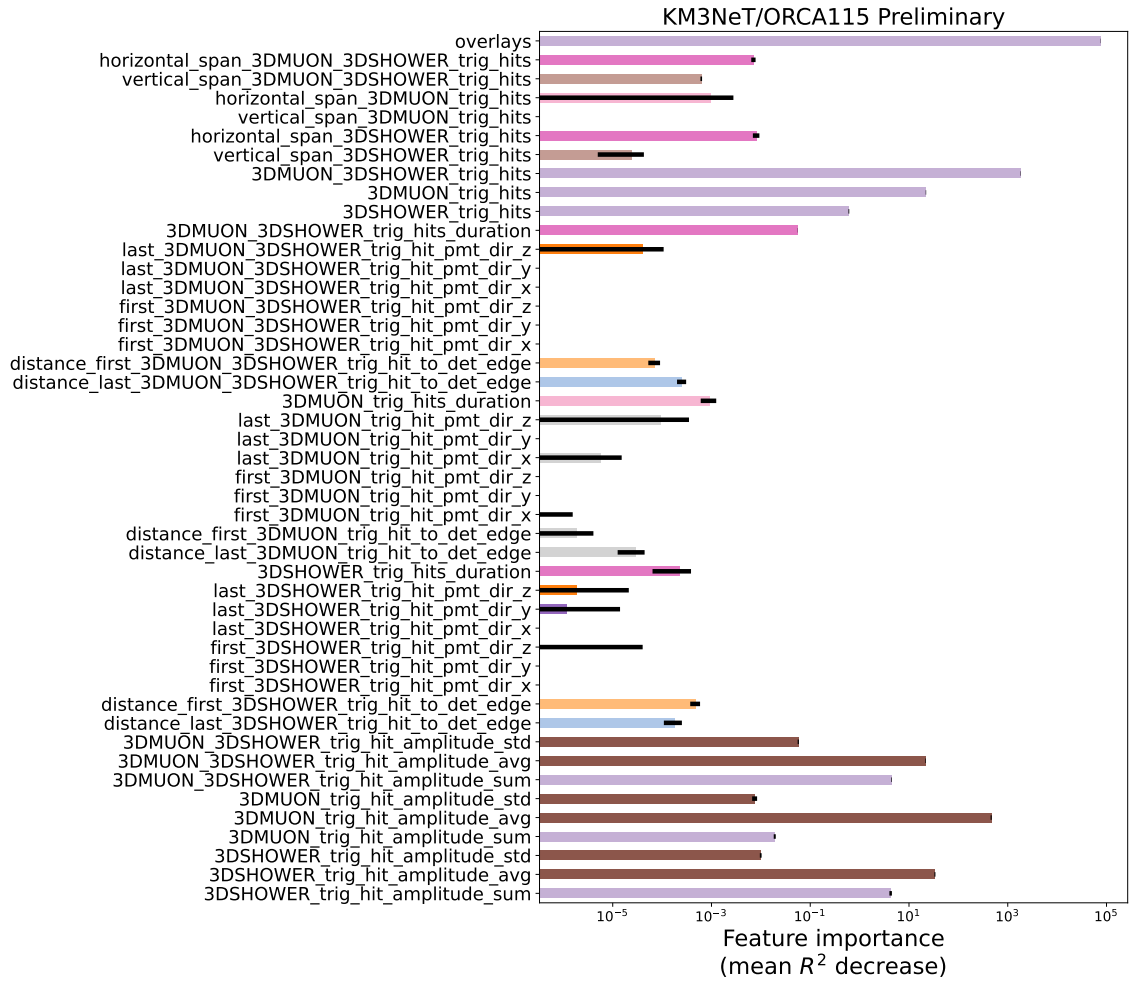


FIGURE A.5.10.: Feature importance for ORCA115 for the multiplicity reconstruction.

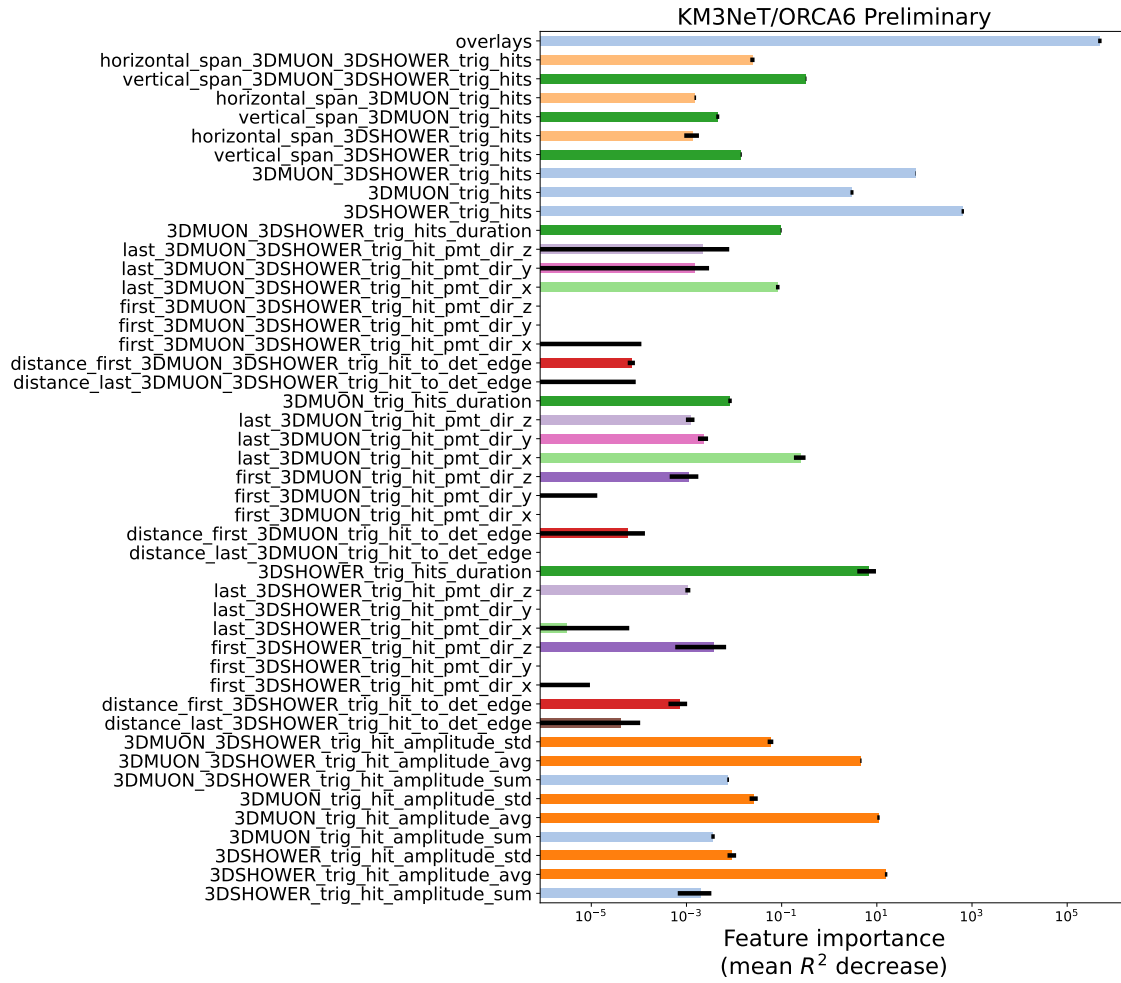


FIGURE A.5.11.: Feature importance for ORCA6 for the energy reconstruction.

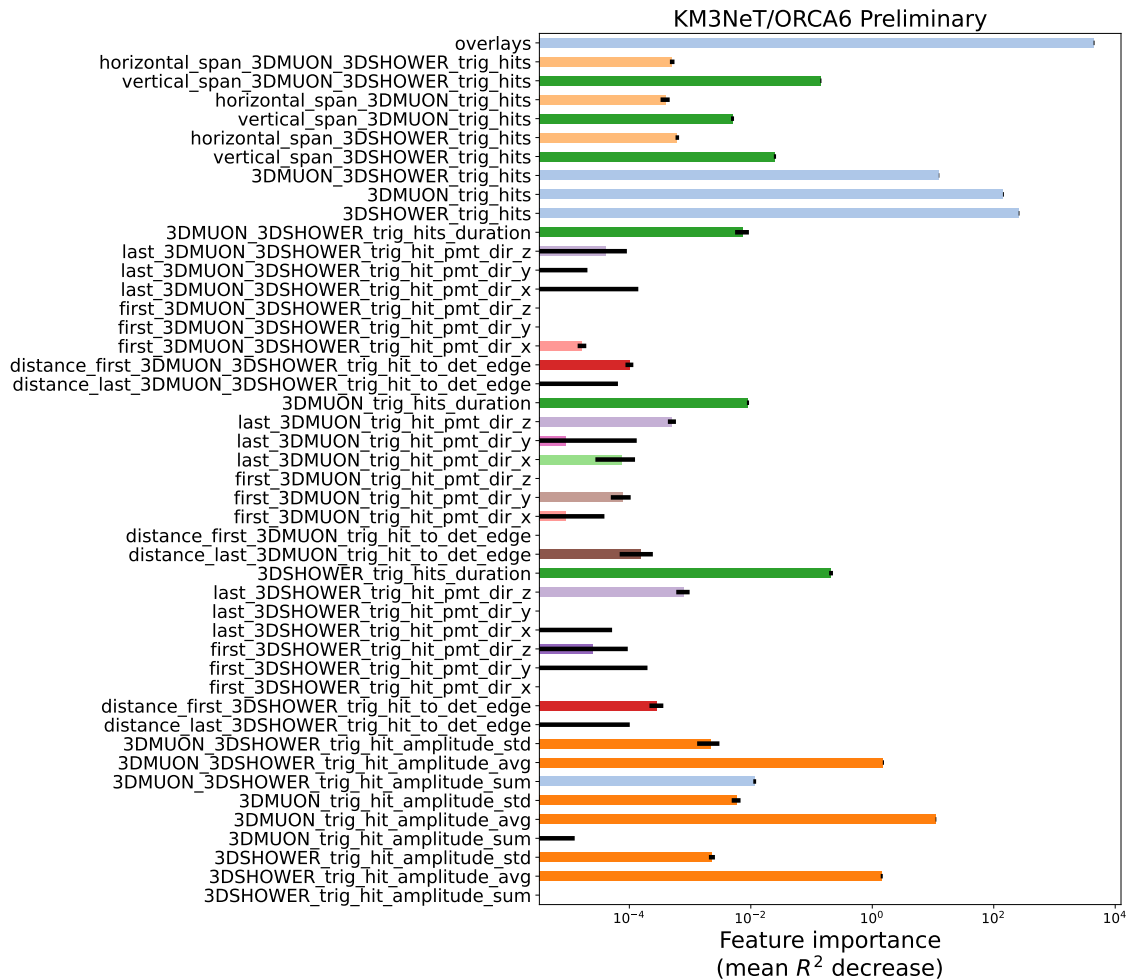


FIGURE A.5.12.: Feature importance for ORCA6 for the multiplicity reconstruction.

A.5.4. Hyperparameter tuning

The tuning of hyperparameters has been carried out using the Optuna framework, which offers easy parallelisation options, smart parameter space searching and pruning of unpromising trials Akiba et al. [222]. All these traits were crucial, since scanning a multi-dimensional hyperparameter space can be a very costly endeavour. The resulting best-fit parameters were summarised in Tab. A.5.3.

TABLE A.5.3.: Optimal LightGBM hyperparameters obtained with Optuna by scanning over 120 sampled sets of parameters. A separate hyperparameter scan has been performed for energy and multiplicity and for each of the 4 used detector configurations.

Parameter	ARCA115		ARCA6		ORCA115		ORCA6	
	E	N_μ	E	N_μ	E	N_μ	E	N_μ
learning_rate	0.06	0.08	0.02	0.05	0.06	0.05	0.02	0.06
num_iterations	910	1000	494	759	578	972	879	904
colsample_bytree	0.89	0.60	0.72	0.97	0.65	0.98	0.87	0.72
min_child_samples	194	462	541	158	21	515	695	918
min_child_weight	$2.70 \cdot 10^{-5}$	0.59	$1.40 \cdot 10^{-3}$	$1.62 \cdot 10^{-3}$	$5.12 \cdot 10^{-4}$	0.19	0.13	$1.51 \cdot 10^{-4}$
n_estimators	675	492	568	783	474	259	19	87
num_leaves	473	95	288	25	416	337	429	170
reg_alpha	74.08	48.74	83.24	4.63	18.95	55.32	132.17	39.83
reg_lambda	169.07	79.11	0.19	138.49	183.73	80.26	5.41	28.98
subsample	0.97	0.72	0.84	0.84	0.73	0.81	0.86	0.94
subsample_for_bin	10926	82921	40448	10488	58336	81283	32516	60497

A.6. Prompt muon analysis

Here, all the supplementary materials for Chap. 7 were gathered.

A.6.1. Hadrons implemented in CORSIKA

The following tables list the hadrons handled by CORSIKA and the ones, which were not implemented.

TABLE A.6.1.: Hadrons implemented in CORSIKA. It is not differentiated here between the charged and neutral species, or between particles and antiparticles for the sake of simplicity. C, S, B indicate, whether the hadron contains heavier quarks: c , s , or b respectively.

Meson	C	S	B
π			
K		×	
ρ			
ω			
ϕ		×	
η		×	
η_c	×		
D	×		
D_s	×	×	
J/ψ	×		

Baryon	C	S	B
p			
n			
Λ		×	
Λ_b			×
Λ_c	×		
Σ		×	
Σ_c	×		
Σ_b			×
Δ			
Ξ		×	
Ξ_c	×	×	
Ξ_b		×	×
Ω		×	
Ω_c	×	×	
Ω_b		×	×

TABLE A.6.2.: Hadrons so far not implemented in CORSIKA. C, S, B indicate, whether the hadron contains heavier quarks: c , s , or b respectively.

Meson	C	S	B
η_b			×
B			×
B_c	×		×
B_s		×	×
Υ			×

Baryon	C	S	B
Ξ_{cc}	×		

In addition to the particles listed in Tab. A.6.2, some subdominant processes are not implemented in CORSIKA as well:

- nuclear μ interactions,
- heavy pair production:
 - $\gamma \longrightarrow \mu^+ \mu^-$ (cross-section suppressed by a factor $\sim 10^{-4}$ w.r.t. $\gamma \longrightarrow e^+ e^-$),
 - $\gamma \longrightarrow \tau^+ \tau^-$ (cross-section suppressed by a factor $\sim 10^{-10}$ w.r.t. $\gamma \longrightarrow e^+ e^-$).

A.6.2. Classification of parent particles into conventional and prompt by lifetime

In general, a probability for a particle to decay is described by:

$$P(t) = e^{-\frac{t}{\gamma\tau}}, \quad (\text{A.6.1})$$

where $\gamma = \frac{1}{\sqrt{1-(\frac{v}{c})^2}}$ is the gamma factor of the particle, v is its velocity and c is the speed of light in vacuum, and t is the time.

The basic criterion of classification of muons was the lifetime τ of their parent particles, as in [105]:

- **prompt**: if parent particle has $\tau < \tau_{K_S^0} = 8.95 \cdot 10^{-5} \mu\text{s}$,
- **conv**: if parent $\tau \geq \tau_{K_S^0}$.

The table below compiles all parent particle types that are produced in the CORSIKA simulation as of version v7.7410.

TABLE A.6.3.: List of all parent particles found in the CORSIKA MC with their lifetimes and classification as contributing either to **conventional** or to the **prompt** muon flux. The masses and lifetimes are rounded values, obtained with [223].

#	PDG ID	Symbol	Rest mass m_0 [$\frac{\text{MeV}}{c^2}$]	Lifetime τ [μs]	Category	Comment
1	-	Cherenkov γ	-	-	conv	CORSIKA-specific
2	-	decaying μ^\pm	-	-	conv	CORSIKA-specific
3	-	$\eta \rightarrow 2\gamma$	-	-	conv	CORSIKA-specific
4	-	$\eta \rightarrow 3\pi^0$	-	-	conv	CORSIKA-specific
5	-	$\eta \rightarrow \pi^+ \pi^- \pi^0$	-	-	conv	CORSIKA-specific
6	-	$\eta \rightarrow \pi^+ \pi^- \gamma$	-	-	conv	CORSIKA-specific

APPENDIX A. APPENDIX

#	PDG ID	Symbol	Rest mass m_0 [$\frac{\text{MeV}}{c^2}$]	Lifetime τ [μs]	Category	Comment
7	-	μ^\pm add. info	-	-	conv	CORSIKA-specific
8	13	μ^+	105.66	2.20	conv	
9	-13	μ^-	105.66	2.20	conv	
10	22	γ	-	-	conv	stable
11	111	π^0	134.98	$8.43 \cdot 10^{-11}$	prompt	
12	113	ρ^0	775.26	$4.41 \cdot 10^{-18}$	prompt	
13	130	K_L^0	497.61	$5.11 \cdot 10^{-2}$	conv	
14	-211	π^+	139.57	$2.60 \cdot 10^{-2}$	conv	
15	211	π^-	139.57	$2.60 \cdot 10^{-2}$	conv	
16	-213	ρ^+	775.26	$4.41 \cdot 10^{-18}$	prompt	
17	213	ρ^-	775.26	$4.41 \cdot 10^{-18}$	prompt	
18	221	η	547.86	$5.02 \cdot 10^{-13}$	prompt	
19	223	ω	782.65	$7.75 \cdot 10^{-17}$	prompt	
20	310	K_S^0	497.61	$8.95 \cdot 10^{-5}$	conv	
21	-313	K^{*0}	895.55	$1.39 \cdot 10^{-17}$	prompt	
22	313	\bar{K}^{*0}	895.55	$1.39 \cdot 10^{-17}$	prompt	
23	-321	K^+	493.68	$1.24 \cdot 10^{-2}$	conv	
24	321	K^-	493.68	$1.24 \cdot 10^{-2}$	conv	
25	-323	K^{*+}	891.66	$1.30 \cdot 10^{-17}$	prompt	
26	323	\bar{K}^{*-}	891.66	$1.30 \cdot 10^{-17}$	prompt	
27	333	ϕ	1019.46	$1.54 \cdot 10^{-16}$	prompt	
28	-411	D^+	1869.65	$1.03 \cdot 10^{-6}$	prompt	
29	411	\bar{D}^-	1869.65	$1.03 \cdot 10^{-6}$	prompt	
30	-413	D^{*+}	2010.26	$7.89 \cdot 10^{-15}$	prompt	
31	413	\bar{D}^{*-}	2010.26	$7.89 \cdot 10^{-15}$	prompt	
32	-421	D^0	1864.83	$4.10 \cdot 10^{-7}$	prompt	
33	421	\bar{D}^0	1864.83	$4.10 \cdot 10^{-7}$	prompt	
34	-423	D^{*0}	2006.85	$3.13 \cdot 10^{-16}$	prompt	
35	423	\bar{D}^{*0}	2006.85	$3.13 \cdot 10^{-16}$	prompt	
36	-431	D_s^+	1968.34	$5.04 \cdot 10^{-7}$	prompt	
37	431	\bar{D}_s^-	1968.34	$5.04 \cdot 10^{-7}$	prompt	
38	-433	\bar{D}_s^{*-}	2112.20	unknown	prompt	τ probably short
39	433	D_s^{*-}	2112.20	unknown	prompt	τ probably short
40	441	η_c	2983.90	$2.06 \cdot 10^{-17}$	prompt	
41	443	J/ψ	3096.90	$7.08 \cdot 10^{-15}$	prompt	
42	-1114	$\bar{\Delta}^+$	1232.00	$5.62 \cdot 10^{-18}$	prompt	
43	1114	Δ^-	1232.00	$5.62 \cdot 10^{-18}$	prompt	
44	-2112	\bar{n}	939.57	$8.79 \cdot 10^8$	conv	
45	2112	n	939.57	$8.79 \cdot 10^8$	conv	
46	-2114	$\bar{\Delta}^0$	1232.00	$5.62 \cdot 10^{-18}$	prompt	

#	PDG ID	Symbol	Rest mass m_0 [$\frac{\text{MeV}}{c^2}$]	Lifetime τ [μs]	Category	Comment
47	2114	Δ^0	1232.00	$5.62 \cdot 10^{-18}$	prompt	
48	-2212	\bar{p}	938.27	-	conv	stable
49	2212	p	938.27	-	conv	stable
50	-2214	Δ^+	1232.00	$5.62 \cdot 10^{-18}$	prompt	
51	2214	$\bar{\Delta}^-$	1232.00	$5.62 \cdot 10^{-18}$	prompt	
52	-2224	$\bar{\Delta}^{--}$	1232.00	$5.62 \cdot 10^{-18}$	prompt	
53	2224	Δ^{++}	1232.00	$5.62 \cdot 10^{-18}$	prompt	
54	-3112	Σ^-	1197.45	$1.48 \cdot 10^{-4}$	conv	
55	3112	$\bar{\Sigma}^+$	1197.45	$1.48 \cdot 10^{-4}$	conv	
56	3122	Λ	1115.68	$2.63 \cdot 10^{-4}$	conv	
57	-3122	$\bar{\Lambda}$	1115.68	$2.63 \cdot 10^{-4}$	conv	
58	3212	Σ^0	1192.64	$7.39 \cdot 10^{-14}$	prompt	
59	-3212	$\bar{\Sigma}^0$	1192.64	$7.39 \cdot 10^{-14}$	prompt	
60	-3222	Σ^+	1189.37	$8.01 \cdot 10^{-5}$	conv	
61	3222	$\bar{\Sigma}^-$	1189.37	$8.01 \cdot 10^{-5}$	conv	
62	-3312	$\bar{\Xi}^+$	1321.71	$1.64 \cdot 10^{-4}$	conv	
63	3312	Ξ^-	1321.71	$1.64 \cdot 10^{-4}$	conv	
64	3322	Ξ^0	1314.86	$2.90 \cdot 10^{-4}$	conv	
65	-3322	$\bar{\Xi}^0$	1314.86	$2.90 \cdot 10^{-4}$	conv	
66	-3334	$\bar{\Omega}^+$	1672.45	$8.15 \cdot 10^{-5}$	conv	
67	3334	Ω^-	1672.45	$8.15 \cdot 10^{-5}$	conv	
68	4112	Σ_c^0	2453.75	$3.59 \cdot 10^{-16}$	prompt	
69	-4112	$\bar{\Sigma}_c^0$	2453.75	$3.59 \cdot 10^{-16}$	prompt	
70	4114	Σ_c^{*0}	2518.48	$4.30 \cdot 10^{-17}$	prompt	
71	-4114	$\bar{\Sigma}_c^{*0}$	2518.48	$4.30 \cdot 10^{-17}$	prompt	
72	-4122	$\bar{\Lambda}_c^-$	2286.46	$1.99 \cdot 10^{-7}$	prompt	
73	4122	Λ_c^+	2286.46	$1.99 \cdot 10^{-7}$	prompt	
74	4132	Ξ_c^0	2470.91	$1.11 \cdot 10^{-7}$	prompt	
75	-4132	$\bar{\Xi}_c^0$	2470.91	$1.11 \cdot 10^{-7}$	prompt	
76	-4212	Σ_c^+	2452.90	$1.43 \cdot 10^{-16}$	prompt	
77	4212	$\bar{\Sigma}_c^-$	2452.90	$1.43 \cdot 10^{-16}$	prompt	
78	-4214	$\bar{\Sigma}_c^{*-}$	2517.50	$3.87 \cdot 10^{-17}$	prompt	
79	-4222	Σ_c^{++}	2453.97	$3.48 \cdot 10^{-16}$	prompt	
80	4222	$\bar{\Sigma}_c^{--}$	2453.97	$3.48 \cdot 10^{-16}$	prompt	
81	-4224	$\bar{\Sigma}_c^{*-}$	2518.41	$4.45 \cdot 10^{-17}$	prompt	
82	4224	Σ_c^{*++}	2518.41	$4.45 \cdot 10^{-17}$	prompt	
83	4232	Ξ_c^+	2467.93	$4.41 \cdot 10^{-7}$	prompt	
84	-4232	$\bar{\Xi}_c^-$	2467.93	$4.41 \cdot 10^{-7}$	prompt	
85	-4332	$\bar{\Omega}_c^0$	2695.20	$2.67 \cdot 10^{-7}$	prompt	
86	4332	Ω_c^0	2695.20	$2.67 \cdot 10^{-7}$	prompt	

A.6.3. Verification of the prompt muon definition

All the combinations from Tab. 7.1.1 were explicitly verified with $d_{\mu\text{prod}}$ plots. The test was done on ORCA115 MC, since ORCA is located shallower and thus, a greater muon statistics was available. The muons at sea level were plotted, which means that if a shower reaches ORCA115, even muons not reaching the can are included. The following abbreviations were used:

- gmom: grandmother,
- mom: mother,
- nucl: nucleus,
- prim: primary.

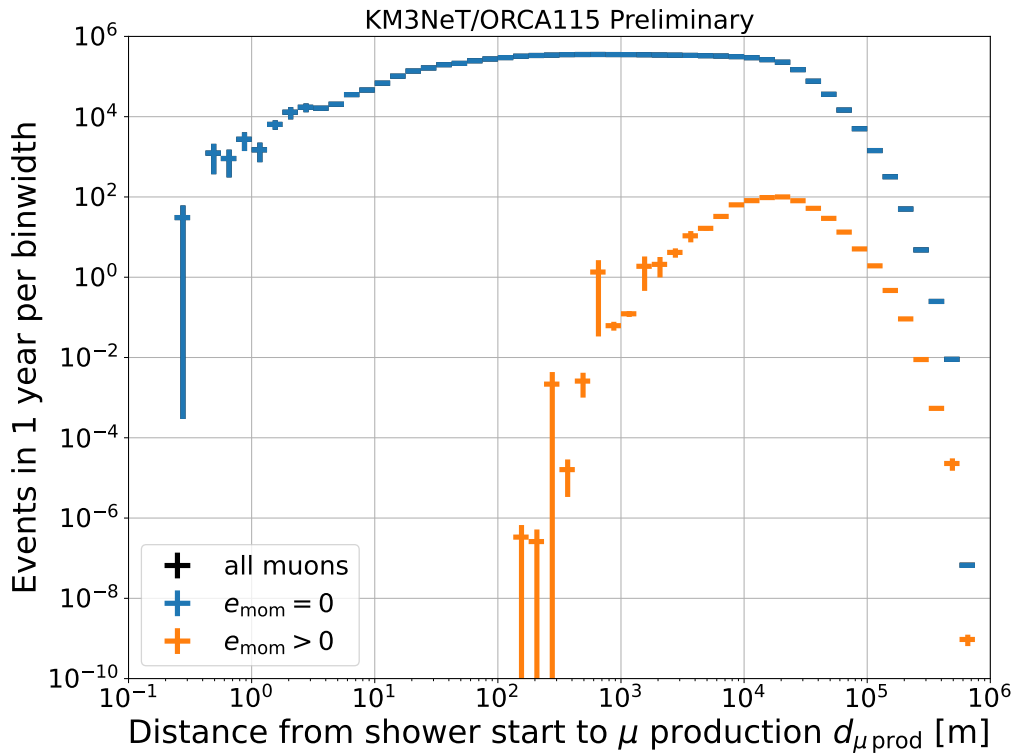


FIGURE A.6.1.: Distributions of $d_{\mu\text{prod}}$ for μ with different mother EM counter e_{mom} values. The distribution for e_{μ} is not plotted, since it is always equal to zero. The distribution for all muons is not visible, because it is covered by the one for $e_{\text{mom}} = 0$.

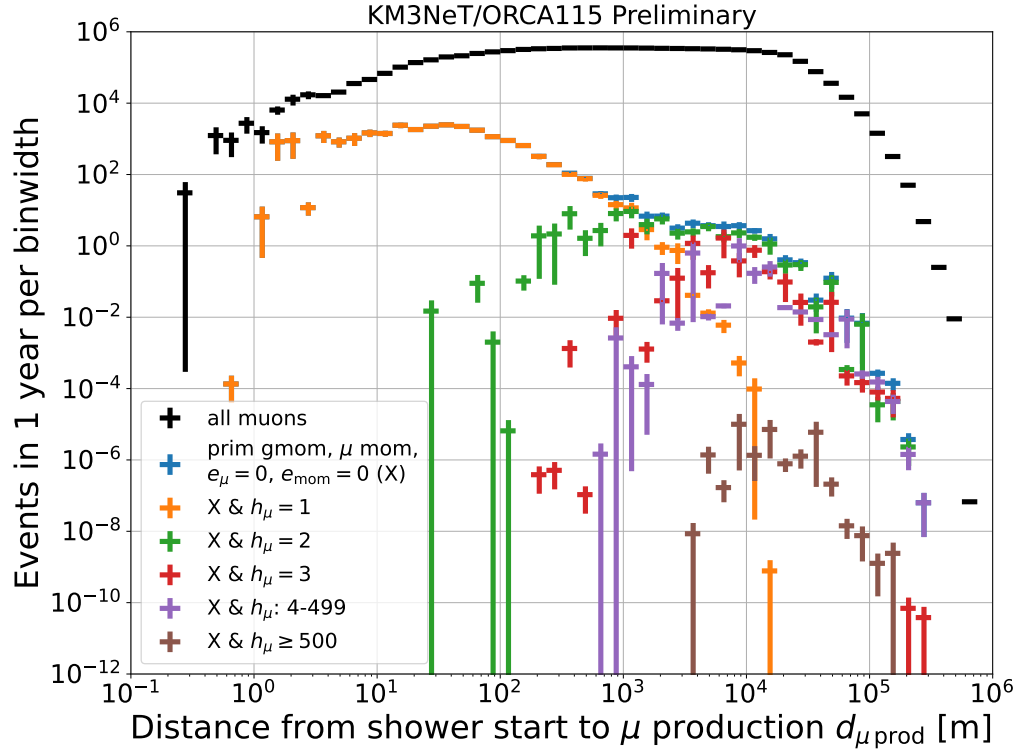


FIGURE A.6.2.: Distributions of $d_{\mu\text{prod}}$ for μ with prim gmom and μ mom, but different h_{μ} counter values.

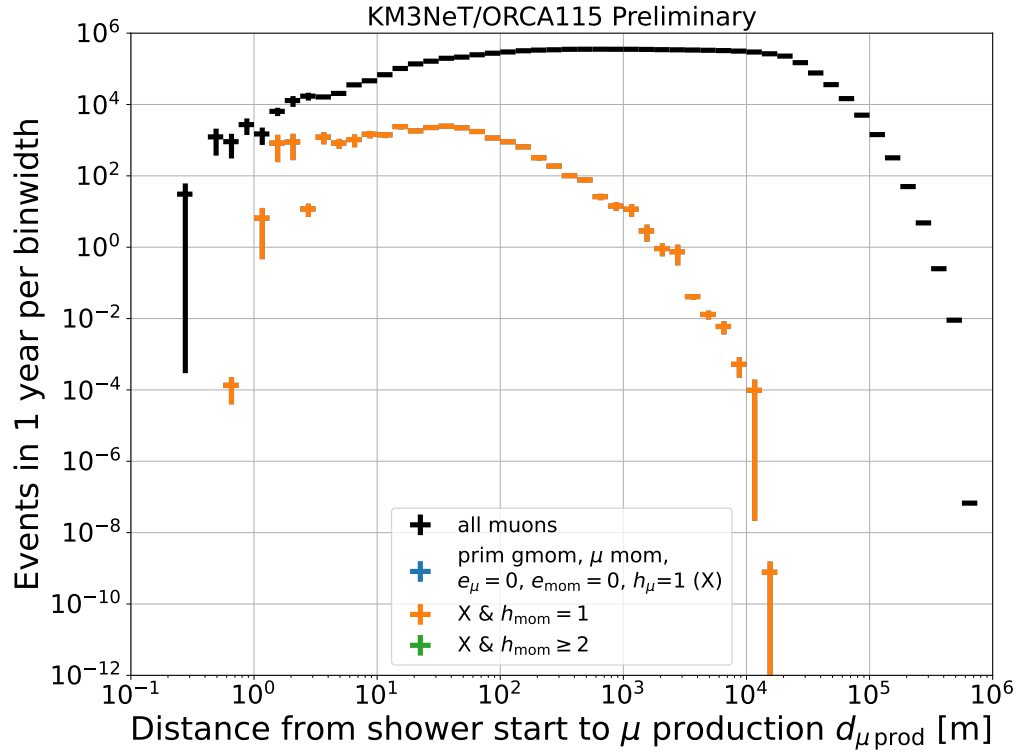


FIGURE A.6.3.: Distributions of $d_{\mu\text{prod}}$ for μ with prim gmom, μ mom, and $h_{\mu} = 1$. The plot demonstrates that in fact for $h_{\mu} = 1$, the only contribution comes from $h_{\text{mom}} = 1$.

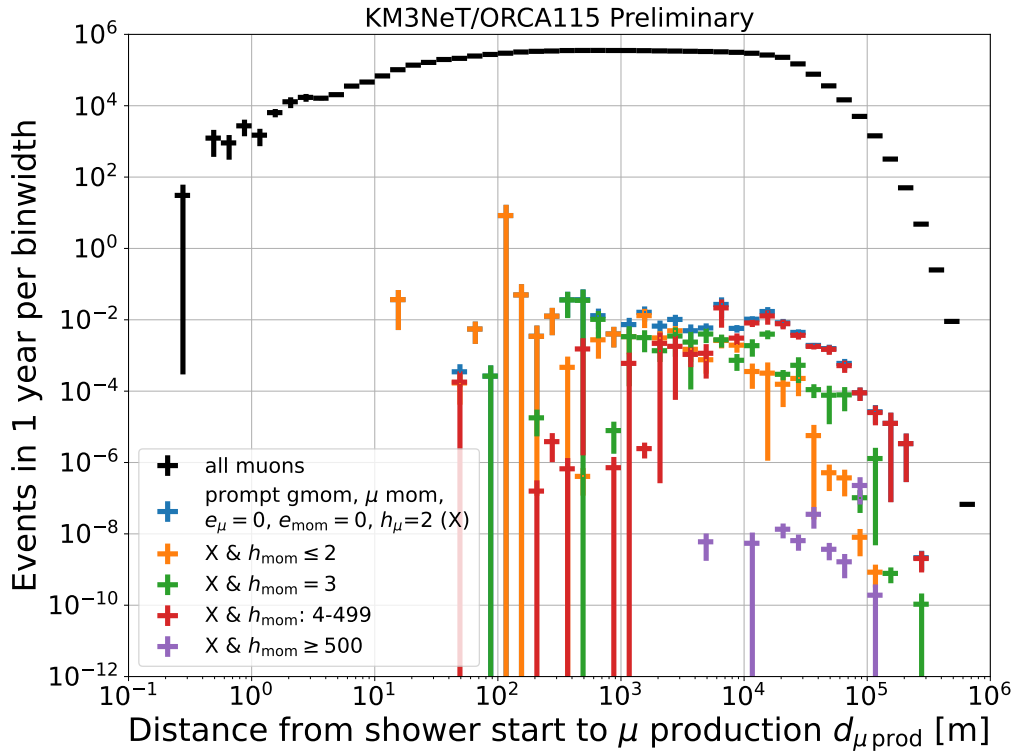


FIGURE A.6.4.: Distributions of $d_{\mu\text{prod}}$ for μ with prompt gmom, μ mom, and different h_μ values.

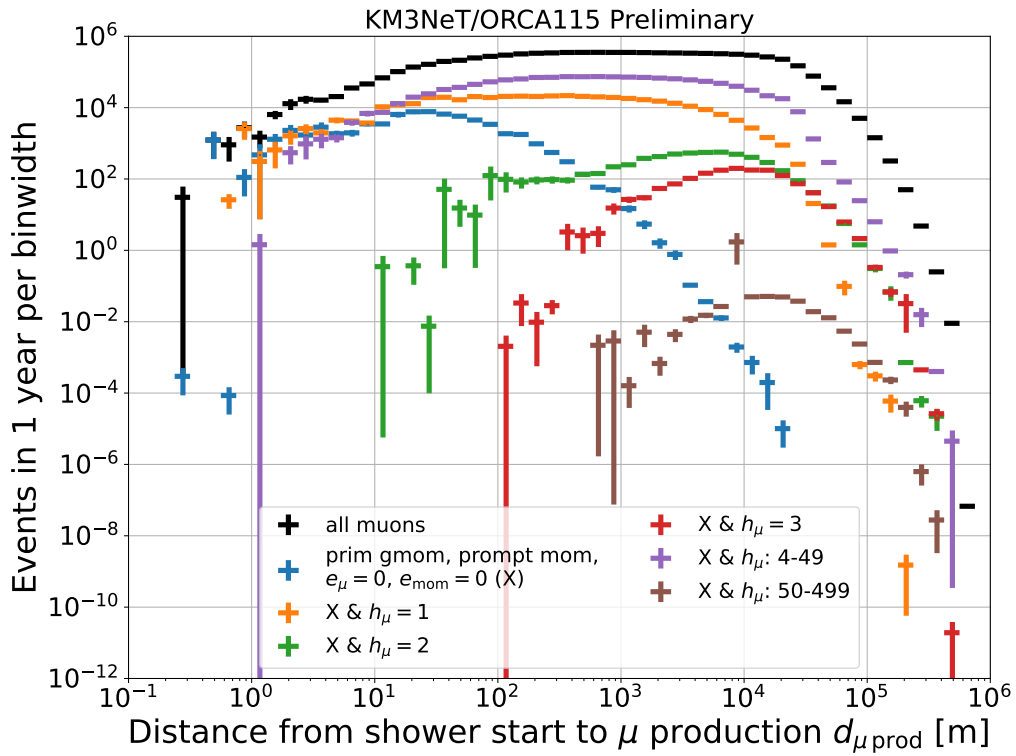
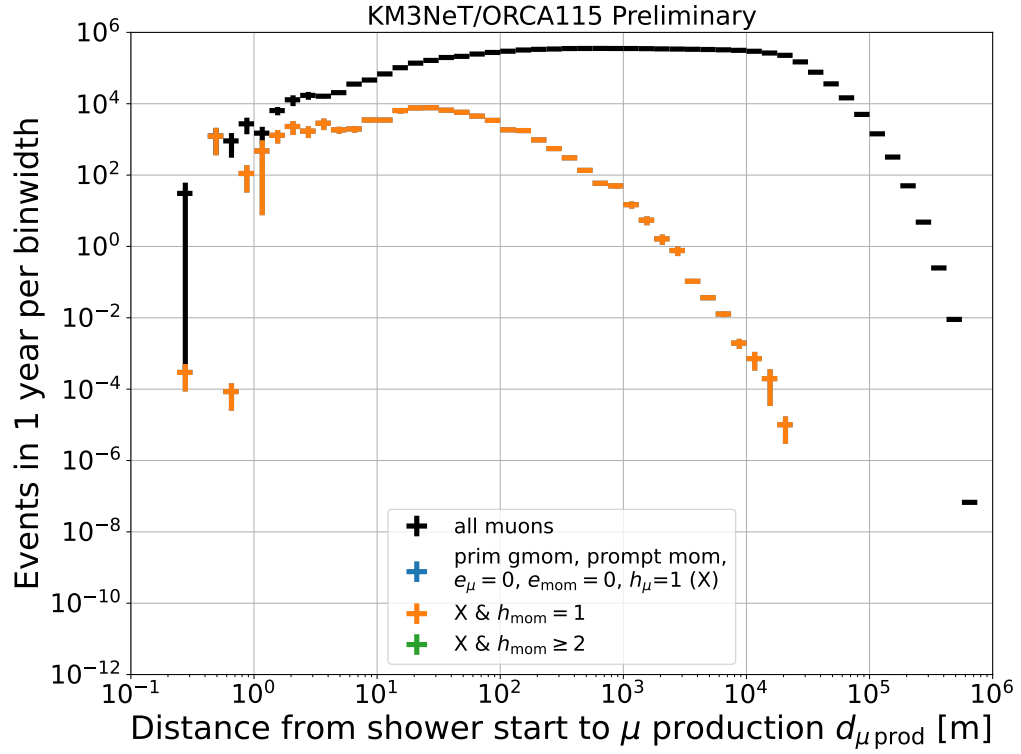
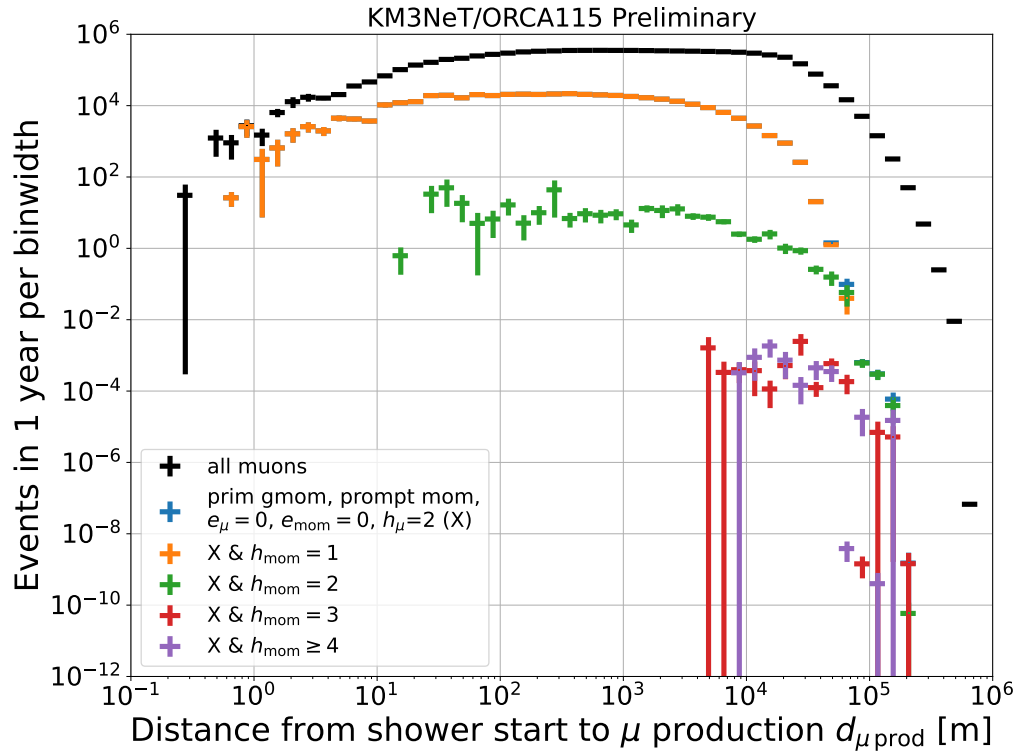


FIGURE A.6.5.: Distributions of $d_{\mu\text{prod}}$ for μ with prim gmom and prompt mom.

FIGURE A.6.6.: Distributions of $d_{\mu\text{prod}}$ for μ with prim gmom, prompt mom, and $h_{\mu}=1$.FIGURE A.6.7.: Distributions of $d_{\mu\text{prod}}$ for μ with prim gmom, prompt mom, and $h_{\mu}=2$.

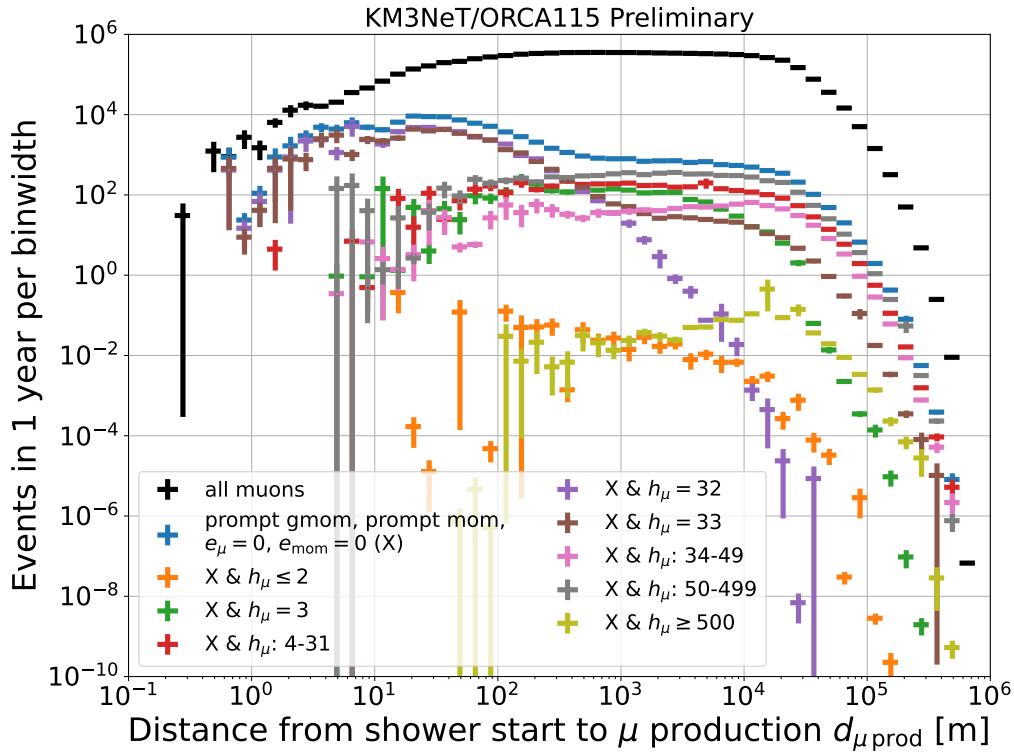


FIGURE A.6.8.: Distributions of $d_{\mu\text{prod}}$ for μ with prompt gmom and prompt mom.

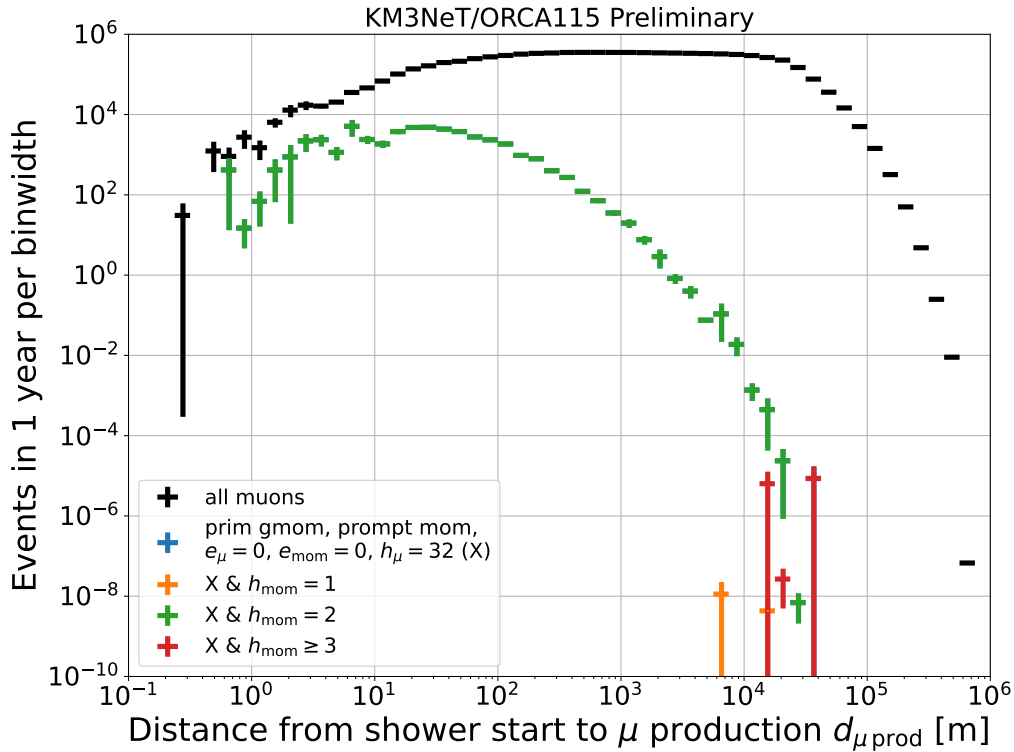


FIGURE A.6.9.: Distributions of $d_{\mu\text{prod}}$ for μ with prompt gmom, prompt mom, and $h_{\mu} = 32$.

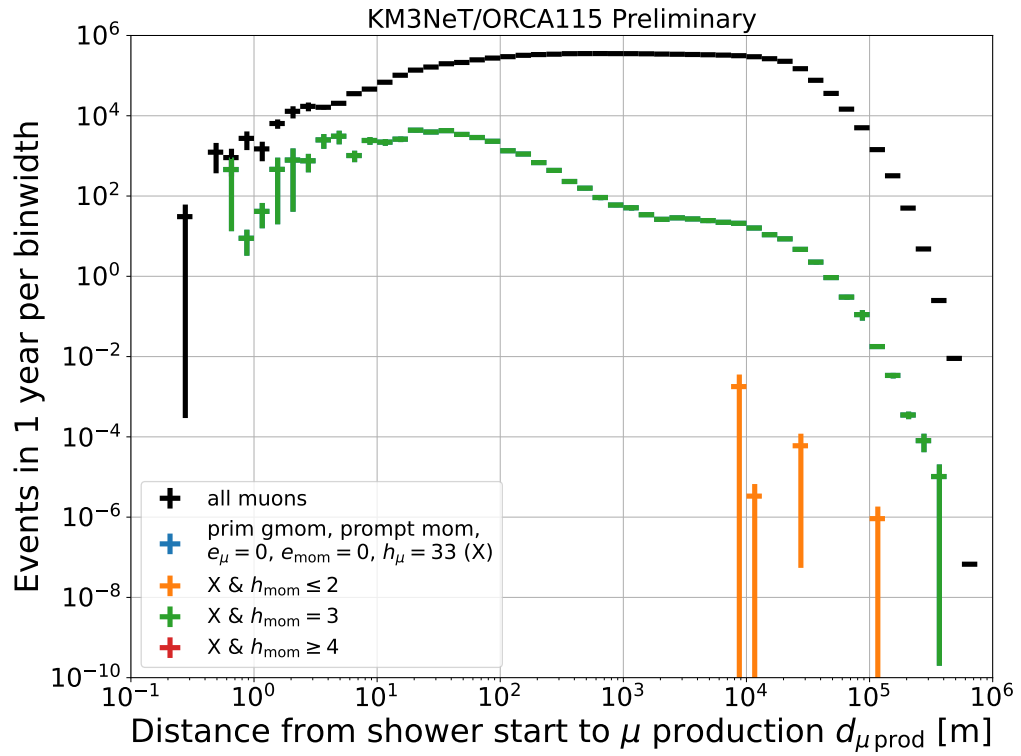


FIGURE A.6.10.: Distributions of $d_{\mu\text{prod}}$ for μ with prompt gmom, prompt mom, and $h_{\mu} = 33$.

Acknowledgements

Here, I would like to express my gratitude towards people and institutions, who contributed to the successful completion of this thesis.

Supervision

I would like to thank in the first line my thesis supervisors:

- **Prof. dr hab. Ewa Rondio**, for many discussions with deep insights, which often drove me to rethink my approach and improve my analysis. I am grateful for her generous sharing of rich experimental experience, while making sure I do not deviate from the track too far. Her devotion in supporting my work, despite being involved in key roles at NCBJ and in the T2K and HK Collaborations was truly remarkable.
- **Dr Piotr Mijakowski**, for introducing me to the wonderful community of the KM3NeT experiment, believing in me, and encouraging to pursue even most ambitious goals. I owe the success of my efforts to his guidance and expertise, in particular in the field of machine learning.

Funding

This work was accomplished under the financial support of the **National Science Centre**:

- NCN Sonata Bis 2015/18/E/ST2/00758, ‘*Indirect search for dark matter with water neutrino detectors*’, PI: dr Piotr Mijakowski
- NCN Preludium 2021/41/N/ST2/01177, ‘*Measurement of muon flux with KM3NeT-ARCA and KM3NeT-ORCA detectors*’, PI: Piotr Kalaczyński



Piotr Kalaczyński is supported by the grant ‘*AstroCeNT: Particle Astrophysics Science and Technology Centre*’, carried out within the International Research Agendas programme of the Foundation for Polish Science financed by the European Union under the European Regional Development Fund.



Computing

The services provided by the Świerk Computing Centre (CIŚ) were crucial for the computationally-intensive MC simulations, which were the backbone of this thesis. Here, I would like to extend my gratitude in particular to **Henryk Gienza**, who was my main contact person at CIŚ and has always been very responsive and helpful with all the trouble that needed solving and requests that I had.



I am also grateful to the IN2P3's Computing Centre in Lyon, France for delivering a smoothly running computing service, with a dedicated KM3NeT ecosystem, which I made frequent use of.



Software

The CORSIKA code [104] has been the main software, without which none of the results of this thesis would have been possible. I am not only grateful to the authors for providing the CORSIKA package to the astroparticle physics community, but also for the organisation of very useful CORSIKA Workshops, and for many informative discussions. Here, I want to especially mention **dr Tanguy Pierog**, **dr Felix Riehn**, and **dr Sergey Ostapchenko**.

I acknowledge the service provided in form of the pym sis package by the University of Colorado Space Weather Technology, Research and Education Center (SWx TREC), which allowed me to conveniently access the NRLMSIS-2.0 [146] and NRLMSISE-00 [216] model predictions .



The crflux [131] and MCEq codes [189], developed by **dr Anatoli Feydnitch**, were of great help for this work. I thank Anatoli for fruitful discussions on potential applications and extensions of his software.

Others

I am also deeply grateful to all my professors and colleagues from NCBJ Warsaw and KM3NeT Collaboration. They made my time as a PhD student a memorable experience and have helped me to accumulate knowledge and skills necessary to complete this thesis.

My PhD experience would not be the same without the great people from the Warsaw Neutrino Group: **dr Magdalena Posiadala-Zezula**, **dr Joanna Zalipska**, **dr Katarzyna Kowalik**, **Yashwanth S. Prabhu**, **Maitrayee Mandal**, **dr Lakshmi S. Mohan**, **dr Tomas Nosek**, **dr Katarzyna Frankiewicz**, **dr Jerzy Mańczak**, **dr Rafał Wojaczyński**, **dr Meghna Kunhikannan Kannichankandy**, **dr Katarzyna Grzelak** and notably: **dr Kamil Skwarczyński**, with whom I not only shared the passion for neutrinos & Co., but also for climbing and exquisite memes, **dr Grzegorz Żarnecki**, who has inspired me with his determination and dedication, **dr Justyna Łagoda**, who was extremely helpful both in technical discussions, and in formal issues. A honorary mention goes to **prof. Maria „Hula” Szeptycka**†, who has been extremely active member of the group and showed curiosity in all the discussions. She regrettably passed away on 23.01.2022, unable to see the conclusion of this work.

The environment within the KM3NeT Collaboration was no less welcoming than at NCBJ. I am most thankful to have met **Tamás Gal**. His expertise and devotion to KM3NeT are truly amazing. I always wondered, how he still managed to always find the time to help me understand the nuances of KM3NeT-specific software and programming in general. The only person I can think of, who can match his zeal, if undoubtedly **prof. Maarten de Jong**, who basically breathes KM3NeT and devotes all his energy to the success of the collaboration. I deeply valued my technical discussions with him, always displaying sharp understanding of various complex aspects of the experiment, and straight to the point. I very much appreciate the supportive and encouraging attitude of **prof. Annarita Margiotta**, who worked tirelessly to make sure that all the publications within the collaboration, including mine conformed to best scientific practices. My introduction to CORSIKA simulations was a smooth process thanks to **dr Konstantinos Pikounis** and his readiness to address any of my questions or doubts. I have many things to thank **dr Vladimir Kulikovskiy** for: he was the best analysis reviewer I could have wished for, he introduced me to rock climbing, and he was just a cheerful, friendly colleague, who I could rely on. I am no less appreciative of my second reviewer, **dr Luigi Antonio Fusco**, for pointing out things in the spirit of improving the analysis together. The whole work was coordinated by the Cosmic Ray Working Group leader, **dr Ronald Brujin**, who always kept track of the bigger picture. My early MC work within KM3NeT was certainly heavily influenced by discussions with **dr Rosa Coniglione**, a true expert on the matter. Developing the gSeaGen code was a group effort from the very beginning. I was all the time in tight cooperation with its original author, **dr Carla Distefano**, and main co-developer, **dr Alfonso Garcia Andres Soto**. I definitely enjoyed the work on the gSeaGen team and hope to be able to do some more in the future! My machine learning work has been marked by numerous fruitful conversations and exchanges of ideas with **dr Stefan Reck**, who worked on a similar problem in his thesis [9]. It is not an exaggeration to state that I would need at least one more year to finish the CORSIKA MC production work, if it was not for **dr Andrey Romanov’s** assistance. He not only took a significant part of the job onto himself, but also actively worked with me to

further improve the simulation. He also contributed significantly to my work on processing the CORSIKA files with gSeaGen and to the evaluation of the systematic uncertainties.

I also want to mention here other people, I enjoyed collaborating with on various subjects within KM3NeT: **prof. Antonio Capone**, **dr Thomas Eberl**, **dr Alba Domi**, **dr Brian Ó Fearraigh**, **Louis Bailly-Salins**, and **dr Jannik Hofestädt**.

Bibliography

- [1] A. Margiotta. The km3net deep-sea neutrino telescope, August 2014. DOI: [10.1016/j.nima.2014.05.090](https://doi.org/10.1016/j.nima.2014.05.090). arXiv: [1408.1392](https://arxiv.org/abs/1408.1392) [astro-ph.IM].
- [2] S. Adrián-Martínez et al. Letter of intent for KM3net 2.0. *Journal of Physics G: Nuclear and Particle Physics*, 43(8):084001, 2016. DOI: [10.1088/0954-3899/43/8/084001](https://doi.org/10.1088/0954-3899/43/8/084001).
- [3] C. Distefano. gSeaGen: a GENIE-based code for neutrino telescopes. *EPJ Web of Conferences*, 116:08001, 2016. A. Capone et al., editors. DOI: [10.1051/epjconf/201611608001](https://doi.org/10.1051/epjconf/201611608001).
- [4] S. Aiello et al. gSeaGen: the KM3net GENIE-based code for neutrino telescopes. *Computer Physics Communications*, 256:107477, 2020. DOI: [10.1016/j.cpc.2020.107477](https://doi.org/10.1016/j.cpc.2020.107477).
- [5] D. Heck and T. Pierog. Extensive air shower simulation with corsika: a user's guide.
- [6] A. Garcia Soto and others on behalf of the KM3NeT collaboration. Upgrading gseagen: from mev to pev neutrinos. *Journal of Instrumentation*, 16(09):C09008, 2021. DOI: [10.1088/1748-0221/16/09/C09008](https://doi.org/10.1088/1748-0221/16/09/C09008). URL: <https://dx.doi.org/10.1088/1748-0221/16/09/C09008>.
- [7] J. Schnabel and others on behalf of the KM3NeT collaboration. Meeting the challenge of open science in km3net. *Journal of Instrumentation*, 16(10):C10002, 2021. DOI: [10.1088/1748-0221/16/10/C10002](https://doi.org/10.1088/1748-0221/16/10/C10002). URL: <https://dx.doi.org/10.1088/1748-0221/16/10/C10002>.
- [8] T. Pierog et al. Corsika, version 7.7410, May 2021. DOI: [10.5281/zenodo.5246070](https://doi.org/10.5281/zenodo.5246070). URL: <https://doi.org/10.5281/zenodo.5246070>.
- [9] S. Reck. *Cosmic ray composition measurement using Graph NeuralNetworks for KM3NeT/ORCA*. PhD thesis, University of Erlangen–Nuremberg, 2022.
- [10] A. Romanov and P. Kalaczyński. Comparison of the atmospheric muon flux measured by the KM3net detectors with the CORSIKA simulation using the global spline fit model. In *Proceedings of 38th International Cosmic Ray Conference — PoS(ICRC2023)*. Sissa Medialab, 2023. DOI: [10.22323/1.444.0338](https://doi.org/10.22323/1.444.0338).
- [11] M. Ageron et al. Comparison of the measured atmospheric muon rate with monte carlo simulations and sensitivity study for detection of prompt atmospheric muons with km3net. In *Proceedings of 37th International Cosmic Ray Conference — PoS(ICRC2021)*, volume 395, page 1112. Sissa Medialab, 2021. DOI: [10.22323/1.395.1112](https://doi.org/10.22323/1.395.1112).
- [12] P. Kalaczyński on behalf of the KM3NeT Collaboration. Comparison of the measured atmospheric muon rate with monte carlo simulations and sensitivity study for detection of prompt atmospheric muons with km3net. *Journal of Instrumentation*, 16(09):C09035, 2021. DOI: [10.1088/1748-0221/16/09/C09035](https://doi.org/10.1088/1748-0221/16/09/C09035). URL: <https://dx.doi.org/10.1088/1748-0221/16/09/C09035>.

- [13] P. Kalaczyński and R. Coniglione on behalf of the KM3NeT Collaboration. Comparison of the measured atmospheric muon flux with monte carlo simulations for the first KM3net detection units. In *Proceedings of 36th International Cosmic Ray Conference — PoS(ICRC2019)*. Sissa Medialab, 2019. DOI: [10.22323/1.358.0927](https://doi.org/10.22323/1.358.0927).
- [14] P. Kalaczyński on behalf of the KM3NeT Collaboration. KM3NeT/ORCA: status and perspectives for neutrino oscillation and mass hierarchy measurements. In *Proceedings of 40th International Conference on High Energy physics — PoS(ICHEP2020)*, volume 390, page 149, 2021. DOI: [10.22323/1.390.0149](https://doi.org/10.22323/1.390.0149).
- [15] A. G. Bogdanov et al. Energy spectrum of cosmic ray muons in ~ 100 TeV energy region reconstructed from the BUST data. *Astroparticle Physics*, 36(1):224–236, 2012. DOI: [10.1016/j.astropartphys.2012.06.004](https://doi.org/10.1016/j.astropartphys.2012.06.004).
- [16] D. Soldin. Atmospheric muons measured with IceCube. *EPJ Web of Conferences*, 208:08007, 2019. B. Pattison et al., editors. DOI: [10.1051/epjconf/201920808007](https://doi.org/10.1051/epjconf/201920808007).
- [17] A. Schneider on behalf of the IceCube Collaboration. Characterization of the astrophysical diffuse neutrino flux with IceCube high-energy starting events. In *Proceedings of 36th International Cosmic Ray Conference — PoS(ICRC2019)*. Sissa Medialab, 2019. DOI: [10.22323/1.358.1004](https://doi.org/10.22323/1.358.1004).
- [18] M. Aglietta et al. Upper limit on the prompt muon flux derived from the LVD underground experiment. *Physical Review D*, 60(11):112001, 1999. DOI: [10.1103/physrevd.60.112001](https://doi.org/10.1103/physrevd.60.112001).
- [19] Wikimedia Commons. File:standard model of elementary particles.svg — wikimedia commons, the free media repository. Wikimedia Commons, the free media repository. 2022. URL: https://commons.wikimedia.org/w/index.php?title=File:Standard_Model_of_Elementary_Particles.svg&oldid=682311513. [Online; accessed 22-August-2023].
- [20] R. L. Workman et al. Review of particle physics. *Progress of Theoretical and Experimental Physics*, 2022(8), 2022. DOI: [10.1093/ptep/ptac097](https://doi.org/10.1093/ptep/ptac097).
- [21] J. Street and E. Stevenson. New evidence for the existence of a particle of mass intermediate between the proton and electron. *Physical Review*, 52(9):1003–1004, 1937. DOI: [10.1103/physrev.52.1003](https://doi.org/10.1103/physrev.52.1003).
- [22] B. Abi et al. Measurement of the positive muon anomalous magnetic moment to 0.46 ppm. *Physical Review Letters*, 126(14):141801, 2021. DOI: [10.1103/physrevlett.126.141801](https://doi.org/10.1103/physrevlett.126.141801).
- [23] K. Geyer. *Measurements of the atmospheric muon rate with the ANTARES neutrino telescope*. PhD thesis, FAU Erlangen-Nürnberg, 2015. URL: <https://ecap.nat.fau.de/wp-content/uploads/2021/03/KlausGeyerDissertation.pdf>.
- [24] A. Einstein. Zur elektrodynamik bewegter körper. *Annalen der Physik*, 322(10):891–921, 1905. DOI: [10.1002/andp.19053221004](https://doi.org/10.1002/andp.19053221004).
- [25] J.-H. Koehne et al. PROPOSAL: a tool for propagation of charged leptons. *Computer Physics Communications*, 184(9):2070–2090, 2013. DOI: [10.1016/j.cpc.2013.04.001](https://doi.org/10.1016/j.cpc.2013.04.001).
- [26] G. W. Bennett et al. Final report of the e821 muon anomalous magnetic moment measurement at BNL. *Physical Review D*, 73(7):072003, 2006. DOI: [10.1103/physrevd.73.072003](https://doi.org/10.1103/physrevd.73.072003).

- [27] P. Abbon et al. The COMPASS experiment at CERN. *Nuclear Instruments and Methods in Physics Research Section A: Accelerators, Spectrometers, Detectors and Associated Equipment*, 577(3):455–518, 2007. DOI: [10.1016/j.nima.2007.03.026](https://doi.org/10.1016/j.nima.2007.03.026).
- [28] S. E. Kuhn et al. Spin structure of the nucleon—status and recent results. *Progress in Particle and Nuclear Physics*, 63(1):1–50, 2009. DOI: [10.1016/j.ppnp.2009.02.001](https://doi.org/10.1016/j.ppnp.2009.02.001).
- [29] P. D. Meyers et al. Measurement of the nucleon structure function in iron using 215- and 93-GeV muons. *Physical Review D*, 34(5):1265–1304, 1986. DOI: [10.1103/physrevd.34.1265](https://doi.org/10.1103/physrevd.34.1265).
- [30] V. K. Bharadwaj. *Deep Inelastic Muon Nucleon Scattering*. PhD thesis, Oxford U., 1977. DOI: [10.2172/1406599](https://doi.org/10.2172/1406599).
- [31] CERN Yellow Reports: Monographs. Cern yellow reports: monographs, vol. 1 (2022): european strategy for particle physics - accelerator r&d roadmap. en, 2022. DOI: [10.23731/CYRM-2022-001](https://doi.org/10.23731/CYRM-2022-001).
- [32] K. R. Long et al. Muon colliders to expand frontiers of particle physics. *Nature Physics*, 17(3):289–292, 2021. DOI: [10.1038/s41567-020-01130-x](https://doi.org/10.1038/s41567-020-01130-x).
- [33] R. Capdevilla et al. Discovering the physics of $(g - 2)_\mu$ at future muon colliders. *Physical Review D*, 103(7):075028, 2021. DOI: [10.1103/physrevd.103.075028](https://doi.org/10.1103/physrevd.103.075028).
- [34] A. Taroni. Nobel prize 2015: kajita and McDonald. *Nature Physics*, 11(11):891–891, 2015. DOI: [10.1038/nphys3543](https://doi.org/10.1038/nphys3543).
- [35] K. Eguchi et al. First results from kamland: evidence for reactor antineutrino disappearance. *Phys. Rev. Lett.*, 90:021802, 2, 2003. DOI: [10.1103/PhysRevLett.90.021802](https://doi.org/10.1103/PhysRevLett.90.021802). URL: <https://link.aps.org/doi/10.1103/PhysRevLett.90.021802>.
- [36] M. Apollonio et al. Search for neutrino oscillations on a long base-line at the CHOOZ nuclear power station. *The European Physical Journal C*, 27(3):331–374, 2003. DOI: [10.1140/epjc/s2002-01127-9](https://doi.org/10.1140/epjc/s2002-01127-9).
- [37] Y. Abe et al. Improved measurements of the neutrino mixing angle θ_{13} with the double chooz detector. *Journal of High Energy Physics*, 2014(10), 2014. DOI: [10.1007/jhep10\(2014\)086](https://doi.org/10.1007/jhep10(2014)086).
- [38] F. P. An et al. Observation of electron-antineutrino disappearance at daya bay. *Phys. Rev. Lett.*, 108:171803, 17, 2012. DOI: [10.1103/PhysRevLett.108.171803](https://doi.org/10.1103/PhysRevLett.108.171803). URL: <https://link.aps.org/doi/10.1103/PhysRevLett.108.171803>.
- [39] J. H. Choi et al. Observation of energy and baseline dependent reactor antineutrino disappearance in the reno experiment. *Phys. Rev. Lett.*, 116:211801, 21, 2016. DOI: [10.1103/PhysRevLett.116.211801](https://doi.org/10.1103/PhysRevLett.116.211801). URL: <https://link.aps.org/doi/10.1103/PhysRevLett.116.211801>.
- [40] D. Svirida. DANSS experiment: current status and future plans. *Journal of Physics: Conference Series*, 1690(1):012179, 2020. DOI: [10.1088/1742-6596/1690/1/012179](https://doi.org/10.1088/1742-6596/1690/1/012179).
- [41] Y. J. Ko et al. Sterile neutrino search at the neos experiment. *Phys. Rev. Lett.*, 118:121802, 12, 2017. DOI: [10.1103/PhysRevLett.118.121802](https://doi.org/10.1103/PhysRevLett.118.121802). URL: <https://link.aps.org/doi/10.1103/PhysRevLett.118.121802>.

- [42] H. Almazán et al. Improved sterile neutrino constraints from the stereo experiment with 179 days of reactor-on data. *Phys. Rev. D*, 102:052002, 5, 2020. DOI: [10.1103/PhysRevD.102.052002](https://doi.org/10.1103/PhysRevD.102.052002). URL: <https://link.aps.org/doi/10.1103/PhysRevD.102.052002>.
- [43] Y. Abreu et al. Solid: a short baseline reactor neutrino experiment. *Journal of Instrumentation*, 16(02):P02025, 2021. DOI: [10.1088/1748-0221/16/02/P02025](https://doi.org/10.1088/1748-0221/16/02/P02025). URL: <https://dx.doi.org/10.1088/1748-0221/16/02/P02025>.
- [44] A. Haghghat et al. Observation of reactor antineutrinos with a rapidly deployable surface-level detector. *Phys. Rev. Appl.*, 13:034028, 3, 2020. DOI: [10.1103/PhysRevApplied.13.034028](https://doi.org/10.1103/PhysRevApplied.13.034028). URL: <https://link.aps.org/doi/10.1103/PhysRevApplied.13.034028>.
- [45] K. Abe et al. The t2k experiment. *Nuclear Instruments and Methods in Physics Research Section A: Accelerators, Spectrometers, Detectors and Associated Equipment*, 659(1):106–135, 2011. DOI: [10.1016/j.nima.2011.06.067](https://doi.org/10.1016/j.nima.2011.06.067).
- [46] V. N. Gavrin. Contribution of gallium experiments to the understanding of solar physics and neutrino physics. *Physics of Atomic Nuclei*, 76(10):1238–1243, 2013. DOI: [10.1134/s106377881309007x](https://doi.org/10.1134/s106377881309007x).
- [47] J. M. Gelb et al. Implications of new GALLEX results for the mikheyev-smirnov-wolfenstein solution of the solar neutrino problem. *Physical Review Letters*, 69(13):1864–1866, 1992. DOI: [10.1103/physrevlett.69.1864](https://doi.org/10.1103/physrevlett.69.1864).
- [48] Borexino Collaboration. Neutrinos from the primary proton–proton fusion process in the sun. *Nature*, 512(7515):383–386, 2014. DOI: [10.1038/nature13702](https://doi.org/10.1038/nature13702).
- [49] J. Boger et al. The sudbury neutrino observatory. *Nuclear Instruments and Methods in Physics Research Section A: Accelerators, Spectrometers, Detectors and Associated Equipment*, 449(1-2):172–207, 2000. DOI: [10.1016/s0168-9002\(99\)01469-2](https://doi.org/10.1016/s0168-9002(99)01469-2).
- [50] S. Fukuda et al. The super-kamiokande detector. *Nuclear Instruments and Methods in Physics Research Section A: Accelerators, Spectrometers, Detectors and Associated Equipment*, 501(2-3):418–462, 2003. DOI: [10.1016/s0168-9002\(03\)00425-x](https://doi.org/10.1016/s0168-9002(03)00425-x).
- [51] J. N. Bahcall and R. Davis. Solar neutrinos: a scientific puzzle. *Science*, 191(4224):264–267, 1976. DOI: [10.1126/science.191.4224.264](https://doi.org/10.1126/science.191.4224.264).
- [52] V. N. Gavrin. The russian-american gallium experiment SAGE. *Physics-Uspekhi*, 54(9):941–949, 2011. DOI: [10.3367/ufne.0181.201109g.0975](https://doi.org/10.3367/ufne.0181.201109g.0975).
- [53] P. Heix et al. Seasonal variation of atmospheric neutrinos in icecube. In *Proceedings of 36th International Cosmic Ray Conference — PoS(ICRC2019)*. Sissa Medialab, July 2019. DOI: [10.48550/ARXIV.1909.02036](https://doi.org/10.48550/ARXIV.1909.02036).
- [54] A. D. Morozova et al. The comparison of the calculated atmospheric neutrino spectra with the measurements of IceCube and ANTARES experiments. *Journal of Physics: Conference Series*, 798:012101, 2017. DOI: [10.1088/1742-6596/798/1/012101](https://doi.org/10.1088/1742-6596/798/1/012101).
- [55] E. Akhmedov et al. Matter effects in atmospheric neutrino oscillations. *Physics Letters B*, 300(1-2):128–136, 1993. DOI: [10.1016/0370-2693\(93\)90759-b](https://doi.org/10.1016/0370-2693(93)90759-b).

- [56] A. Sinopoulou and others on behalf of the KM3NeT collaboration. Atmospheric neutrinos with the first detection units of km3net/arca. *Journal of Instrumentation*, 16(11):C11015, 2021. DOI: [10.1088/1748-0221/16/11/C11015](https://doi.org/10.1088/1748-0221/16/11/C11015). URL: <https://dx.doi.org/10.1088/1748-0221/16/11/C11015>.
- [57] A. D. Avrorin et al. Baikal-GVD: status and prospects. *EPJ Web of Conferences*, 191:01006, 2018. V. Volkova et al., editors. DOI: [10.1051/epjconf/201819101006](https://doi.org/10.1051/epjconf/201819101006).
- [58] K. Abe et al. Diffuse supernova neutrino background search at super-kamiokande. *Physical Review D*, 104(12):122002, 2021. DOI: [10.1103/physrevd.104.122002](https://doi.org/10.1103/physrevd.104.122002).
- [59] M. Aartsen et al. Neutrino emission from the direction of the blazar TXS 0506+056 prior to the IceCube-170922a alert. *Science*, 361(6398):147–151, 2018. DOI: [10.1126/science.aat2890](https://doi.org/10.1126/science.aat2890).
- [60] M. Aartsen et al. Multimessenger observations of a flaring blazar coincident with high-energy neutrino IceCube-170922a. *Science*, 361(6398), 2018. DOI: [10.1126/science.aat1378](https://doi.org/10.1126/science.aat1378).
- [61] M. Agostini et al. Comprehensive geoneutrino analysis with borexino. *Physical Review D*, 101(1):012009, 2020. DOI: [10.1103/physrevd.101.012009](https://doi.org/10.1103/physrevd.101.012009).
- [62] T. Araki et al. Experimental investigation of geologically produced antineutrinos with KamLAND. *Nature*, 436(7050):499–503, 2005. DOI: [10.1038/nature03980](https://doi.org/10.1038/nature03980).
- [63] J. A. Formaggio and G. P. Zeller. From ν_e to $\bar{\nu}_e$: neutrino cross sections across energy scales. *Rev. Mod. Phys.* 84, 1307 (2012), May 2013. DOI: [10.1103/RevModPhys.84.1307](https://doi.org/10.1103/RevModPhys.84.1307). arXiv: [1305.7513 \[hep-ex\]](https://arxiv.org/abs/1305.7513).
- [64] B. Zhou and J. F. Beacom. W -boson and trident production in TeV – PeV neutrino observatories. *Phys. Rev. D*, 101:036010, 3, 2020. DOI: [10.1103/PhysRevD.101.036010](https://doi.org/10.1103/PhysRevD.101.036010). URL: <https://link.aps.org/doi/10.1103/PhysRevD.101.036010>.
- [65] S. L. Glashow. Resonant scattering of antineutrinos. *Physical Review*, 118(1):316–317, 1960. DOI: [10.1103/physrev.118.316](https://doi.org/10.1103/physrev.118.316).
- [66] B. Kayser. Are neutrinos their own antiparticles? *J.Phys.Conf.Ser.* 173:012013, 2009, March 2009. DOI: [10.1088/1742-6596/173/1/012013](https://doi.org/10.1088/1742-6596/173/1/012013). arXiv: [0903.0899 \[hep-ph\]](https://arxiv.org/abs/0903.0899).
- [67] I. Esteban et al. Global analysis of three-flavour neutrino oscillations: synergies and tensions in the determination of θ_{23} , δCP , and the mass ordering. *Journal of High Energy Physics*, 2019(1), 2019. DOI: [10.1007/jhep01\(2019\)106](https://doi.org/10.1007/jhep01(2019)106).
- [68] C. Giunti. No effect of majorana phases in neutrino oscillations. *Physics Letters B*, 686(1):41–43, 2010. ISSN: 0370-2693. DOI: <https://doi.org/10.1016/j.physletb.2010.02.020>. URL: <https://www.sciencedirect.com/science/article/pii/S0370269310001942>.
- [69] I. Esteban et al. The fate of hints: updated global analysis of three-flavor neutrino oscillations. *Journal of High Energy Physics*, 2020, September 2020. DOI: [10.1007/JHEP09\(2020\)178](https://doi.org/10.1007/JHEP09(2020)178).
- [70] D. J. Griffiths. *Introduction to Quantum Mechanics*. Cambridge University Press, 2016, page 465. ISBN: 9781107179868.
- [71] L. Ludhova et al. Solar neutrino physics with borexino i. *21st Conference on High Energy Physics, IFAE 2009*, May 2012. DOI: [10.1393/ncc/i2009-10475-7](https://doi.org/10.1393/ncc/i2009-10475-7).

- [72] K. Abe et al. Measurements of neutrino oscillation in appearance and disappearance channels by the t2k experiment with 6.6×10^{20} protons on target. *Physical Review D*, 91(7):072010, 2015. DOI: [10.1103/physrevd.91.072010](https://doi.org/10.1103/physrevd.91.072010).
- [73] C. Giunti and E. M. Zavanin. Predictions for neutrinoless double-beta decay in the 3+1 sterile neutrino scenario, May 2015. DOI: [10.1007/JHEP07\(2015\)171](https://doi.org/10.1007/JHEP07(2015)171). arXiv: [1505.00978](https://arxiv.org/abs/1505.00978) [hep-ph].
- [74] Nobel prize for physics: prof. victor f. hess. *Nature*, 138(3499):873–873, 1936. DOI: [10.1038/138873b0](https://doi.org/10.1038/138873b0).
- [75] F. Donnini. Cosmic ray nuclei: results from AMS-02. *Physics of Atomic Nuclei*, 84(6):956–965, 2021. DOI: [10.1134/s1063778821130081](https://doi.org/10.1134/s1063778821130081).
- [76] L. Accardo et al. High statistics measurement of the positron fraction in primary cosmic rays of 0.5–500 GeV with the alpha magnetic spectrometer on the international space station. *Physical Review Letters*, 113(12):121101, 2014. DOI: [10.1103/physrevlett.113.121101](https://doi.org/10.1103/physrevlett.113.121101).
- [77] M. Aguilar et al. Antiproton flux, antiproton-to-proton flux ratio, and properties of elementary particle fluxes in primary cosmic rays measured with the alpha magnetic spectrometer on the international space station. *Physical Review Letters*, 117(9):091103, 2016. DOI: [10.1103/physrevlett.117.091103](https://doi.org/10.1103/physrevlett.117.091103).
- [78] K. Greisen. End to the cosmic-ray spectrum? *Physical Review Letters*, 16(17):748–750, 1966. DOI: [10.1103/physrevlett.16.748](https://doi.org/10.1103/physrevlett.16.748).
- [79] G. T. Zatsepin and V. A. Kuz'min. Upper Limit of the Spectrum of Cosmic Rays. *Soviet Journal of Experimental and Theoretical Physics Letters*, 4:78, August 1966.
- [80] A. D. Unanue et al. The neutron as an alternative explanation for the trans gzk cosmic rays. *Mod.Phys.Lett.A22:2593-2603,2007*, May 2006. DOI: [10.1142/S0217732307022943](https://doi.org/10.1142/S0217732307022943). arXiv: [hep-ph/0605239](https://arxiv.org/abs/hep-ph/0605239) [hep-ph].
- [81] B. H. J. Mckellar et al. Neutrino clustering and the z-burst model, June 2001. arXiv: [hep-ph/0106123](https://arxiv.org/abs/hep-ph/0106123) [hep-ph].
- [82] T. J. Weiler. Relic Neutrinos, Z-Bursts, and Cosmic Rays above 10^{20} eV, October 1999. arXiv: [hep-ph/9910316](https://arxiv.org/abs/hep-ph/9910316) [hep-ph].
- [83] M. Drees. The top-down interpretation of ultra-high energy cosmic rays. *Journal of the Physical Society of Japan*, 77:16–18, 2003. URL: <https://api.semanticscholar.org/CorpusID:15238792>.
- [84] C. Barbot et al. Neutrinos associated with cosmic rays of top-down origin. *Phys.Lett.B555:22-32,2003*, May 2002. DOI: [10.1016/S0370-2693\(03\)00039-X](https://doi.org/10.1016/S0370-2693(03)00039-X). arXiv: [hep-ph/0205230](https://arxiv.org/abs/hep-ph/0205230) [hep-ph].
- [85] H. J. de Vega and N. Sanchez. Extreme energy cosmic rays: bottom-up vs. top-down scenarii, January 2003. arXiv: [astro-ph/0301039](https://arxiv.org/abs/astro-ph/0301039) [astro-ph].
- [86] L. Maccione and S. Liberati. Gzk photon constraints on planck scale lorentz violation in qed. *JCAP 0808:027,2008*, May 2008. DOI: [10.1088/1475-7516/2008/08/027](https://doi.org/10.1088/1475-7516/2008/08/027). arXiv: [0805.2548](https://arxiv.org/abs/0805.2548) [astro-ph].

- [87] S. T. Scully and F. W. Stecker. Lorentz invariance violation and the observed spectrum of ultrahigh energy cosmic rays. *Astropart.Phys.*31:220-225,2009, November 2008. DOI: [10.1016/j.astropartphys.2009.01.002](https://doi.org/10.1016/j.astropartphys.2009.01.002). arXiv: [0811.2230](https://arxiv.org/abs/0811.2230) [astro-ph].
- [88] W. Bietenholz. Cosmic rays and the search for a lorentz invariance violation, June 2008. DOI: [10.1016/j.physrep.2011.04.002](https://doi.org/10.1016/j.physrep.2011.04.002). arXiv: [0806.3713](https://arxiv.org/abs/0806.3713) [hep-ph].
- [89] L. A. Anchordoqui. Ultrahigh energy cosmic rays: facts, myths, and legends, April 2011. arXiv: [1104.0509](https://arxiv.org/abs/1104.0509) [hep-ph].
- [90] I. C. Maris. The flux and the composition of ultra high energy cosmic rays measured by the pierre auger observatory. In *43rd Rencontres de Moriond on Electroweak Interactions and Unified Theories*, pages 493–498, Paris, France. Moriond, 2008.
- [91] D. J. Bird et al. The cosmic-ray energy spectrum observed by the fly’s eye. 424:491, 1994. DOI: [10.1086/173906](https://doi.org/10.1086/173906).
- [92] C. Evoli. The cosmic-ray energy spectrum, December 2020. DOI: [10.5281/zenodo.4396125](https://doi.org/10.5281/zenodo.4396125). URL: <https://doi.org/10.5281/zenodo.4396125>.
- [93] M. G. Aartsen et al. Measurement of the cosmic ray energy spectrum with IceTop-73. *Physical Review D*, 88(4):042004, 2013. DOI: [10.1103/physrevd.88.042004](https://doi.org/10.1103/physrevd.88.042004).
- [94] N. Busca et al. Pierre auger data, photons, and top-down cosmic ray models. *Physical Review D*, 73(12):123001, 2006. DOI: [10.1103/physrevd.73.123001](https://doi.org/10.1103/physrevd.73.123001).
- [95] D. V. Semikoz. Constraints on top-down models for the origin of uhecrs from the pierre auger observatory data, June 2007. arXiv: [0706.2960](https://arxiv.org/abs/0706.2960) [astro-ph].
- [96] E. Fermi. On the origin of the cosmic radiation. *Physical Review*, 75(8):1169–1174, 1949. DOI: [10.1103/physrev.75.1169](https://doi.org/10.1103/physrev.75.1169).
- [97] M. Ahlers et al. Neutrinos on the rocks: The IceCube yellow book. Research report FERMILAB-FN-0847-A, YITP-SB-10-01, 2010.
- [98] M. G. Aartsen et al. Astrophysical neutrinos and cosmic rays observed by IceCube. *Advances in Space Research*, 62(10):2902–2930, 2018. DOI: [10.1016/j.asr.2017.05.030](https://doi.org/10.1016/j.asr.2017.05.030).
- [99] A. M. Hillas. The origin of ultra-high-energy cosmic rays. *Annual Review of Astronomy and Astrophysics*, 22(1):425–444, 1984. DOI: [10.1146/annurev.aa.22.090184.002233](https://doi.org/10.1146/annurev.aa.22.090184.002233).
- [100] J. K. F. Schmidt. Corsika shower images, 2005. URL: <https://www-zeuthen.desy.de/~jknapp/fs/showerimages.html>.
- [101] M. G. Aartsen et al. Observation and Characterization of a Cosmic Muon Neutrino Flux from the Northern Hemisphere using six years of IceCube data. *The Astrophysical Journal*, 833(1):3, 2016. DOI: [10.3847/0004-637x/833/1/3](https://doi.org/10.3847/0004-637x/833/1/3).
- [102] M. G. Aartsen et al. Characteristics of the diffuse astrophysical electron and tau neutrino flux with six years of icecube high energy cascade data. *Phys. Rev. Lett.* 125, 121104 (2020), January 2020. DOI: [10.1103/PhysRevLett.125.121104](https://doi.org/10.1103/PhysRevLett.125.121104). arXiv: [2001.09520](https://arxiv.org/abs/2001.09520) [astro-ph.HE].

- [103] M. Ageron et al. ANTARES: the first undersea neutrino telescope. *Nuclear Instruments and Methods in Physics Research Section A: Accelerators, Spectrometers, Detectors and Associated Equipment*, 656(1):11–38, 2011. DOI: [10.1016/j.nima.2011.06.103](https://doi.org/10.1016/j.nima.2011.06.103).
- [104] D. Heck et al. Corsika: a monte carlo code to simulate extensive air showers, February 1998.
- [105] A. Fedynitch et al. Calculation of conventional and prompt lepton fluxes at very high energy. *EPJ Web of Conferences*, 99:08001, 2015. D. Berge et al., editors. DOI: [10.1051/epjconf/20159908001](https://doi.org/10.1051/epjconf/20159908001).
- [106] T. Sjöstrand et al. A brief introduction to PYTHIA 8.1. *Computer Physics Communications*, 178(11):852–867, 2008. DOI: [10.1016/j.cpc.2008.01.036](https://doi.org/10.1016/j.cpc.2008.01.036).
- [107] R. S. Fletcher et al. Sibyll: an event generator for simulation of high energy cosmic ray cascades. *Physical Review D*, 50(9):5710–5731, 1994. DOI: [10.1103/physrevd.50.5710](https://doi.org/10.1103/physrevd.50.5710).
- [108] S. J. Brodsky et al. The intrinsic charm of the proton. *Physics Letters B*, 93(4):451–455, 1980. DOI: [10.1016/0370-2693\(80\)90364-0](https://doi.org/10.1016/0370-2693(80)90364-0).
- [109] F. Riehn et al. Hadronic interaction model sibyll 2.3d and extensive air showers. *Physical Review D*, 102(6):063002, 2020. DOI: [10.1103/physrevd.102.063002](https://doi.org/10.1103/physrevd.102.063002).
- [110] K. Abe et al. First gadolinium loading to super-kamiokande. *Nuclear Instruments and Methods in Physics Research Section A: Accelerators, Spectrometers, Detectors and Associated Equipment*, 1027:166248, 2022. DOI: [10.1016/j.nima.2021.166248](https://doi.org/10.1016/j.nima.2021.166248).
- [111] Nobel Lectures and Nobelstiftelsen. *Physics: 1942-1962*. Nobel lectures, including presentation speeches and laureates’ biographies. Nobel Foundation, 1964. URL: <https://books.google.pl/books?id=42y6wAEACAAJ>.
- [112] J. D. Jackson. *Classical Electrodynamics*. Wiley, 1998, page 832. ISBN: 9780471309321.
- [113] D. J. Griffiths. *Introduction to Electrodynamics*. Cambridge University Press, page 620. ISBN: 9781108420419.
- [114] S. Mangano. Optical Properties in Deep Sea Water at the Site of the ANTARES Detector. In *32nd International Cosmic Ray Conference*, volume 4, page 119, August 2011. DOI: [10.7529/ICRC2011/V04/0100](https://doi.org/10.7529/ICRC2011/V04/0100).
- [115] S. Aiello et al. Characterisation of the hamamatsu photomultipliers for the KM3net neutrino telescope. *Journal of Instrumentation*, 13(05):P05035–P05035, 2018. DOI: [10.1088/1748-0221/13/05/p05035](https://doi.org/10.1088/1748-0221/13/05/p05035).
- [116] I. Obodovskiy. Radiation. Fundamentals, applications, risks, and safety, San Diego, 2019.
- [117] T. Hakamata and Editorial Committee. *Photomultiplier Tubes: Basics and Applications*. 3a edition. Hamamatsu Photonics K. K. 3a edition, 2007. URL: https://www.hamamatsu.com/resources/pdf/etd/PMT_handbook_v3aE.pdf.
- [118] H. van Haren. Convection and intermittency noise in water temperature near a deep Mediterranean seafloor. *Physics of Fluids*, 35(2):026604, February 2023. ISSN: 1070-6631. DOI: [10.1063/5.0139474](https://doi.org/10.1063/5.0139474). eprint: https://pubs.aip.org/aip/pof/article-pdf/doi/10.1063/5.0139474/16681310/026604_1_online.pdf. URL: <https://doi.org/10.1063/5.0139474>.

- [119] H. van Haren et al. Half a cubic hectometer mooring array of 3000 temperature sensors in the deep sea. *Journal of Atmospheric and Oceanic Technology*, 38(9):1585–1597, 2021. DOI: <https://doi.org/10.1175/JTECH-D-21-0045.1>. URL: <https://journals.ametsoc.org/view/journals/atot/38/9/JTECH-D-21-0045.1.xml>.
- [120] S. Aiello et al. Determining the neutrino mass ordering and oscillation parameters with KM3net/ORCA. *The European Physical Journal C*, 82(1), 2022. DOI: [10.1140/epjc/s10052-021-09893-0](https://doi.org/10.1140/epjc/s10052-021-09893-0).
- [121] J. Hofestädt et al. Super-ORCA: measuring the leptonic CP-phase with atmospheric neutrinos and beam neutrinos. In *Proceedings of 36th International Cosmic Ray Conference — PoS(ICRC2019)*. Sissa Medialab, 2019. DOI: [10.22323/1.358.0911](https://doi.org/10.22323/1.358.0911).
- [122] A. V. Akindinov et al. Letter of interest for a neutrino beam from protvino to KM3net/ORCA. *The European Physical Journal C*, 79(9), 2019. DOI: [10.1140/epjc/s10052-019-7259-5](https://doi.org/10.1140/epjc/s10052-019-7259-5).
- [123] S. Aiello et al. The KM3net multi-PMT optical module. *Journal of Instrumentation*, 17(07):P07038, 2022. DOI: [10.1088/1748-0221/17/07/p07038](https://doi.org/10.1088/1748-0221/17/07/p07038).
- [124] M. Ageron et al. Dependence of atmospheric muon flux on seawater depth measured with the first KM3net detection units. *The European Physical Journal C*, 80(2), 2020. DOI: [10.1140/epjc/s10052-020-7629-z](https://doi.org/10.1140/epjc/s10052-020-7629-z).
- [125] G. Carminati et al. Atmospheric MUons from PArametric formulas: a fast GEnerator for neutrino telescopes (MUPAGE). *Computer Physics Communications*, 179(12):915–923, 2008. DOI: [10.1016/j.cpc.2008.07.014](https://doi.org/10.1016/j.cpc.2008.07.014).
- [126] T. Antoni et al. The cosmic-ray experiment kascade. *Nuclear Instruments and Methods in Physics Research Section A: Accelerators, Spectrometers, Detectors and Associated Equipment*, 513(3):490–510, 2003. ISSN: 0168-9002. DOI: [https://doi.org/10.1016/S0168-9002\(03\)02076-X](https://doi.org/10.1016/S0168-9002(03)02076-X). URL: <https://www.sciencedirect.com/science/article/pii/S016890020302076X>.
- [127] T. K. Gaisser et al. Cosmic ray energy spectrum from measurements of air showers, March 2013. arXiv: [1303.3565](https://arxiv.org/abs/1303.3565) [astro-ph.HE].
- [128] J. R. Hörandel. On the knee in the energy spectrum of cosmic rays. *Astroparticle Physics*, 19(2):193–220, 2003. DOI: [10.1016/s0927-6505\(02\)00198-6](https://doi.org/10.1016/s0927-6505(02)00198-6).
- [129] O. Adriani et al. PAMELA measurements of cosmic-ray proton and helium spectra. *Science*, 332(6025):69–72, 2011. DOI: [10.1126/science.1199172](https://doi.org/10.1126/science.1199172).
- [130] T. K. Gaisser and M. Honda. Flux of atmospheric neutrinos. *Annual Review of Nuclear and Particle Science*, 52(1):153–199, 2002. DOI: [10.1146/annurev.nucl.52.050102.090645](https://doi.org/10.1146/annurev.nucl.52.050102.090645). eprint: <https://doi.org/10.1146/annurev.nucl.52.050102.090645>.
- [131] A. Fedynitch et al. Influence of hadronic interaction models and the cosmic ray spectrum on the high energy atmospheric muon and neutrino flux. *Phys. Rev. D*, 86:114024, 11, 2012. DOI: [10.1103/PhysRevD.86.114024](https://doi.org/10.1103/PhysRevD.86.114024). URL: <https://link.aps.org/doi/10.1103/PhysRevD.86.114024>.

- [132] T. K. Gaisser. Spectrum of cosmic-ray nucleons, kaon production, and the atmospheric muon charge ratio. *Astroparticle Physics*, 35(12):801–806, 2012. DOI: [10.1016/j.astropartphys.2012.02.010](https://doi.org/10.1016/j.astropartphys.2012.02.010).
- [133] M. Thunman et al. Charm production and high energy atmospheric muon and neutrino fluxes. *Astroparticle Physics*, 5(3-4):309–332, 1996. DOI: [10.1016/0927-6505\(96\)00033-3](https://doi.org/10.1016/0927-6505(96)00033-3).
- [134] A. Ferrari et al. FLUKA: A Multi-Particle Transport Code. Technical report, 2005. DOI: [10.2172/877507](https://doi.org/10.2172/877507).
- [135] H. Fesefeldt. The Simulation of Hadronic Showers: Physics and Applications. Technical report PITHA-85/02, RWTH Aachen, 1985. URL: <http://cds.cern.ch/record/162911/files/CM-P00055931.pdf>.
- [136] S. Bass. Microscopic models for ultrarelativistic heavy ion collisions. *Progress in Particle and Nuclear Physics*, 41:255–369, 1998. DOI: [10.1016/s0146-6410\(98\)00058-1](https://doi.org/10.1016/s0146-6410(98)00058-1).
- [137] K. Werner. Strings, pomerons and the VENUS model of hadronic interactions at ultrarelativistic energies. *Physics Reports*, 232(2-5):87–299, 1993. DOI: [10.1016/0370-1573\(93\)90078-r](https://doi.org/10.1016/0370-1573(93)90078-r).
- [138] S. Ostapchenko. Hadronic interactions at cosmic ray energies. *Nuclear Physics B - Proceedings Supplements*, 175-176:73–80, 2008. DOI: [10.1016/j.nuclphysbps.2007.10.011](https://doi.org/10.1016/j.nuclphysbps.2007.10.011).
- [139] N. N. Kalmykov et al. The Nucleus-nucleus interaction, nuclear fragmentation, and fluctuations of extensive air showers. *Phys. Atom. Nucl.*, 56:346–353, 1993.
- [140] S. Ostapchenko. QGSJET-II: towards reliable description of very high energy hadronic interactions. *Nuclear Physics B - Proceedings Supplements*, 151(1):143–146, 2006. DOI: [10.1016/j.nuclphysbps.2005.07.026](https://doi.org/10.1016/j.nuclphysbps.2005.07.026).
- [141] T. Pierog et al. EPOS LHC: test of collective hadronization with data measured at the CERN large hadron collider. *Physical Review C*, 92(3):034906, 2015. DOI: [10.1103/physrevc.92.034906](https://doi.org/10.1103/physrevc.92.034906).
- [142] E.-J. Ahn et al. Cosmic ray interaction event generator SIBYLL 2.1. *Physical Review D*, 80(9):094003, 2009. DOI: [10.1103/physrevd.80.094003](https://doi.org/10.1103/physrevd.80.094003).
- [143] A. Fedynitch et al. Hadronic interaction model sibyll 2.3c and inclusive lepton fluxes. *Physical Review D*, 100(10):103018, 2019. DOI: [10.1103/physrevd.100.103018](https://doi.org/10.1103/physrevd.100.103018).
- [144] R. Engel et al. The hadronic interaction model sibyll 2.3c and feynman scaling. In *Proceedings of 35th International Cosmic Ray Conference — PoS(ICRC2017)*. Sissa Medialab, 2017. DOI: [10.22323/1.301.0301](https://doi.org/10.22323/1.301.0301).
- [145] M. Rodell et al. The global land data assimilation system. *Bulletin of the American Meteorological Society*, 85(3):381–394, 2004. DOI: [10.1175/bams-85-3-381](https://doi.org/10.1175/bams-85-3-381).
- [146] J. T. Emmert et al. NRLMSIS 2.0: a whole-atmosphere empirical model of temperature and neutral species densities. *Earth and Space Science*, 8(3), 2021. DOI: [10.1029/2020ea001321](https://doi.org/10.1029/2020ea001321).
- [147] P. Virtanen et al. SciPy 1.0: fundamental algorithms for scientific computing in python. *Nature Methods*, 17(3):261–272, 2020. DOI: [10.1038/s41592-019-0686-2](https://doi.org/10.1038/s41592-019-0686-2).

- [148] A. Romanov. *Cosmic ray studies with the KM3NeT neutrino telescope*. PhD thesis, Dipartimento di Fisica dell'Università di Genova, 2023.
- [149] B. Ó Fearraigh. Tuning parametric models of the atmospheric muon flux in MUPAGE to data from the KM3NeT detector. In *Proceedings of 37th International Cosmic Ray Conference — PoS(ICRC2021)*, volume 395, page 1176, 2021. DOI: [10.22323/1.395.1176](https://doi.org/10.22323/1.395.1176).
- [150] M. Reininghaus and R. Ulrich. CORSIKA 8 – towards a modern framework for the simulation of extensive air showers. *EPJ Web of Conferences*, 210:02011, 2019. I. Lhenry-Yvon et al., editors. DOI: [10.1051/epjconf/201921002011](https://doi.org/10.1051/epjconf/201921002011).
- [151] G. Riccobene et al. Deep seawater inherent optical properties in the southern ionian sea. *Astroparticle Physics*, 27(1):1–9, 2007. ISSN: 0927-6505. DOI: [10.1016/j.astropartphys.2006.08.006](https://doi.org/10.1016/j.astropartphys.2006.08.006).
- [152] C. Andreopoulos et al. The GENIE neutrino monte carlo generator. *Nuclear Instruments and Methods in Physics Research Section A: Accelerators, Spectrometers, Detectors and Associated Equipment*, 614(1):87–104, 2010. DOI: [10.1016/j.nima.2009.12.009](https://doi.org/10.1016/j.nima.2009.12.009).
- [153] P. Antonioli et al. A three-dimensional code for muon propagation through the rock: MUSIC. *Astroparticle Physics*, 7(4):357–368, 1997. DOI: [10.1016/s0927-6505\(97\)00035-2](https://doi.org/10.1016/s0927-6505(97)00035-2).
- [154] M. de Jong. Multi-dimensional interpolations in c++, July 2019. arXiv: [1907.02597](https://arxiv.org/abs/1907.02597) [cs.MS].
- [155] S. Agostinelli et al. Geant4—a simulation toolkit. *Nuclear Instruments and Methods in Physics Research Section A: Accelerators, Spectrometers, Detectors and Associated Equipment*, 506(3):250–303, 2003. DOI: [10.1016/s0168-9002\(03\)01368-8](https://doi.org/10.1016/s0168-9002(03)01368-8).
- [156] D. Bailey. *Monte Carlo tools and analysis methods for understanding the ANTARES experiment and predicting its sensitivity to dark matter*. PhD thesis, University of Oxford, 2002.
- [157] R. Brun et al. *GEANT 3: user's guide Geant 3.10, Geant 3.11; rev. version*. CERN, Geneva, 1987. URL: <https://cds.cern.ch/record/1119728>.
- [158] B. D. Marshall. Potassium-calcium decay system. In *Encyclopedia of Earth Science*, pages 525–526. Kluwer Academic Publishers. DOI: [10.1007/1-4020-4496-8_260](https://doi.org/10.1007/1-4020-4496-8_260).
- [159] K. Bachas et al. Studies of catastrophic muon energy losses in ATLAS h8 combined testbeam data. *Nuclear Physics B - Proceedings Supplements*, 177-178:320–321, 2008. DOI: [10.1016/j.nuclphysbps.2007.11.145](https://doi.org/10.1016/j.nuclphysbps.2007.11.145).
- [160] A. Heijboer et al. KM3net/ARCA event reconstruction algorithms. In *Proceedings of 35th International Cosmic Ray Conference — PoS(ICRC2017)*. Sissa Medialab, 2017. DOI: [10.22323/1.301.0950](https://doi.org/10.22323/1.301.0950).
- [161] J. R. Koza et al. Automated design of both the topology and sizing of analog electrical circuits using genetic programming. In *Artificial Intelligence in Design '96*, pages 151–170. Springer Netherlands, 1996. DOI: [10.1007/978-94-009-0279-4_9](https://doi.org/10.1007/978-94-009-0279-4_9).
- [162] A. L. Samuel. Some studies in machine learning using the game of checkers. *IBM Journal of Research and Development*, 3(3):210–229, 1959. DOI: [10.1147/rd.33.0210](https://doi.org/10.1147/rd.33.0210).

- [163] F. Rosenblatt. The perceptron: a probabilistic model for information storage and organization in the brain. *Psychological Review*, 65(6):386–408, 1958. DOI: [10.1037/h0042519](https://doi.org/10.1037/h0042519).
- [164] B. Widrow and M. A. Lehr. 30 years of adaptive neural networks: perceptron, madaline, and backpropagation. *Proceedings of the IEEE*, 78(9):1415–1442, 1990. DOI: [10.1109/5.58323](https://doi.org/10.1109/5.58323).
- [165] S. Islam. Introduction to machine learning. <https://augnitive.com/introduction-to-machine-learning/>, July 2019. URL: <https://augnitive.com/introduction-to-machine-learning/>.
- [166] E. Alpaydin. *Introduction to machine learning*. MIT Press, 2010. ISBN: 9780262012430.
- [167] C. Sammut and G. I. Webb, editors. *Encyclopedia of Machine Learning*. Springer US, 2010. DOI: [10.1007/978-0-387-30164-8](https://doi.org/10.1007/978-0-387-30164-8).
- [168] F. Pedregosa et al. Scikit-learn: machine learning in Python. *Journal of Machine Learning Research*, 12:2825–2830, 2011.
- [169] T. Chen and C. Guestrin. XGBoost: a scalable tree boosting system. In *Proceedings of the 22nd ACM SIGKDD International Conference on Knowledge Discovery and Data Mining, KDD '16*, pages 785–794, San Francisco, California, USA. ACM, 2016. ISBN: 978-1-4503-4232-2. DOI: [10.1145/2939672.2939785](https://doi.org/10.1145/2939672.2939785). URL: <http://doi.acm.org/10.1145/2939672.2939785>.
- [170] G. Ke et al. Lightgbm: a highly efficient gradient boosting decision tree. In I. Guyon et al., editors, *Advances in Neural Information Processing Systems*, volume 30. Curran Associates, Inc., 2017. URL: <https://proceedings.neurips.cc/paper/2017/file/6449f44a102fde848669bdd9eb6b76fa-Paper.pdf>.
- [171] Y. Pati et al. Orthogonal matching pursuit: recursive function approximation with applications to wavelet decomposition. In *Proceedings of 27th Asilomar Conference on Signals, Systems and Computers*, 40–44 vol.1, 1993. DOI: [10.1109/ACSSC.1993.342465](https://doi.org/10.1109/ACSSC.1993.342465).
- [172] K. Crammer et al. Online passive-aggressive algorithms. *Journal of Machine Learning Research*, 7:551–585, March 2006.
- [173] M. A. Fischler and R. C. Bolles. Random sample consensus: a paradigm for model fitting with applications to image analysis and automated cartography. *Commun. ACM*, 24(6):381–395, 1981. ISSN: 0001-0782. DOI: [10.1145/358669.358692](https://doi.org/10.1145/358669.358692). URL: <https://doi.org/10.1145/358669.358692>.
- [174] M. G. Akritas et al. The theil-sen estimator with doubly censored data and applications to astronomy. *Journal of the American Statistical Association*, 90(429):170–177, 1995. ISSN: 01621459. URL: <http://www.jstor.org/stable/2291140> (visited on 03/09/2023).
- [175] P. Huber and E. Ronchetti. *Robust Statistics*. Wiley Series in Probability and Statistics. Wiley, 2011. ISBN: 9781118210338. URL: https://books.google.pl/books?id=j10hquR_j88C.
- [176] E. Fix and J. L. Hodges. Discriminatory analysis. nonparametric discrimination: consistency properties. *International Statistical Review / Revue Internationale de Statistique*, 57(3):238–247, 1989. ISSN: 03067734, 17515823. URL: <http://www.jstor.org/stable/1403797> (visited on 03/09/2023).

- [177] L. Breiman. Random forests. *Machine Learning*, 45:5–32, October 2001. DOI: [10.1023/A:1010950718922](https://doi.org/10.1023/A:1010950718922).
- [178] P. Geurts et al. Extremely randomized trees. *Machine Learning*, 63:3–42, April 2006. DOI: [10.1007/s10994-006-6226-1](https://doi.org/10.1007/s10994-006-6226-1).
- [179] L. Breiman. Bagging Predictors. *Machine Learning*, 24:123–140, 1996. DOI: [10.1007/BF00058655](https://doi.org/10.1007/BF00058655).
- [180] H. Drucker. Improving regressors using boosting techniques. *Proceedings of the 14th International Conference on Machine Learning*, August 1997.
- [181] Y. Freund and R. E. Schapire. A decision-theoretic generalization of on-line learning and an application to boosting. *Journal of Computer and System Sciences*, 55(1):119–139, 1997. DOI: [10.1006/jcss.1997.1504](https://doi.org/10.1006/jcss.1997.1504).
- [182] J. H. Friedman. Greedy function approximation: a gradient boosting machine. *The Annals of Statistics*, 29(5):1189–1232, 2001. ISSN: 00905364. URL: <http://www.jstor.org/stable/2699986> (visited on 03/09/2023).
- [183] A. Tharwat. Classification assessment methods. *Applied Computing and Informatics*, 17(1):168–192, 2020. DOI: [10.1016/j.aci.2018.08.003](https://doi.org/10.1016/j.aci.2018.08.003).
- [184] A. Botchkarev. A new typology design of performance metrics to measure errors in machine learning regression algorithms. *Interdisciplinary Journal of Information, Knowledge, and Management*, 14:045–076, 2019. DOI: [10.28945/4184](https://doi.org/10.28945/4184).
- [185] J. H. W. Jr. Hierarchical grouping to optimize an objective function. *Journal of the American Statistical Association*, 58(301):236–244, 1963. DOI: [10.1080/01621459.1963.10500845](https://doi.org/10.1080/01621459.1963.10500845). eprint: <https://www.tandfonline.com/doi/pdf/10.1080/01621459.1963.10500845>.
- [186] A. Sinopoulou et al. Atmospheric neutrinos with the first detection units of KM3net-ARCA. In *Proceedings of 37th International Cosmic Ray Conference — PoS(ICRC2021)*. Sissa Medialab, 2021. DOI: [10.22323/1.395.1134](https://doi.org/10.22323/1.395.1134).
- [187] ATLAS Collaboration. The atlas experiment at the cern large hadron collider: a description of the detector configuration for run 3, 2023. DOI: [10.48550/ARXIV.2305.16623](https://doi.org/10.48550/ARXIV.2305.16623).
- [188] V. I. Zatsepin and N. V. Sokolskaya. Three component model of cosmic ray spectra from 10 GeV to 100 PeV. *Astronomy & Astrophysics*, 458(1):1–5, 2006. DOI: [10.1051/0004-6361:20065108](https://doi.org/10.1051/0004-6361:20065108).
- [189] A. Fedynitch et al. Calculation of conventional and prompt lepton fluxes at very high energy, March 2015. arXiv: [1503.00544](https://arxiv.org/abs/1503.00544) [[hep-ph](https://arxiv.org/abs/1503.00544)].
- [190] T. Heid. *Characterizing the diffuse neutrino flux with the future KM3NeT/ARCA detector*. PhD thesis, FAU Erlangen-Nürnberg, 2018. URL: <https://opus4.kobv.de/opus4-fau/files/10568/MasterFile.pdf>.
- [191] H. Dembinski et al. Data-driven model of the cosmic-ray flux and mass composition from 10 GeV to 10^{11} GeV. In *Proceedings of 35th International Cosmic Ray Conference — PoS(ICRC2017)*, volume 301, page 533, 2017. DOI: [10.22323/1.301.0533](https://doi.org/10.22323/1.301.0533).

- [192] J. Albrecht et al. The muon puzzle in cosmic-ray induced air showers and its connection to the large hadron collider. *Astrophysics and Space Science*, 367(3), 2022. DOI: [10.1007/s10509-022-04054-5](https://doi.org/10.1007/s10509-022-04054-5).
- [193] M. Reininghaus et al. Air shower genealogy for muon production. In *Proceedings of 37th International Cosmic Ray Conference — PoS(ICRC2021)*, volume 395, page 463, 2021. DOI: [10.22323/1.395.0463](https://doi.org/10.22323/1.395.0463).
- [194] D. Heck and R. Engel. The ehistory and muprod options of the air shower simulation program corsika. *KIT Scientific Working Papers*, 5, 2013. ISSN: 2194-1629. DOI: [10.5445/IR/1000034601](https://doi.org/10.5445/IR/1000034601). 51.53.01; LK 02.
- [195] T.-P. Li and Y.-Q. Ma. Analysis methods for results in gamma-ray astronomy. *The Astrophysical Journal*, 272:317, 1983. DOI: [10.1086/161295](https://doi.org/10.1086/161295).
- [196] R. D. Cousins et al. Evaluation of three methods for calculating statistical significance when incorporating a systematic uncertainty into a test of the background-only hypothesis for a poisson process. *Nuclear Instruments and Methods in Physics Research Section A: Accelerators, Spectrometers, Detectors and Associated Equipment*, 595(2):480–501, 2008. DOI: [10.1016/j.nima.2008.07.086](https://doi.org/10.1016/j.nima.2008.07.086).
- [197] M. J. Basso. Asymptotic formulae for estimating statistical significance in particle physics analyses. *Journal of Physics G: Nuclear and Particle Physics*, 49(2):025001, 2021. DOI: [10.1088/1361-6471/ac3dcd](https://doi.org/10.1088/1361-6471/ac3dcd).
- [198] G. Cowan et al. Asymptotic formulae for likelihood-based tests of new physics. *The European Physical Journal C*, 71(2), 2011. DOI: [10.1140/epjc/s10052-011-1554-0](https://doi.org/10.1140/epjc/s10052-011-1554-0).
- [199] S. S. Wilks. The large-sample distribution of the likelihood ratio for testing composite hypotheses. *The Annals of Mathematical Statistics*, 9(1):60–62, 1938. DOI: [10.1214/aoms/1177732360](https://doi.org/10.1214/aoms/1177732360).
- [200] M. G. Aartsen et al. Characterization of the atmospheric muon flux in IceCube. *Astroparticle Physics*, 78:1–27, 2016. DOI: [10.1016/j.astropartphys.2016.01.006](https://doi.org/10.1016/j.astropartphys.2016.01.006).
- [201] R. Enberg et al. Prompt neutrino fluxes from atmospheric charm. *Physical Review D*, 78(4):043005, 2008. DOI: [10.1103/physrevd.78.043005](https://doi.org/10.1103/physrevd.78.043005).
- [202] T. Pierog et al. EPOS 3 and air showers. *EPJ Web of Conferences*, 210:02008, 2019. I. Lhenry-Yvon et al., editors. DOI: [10.1051/epjconf/201921002008](https://doi.org/10.1051/epjconf/201921002008).
- [203] S. Ostapchenko. QGSJET-III model: physics and preliminary results. *EPJ Web of Conferences*, 208:11001, 2019. B. Pattison et al., editors. DOI: [10.1051/epjconf/201920811001](https://doi.org/10.1051/epjconf/201920811001).
- [204] R. Engel et al. The hadronic interaction model sibyll – past, present and future. *EPJ Web of Conferences*, 145:08001, 2017. B. Pattison, editor. DOI: [10.1051/epjconf/201714508001](https://doi.org/10.1051/epjconf/201714508001).
- [205] H. Dembinski et al. Future proton-oxygen beam collisions at the LHC for air shower physics. In *Proceedings of 36th International Cosmic Ray Conference — PoS(ICRC2019)*. Sissa Medialab, 2019. DOI: [10.22323/1.358.0235](https://doi.org/10.22323/1.358.0235).

- [206] E. Berti et al. LHCf plan for proton-oxygen collisions at LHC. In *Proceedings of 37th International Cosmic Ray Conference — PoS(ICRC2021)*. Sissa Medialab, 2021. DOI: [10.22323/1.395.0348](https://doi.org/10.22323/1.395.0348).
- [207] M. Pitt. Reducing model uncertainties using proton-oxygen collisions with proton/neutron tagging at the LHC. In *Proceedings of 38th International Cosmic Ray Conference — PoS(ICRC2023)*. Sissa Medialab, 2023. DOI: [10.22323/1.444.0426](https://doi.org/10.22323/1.444.0426).
- [208] N. Tomassetti. Direct measurements of galactic cosmic rays. In *Proceedings of 27th European Cosmic Ray Symposium — PoS(ECRS)*. Sissa Medialab, 2023. DOI: [10.22323/1.423.0007](https://doi.org/10.22323/1.423.0007).
- [209] S. Coutu. Galactic cosmic rays: direct measurements, status and perspectives. *Journal of Physics: Conference Series*, 2429(1):012001, 2023. DOI: [10.1088/1742-6596/2429/1/012001](https://doi.org/10.1088/1742-6596/2429/1/012001).
- [210] T. Bister et al. Constraining models for the origin of ultra-high-energy cosmic rays with spectrum, composition, and arrival direction data measured at the pierre auger observatory. In *Proceedings of 38th International Cosmic Ray Conference — PoS(ICRC2023)*. Sissa Medialab, 2023. DOI: [10.22323/1.444.0258](https://doi.org/10.22323/1.444.0258).
- [211] L. Bailly-Salins. Selecting stopping muons with KM3net/ORCA. In *Proceedings of 38th International Cosmic Ray Conference — PoS(ICRC2023)*. Sissa Medialab, 2023. DOI: [10.22323/1.444.0203](https://doi.org/10.22323/1.444.0203).
- [212] T. K. Gaisser et al. Generalized self-veto probability for atmospheric neutrinos. *Phys. Rev. D*, 90:023009, 2, 2014. DOI: [10.1103/PhysRevD.90.023009](https://doi.org/10.1103/PhysRevD.90.023009). URL: <https://link.aps.org/doi/10.1103/PhysRevD.90.023009>.
- [213] S. D. Drell and T.-M. Yan. Massive lepton-pair production in hadron-hadron collisions at high energies. *Physical Review Letters*, 25(5):316–320, 1970. DOI: [10.1103/physrevlett.25.316](https://doi.org/10.1103/physrevlett.25.316).
- [214] R. Abbasi et al. Ictop: the surface component of icecube. *Nuclear Instruments and Methods in Physics Research Section A: Accelerators, Spectrometers, Detectors and Associated Equipment*, 700:188–220, 2013. ISSN: 0168-9002. DOI: <https://doi.org/10.1016/j.nima.2012.10.067>. URL: <https://www.sciencedirect.com/science/article/pii/S016890021201217X>.
- [215] L. D. Landau and I. Pomeranchuk. Electron cascade process at very high-energies. *Dokl. Akad. Nauk Ser. Fiz.*, 92:735–738, 1953.
- [216] J. M. Picone et al. NRLMSISE-00 empirical model of the atmosphere: statistical comparisons and scientific issues. *Journal of Geophysical Research: Space Physics*, 107(A12):SIA 15–1–SIA 15–16, 2002. DOI: [10.1029/2002ja009430](https://doi.org/10.1029/2002ja009430).
- [217] T. Gaisser et al. Seasonal variation of atmospheric muons in IceCube. In *Proceedings of 36th International Cosmic Ray Conference — PoS(ICRC2019)*. Sissa Medialab, 2019. DOI: [10.22323/1.358.0894](https://doi.org/10.22323/1.358.0894).
- [218] P. Alken et al. International geomagnetic reference field: the thirteenth generation. *Earth, Planets and Space*, 73(1), 2021. DOI: [10.1186/s40623-020-01288-x](https://doi.org/10.1186/s40623-020-01288-x).
- [219] E. Weisstein. Point-line distance–3-dimensional. 2002. URL: <https://mathworld.wolfram.com/Point-LineDistance3-Dimensional.html>.

- [220] P. Bourke. Spheres, equations and terminology. April 1992. URL: <http://paulbourke.net/geometry/circlesphere/>.
- [221] I. Cole. *Modelling CPV*. PhD thesis, June 2015. URL: https://repository.lboro.ac.uk/articles/thesis/Modelling_CPV/9523520.
- [222] T. Akiba et al. Optuna. In *Proceedings of the 25th ACM SIGKDD International Conference on Knowledge Discovery & Data Mining*. ACM, 2019. DOI: [10.1145/3292500.3330701](https://doi.org/10.1145/3292500.3330701).
- [223] E. Rodrigues and H. Schreiner. Scikit-hep/particle: version 0.23.0, version v0.23.0, July 2023. DOI: [10.5281/zenodo.8112280](https://doi.org/10.5281/zenodo.8112280). URL: <https://doi.org/10.5281/zenodo.8112280>.